University of Mohamed Boudiaf - M'sila
FACULTY OF TECHNOLOGY
DEPARTMENT OF MECHANICAL ENGINEERING

Serial number: ……

Registration number: **D.GM/3C/03/23**

Thesis
Presented for the graduation of:
DOCTORAT LMD
Sector: Mechanical Engineering
Option: Materials Engineering

THEME

Numerical modeling of a bio composite material reinforced with lignocellulosic fibers grown in the M'sila region

Presented by

Khalil Zouaoui

Supported on: .. / .. / 2026

Examining Committee Members:

First & Family Name	Grade	Establishment	Quality
Abdelkader Djerad	A. Professor	Univ. Of M'sila	President
Mohamed Said Chebbah	Professor	Univ. Of Biskra	Supervisor
Salah Amroune	Professor	Univ. Of M'sila	Co-Supervisor
Mohamed Slamani	Professor	Univ. Of M'sila	Examiner
Said Zergane	Professor	Univ. Of M'sila	Examiner
Mosbah Zidani	Professor	Univ of Batna 2	Examiner
Saib Cherif	Professor	Univ. Of M'sila	Invited

Academic year : 2025/2026

بِسْمِ ٱللَّهِ ٱلرَّحْمَٰنِ ٱلرَّحِيمِ

Acknowledgments

الحمد لله

First and foremost, all praise and gratitude are due to **Allah**, the Almighty, for granting me the strength, patience, and will to complete this work.

My deepest gratitude goes to my thesis supervisor, **Pr. Mohamed Said Chebbah**, and my co-supervisor, **Pr. Salah Amroune**, for their invaluable guidance, unwavering support, and scientific mentorship. Their deep expertise, rigorous academic standards, and continuous encouragement have profoundly shaped my development as a researcher and made this work possible.

I am deeply honoured to present this work before the examining committee. My sincere thanks go to **Dr. Abdelkader Djerad**, who graciously accepted to preside over this jury. I also extend my profound gratitude to the esteemed examiners: **Pr. Mohamed Slamani**, **Pr. Said Zergane**, **Pr. Mosbah Zidani**, and **Pr. Saib Cherif** for generously dedicating their time to review this manuscript and for their insightful evaluation of my work. I extend particular thanks to **Pr. Saib Cherif**, both for his role as examiner and for fostering a supportive academic environment in his capacity as Head of the Mechanical Engineering Department.

I would also like to express my sincere gratitude to **Pr. Messaoud Titoum**, Head of the Laboratory of Materials and Mechanics of Structures (LMMS), as well as to **Pr. Tuncay Yalcinkaya**, Professor at Middle East Technical University in Turkey, and **Dr. Lamia Benhamadouche**. I also extend my thanks to **PhD. Sami Salhi**, **Dr. Abd Raouf Khaldoune**, and **Dr. Belkacem Aoufi**, Assistant Engineers at the University of M'sila, as well as **Djerradi Farouk**, Assistant Engineer at the University of Biskra, and **Dr. Sarra Tablit** from the Laboratory of Multiphasic Polymeric Materials (LMPMP), Faculty of Technology, University Ferhat Abbas Sétif-1, Sétif, and **Dr. Karima Larkat** from the laboratory of City, Environment, Hydraulic and Sustainable Development Faculty of Sciences,University of M’sila, for their invaluable technical assistance.

My sincere thanks also go to my colleagues for the stimulating discussions and shared camaraderie that made the long days in the Laboratory much more rewarding. In particular, I would like to thank my dear friends: **Dr. Aymen Elouanas Asseli**, **Dr. Riyadh Benyettou**, **PhD. Khadraoui Seif Eddine**, and Sheikh **Ammar Soltani**.

To everyone who contributed, directly or indirectly, to the realisation of this thesis:

Thank you.

Dedication

To **my parents**, may God protect them, whose endless sacrifices, unconditional love, and constant prayers have been the bedrock of my life and education, and to **my brothers** and **sisters**, especially my brother **Sofiane** who stood by my side throughout this journey; I dedicate this achievement to you, and to **her** who will share every road ahead.

Table of contents

Abstract I

ملخص II

Résumé III

General Introduction 1

Chapter I

Composite Materials and Sandwich Structures: Overview and Literature Review

I.1 Introduction 5

I.2 History and evolution of materials use 5

I.3 Composite materials: definition and general principles 7

I.4 Classification of composite materials 8

I.4.1 Classification based on the matrix material 9

I.4.2 Classification based on reinforcement types 12

I.4.2.2 Classification by nature of the fibres 14

I.4.2.2.1 Synthetic (synthetic-fibre) reinforcements 14

I.5 Focus: plant fibres relevant to this thesis 18

I.5.1 Flax fibre 18

I.5.2 Jute fibre 19

I.5.3 Sisal fibre 20

I.5.4 Kenaf fibre 20

I.5.5 Palm fibre (Phoenix dactylifera) 21

I.6 Fibre–matrix interface and adhesion 23

I.7 Additive manufacturing of polymer composites 24

I.7.1 Overview of the main additive manufacturing technologies 24

I.7.2 Fused deposition modelling: principle and evolution 26

I.7.3 Fibre-reinforced FDM filaments 27

I.7.4 Geometric and structural factors in FDM parts 29

I.8 Sandwich structures with cellular cores 30

I.8.1 Historical development and applications 30

I.8.2 Conventional cores versus bio-based additively manufactured cores 31

I.8.3 Core topologies reported in the literature 32

I.8.4 Face-sheet materials and face-sheet/core interface 34

I.9 Numerical simulation of biocomposite sandwich panels 35
I.9.1 Governing equations and finite element discretisation 35
I.9.2 Constitutive modelling of composite sandwich constituents 37
I.9.2.1 Orthotropic elastic model for the face-sheet laminate 37
I.9.2.2 Isotropic elastic-plastic model for the core 37
I.9.2.3 Element types and interface treatment 38
I.9.3 Validation metrics 38
I.9.4 Prior work on the numerical simulation of FDM-printed biocomposite sandwich panels 39
I.10 Conclusion 43

Chapter II: **Materials and Methods**

II.1 Introduction 46
II.2 Raw materials 46
II.2.1 Lignocellulosic fibres 46
II.2.2 Epoxy matrix 46
II.2.3 Thermoplastic filaments 46
II.3 Fibre extraction and treatment 47
II.3.1 Plant provenance and pre-extraction handling 47
II.3.2 Typha latifolia: alkaline delignification 48
II.3.3 Agave americana: mechanical decortication 48
II.4 Physicochemical, thermal and single-fibre mechanical characterisation 51
II.4.1 Fourier transform infrared spectroscopy (FTIR) 51
II.4.2 Thermogravimetric analysis (TGA) 51
II.4.3 X-ray diffraction and cellulose crystallinity 52
II.4.4 Single-fibre tensile testing 53
II.5 Face-sheet fabrication 55
II.5.1 Epoxy matrix working properties 55
II.5.2 Layup sequence and hand lamination 56
II.5.3 Cold pressing, curing, and specimen sectioning 56
II.6 Core design and additive manufacturing 57
II.6.1 Core geometries 57
II.7 Sandwich panel assembly 59
II.8 Mechanical testing protocols 60
II.8.1 Tensile testing 60

II.8.2 Three-point bending of sandwich specimens 62
II.8.3 Energy absorption metrics 63
II.9 Statistical analysis (Kruskal–Wallis) 64
II.10 Process-parameter study on FDM-printed PLA tensile coupons 65
II.10.1 Experimental design 65
II.10.2 Taguchi signal-to-noise analysis 66
II.10.3 Artificial neural network modelling 67
II.11 Finite element modelling in ABAQUS 68
II.11.1 Tensile finite element model of FDM-printed PLA specimens with paired apertures (ABAQUS/Explicit) 69
II.11.2 Three-point bending finite element model of the sandwich panels (ABAQUS/CAE Standard) 73
II.12 Conclusion 76
Chapter III: Characterisation of Typha latifolia and Agave americana fibres
III.1 Introduction 79
III.2 FTIR analysis 79
III.2.1 Spectral signatures of Typha and Agave 79
III.2.2 Comparative interpretation 80
III.3 Thermogravimetric and derivative thermogravimetric analysis (TGA-DTG) 80
III.3.1 Mass-loss curves and decomposition stages 80
III.3.2 Char residue and thermal stability indicators 81
III.4 X-ray diffraction and cellulose crystallinity 82
III.4.1 Diffractograms and cellulose-Iβ identification 82
III.4.2 Segal crystallinity index 83
III.4.3 Apparent crystallite size along the [200] direction 84
III.5 Single-fibre tensile testing 85
III.5.1 Fibre cross-section measurement 85
III.5.2 Test campaign and stress–strain behaviour 86
III.5.3 Statistical scatter and coefficient of variation 88
III.5.4 Tensile strength and Young's modulus 88
III.5.5 Synthesis of the single-fibre tensile results 89
III.6 Comparative summary and benchmarking 90
III.6.1 Synthesis table 90
III.6.2 Comparative interpretation 92
III.6.3 Structure property synthesis 93

III.7 Conclusion 94

Chapter IV: Mechanical and numerical study of FDM-printed PLA

IV.1 Introduction 96

IV.2 Tensile response of FDM-printed PLA 96

IV.2.1 Test campaign 96

IV.2.2 Stress–strain behaviour of the 27 specimens 97

IV.2.3 Rationale for predictive modelling 98

IV.3 Taguchi L9 signal-to-noise analysis 99

IV.3.1 Main-effect analysis 99

IV.3.2 Optimal parameter set and correlation with the experimental data 101

IV.4 Artificial neural network modelling 102

IV.4.1 Network architecture and training 102

IV.4.2 Predicted versus experimental responses 103

IV.4.3 Comparison with the Taguchi predictive model 104

IV.5 Effect of aperture (hole) angle on FDM-PLA tensile behaviour 105

IV.5.1 Experimental stress–strain response 105

IV.5.2 Maximum gross-section nominal stress ($\sigma_{nom,max}$) versus aperture angle 106

IV.5.3 Apparent (structural) Young's modulus (E_{app}) versus aperture angle 107

IV.5.4 Synthesis of the experimental results 109

IV.6 ABAQUS/Explicit finite element modelling of the apertured specimens 110

IV.6.1 Constitutive calibration from the experimental tensile data 110

IV.6.2 Validation against the experimental stress–strain curves 110

IV.6.3 Von Mises stress field analysis 113

IV.7 Conclusion 114

Chapter V

Sandwich panels: mechanical performance, energy absorption and finite element simulation

V.1 Introduction 116

V.2 Tensile behaviour of the sandwich constituents 116

V.2.1 Test matrix 116

V.2.2 Stress–strain response 116

V.3 Three-point bending of the sandwich panels 117

V.3.1 Flexural response by core geometry 117

V.3.2 Core shear stress and flexural modulus 120

V.3.3 Interface integrity and failure modes 121
V.4 Energy absorption analysis 122
V.4.1 Analytical and numerical integration 122
V.4.2 Energy absorption by core material and geometry 123
V.4.3 Specific energy absorption (SEA) 124
V.4.4 Mechanistic synthesis 125
V.5 Statistical analysis of the mechanical performance 126
V.5.1 Kruskal–Wallis analysis 126
V.5.2 Post-hoc pairwise comparisons (Dunn–Bonferroni) 129
V.5.3 Reliability and scatter analysis 129
V.6 Finite element modelling of the honeycomb sandwich 130
V.6.1 Modelling scope and calibration 130
V.6.2 Load–deflection validation 131
V.6.3 Deformation field and failure zones 133
V.6.4 Limitations and implications 134
V.7 Conclusion 135
General Conclusion 137
References 140

List of Figures

Chapter Ⅰ

Fig. I. 1 Chronological timeline of the evolution of engineering materials 7
Fig. I. 2 Schematic cross-section of a generic fibre-reinforced composite illustrating the three essential constituents: fibre, matrix, and the fibre-matrix interface. 8
Fig. I. 3 Hierarchical classification tree of composite materials 9
Fig. I. 4 The microstructure of Hybrid Metal Matrix Composite. 10
Fig. I. 5 Representative example of a Ceramic Matrix Composite: SEM micrograph of a SiC/SiC. 11
Fig. I. 6 Schematic of the main architectures of continuous and discontinuous fibre reinforcement 13
Fig. I. 7 Representative synthetic fibre reinforcements: (a) glass fibre, (b) carbon fibre, (c) aramid fibre, and (d) steel fibre (MFRPs). 15
Fig. I. 8 natural fiber Chemical composition. 18
Fig. I. 9 Flax fiber structure 19
Fig. I. 10 (a) Jute plant ; (b) Raw jute fabric ; (c) Unidirectional jute fiber ; (d) Woven jute fiber 19
Fig. I. 11 Sisal fiber 20
Fig. I. 12 Kenaf fibre 21
Fig. I. 13 Palm fibre (Phoenix dactylifera) 22
Fig. I. 14 Schematic comparison of the main polymer additive manufacturing technologies .25
Fig. I. 15 Working principle of an FDM machine 27
Fig. I. 16 Fabrication of filament from HDPE and glass-fibre composites 28
Fig. I. 17 The various composite filaments, (a) PLA/PP filament, (b) ArF reinforced filament, from left to right, Un, Alk and SLN respectively. 29
Fig. I. 18 Different core structures in sandwich composites. 30
Fig. I. 19 A schematic diagram illustrating the optimization calculation, preparation, and application of the natural honeycomb mechanical properties. 32
Fig. I. 20 Cellular core topologies for FDM-printed sandwich panels. 34
Fig. I. 21 Experimental and numerical simulation load–displacement plots. 35
Fig. I. 22 Three-Point Bending Simulation and Stress Analysis of Cellular Structures 39
Fig. I. 23 The boundary conditions and sample after failure with the failed region. 40

Fig. I. 24 Failure modes of sandwich panels (using a honeycomb structure as an example) at maximum load, as observed in experiments and simulated via finite element (FE) results: (a) O-PLA; (b) B-PLA. 41
Fig. I. 25 Boundary conditions and loading direction applied in the finite element (FE) model. 42
Fig. I. 26 Effect of cell size on the bending response and panel wrinkling deformation in origami-enhanced honeycomb (OHB) sandwich beams. 43

Chapter Ⅱ

Fig. II. 1 Schematic representation of the fibre extraction procedures. 49
Fig. II. 2 Fibre extraction sequences for Typha latifolia stems and Agave americana leaves. 50
II. 3 Single-fibre tensile test configuration on cardboard frame (ASTM D3822, 30 mm gauge length)..... 54
Fig. II. 4 Hybrid Typha/Agave/epoxy face-sheet fabrication. 57
Fig. II. 5 Core preparation: filament feedstock, FDM printing, completed cores, and unit-cell geometry. 59
Fig. II. 6 Sandwich panel assembly (PATECs and PFATECs configurations). 60
Fig. II. 7 CNC machining of Agave/Typha-epoxy tensile coupons (ASTM D618 geometry).61
Fig. II. 8 Tensile test setup on Instron UTM (ASTM D618, 10 kN load cell, 2 mm·min^{-1}). .. 62
Fig. II. 9 Three-point bending test of sandwich specimens (ASTM C393, Instron 5969, 136 mm support span). 63
Fig. II. 10 FDM-printed neat PLA tensile specimens (27 coupons) and tensile-test setup..... 66
Fig. II. 11 Schematic of the artificial neural network architecture..... 67
Fig. II. 12 Specimen geometry and aperture-angle configurations. 70
Fig. II. 13 FDM-printed PLA aperture specimens during and after printing. 71
Fig. II. 14 Loading and meshing parameters of the tensile finite element model in ABAQUS/Explicit. 73
Fig. II. 15 Three-point bending finite element model of the sandwich panel in ABAQUS/CAE Standard. 76

Chapter Ⅲ

Fig. III. 1 FTIR spectra of Typha latifolia and Agave americana fibres. 80
Fig. III. 2 Thermal decomposition analysis of Typha latifolia and Agave americana fibres. .. 82
Fig. III. 3 X-ray diffraction patterns of Typha latifolia and Agave americana fibres. 83
Fig. III. 4 Optical micrographs of single fibres with positional diameter measurements. 86

Fig. III. 5 Representative stress–strain curves of single Agave and Typha fibres. 87

Chapter Ⅳ

Fig. IV. 1 Engineering stress vs strain curves of the 27 FDM-printed PLA coupons..... 97
Fig. IV. 2 FDM-printed PLA tensile specimens grouped by extruder temperature and filling density. 98
Fig. IV. 3 Taguchi main-effect plots of the three mechanical responses. 100
Fig. IV. 4 ANN training convergence and regression plots. 103
Fig. IV. 5 Comparative predictive performance of the Taguchi signal-to-noise analysis and the artificial neural network model on the 27 FDM-printed PLA coupons. 104
Fig. IV. 6 Stress vs strain curves of the apertured FDM-PLA specimens. 105
Fig. IV. 7 All 27 specimens after tensile test 106
Fig. IV. 9 Comprehensive mechanical properties analysis: (a) σnom,max vs. Eapp scatter plot for all 27 specimens, (b) Mean σnom,max variation with aperture angle, (c) Percentage reduction in σnom,max relative to solid configuration, and (d) Mean Eapp variation with aperture angle. 109
Fig. IV. 10 Finite element prediction of Von Mises stress field and fracture at $\sigma_{nom,max}$ for solid specimen. 111
Fig. IV. 11 Finite element validation: experimental vs. simulated curves. 112

Chapter Ⅴ

Fig. V. 1 Tensile stress–strain responses of neat PLA, PLA/flax biocomposite and Typha/Agave/epoxy hybrid laminate under ASTM D618 testing conditions. 117
Fig. V. 2 Load–deflection response of the six sandwich configurations in three-point bending: (a) neat PLA cores with three core geometries (honeycomb, circular, tri-grid); (b) PLA/flax biocomposite cores with the same three core geometries. 118
Fig. V. 3 Energy absorption per unit volume of the six sandwich configurations, grouped by core material and core geometry. 124
Fig. V. 4. Specific energy absorption (SEA) of the six sandwich configurations..... 125
Fig. V. 5. Box-plot visualisation of the mechanical performance of the sandwich panels with the three core geometries: (a) core shear strength τ; (b) flexural modulus E; (c) energy absorption EA. Each panel reports the PLA/flax and the neat PLA data side by side. 127

Fig. V. 6. Load–deflection validation: overlay of the experimental (solid lines) and the ABAQUS/CAE-predicted (dashed lines) responses for (a) the PLA/flax honeycomb sandwich and (b) the neat PLA honeycomb sandwich..... 132
Fig. V. 7 ABAQUS/CAE-predicted deformation patterns and von Mises stress contours at peak load of the honeycomb sandwich configurations: (a) PLA/flax core; (b) neat PLA core..... 134

List of Tables

Chapter Ⅰ

Table I. 1 Chemical composition of different natural fibres 17
Table I. 2 Comparison of the geometrical and mechanical properties for date palm fiber with values reported in the literature for other fibers 22
Table I. 3 Summary of 3D printing techniques and their specifications 25

Chapter Ⅱ

Table II. 1 Filament specifications and nominal properties (manufacturer data). 47
Table II. 2 Geographical and climatic characteristics of the collection sites. 48
Table II. 3 Key extraction parameters for both fibre types. 50
Table II. 4 Summary of the fibre characterisation techniques. 55
Table II. 5 Epoxy resin system working properties (manufacturer data, TDS rev. 07, 08/2020). 56
Table II. 6 Core configuration summary. 58
Table II. 7 FDM process parameters used for the sandwich cores. 58
Table II. 8 Factors and levels of the FDM process-parameter study (3^3 factorial, 27 specimens). 66
Table II. 9 Filament specifications and FDM print parameters held constant across all 27 apertured specimens. 70
Table II. 10 Material Properties. 74

Chapter Ⅲ

Table III. 1 Thermal stability indicators of Typha latifolia and Agave americana fibres extracted from the TGA-DTG analysis..... 81
Table III. 2 Segal crystallinity index of Typha latifolia and Agave americana fibres. 83
Table III. 3 Apparent crystallite size along the [200] direction obtained from the Scherrer equation (K = 0.9, λ = 1.5406 Å, instrumental broadening 0.1° assumed Gaussian). 84
Table III. 4 Single-fibre tensile properties of Typha latifolia and Agave americana: ultimate tensile strength, Young's modulus, and coefficient of variation (n = 15 per species). CE = chemically extracted; ME = mechanically extracted. 89
Table III. 5 Comparison of physical, chemical, mechanical, crystallographic and thermal properties of Typha latifolia and Agave americana (this study) with literature data for four reference natural fibres. CE = chemical extraction; ME = mechanical extraction; (in) = inferred from FTIR / TGA analyses..... 91

Chapter Ⅳ

Table IV. 1 Correlation coefficients between the Taguchi-predicted and the experimentally measured responses of the 27 FDM-printed PLA coupons. 101

Table IV. 2 Experimental maximum gross-section nominal stress ($\sigma_{nom,max}$)for all nine configurations, n = 3 replicates per configuration. The percentage reduction is computed against the solid reference (27.23 MPa). 106

Table IV. 3 Experimental apparent (structural) Young's modulus (E_{app})for all nine configurations, extracted from the linear regression of σ_{nom} on engineering strain over the 5–40 % $\sigma_{nom,\,max}$ range, n = 3 replicates per configuration. 108

Chapter Ⅴ

Table V. 2 Tensile properties of the three sandwich constituents (ASTM D618). 117

Table V. 3 Maximum bending stress of the six sandwich configurations in three-point bending (ASTM C393). 118

Table V. 4 Mean energy absorption per unit volume of the six sandwich configurations ($MJ \cdot m^{-3}$). 123

Table V. 5 Kruskal–Wallis analysis of the mechanical properties of the sandwich panels. 126

Table V. 6 Dunn–Bonferroni post-hoc pairwise comparisons of core shear strength (τ), apparent flexural modulus (E), and energy absorption (EA) across the three core geometries. 129

Table V. 7 Finite element validation metrics for the honeycomb sandwich configurations. 132

Abbreviations

PLA: Polylactic Acid

PLA/flax: Polylactic Acid / Flax Biocomposite

PE: Polyethylene

PP: Polypropylene

ABS: Acrylonitrile-Butadiene-Styrene

PETG: Polyethylene Terephthalate Glycol-Modified

PA: Polyamide

PHA: Polyhydroxyalkanoate

PBS: Polybutylene Succinate

PVC: Polyvinyl Chloride

UP: Unsaturated Polyester

MMCs: Metal Matrix Composites

CMCs: Ceramic Matrix Composites

PMCs: Polymer Matrix Composites

GFRP: Glass Fiber-Reinforced Polymer

CFRP: Carbon Fiber-Reinforced Polymer

AFRP: Aramid Fiber-Reinforced Polymer

MFRPs: Metallic Fibre-Reinforced Composites

NFRCs: Natural Fiber Reinforced Composites

SFRC: Steel-Fibre-Reinforced Concrete

PATECs: Sandwich panels with hybrid Agave/Typha/epoxy face sheets and Neat PLA cores

PFATECs: Sandwich panels with hybrid Agave/Typha/epoxy face sheets and PLA/Flax biocomposite cores

FDM: Fused Deposition Modelling

FFF: Fused Filament Fabrication

SLA: Stereolithography

DLP: Digital Light Processing

SLS: Selective Laser Sintering

CNC: Computer Numerical Control

AM: Additive Manufacturing

ASTM: American Society for Testing and Materials

ISO: International Organization for Standardization

FTIR: Fourier Transform Infrared Spectroscopy

ATR-FTIR: Attenuated Total Reflectance – Fourier Transform Infrared Spectroscopy

TGA: Thermogravimetric Analysis

DTG: Derivative Thermogravimetric

XRD: X-ray Diffraction

SEM: Scanning Electron Microscopy

ANN: Artificial Neural Network

RSM: Response Surface Methodology

DOE: Design of Experiments

ANOVA: Analysis of Variance

S/N: Signal-to-Noise Ratio

MSE: Mean Squared Error

FEA: Finite Element Analysis

FEM: Finite Element Method

Notations

A: Cross-sectional area (mm^2)

A_o: Gross (unperforated) cross-sectional area (mm^2)

A_{net}: Net cross-sectional area (mm^2)

E: Young's modulus (GPa or MPa)

E_{app}: Apparent (structural) Young's modulus (MPa)

EA: Total energy absorption (J or $MJ \cdot m^{-3}$)

F: Force or applied load (N)

F_{max}: Maximum force or peak load (N)

I_{200}: Intensity of the (200) crystalline reflection (counts)

I_{am}: Intensity of the amorphous background (counts)

K: Scherrer constant (0.9, dimensionless)

L_{200}: Apparent crystallite size along the [200] direction (nm)

m: Mass (g or kg)

MCF: Mean crushing force (N)

P: Applied load (N)

PCF: Peak crushing force (N)

SEA: Specific energy absorption ($J \cdot kg^{-1}$)

T_{onset}: Onset degradation temperature (°C)

T_{max}: Peak degradation temperature (°C)

U: Absorbed strain energy per unit volume ($MJ \cdot m^{-3}$)

U_{trapz}: Energy absorption by trapezoidal integration ($MJ \cdot m^{-3}$)

U_{vol}: Energy absorption by closed-form approximation ($MJ \cdot m^{-3}$)

δ: Displacement or deflection (mm)

ε: Engineering strain (dimensionless or %)

ε_{eng}: Engineering strain

ε_{true}: True strain

ε_{max}: Maximum strain

θ: Aperture angle or diffraction angle (°)

θ_c: Threshold angle between two-hole-cut and one-hole-cut regime (°)

λ: Wavelength (Å)

ν: Poisson's ratio (dimensionless)

ρ: Density ($g \cdot cm^{-3}$)

σ: Engineering stress (MPa)

σ_u: Ultimate tensile strength (MPa)

$\sigma_{nom,max}$: Maximum gross-section nominal stress (MPa)

$\sigma_{net,max}$: Maximum net-section stress (MPa)

σ_{true}: True stress (MPa)

τ: Core shear stress (MPa)

CrI: Crystallinity Index by the Segal method (%)

FWHM: Full-Width at Half-Maximum of the (200) reflection (°)

Abstract

The growing demand for sustainable materials has intensified the search for bio-based alternatives to synthetic composites, yet numerous regional lignocellulosic resources remain underexploited in structural applications. This doctoral thesis addresses this gap by developing hybrid sandwich panels reinforcing Typha latifolia and Agave americana fibres, harvested from the M'Sila Province, as face sheets bonded to FDM-printed neat PLA and PLA/flax cores. Fibres were extracted through mild alkaline delignification and mechanical decortication, then characterised through infrared spectroscopy, thermogravimetry, X-ray diffraction, and single-fibre tensile testing, revealing a clear structure property complementarity between the two species. Preparatory studies optimised FDM-printed PLA through a combined Taguchi–neural network framework and validated an explicit finite element model of apertured-tensile behaviour. Hybrid face sheets bonded to honeycomb, circular, and tri-grid cores were then tested in three-point bending and simulated in ABAQUS. The tri-grid core delivered the highest flexural strength for both core materials. A notable inversion of the energy-absorption ranking also emerged: the circular core, which did not lead with neat PLA, became the most energy-absorbent configuration when the flax-reinforced core was used, outperforming all other geometries. The finite element model reproduced the experimental load–deflection response with close quantitative agreement. This work demonstrates that lignocellulosic fibres from the semi-arid lands of M'Sila can be transformed into hybrid sandwich structures mechanically competitive with conventional composites, furnishing a validated experimental and numerical framework for their structural exploitation.

Keywords: Hybrid sandwich panels; Typha latifolia; Agave americana fibres; Fused deposition modelling (FDM); PLA/flax bio composite; ABAQUS finite element simulation.

ملخص

تزايد الطلب على المواد المستدامة كثّف البحث عن بدائل حيوية للمركبات الاصطناعية، غير أن العديد من الموارد الليجنوسليلوزية المحلية لا تزال غير مستغلة في التطبيقات الهيكلية. تعالج هذه الأطروحة هذه الفجوة عبر تطوير ألواح شطيرة هجينة بألياف التيفا لاتيفوليا والأغاف أمريكانا، المجنية من ولاية المسيلة، كألواح وجه ملتصقة بنوى مطبوعة بتقنية النمذجة بالترسيب المنصهر من حمض عديد اللبنيك النقي ومن خليطه مع ألياف الكتان. استُخلصت الألياف بمعالجة قلوية معتدلة وتقشير ميكانيكي، ثم خضعت لتوصيف بالتحليل الطيفي بالأشعة تحت الحمراء، والتحليل الحراري الوزني، وحيود الأشعة السينية، واختبار الشد على الليف الواحد، مما كشف عن تكامل بنيوي-وظيفي واضح بين النوعين. تضمنت الدراسات التحضيرية تحسين طباعة PLA بإطار مدمج من طريقة تاقوتشي والشبكات العصبونية، والتحقق من نموذج عناصر منتهية صريح لسلوك الشد بوجود ثقوب. بعدها صُنعت ألواح وجه هجينة ملتصقة بنوى قرص العسل والدائرية والشبكية الثلاثية، واختُبرت بالانحناء ثلاثي النقاط وحوْسبت في برنامج ABAQUS. أظهرت النوى الشبكية الثلاثية أعلى مقاومة انحناء لكلا النوعين. كما برز انعكاس لافت في ترتيب امتصاص الطاقة: النواة الدائرية، التي لم تتصدر مع PLA النقي، أصبحت الأكثر امتصاصاً للطاقة مع القلب المدعّم بالكتان، متجاوزةً سائر التكوينات. استطاع نموذج العناصر المنتهية محاكاة منحنييْ الحمل-الانحناء التجريبيين بتطابق كمي وثيق. يثبت هذا العمل إمكانية تحويل ألياف المسيلة شبه الجافة إلى هياكل شطيرة هجينة تنافس ميكانيكياً المركبات التقليدية، مقدماً إطاراً تجريبياً وعددياً موثقاً لتثمينها هيكلياً.

الكلمات المفتاحية: ألواح الشطيرة الهجينة؛ ألياف التيفا لاتيفوليا؛ ألياف الأغاف أمريكانا؛ النمذجة بالترسيب المنصهر؛ مركب PLA/كتان الحيوي؛ محاكاة العناصر المنتهية ABAQUS.

Résumé

La demande croissante en matériaux durables a intensifié la recherche d'alternatives biosourcées aux composites synthétiques, pourtant de nombreuses ressources lignocellulosiques régionales restent sous-exploitées dans les applications structurales. Cette thèse de doctorat comble cette lacune en développant des panneaux sandwich hybrides renforcés de fibres de Typha latifolia et d'Agave americana, récoltées dans la wilaya de M'Sila, comme semelles collées à des cœurs imprimés par modélisation par dépôt de fil fondu en PLA pur et en biocomposite PLA/lin. Les fibres ont été extraites par traitement alcalin doux et décorticage mécanique, puis caractérisées par spectroscopie infrarouge, thermogravimétrie, diffraction des rayons X et essai de traction sur fibre unitaire, révélant une complémentarité structure–propriétés claire entre les deux espèces. Des études préparatoires ont optimisé le PLA imprimé par un cadre combiné Taguchi–réseau de neurones et ont validé un modèle éléments finis explicite du comportement en traction avec ouvertures. Des semelles hybrides collées à des cœurs en nid d'abeille, circulaires et tri-grille ont ensuite été testées en flexion trois points et simulées sous ABAQUS. Le cœur tri-grille a fourni la plus haute résistance en flexion pour les deux matériaux. Une inversion notable du classement de l'absorption d'énergie est également apparue : le cœur circulaire, qui ne menait pas avec le PLA pur, est devenu la configuration la plus absorbante avec le cœur renforcé de lin, surpassant toutes les autres géométries. Le modèle éléments finis a reproduit la réponse expérimentale charge–flèche avec une concordance quantitative étroite. Ce travail démontre que les fibres lignocellulosiques issues des terres semi-arides de M'Sila peuvent être transformées en structures sandwich hybrides mécaniquement compétitives face aux composites conventionnels, fournissant un cadre expérimental et numérique validé pour leur valorisation structurale.

Mots-clés : Panneaux sandwich hybrides ; Typha latifolia ; fibres d’Agave americana ; Modélisation par dépôt de fil fondu (FDM) ; Biocomposite PLA/lin ; Simulation par éléments finis ABAQUS.

General Introduction

General Introduction

Conventional engineering materials used in structural and semi-structural applications have long relied on non-renewable resources and on manufacturing routes whose environmental footprints are increasingly difficult to reconcile with contemporary sustainability requirements. The depletion of fossil feedstocks, the accumulation of non-biodegradable end-of-life waste,[1] and the tightening of regulatory pressure on synthetic polymer composites have generated a strong industrial demand for bio-based structural alternatives capable of delivering competitive mechanical performance at a reduced environmental cost[2].

Among the candidate alternatives, composites reinforced with lignocellulosic plant fibres have emerged as one of the most promising families,thanks to the renewability of the reinforcement, the low embodied energy of the processing chain, and the biodegradability of the end of life products. The parallel maturation of polymer additive manufacturing, and more specifically of fused deposition modelling (FDM), has opened a new design space in which cellular cores with complex topologies can be produced directly from bio-based filaments. The assembly of such additively manufactured cores with natural-fibre-reinforced laminated face sheets defines a new generation of bio-based sandwich panels whose mechanical performance, reliability and numerical predictability must now be systematically established[3].

Several questions remain insufficiently addressed in the current literature. The lignocellulosic species Typha latifolia and Agave americana, which grow without irrigation in the semi-arid province of M'Sila, have received only fragmented attention as reinforcements for structural biocomposites, and their intrinsic properties have not been systematically characterised as a prerequisite for any numerical treatment. The experimental programme, within which the numerical framework is embedded, combines regional natural-fibre laminates with FDM-printed bio-based cores of various cellular topologies has not yet been investigated in an integrated manner in the published literature. Finally, a computationally efficient finite element framework predicting the mechanical response of such hybrid biocomposite assemblies from the constituent properties has not yet been proposed or experimentally validated. These three gaps, taken together, define the problematic of the present thesis.

The main goal of this thesis is to comprehensively investigate the experimental and numerical behaviour of hybrid sandwich panels comprising regionally sourced natural-fibre face sheets and FDM-printed bio-based cellular cores. The specific objectives encompass:

- Fibre Characterisation: To assess the chemical, thermal, crystallographic, and mechanical properties of regional Typha latifolia and Agave americana fibres using a comprehensive four-technique pipeline (FTIR, TGA, XRD, and single-fibre tensile testing).

- Process Modelling: To establish a predictive process–property framework for FDM-printed neat PLA and PLA/flax using Taguchi and ANN methodologies, and to quantify the impact of geometric apertures on the polymer's tensile response.
- Hybrid Sandwich Assessment: To manufacture and systematically evaluate the flexural performance, energy-absorption capacity, and failure modes of panels combining the regional face sheets with multi-topology FDM-printed cores, supported by a non-parametric statistical framework.
- Numerical Validation: To develop and experimentally validate a computationally efficient finite element framework (ABAQUS) capable of predicting the mechanical response of the manufactured materials and hybrid assemblies.The ultimate aim is to propose an integrated experimental numerical framework that links the intrinsic properties of the regional lignocellulosic fibres, the FDM processability of the core material, and the mechanical performance of the assembled sandwich panel, so that the resulting design rules can guide the subsequent industrial exploitation of this material system in lightweight structural applications.

The present thesis is organised into five chapters in addition to this general introduction and a final general conclusion.

The first chapter presents a comprehensive literature review of the scientific and technical domains relevant to the thesis. It traces the historical evolution of engineering materials, introduces the general principles of composite materials and their classification, reviews the main families of polymer matrices (polyester, epoxy, PLA) and of fibre reinforcements (synthetic and natural), and presents in detail the lignocellulosic plant fibres most relevant to the work. The chapter then surveys the fibre matrix interface mechanisms, the additive manufacturing of polymer composites through FDM, the sandwich structures with cellular cores, and the numerical simulation frameworks commonly applied to these materials.

The second chapter describes the full experimental and numerical protocol of the thesis. It details the geographical origin of the lignocellulosic fibres, their extraction routes, the matrix systems used for the face sheets and the cores, the FDM machine and printing parameters, the assembly of the sandwich panels, the tensile and flexural testing campaigns, the statistical framework and the finite element models developed in ABAQUS/CAE Standard and ABAQUS/Explicit. This chapter establishes the unified experimental and numerical protocol that underpins all the results presented in the three subsequent chapters.

The third chapter reports the experimental characterisation of the two lignocellulosic species through the four-technique pipeline of FTIR, TGA-DTG, XRD and single-fibre tensile testing, benchmarks the results against the four reference natural fibres of the literature (flax,

jute, sisal, kenaf), and establishes the complementarity between the two species that underpins the hybrid face-sheet design of the subsequent chapters.

The fourth chapter reports the mechanical response of FDM-printed PLA through two complementary studies. The first identifies the dominant FDM process parameters through a Taguchi orthogonal-array campaign and an artificial neural network model. The second examines the effect of through-thickness circular apertures at controlled angular orientations on the tensile response of the printed coupons, and validates the experimental observations through an ABAQUS/Explicit finite element model.

The fifth chapter reports the mechanical and numerical characterisation of the assembled sandwich panels. It covers the tensile response of the three constituent materials, the three-point bending performance of the six sandwich configurations, the energy-absorption analysis, the Kruskal–Wallis and Dunn post-hoc statistical framework, and the ABAQUS/CAE Standard finite element validation of the honeycomb sandwich.

The thesis closes with a **General Conclusion** that synthesises the principal results, articulates the scientific and technical contributions of the work, and outlines the perspectives for the further development of the hybrid bio-based sandwich concept in the direction of dynamic loading, environmental durability and industrial scalability.

Chapter I

Composite Materials and Sandwich Structures: Overview and Literature Review

I.1 Introduction

The field of composite materials is a significant area of research in advanced materials engineering, owing to the diversity of their constituents and the range of structural applications they support [4]. These materials consistently outperform their monolithic counterparts in specific stiffness, specific strength, and tailorability. The present chapter reviews the fundamentals of composite classification, the principal manufacturing routes, and the structural and chemical factors that govern composite performance.

Within this landscape, plant-derived natural fibres have emerged as a credible alternative to synthetic reinforcements, owing to their natural abundance, low cost, renewability, and environmental compatibility[5]. The chapter examines the classification of plant fibres, their hierarchical morphological structure, their chemical composition, their extraction routes, and their physical, thermal, and single-fibre mechanical properties. Particular attention is given to the species relevant to the experimental programme of the thesis flax, jute, sisal, and kenaf as conventional benchmarks, Typha latifolia and Agave americana[6] .harvested in the M'Sila Province of Algeria, and date palm (Phoenix dactylifera) as a regional reference of significance to North African composite research. The chapter then turns to the fibre–matrix interface, to the thermoset and bio-based polymeric matrices, and to the additive manufacturing technologies and finite element frameworks used to simulate the mechanical response of FDM-printed parts and biocomposite sandwich panels.

Despite the rapid expansion of the international literature on natural-fibre composites and additively manufactured cellular structures, studies that integrate regionally sourced lignocellulosic reinforcements with FDM-printed bio-based cores into a single hybrid sandwich architecture remain relatively limited, and the local influence of the Algerian growth sites has been only partially explored. This gap motivates the present thesis and frames the literature review presented in the sections that follow.

I.2 History and evolution of materials use

The history of human technology is, in a large measure, the history of materials. Anthropologists have long classified the main stages of pre-industrial civilisation by the dominant material of each era the Stone Age, the Bronze Age, the Iron Age a convention that captures the extent to which material availability has shaped the capabilities of a society (Fig. I. 1). In each of these stages, the materials in use were drawn almost exclusively from natural sources, with minimal transformation beyond the shaping and the assembly of pre-existing substances.

The industrial revolution of the eighteenth and nineteenth centuries marked a qualitative transition in this relationship. The systematic exploitation of iron, and later of steel, allowed structural elements to be produced at a scale and with a precision that natural materials alone could not deliver. The late nineteenth century and the first half of the twentieth saw the emergence of aluminium alloys, of reinforced concrete, and of the first synthetic polymers (bakelite, polystyrene, polyvinyl chloride, polyethylene), each of which unlocked new applications that had been inaccessible to the previous generation of materials.

The second half of the twentieth century introduced a further qualitative shift, through the systematic development of engineered composite materials. By combining two or more constituents with complementary properties, composite materials allowed designers to tailor the mechanical response of a part to the specific requirements of its application, rather than to accept the properties of a single monolithic material as given. Glass-fibre-reinforced polymers, carbon-fibre-reinforced polymers, aramid-fibre laminates and ceramic-matrix composites have all emerged from this movement and have become standard materials in aerospace, automotive, marine and civil engineering.

The twenty-first century has brought yet another shift, driven not by the search for higher performance but by the search for lower environmental impact. The depletion of fossil resources, the accumulation of non-biodegradable waste, and the recognition of anthropogenic climate change have placed sustainability at the centre of materials-science research, and have refocused attention on bio-based, bio-inspired and biodegradable alternatives to the synthetic composites of the previous generation. Lignocellulosic-fibre-reinforced polymer composites, and more recently additively manufactured bio-based cellular structures, are among the most visible expressions of this new direction, and they form the material backdrop against which the present thesis is conducted[7].

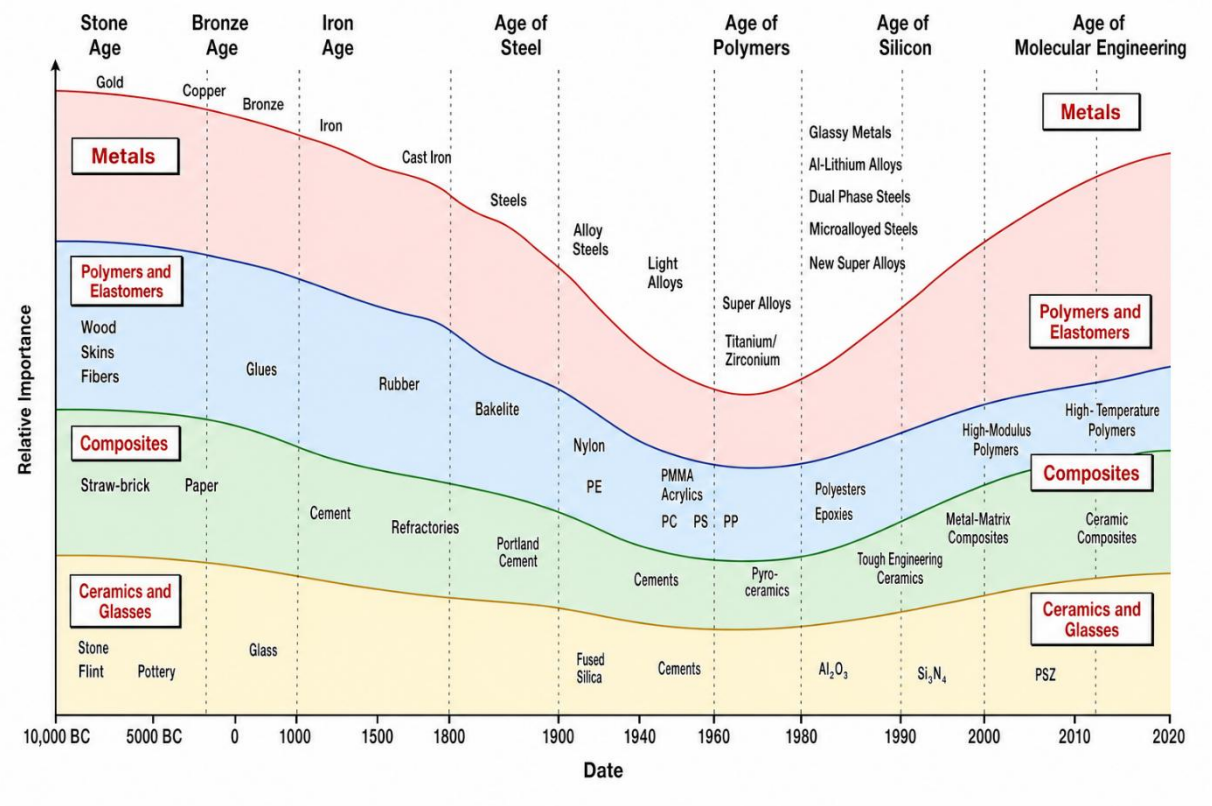


Fig. I. 1 Chronological timeline of the evolution of engineering materials[8]

I.3 Composite materials: definition and general principles

A composite material, in the engineering sense of the term, is a material constituted by the association of two or more distinct constituents whose combination produces properties that none of the constituents would deliver on its own. The two principal constituents of a structural composite are the matrix, which is the continuous phase that binds the reinforcement, transfers the applied loads and protects the reinforcement from environmental aggression, and the reinforcement, which is the discontinuous or continuous phase that carries the bulk of the mechanical load and governs the stiffness and the strength of the composite (Fig. I. 2). A third, often neglected but mechanically essential, constituent is the interface, which is the thin transition zone between the matrix and the reinforcement and which governs the efficiency of the load transfer between them. The design of a composite material therefore involves four families of decisions: the choice of the matrix, the choice of the reinforcement, the geometric arrangement of the reinforcement within the matrix, and the control of the fibre–matrix interface. Each of these decisions admits a wide range of alternatives, and their combined optimisation is what allows composite materials to cover a mechanical response spectrum that extends from highly flexible elastomeric composites to ultra-stiff aerospace laminates[9].

Three general principles govern the mechanical behaviour of composite materials and are relevant to the rest of this chapter. The first is the rule of mixtures, in its various formulations,

which relates the properties of the composite to the volume fractions and the properties of its constituents. The second is the anisotropy principle, which states that the mechanical response of a composite depends strongly on the orientation of the reinforcement with respect to the loading direction, and that the characterisation of a composite therefore requires the specification of at least two or three principal material directions. The third is the length-scale principle, which states that the mechanical response of a composite depends not only on the constitutive behaviours of the matrix and the reinforcement at the macroscopic scale but also on the microstructural organisation of the two phases the fibre diameter, the inter-fibre spacing, the fibre aspect ratio, and the local distribution of the matrix around each fibre.

These three principles will recur, explicitly or implicitly, throughout the literature review that follows [10].

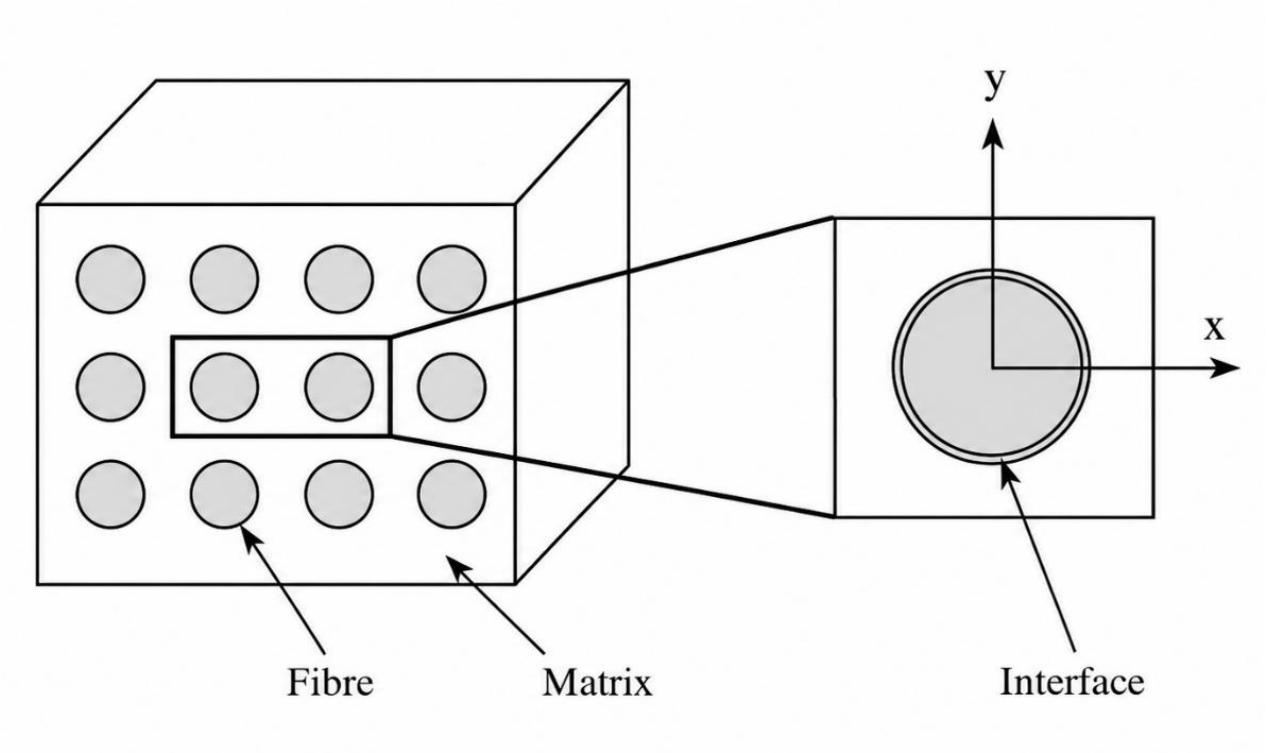


Fig. I. 2 Schematic cross-section of a generic fibre-reinforced composite illustrating the three essential constituents: fibre, matrix, and the fibre-matrix interface.

I.4 Classification of composite materials

Composite materials are conventionally classified along two orthogonal axes: the nature of the matrix and the nature of the reinforcement[11](Fig. I. 3). The present section adopts this dual classification and reviews, in turn, the main families of matrices (Section I.4.1) and the main families of reinforcements (Section I.4.2).

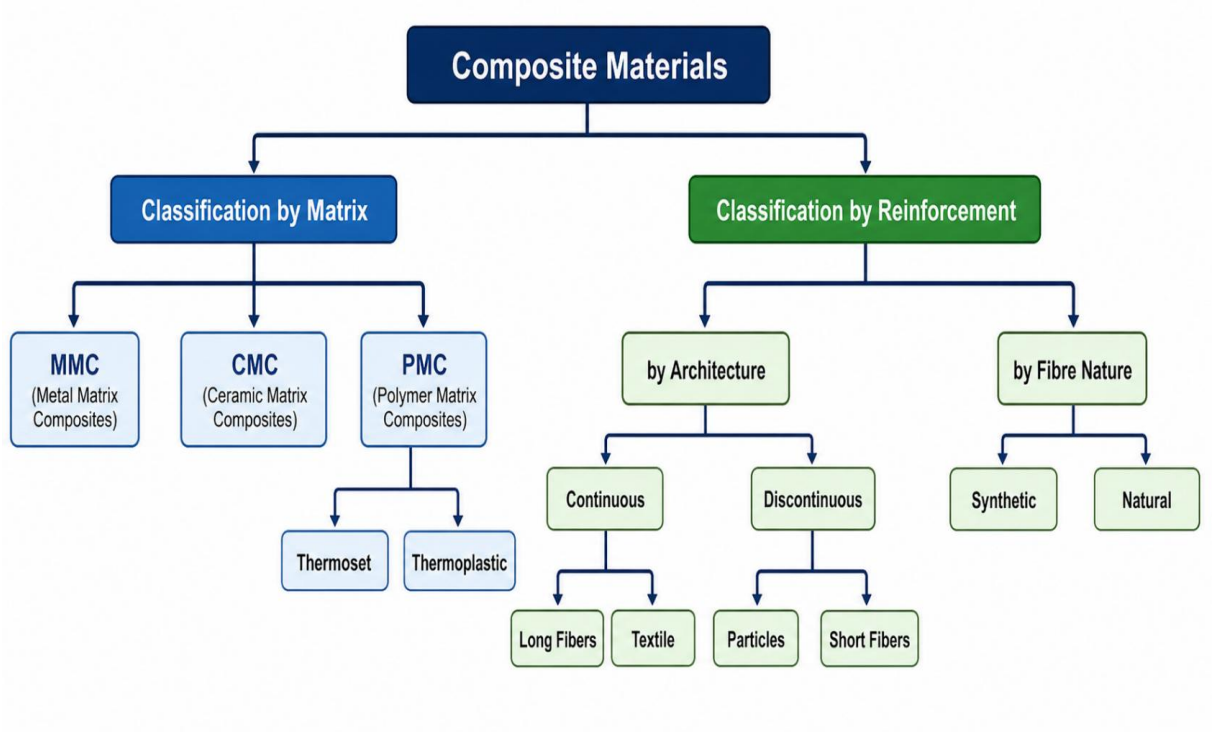


Fig. I. 3 Hierarchical classification tree of composite materials

I.4.1 Classification based on the matrix material

The matrix of a structural composite may be metallic, ceramic or polymeric, and the three families correspond to distinct mechanical regimes, processing routes and application windows[12].

I.4.1.1 Metal Matrix Composites (MMCs)

Metal matrix composites (MMCs) combine a metallic matrix most often aluminium, magnesium, titanium or copper with a reinforcement in the form of continuous fibres, discontinuous fibres, whiskers or particles of ceramic origin (silicon carbide, alumina, boron carbide)[13]. The metallic nature of the matrix confers high thermal and electrical conductivity, a capacity to sustain elevated operating temperatures, and good resistance to moisture and to organic solvents. These properties make MMCs attractive for applications in aerospace components, high-performance engine parts, and electronic heat-sink systems[14], where the operating temperature or the environmental aggression exceeds the domain accessible to polymer-based composites (Fig. I. 4).

The principal drawbacks of MMCs are their elevated processing costs which include specialised infiltration, powder metallurgy or thermal-spray routes and the challenges associated with the control of the fibre–matrix interfacial reactivity at high temperature[15]. MMCs also retain, in their failure mode, a tendency towards the brittle fracture that

characterises ceramic-reinforced systems, which limits their use in applications that require a damage-tolerant response[16].

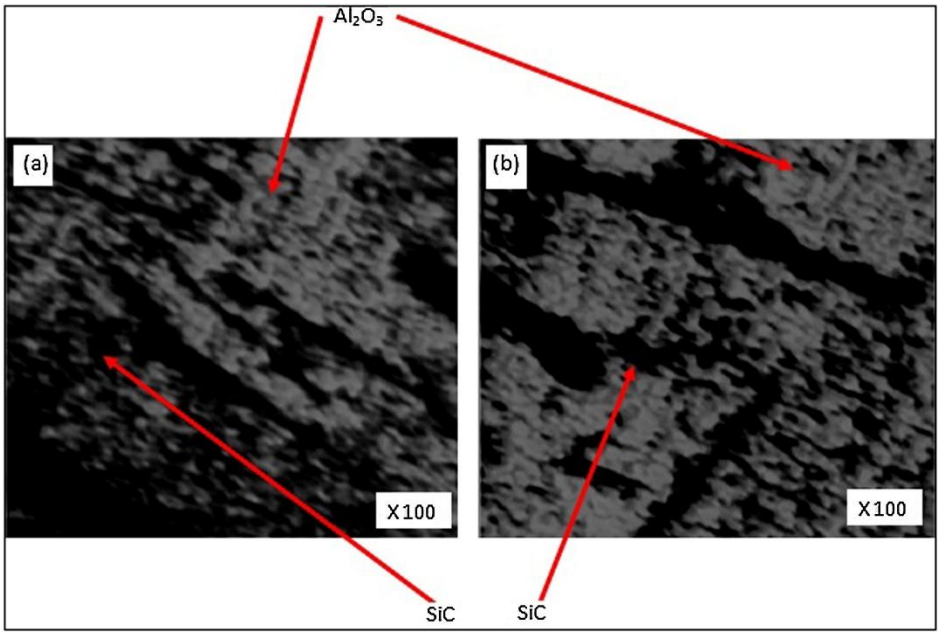


Fig. I. 4 The microstructure of Hybrid Metal Matrix Composite[17]**.**

I.4.1.2 Ceramic Matrix Composites (CMCs)

Ceramic matrix composites (CMCs) combine a ceramic matrix silicon carbide, alumina, carbon, or glass-ceramic systems with a ceramic reinforcement in the form of continuous or woven fibres (Fig. I. 5). The primary motivation for CMCs is the exploitation of the intrinsic temperature resistance of ceramics, which can sustain operating temperatures in excess of 1000 °C without the oxidation and the creep that limit the use of metallic alloys in the same range[18,19]. Applications include turbine blades in the hot section of aero-engines, re-entry thermal protection systems for spacecraft, and brake discs for high-performance vehicles[20].

The inherent brittleness of the ceramic matrix is mitigated by the fibre reinforcement, which generates a set of toughening mechanisms crack deflection at the fibre–matrix interface, crack bridging, and progressive fibre pull-out that transform the catastrophic single-crack failure of the monolithic ceramic into a more graceful progressive damage accumulation. The fabrication of CMCs, however, remains among the most expensive of all composite families, and their use is restricted to the high-value aerospace and defence sectors[21].

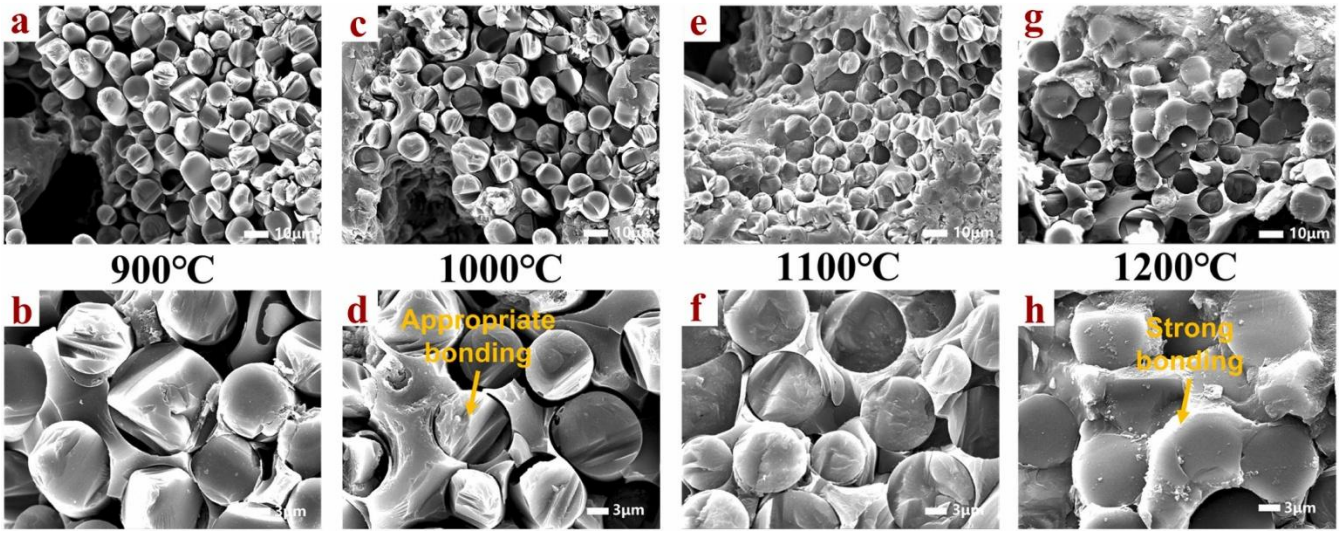


Fig. I. 5 Representative example of a Ceramic Matrix Composite: SEM micrograph of a SiC/SiC[22].

I.4.1.3 Polymer Matrix Composites (PMCs)

Polymer matrix composites (PMCs) are the most widely used family of composites, valued for their low density, room-temperature processability, and low fabrication cost relative to metal and ceramic matrix composites. They are subdivided into **thermosets**, which undergo irreversible curing to form a crosslinked network, and **thermoplastics**, which can be repeatedly melted and reshaped. Among thermosets, **epoxy resins** are the reference matrix for high-performance structural applications, offering tensile strengths that can exceed 70 MPa, elastic moduli in the 3–4 GPa range, excellent fibre–matrix adhesion, and curing shrinkages an order of magnitude lower than those of unsaturated polyesters. These attributes make epoxy the preferred choice for the hand-layup hybrid face sheets of the present thesis. Within the thermoplastic family, **polylactic acid (PLA)** has emerged as the leading bio-based feedstock for fused deposition modelling (FDM), owing to its low melting temperature (170–220 °C), respectable mechanical properties (tensile strength of 50–70 MPa, elastic modulus of 3–4 GPa), and biodegradability. These characteristics, together with the enhanced ductility offered by short-flax-fibre reinforcement, underpin the selection of neat PLA and PLA/flax biocomposite filaments for the additively manufactured cores of the sandwich panels in this work.[23].

I.4.1.3.1 Other FDM-compatible thermoplastics.

Several other thermoplastics are routinely used in FDM applications and deserve a brief mention for context. Acrylonitrile-butadiene-styrene (ABS) is a tough, impact-resistant amorphous thermoplastic with a higher glass transition temperature (≈105 °C) than PLA, at the cost of a higher emission of volatile organic compounds during printing and a fossil origin Polyethylene terephthalate glycol-modified (PETG) combines the printability of PLA with the

impact resistance of ABS and has gained ground in mechanical-engineering applications. Polyamides (PA6, PA12 and their glass- or carbon-filled variants) extend the FDM envelope towards higher mechanical performance at a higher material cost[24] . None of these polymers is, however, bio-based in the strict sense of the term, and they are therefore outside the immediate focus of the present thesis.

I.4.2 Classification based on reinforcement types

The reinforcement of a composite material can be classified along two distinct but complementary axes. The first axis concerns the geometric architecture of the reinforcement whether the fibres are **continuous** or **discontinuous**, whether they are aligned in a single direction or arranged in a woven fabric, and whether they form the bulk of the reinforcement volume or are dispersed as individual elements within the matrix. The second axis concerns the nature of the reinforcement material itself whether it is of **synthetic** origin (glass, carbon, aramid) or of **natural** origin (plant or animal fibres)[25]. The two classifications are adopted in succession below (Fig. I. 6).

I.4.2.1 Architecture of the fibre reinforcement

The geometric arrangement of the reinforcement within the matrix governs the directional response of the composite and is therefore the first engineering decision in the design of a fibre-reinforced composite part[26].

I.4.2.1.1 Continuous fibre-reinforced composites

Continuous fibre composites are those in which the fibres extend along the entire length of the part, or at least a significant fraction of it. Their in-plane mechanical response is dominated by the fibre direction, and their macroscopic anisotropy is correspondingly high. Two principal subfamilies are distinguished:

- Unidirectional composites, in which all the fibres are aligned along a single principal direction, deliver the maximum stiffness and strength in that direction but a much weaker response transversely. They are typically used as building blocks for laminated structures.
- Laminate composites, in which unidirectional plies are stacked with different fibre orientations between successive plies, deliver a balanced in-plane response that can be tailored to the loading conditions through the choice of the stacking sequence (cross-ply, angle-ply, quasi-isotropic). Woven-fabric laminates, in which the fibres are interlaced in two orthogonal directions within each ply, constitute a variant widely used in aerospace and marine applications [27].

I.4.2.1.2 Discontinuous fibre-reinforced composites

Discontinuous fibre composites are those in which the reinforcement consists of short fibres, whiskers or particles whose length is small compared with the part dimensions. Their in-plane response is more isotropic than that of continuous-fibre composites, but their ultimate mechanical performance is systematically lower because the load transfer between matrix and fibres is limited by the shorter fibre aspect ratio. Three principal subfamilies are distinguished [28]:

- Short-fibre composites, in which fibres of length typically between 0.1 and 10 mm are either aligned by the injection-moulding flow or randomly oriented within the matrix. Injection-moulded short-fibre composites dominate high-volume automotive and consumer-goods applications.
- Particle-reinforced composites, in which the reinforcement consists of micro- or nano-particles (carbonate, silica, carbon black, clay) dispersed within a polymer matrix, are used mainly to modify the stiffness, the damping, the thermal conductivity or the optical properties of the base polymer.
- Whisker-reinforced composites, in which single-crystal filaments of high aspect ratio deliver mechanical properties approaching those of continuous fibres, occupy niche applications where short-fibre reinforcement is insufficient.

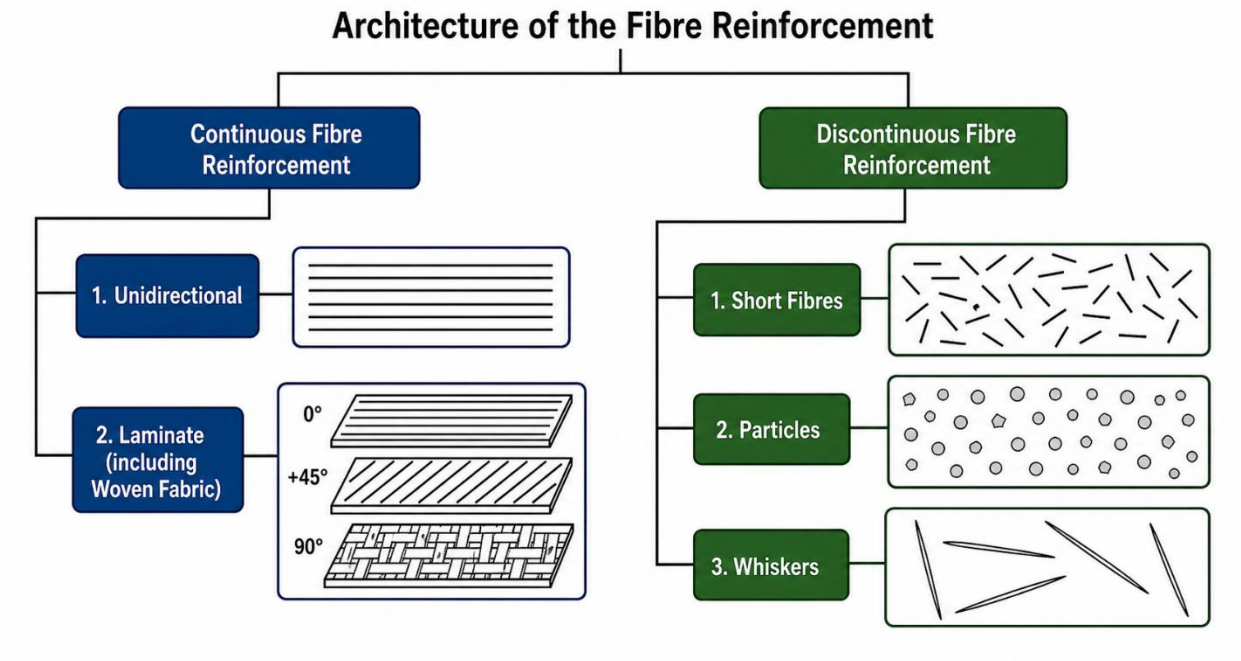


Fig. I. 6 Schematic of the main architectures of continuous and discontinuous fibre reinforcement

I.4.2.2 Classification by nature of the fibres

Beyond their geometric arrangement, fibres are also classified according to their chemical nature and their origin. The most significant division is between synthetic fibres (Fig. I. 7), obtained from petrochemical or mineral precursors, and natural fibres, obtained from plant, animal or mineral sources.

I.4.2.2.1 Synthetic (synthetic-fibre) reinforcements

Three synthetic fibres dominate the high-performance composite market. **Glass fibres**, produced by drawing molten silicate glass, offer a tensile strength of 2000–4500 MPa, an elastic modulus of 70–85 GPa, and a density of approximately 2.5 $g \cdot cm^{-3}$, positioning them as the reinforcement of choice for cost-sensitive, high-volume applications in the marine, wind-energy, and construction industries. **Carbon fibres**, obtained by the controlled pyrolysis of a polymeric precursor, deliver the highest specific stiffness of any conventional reinforcement, with tensile strengths reaching 3500–7000 MPa, elastic moduli between 230 and 600 GPa, and a density below 2.0 $g \cdot cm^{-3}$, making them the reference for aerospace and high-performance automotive components. **Aramid fibres**, such as those commercialised under the trade names Kevlar and Twaron, are characterised by a tensile strength of 2700–3600 MPa, a modulus of 60–130 GPa, and a low density of about 1.44 $g \cdot cm^{-3}$, but their most distinctive attribute is their exceptional impact and abrasion resistance, which has made them the standard reinforcement in ballistic and personal-protection equipment. **The metallic fibre**-reinforced composites (MFRPs), which use steel fibres mainly in cementitious matrices, occupy a niche position and are mentioned here for completeness rather than as candidate reinforcements for the present thesis.[29–33]

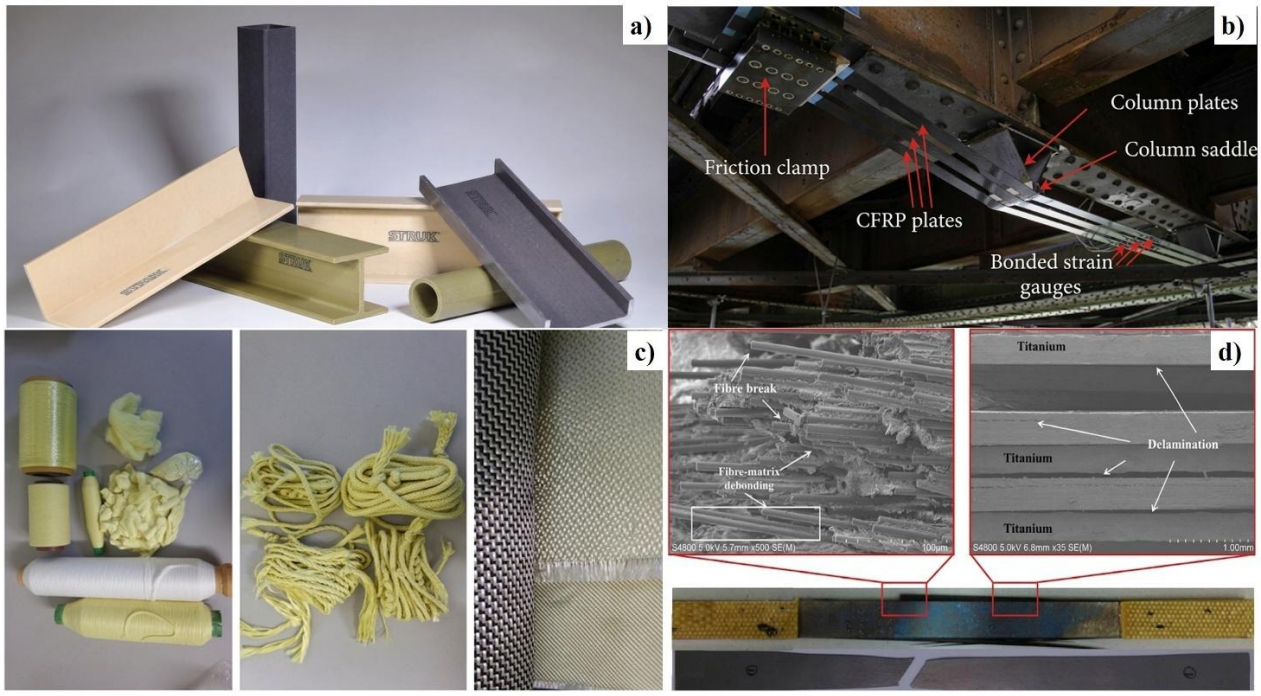


Fig. I. 7 Representative synthetic fibre reinforcements: (a) glass fibre, (b) carbon fibre, (c) aramid fibre, and (d) steel fibre (MFRPs) [34–37].

I.4.2.2.2 Natural (natural-fibre) reinforcements

Natural fibres are of **plant**, **animal** or **mineral** origin[7][38], and the plant-based subfamily the lignocellulosic fibres constitutes the most relevant class for the present thesis. Their composition, anatomy, extraction and characterisation are the subject of Section I.5; the present paragraph introduces their positioning relative to the synthetic fibres reviewed above.

The principal advantages of natural fibres over their synthetic counterparts are their renewability, their biodegradability at end of life, their low density (typically between 1.3 and 1.5 $g \cdot cm^{-3}$, against 2.5 $g \cdot cm^{-3}$ for glass), their low cost, their low abrasiveness on processing equipment, and their low embodied energy. Their principal limitations are their intrinsic variability, which reflects the biological origin of the material; their hydrophilic surface, which generates poor adhesion to hydrophobic polymer matrices and necessitates surface treatment; their limited thermal stability, which typically places an upper processing-temperature ceiling near 200 to 220 °C; and their moderate mechanical properties, which position them below glass and far below carbon and aramid for strength-driven applications[39].

Within these limitations, natural fibres have established themselves as credible reinforcements for semi-structural and non-structural applications in the automotive, construction, furniture and packaging industries, and the expansion of additive manufacturing has opened a new application window in which natural-fibre filaments (PLA/flax, PLA/wood,

PLA/hemp) combine the sustainability of the reinforcement with the design freedom of 3D printing.

Chemical composition and structure of natural fibres (plant fibre).

The mechanical, thermal and hygroscopic signatures of lignocellulosic fibres are direct expressions of the chemical composition and the hierarchical organisation of the plant cell wall (Fig. I. 8). Each elementary fibre is a hollow cell whose wall is built from concentric layers the middle lamella, the primary cell wall and the secondary cell wall, itself sub-divided into the **S1**, **S2** and **S3** sub-layers surrounding a central lumen. The mechanical response of the fibre is dominated by the thick S2 layer, in which crystalline cellulose microfibrils are embedded at a characteristic microfibrillar angle within an amorphous matrix of hemicellulose, lignin and pectin . Four polymeric constituents and a residual fraction of minor compounds together define the chemical composition of the fibre. **Cellulose**, a linear polysaccharide of β-1,4-linked D-glucose units, constitutes the load-bearing skeleton of the cell wall and accounts typically for 40 to 80 per cent of the dry mass depending on the species; its high degree of polymerisation and its capacity to organise into crystalline microfibrils are responsible for the elevated stiffness and tensile strength of the fibre. **Hemicellulose** is a branched, amorphous polysaccharide that bonds the cellulose microfibrils to one another and to the lignin matrix, and its hydrophilic character is the principal source of the moisture sensitivity that limits the dimensional stability of natural-fibre composites .**Lignin** is a three-dimensional aromatic polymer of phenylpropane units that fills the inter-microfibril spaces and confers rigidity, hydrophobicity and resistance to biological attack; its content typically lies between 5 and 25 per cent and increases with the maturity of the plant. Pectin, a complex of galacturonic-acid polysaccharides, is concentrated in the middle lamella and acts as a cementing agent that binds adjacent elementary fibres into the technical fibre bundles harvested for composite use [40] Minor constituents waxes, extractives, water-soluble compounds and inorganic ash complete the composition and influence the surface energy and the thermal degradation profile of the fibre. The substantial variability of these proportions across species, growth conditions, harvest age and extraction protocol is the chemical origin of the well-known dispersion of the mechanical properties of natural-fibre composites, and it justifies the species-by-species characterisation that is the subject of Section I.5 and composition of some different natural fibres in **Table I.1**.

Table I. 1 Chemical composition of different natural fibres [40].

Fibre	Cellulose (%)	Lignin (%)	Hemicellulose (%)	Ash (%)	Pectin (%)	Ref.
Wheat	29–51	16–21	15.00–32.00	4.5–9	–	[41]
Rye	33–50	16–19	27.00–30.00	2–5	–	[41]
Bamboo	26–73.83	10.1–36.18	12.49–31.00	1.7–5	–	[42]
Fibre flax	71	2.2	18.60–20.60	–	2.3	[43]
Hemp	57–77	3.7–13	14.00–20.40	0.8	0.9	[42]
Kenaf	37–49	15–21	18.00–24.00	2–4	–	[44,45]
Sisal	47–78	7–11	10.00–24.00	0.6–1	10	[46]
Rice	28–57	12–19	23.00–33.00	15–20	–	[41]
Banana	60–65	5–10	19.00	–	–	[46]
Coir	32–43	40–45	0.15–0.25	–	–	[43]
Bagasse	55.2	25.3	16.80	–	–	[43][42]
Jute	45–71.6	21–26	13.60–21.00	0.5–2	0.2	13
Cotton	82.7–90	–	5.70	–	–	14
Coconut	32–43.8	40.45	0.15–20	–	3–4	15
Pineapple	81	12.7	–	–	–	16

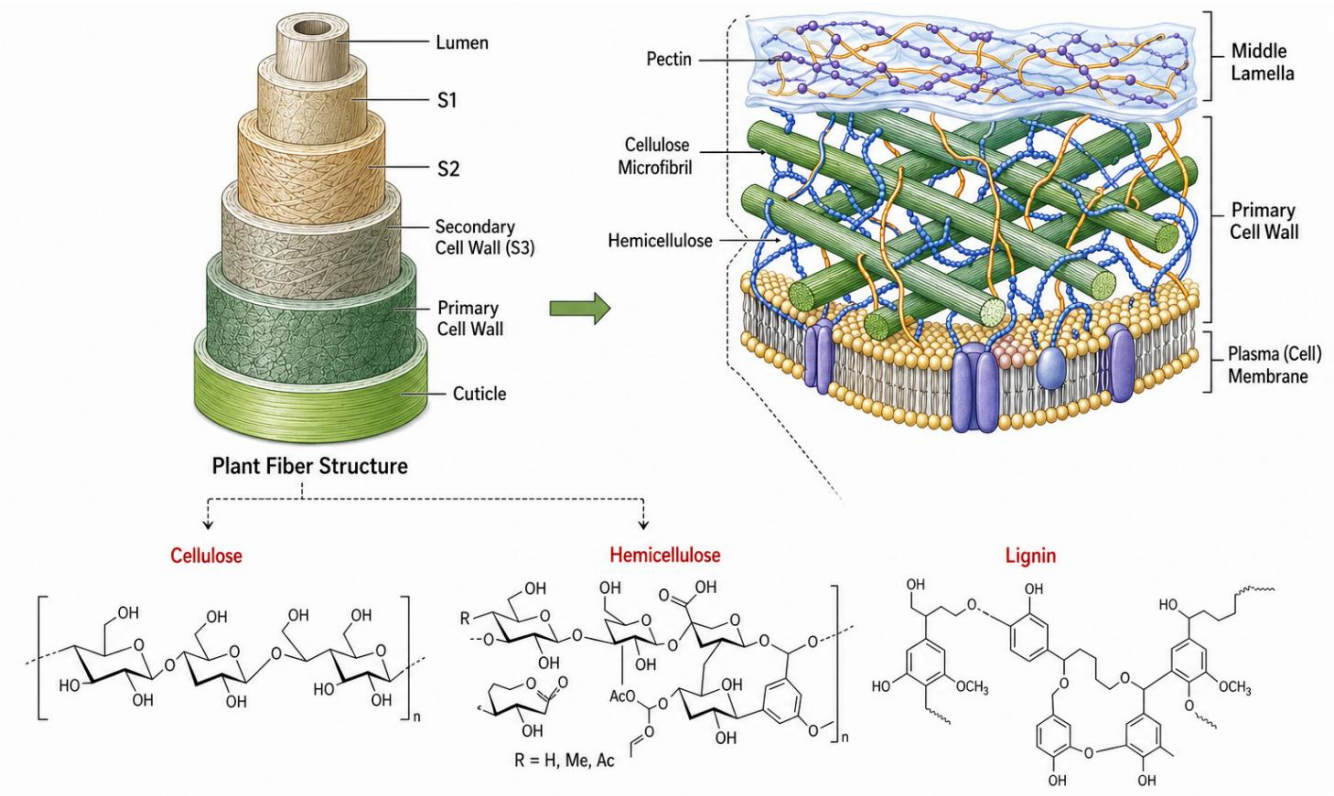


Fig. I. 8 natural fiber Chemical composition[47,48].

I.5 Focus: plant fibres relevant to this thesis

The lignocellulosic family encompasses a wide range of plant fibres whose mechanical, chemical and thermal properties vary with the botanical origin, the part of the plant from which the fibres are extracted (stem, leaf, fruit, seed), and the extraction route. The present section reviews the five species most relevant to the thesis: the five conventional benchmarks flax, jute, sisal, Palm and kenaf.

I.5.1 Flax fibre

Flax (Linum usitatissimum) (Fig. I. 9) is a bast fibre extracted from the stem of the flax plant, cultivated since antiquity for its textile and oil-seed value. Its tensile strength typically lies between 800 and 1500 MPa, its elastic modulus between 50 and 80 GPa, its density near 1.45 g·cm^{-3}, and its elongation at break between 1.2 and 3.2 %. Its cellulose content is among the highest of the natural-fibre family (70–80 % by weight), which accounts for its exceptional stiffness. Flax is the benchmark reinforcement of the European natural-fibre composite industry and is widely used in automotive interior panels, sporting-goods and acoustic-absorption applications[49].

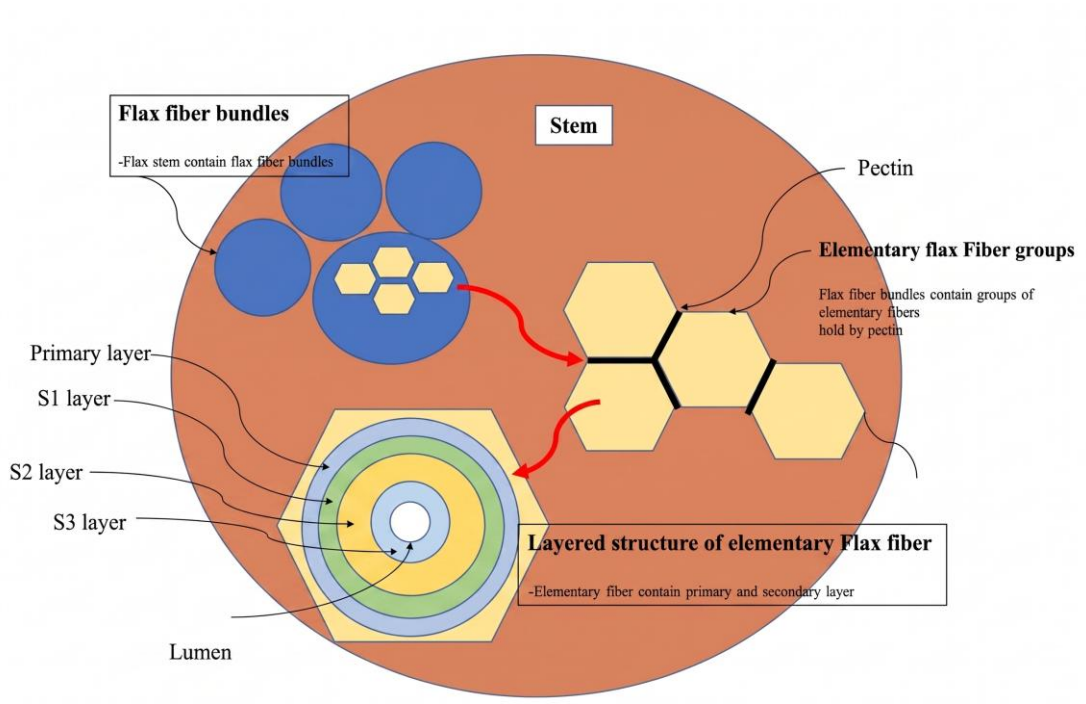


Fig. I. 9 Flax fiber structure [50]

I.5.2 Jute fibre

Jute (Corchorus olitorius and C. capsularis) is a bast fibre cultivated primarily in the Indian subcontinent and West Africa (Fig. I. 10). Its tensile strength lies between 393 and 773 MPa, its elastic modulus between 13 and 30 GPa, its density near 1.3 to 1.5 g·cm^{-3}, and its cellulose content between 61 and 73 %[51]. Jute occupies an intermediate position between flax and sisal in the natural-fibre mechanical hierarchy, and its low cost, wide availability and established processing chain have made it the reference reinforcement of mass-market geotextile, packaging and automotive-panel applications[52].



Fig. I. 10 (a) Jute plant ; (b) Raw jute fabric ; (c) Unidirectional jute fiber ; (d) Woven jute fiber [53] .

I.5.3 Sisal fibre

Sisal (Agave sisalana) is a leaf fibre extracted from the leaves of a succulent plant native to Central America and now cultivated extensively in East Africa, Brazil and Asia (Fig. I. 11). Its tensile strength lies between 400 and 700 MPa, its elastic modulus between 9 and 22 GPa, and its density near 1.3 to 1.5 g·cm^{-3} [54]. Sisal is notable for its high elongation at break, which provides good impact resistance in the resulting composites, and for its relatively high production yield per hectare. It is the reference reinforcement in rope, twine, geotextile and automotive-interior applications.

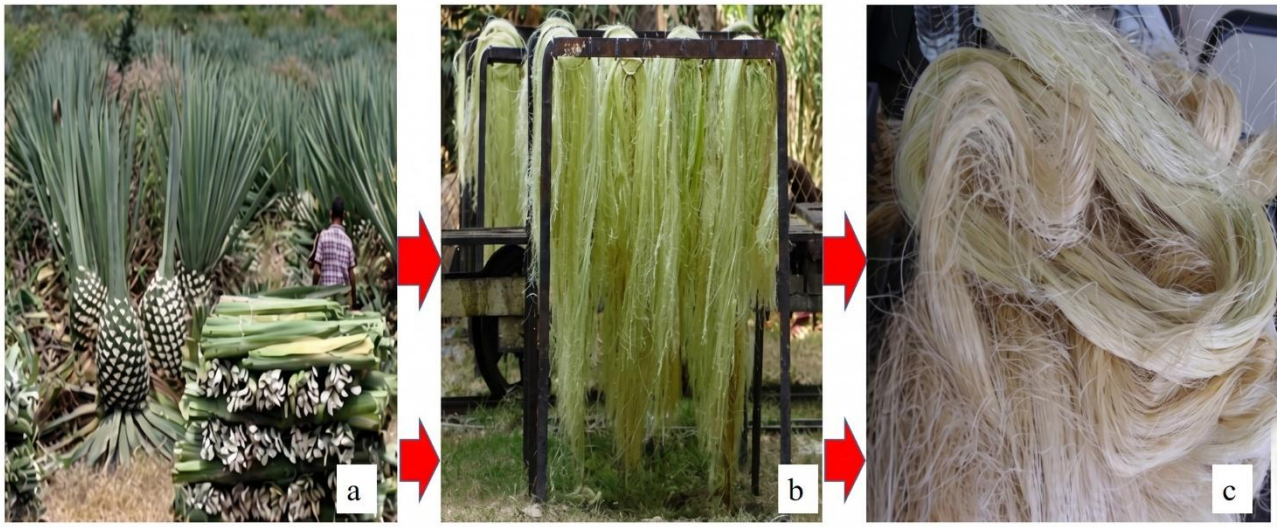


Fig. I. 11 Sisal fiber [55]

I.5.4 Kenaf fibre

Kenaf (Hibiscus cannabinus) is a bast fibre cultivated primarily for paper pulp and fibre production in tropical and subtropical regions (Fig. I. 12). Its tensile strength reaches approximately 1000 MPa, its elastic modulus approximately 53 GPa, and its density near 1.04 g·cm^{-3}, which corresponds to one of the lowest specific weights in the natural-fibre family. Its cellulose content is around 70 %, its hemicellulose near 3 %, and its lignin near 19 %. Kenaf has attracted growing attention as a reinforcement for automotive interiors and for bio-based construction materials, because of its rapid growth cycle and its capacity to fix atmospheric carbon during cultivation[56].

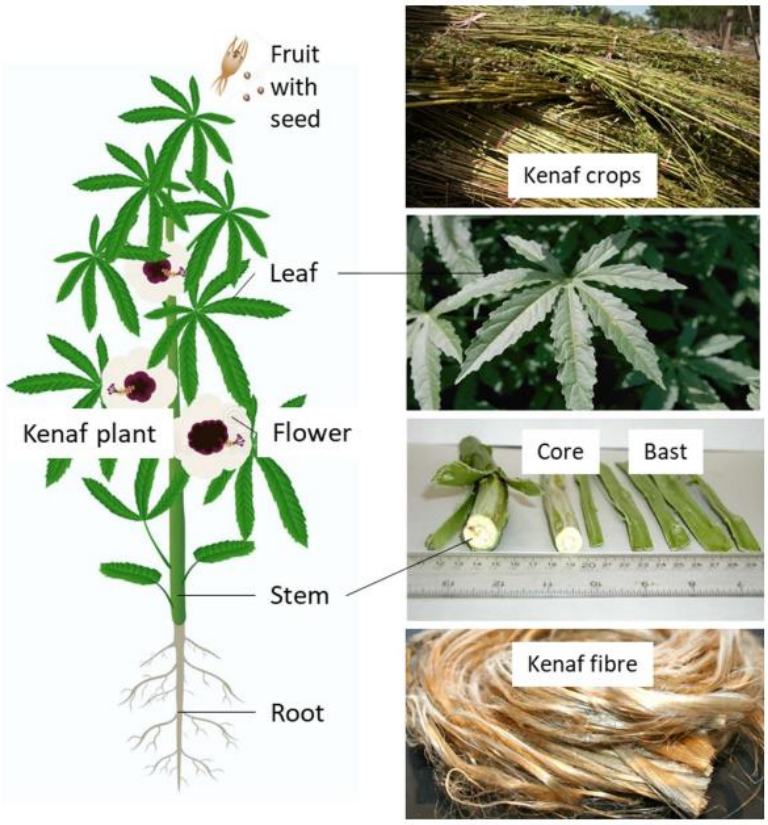


Fig. I. 12 Kenaf fibre [57]

I.5.5 Palm fibre (Phoenix dactylifera)

The date palm (Phoenix dactylifera L.) is a monocotyledonous tree of the family Arecaceae, cultivated since antiquity in the oases of North Africa and the Middle East for its fruit and now firmly established as the dominant cultivated species of the Algerian Saharan belt [94] (Fig. I. 13). Each tree generates a substantial annual lignocellulosic biomass leaflet, rachis (midrib), petiole, leaf-base mesh and trunk fibres most of which is currently treated as agricultural by-product, which makes the date palm a particularly attractive low-cost fibre source for biocomposite applications in arid region. Reported mechanical properties depend strongly on the part of the tree from which the fibres are extracted and on the extraction protocol: date-palm leaflet and rachis fibres typically exhibit ultimate tensile strengths in the 100 to 300 MPa range, elastic moduli between 2 and 12 GPa, densities near 0.9 to 1.2 $g \cdot cm^{-3}$, and elongation at break between 5 and 20 per cent, which positions the species at the lower end of the natural-fibre mechanical hierarchy but at one of the most competitive specific-property ratios because of the unusually low density [60]. The chemical composition reported in the literature places the cellulose content between 33 and 50 per cent, the hemicellulose between 12 and 30 per cent, and the lignin between 17 and 30 per cent of the dry mass, with substantial variability across cultivars and across the anatomical position of the fibres Palm-fibre

composites with thermoset and thermoplastic matrices have been reported in the recent literature for automotive interior, construction-panel, packaging and acoustic-absorption applications[61]. The species is therefore a relevant regional reference for the present thesis even though, in the experimental programme reported in the following chapters.

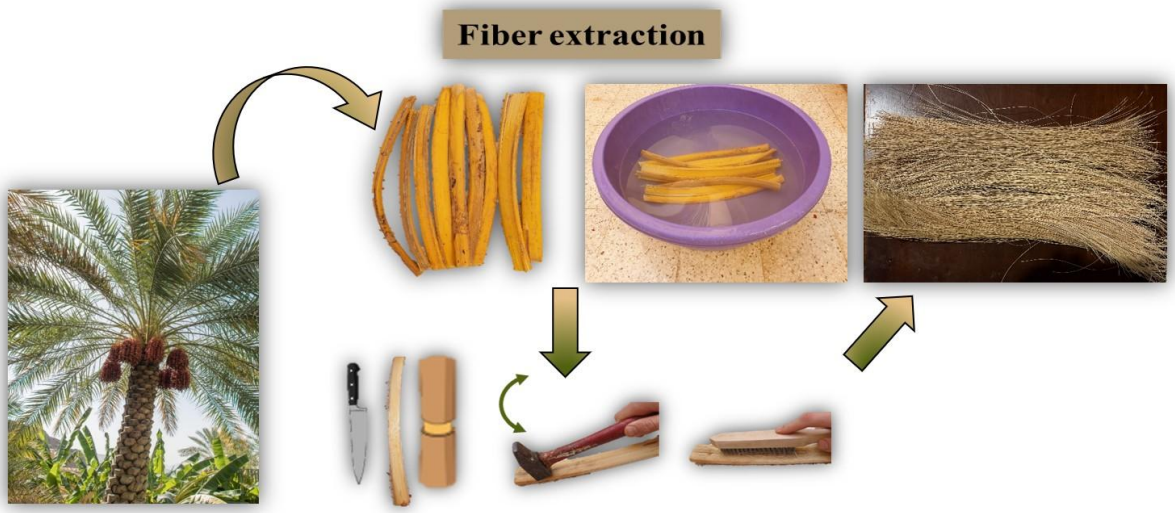


Fig. I. 13 Palm fibre (Phoenix dactylifera) [62].

Table I. 2 Comparison of the geometrical and mechanical properties for date palm fiber with values reported in the literature for other fibers [63].

Fibres types	**GL (mm)**	**Average diameter (µm)**	**Section (mm²)**	**Elongation at break (%)**	**Strength (MPa)**	**Young's modulus (GPa)**	**Ref.**
Pineapple leaf	~50	~120	~0.011	2.2	126.6	4.40	[64]
Ramie	-	-	-	4.1	481	8.4	[65]
Phoenix Sp.	50	577	0.261	1.2	120	4.1	[66]
Spatha	50	150-400	0.017-0.125	6	75.66	3.14	[67]
kenaf	30	200-400	0.031-0.125	7.84	283.5	5.24	[68]
Piassava	50	500-600	0.196-0.282, 0.259	11.9 ± 4.3	131.1 ± 27	2.58 ± 0.39	[69]
Juncus effusus L.	40	280 ± 56	0.168	2.75 ± 0.6	113 ± 36	4.38 ± 1.37	[70]
Palm date C	50	575 ± 60		3.31 ± 0.73	187.15 ± 37	6.40 ± 1.17	[63]
Palm date R	50	575 ± 60		3.31 ± 0.73	287.92 ± 22	9.86 ± 0.77	[63]

Fibres types	GL (mm)	Average diameter (µm)	Section (mm^2)	Elongation at break (%)	Strength (MPa)	Young's modulus (GPa)	Ref.
Pineapple leaf	~50	~120	~0.011	2.2	126.6	4.40	[64]
Ramie				4.1	481	8.4	[65]
Phoenix Sp.	50	577	0.261	1.2	120	4.1	[66]
Spatha	50	150-400	0.017-0.125	6	75.66	3.14	[67]
kenaf	30	200-400	0.031-0.125	7.84	283.5	5.24	[68]
Piassava	50	500-600	0.196-0.282, 0.259	11.9 ± 4.3	131.1 ± 27	2.58 ± 0.39	[69]
Juncus effusus L.	40	280 ± 56	0.168	2.75 ± 0.6	113 ± 36	4.38 ± 1.37	[70]
Palm date C	50	575 ± 60		3.31 ± 0.73	187.15 ± 37	6.40 ± 1.17	[63]
Palm date R	50	575 ± 60		3.31 ± 0.73	287.92 ± 22	9.86 ± 0.77	[63]

Palm date C: The calculation of the section assuming a cylindrical shape of the fiber.

Palm date R: The calculation of the section is taking into account the porosity of the fiber.

I.6 Fibre–matrix interface and adhesion

The fibre–matrix interface is the critical zone across which the applied load is transferred from the matrix to the reinforcement. A weak interface leads to premature failure through fibre pull-out or debonding, regardless of the intrinsic merits of the constituents. The adhesion between a natural fibre and a polymer matrix is inherently challenging because the lignocellulosic surface is hydrophilic, whereas most thermoset and thermoplastic matrices are hydrophobic, resulting in incomplete wetting and a weakened interfacial zone To overcome this incompatibility, the literature has explored various surface treatments. Alkaline treatment selectively removes amorphous constituents and roughens the fibre surface, improving mechanical interlocking, while silane coupling agents create covalent bridges between the two phases. Other routes acetylation, benzoylation, enzymatic treatment, and plasma activation occupy narrower application windows[71].

The present thesis does not introduce surface treatments beyond the alkaline delignification used in Section II.3.2 for the preparation of one of the two fibre species. The review above is therefore intended to clarify the rationale behind the fibre–matrix combinations retained in the thesis and to support the interpretation of the composite-level results that follow.

I.7 Additive manufacturing of polymer composites

The emergence of additive manufacturing has introduced a new paradigm in the fabrication of polymer composite parts. Unlike the subtractive and formative processes that have dominated the composite industry for decades hand layup, compression moulding, vacuum infusion, filament winding additive processes build the part layer by layer from a digital model, which releases the geometric constraints imposed by moulds and by fibre placement heads, and which opens the design space to cellular, lattice and bio-inspired topologies that conventional processes cannot fabricate [72].

I.7.1 Overview of the main additive manufacturing technologies

Several additive manufacturing technologies are compatible with polymer materials, and each occupies a distinct position in the trade-off between cost, resolution, material diversity and mechanical performance (Fig. I. 14).

Fused deposition modelling (FDM), also referred to as fused filament fabrication (FFF), deposits a molten thermoplastic filament through a heated extrusion nozzle along a programmed toolpath, and builds the part through the successive consolidation of deposited roads. It is by far the most widely adopted additive technology for thermoplastic polymers, because of the low cost of the equipment, the open-source nature of much of the slicing and printing software, and the compatibility with a broad range of commercial filaments[73].

Stereolithography (SLA) and its variants cure a photopolymer resin layer by layer through the controlled exposure of the resin surface to an ultraviolet laser or a digital light-processing (DLP) projector. SLA delivers a surface quality and a feature resolution superior to FDM, but it is restricted to photocurable resins and its material selection is narrower[74].

Selective laser sintering (SLS) uses a laser to sinter a powder bed of thermoplastic particles along the cross-section of each layer. SLS delivers near-isotropic mechanical properties and does not require the support structures that FDM and SLA parts often need, but its equipment cost is substantially higher.

Other polymer additive technologies material jetting, multi-jet fusion, continuous liquid interface production occupy niche application windows and are reviewed in the recent literature [73]. The remainder of this section concentrates on FDM, which is the technology retained for the fabrication of the sandwich cores of the present thesis.

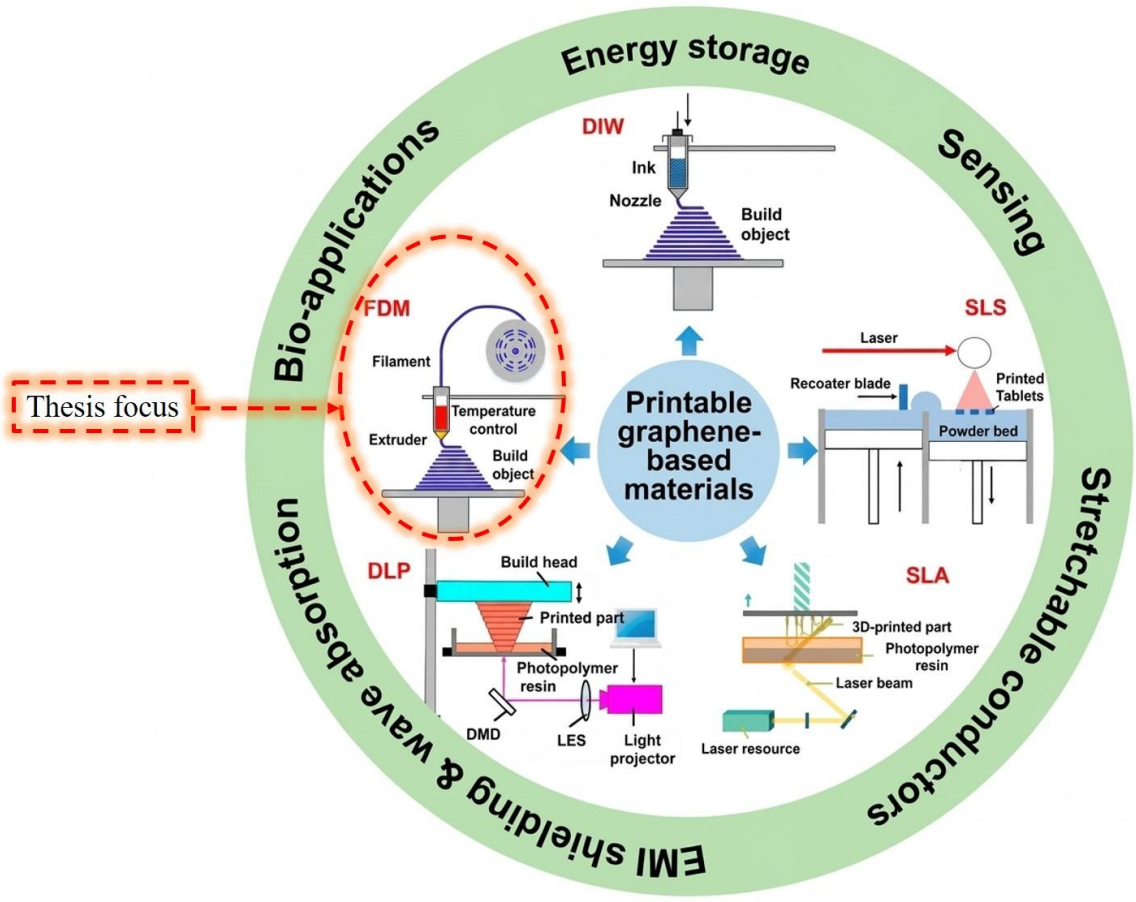


Fig. I. 14 Schematic comparison of the main polymer additive manufacturing technologies **[75].**

Table I. 3 Summary of 3D printing techniques and their specifications [76].

AM technique	Mechanism	Generally used polymer material	Nature of starting material	Advantages	Drawbacks
FDM	Extrusion and deposition of material	Thermoplastic polymers such as PLA, ABS, PC and nylon	Filament	Low cost, high strength, flexible to many materials	Nozzle clogging, anisotropy
PLP	Drop-on-demand binder printing	Any material in powder form, binder needed	Powder	Low cost, flexible to many materials, easy removal of support powder	Binder jet clogging, binder contamination

SLS	Scanning with the help of laser and heat induced sintering	PCL and polyamide powder	Powder	Good strength, easy removal of support powder	Powder surface, high cost
SLA	Scanning with the help of laser and UV induced sintering	Photocurable resin (epoxy or acrylate-based resin)	Liquid photopolymer	High printing resolution	High cost, material limitation, cytotoxicity
Robo casting	Pressurized orifice and heat or UV-assisted curing	PCL, PLA, hydrogel	Liquid or paste	High printing resolution, soft material capability	Slow, low mechanical strength

I.7.2 Fused deposition modelling: principle and evolution

FDM was originally developed by Stratasys in the late 1980s as a rapid-prototyping process dedicated to the fabrication of concept models and engineering mock-ups. The technology has since evolved into a routine production route for functional parts in a wide range of industries, driven by three concurrent trends: the expiration of the original Stratasys patents and the subsequent emergence of an open-source ecosystem (RepRap), the improvement in the quality and the reliability of low-cost desktop machines, and the expansion of the filament catalogue beyond the two original materials ABS and PLA to a diverse range of engineering-grade and fibre-reinforced thermoplastics[77] (Fig. I. 15).

The FDM process itself is governed by a small number of controllable parameters that together determine the mechanical, geometric and surface properties of the printed part. The extrusion temperature controls the melt viscosity of the filament and therefore the inter-road bonding, with insufficient temperature leading to incomplete bonding and excessive temperature leading to thermal degradation of the polymer. The build-plate temperature controls the thermal contraction of the first layers and the adhesion of the part to the platform. The layer thickness governs the vertical resolution of the part and the strength of the inter-layer bond. The raster pattern (rectilinear, concentric, honeycomb) and the raster orientation determine the in-plane anisotropy of the printed part. The infill density, which ranges from a few percent for lightweight prototypes to one hundred percent for structural parts, governs the overall mass and stiffness of the part. The print speed influences the cooling rate of the deposited road and therefore its bonding quality to the adjacent roads [78].

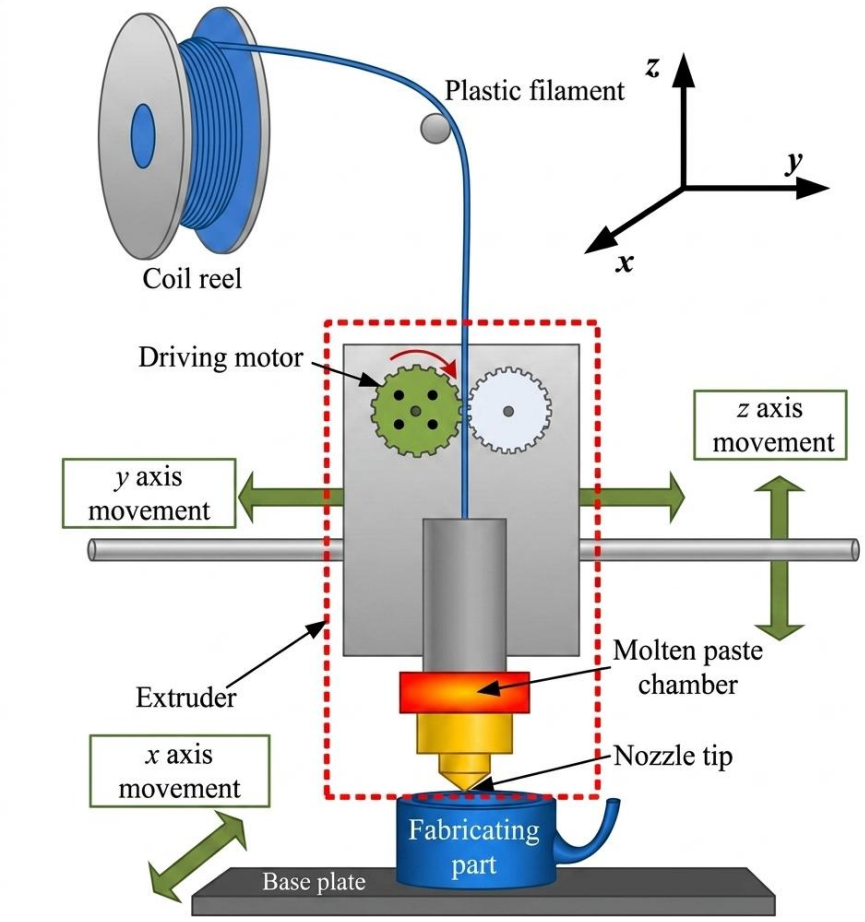


Fig. I. 15 Working principle of an FDM machine [79]

I.7.3 Fibre-reinforced FDM filaments

The introduction of fibre reinforcements into the FDM filament has been one of the most active research directions of the past decade, and it has produced a rapidly expanding family of composite filaments whose mechanical performance now competes with that of conventional injection-moulded thermoplastics. Two subfamilies are distinguished according to the origin of the fibre reinforcement.

Synthetic (synthetic-fibre) filaments (Fig. I. 16). The carbon-fibre-reinforced PLA filament, the glass-fibre-reinforced PLA filament, and the continuous-kevlar reinforcement of the Markforged process are the most widely studied synthetic-fibre FDM systems[80,81]. These filaments deliver elastic moduli and tensile strengths that exceed those of the unfilled thermoplastic matrix by factors of two to five, and they have opened FDM to structural applications in aerospace tooling, high-performance automotive parts and drone components. Their principal limitations are the increased cost of the filament, the wear that the reinforcement imposes on the brass extrusion nozzles (hardened-steel nozzles are typically required), and the persistence of the layer-by-layer anisotropy that characterises all FDM parts.



Fig. I. 16 Fabrication of filament from HDPE and glass-fibre composites[82]

HDPE: High-Density Polyethylene

Bio-based (natural-fibre) filaments (Fig. I. 17). The bio-based filament family combines a thermoplastic matrix (most often PLA, occasionally PHA or PBS) with a natural-fibre or particulate-bio reinforcement (flax, wood, hemp, bamboo, cork, cellulose). These filaments preserve the FDM compatibility of the base matrix while introducing a renewable, biodegradable reinforcement into the printed part. The PLA/flax filament, which is the bio-based system adopted in the present thesis, delivers a modest improvement in the stiffness of the printed part relative to neat PLA, together with a substantial enhancement of its ductility and its energy-absorption capacity under impact loading. The PLA/wood filament offers a characteristic visual and tactile quality that has found its primary application in decorative and architectural models. The PLA/hemp, PLA/cork and PLA/cellulose filaments occupy specialised windows in the bio-based FDM market[83].

The processing of bio-based filaments poses specific challenges that are not encountered with unfilled or synthetic-fibre filaments. The thermal stability of natural fibres typically places a ceiling on the extrusion temperature near 220 °C, which restricts the choice of the compatible matrix and constrains the processing window. The hygroscopicity of the fibres requires careful storage and pre-printing drying to avoid the bubbling and the voids that absorbed moisture would generate during extrusion. The fibre–matrix adhesion within the filament itself not to be confused with the inter-road adhesion of the printed part depends on the surface treatment applied to the fibres during compounding, and it is a determining factor of the mechanical performance of the final printed part [84].



Fig. I. 17 The various composite filaments, (a) PLA/PP filament, (b) ArF reinforced filament, from left to right, Un, Alk and SLN respectively[85]**.**

I.7.4 Geometric and structural factors in FDM parts

Beyond the process parameters, the mechanical response of an FDM part is governed by a set of geometric and structural factors that arise from the layer-by-layer nature of the deposition process itself. These factors are intrinsic to the FDM technology and persist even when the process parameters are held at their optimum values.

The voids between adjacent roads and between successive layers are the most pervasive source of property degradation in FDM parts. They reduce the effective cross-section of the part, they introduce stress concentrations at the onset of loading, and they act as preferred nucleation sites for fatigue cracks. Their size and distribution depend on the extrusion temperature, the layer thickness, the raster pattern and the print speed, and their complete elimination is impossible with the current FDM technology [86].

The raster orientation governs the in-plane anisotropy of the printed part. A part printed with a unidirectional raster pattern exhibits a tensile response that differs significantly between the raster direction and the transverse direction, with the raster-parallel strength typically exceeding the transverse strength by a factor of one-and-a-half to two. A cross-raster pattern at ±45° reduces this anisotropy at the cost of a slightly lower peak strength in either direction[87].

The inter-layer bonding governs the out-of-plane response of the printed part. The strength in the build direction is typically the weakest of the three principal directions, because the inter-layer bond relies on the thermal diffusion between the deposited layer and the already-solidified layer below it, which is itself limited by the cooling rate of the deposited road. A part loaded in

tension along the build direction can therefore fail by delamination between layers at stress levels well below its in-plane tensile strength[88].

The surface roughness of an FDM part is intrinsically high because of the layer stepping along the build direction, and it requires post-processing (sanding, vapour smoothing, chemical polishing) to meet the surface-quality requirements of applications such as aerodynamics, optics or medical implants[89].

I.8 Sandwich structures with cellular cores

Sandwich structures constitute a specific class of composite assemblies in which two thin, stiff face sheets are bonded to a thick, lightweight core (Fig. I. 18). The structural rationale of the assembly is derived from beam theory: separating the two face sheets by a low-density core dramatically increases the second moment of area of the cross-section, which in turn increases the bending stiffness and the bending strength of the assembly at a minimal mass cost. The sandwich concept therefore delivers one of the highest specific stiffnesses and specific strengths of any structural assembly, and it has been adopted across aerospace, marine, automotive, civil and sporting-goods industries for over half a century[90].

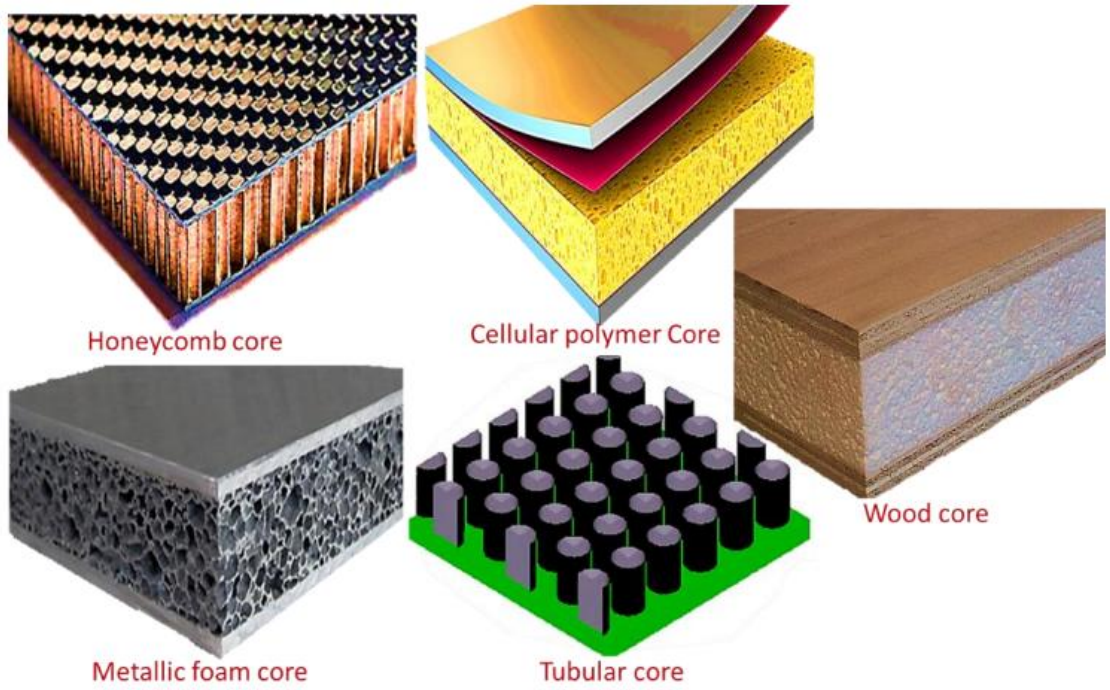


Fig. I. 18 Different core structures in sandwich composites[91].

I.8.1 Historical development and applications

The modern sandwich panel emerged during the second world war through the extensive use of plywood-balsa-plywood assemblies in the British Mosquito aircraft, and the concept was subsequently refined in the post-war aerospace industry through the introduction of aluminium

honeycomb cores and metallic face sheets. The aerospace application remained the principal driver of sandwich technology through the 1960s and 1970s, during which aluminium and later composite face sheets were combined with aluminium or Nomex honeycomb cores to produce the primary and secondary structures of commercial airliners and military aircraft[92].

The expansion of sandwich panels into the marine, automotive, civil-construction and wind-energy industries during the 1980s and the 1990s was driven by two developments: the maturation of glass-fibre-reinforced-polymer face sheets, which brought the cost of composite face sheets into a range compatible with high-volume industrial applications, and the development of rigid polymeric foams (polyurethane, polystyrene, PVC) as lower-cost alternatives to the honeycomb core. The contemporary sandwich-panel market is therefore characterised by a wide diversity of face-sheet and core materials, each adapted to the performance and cost requirements of its target application [93].

I.8.2 Conventional cores versus bio-based additively manufactured cores

Conventional sandwich cores fall into three principal families. Honeycomb cores, produced by the expansion of glued strips of aluminium or aramid paper (Nomex), deliver the highest specific stiffness of any conventional core and dominate the aerospace sandwich market. Polymeric foam cores (polyurethane, polystyrene, PVC, PET) are obtained by the chemical or physical expansion of a polymer melt, and they deliver a continuous, closed-cell structure at a substantially lower cost than honeycomb, although at the expense of a lower specific stiffness. Balsa-wood cores, derived from the processed timber of the balsa tree, occupy a specific niche in the marine industry where their natural grain structure and their low density ($\approx$150 kg·m^{-3}) deliver an attractive combination of stiffness and energy absorption[94].

The emergence of fused deposition modelling has opened a fourth and rapidly growing family of sandwich cores: additively manufactured cellular cores, in which the internal topology of the core is designed pixel by pixel in a digital model and then printed layer by layer as a single monolithic part. This approach frees the core geometry from the constraints imposed by the expanded-honeycomb forming process and by the chemical-foaming physics of polymeric foams, and it opens the design space to a broad range of cellular topologies re-entrant, auxetic, Kagome, tri-grid, chiral, hybrid whose mechanical response can be tailored to the specific loading scenario of the target application[95]. When the additively manufactured core is printed from a bio-based filament such as PLA or PLA/flax, the resulting sandwich panel combines the geometric tailoring of AM with the sustainability advantages of bio-based materials, and it defines the specific design space that the present thesis addresses.

I.8.3 Core topologies reported in the literature

The diversity of cellular topologies that can be printed by FDM has given rise to an active research direction on the optimisation of the core geometry for sandwich applications. Six topologies dominate the recent literature and deserve a brief overview.

The honeycomb topology remains the reference configuration in the sandwich community, because of its historical precedence, its relative ease of FDM reproduction, and the large body of experimental and analytical data available for comparison (Fig. I. 19). The hexagonal cell geometry delivers a specific stiffness that is competitive with the best alternative topologies under out-of-plane compression and a failure mode that is dominated by the controlled buckling of the cell walls[96].

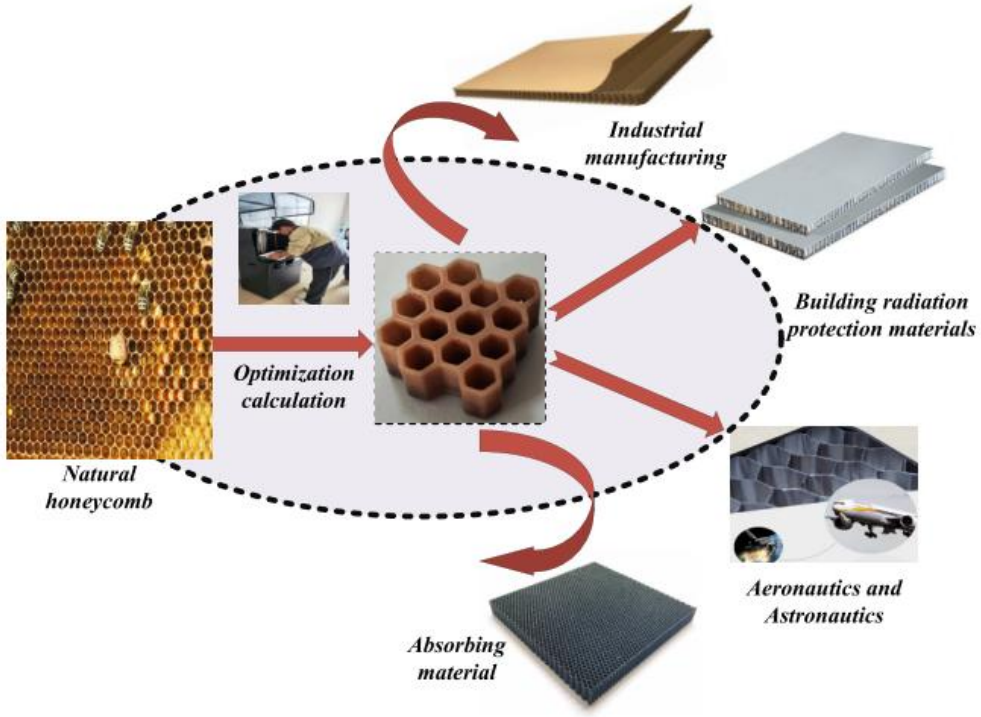


Fig. I. 19 A schematic diagram illustrating the optimization calculation, preparation, and application of the natural honeycomb mechanical properties[97]**.**

The circular (hollow-cylinder) topology replaces the hexagonal cells of the honeycomb with cylindrical voids aligned with the out-of-plane direction of the panel. This topology is simpler to model analytically than the honeycomb and delivers a more uniform stress distribution along the wall of each cell, at the cost of a slightly lower specific stiffness. Its energy-absorption capacity depends strongly on the wall thickness and on the diameter of the cylindrical voids [95].

The tri-grid topology, in which three families of rectilinear struts intersect at sixty-degree angles to form a triangular-mesh structure, has emerged as one of the most promising cellular

topologies for FDM-printed sandwich cores. The interconnected-strut architecture redistributes the applied load across multiple redundant paths, which delays the localisation of damage and produces a higher specific stiffness and a higher specific shear strength than the honeycomb and the circular topologies under a wide range of loading scenarios [98].

The re-entrant and auxetic topologies exhibit the unconventional property of a negative Poisson's ratio, which causes the material to contract laterally when it is compressed longitudinally (Fig. I. 20). This behaviour delivers an enhanced indentation resistance and an improved energy-absorption capacity under impact loading, but at the cost of a more complex manufacturing route and of a reduced specific stiffness[99].

The Kagome topology is built from a periodic arrangement of triangular and hexagonal cells that deliver a high shear stiffness in two principal directions. It has been investigated for aerospace applications where multi-axial loading dominates, and its additively manufactured variants have shown encouraging mechanical performance in the recent literature [100].

The hybrid topologies, finally, combine two or more of the above cell geometries within a single core, in order to exploit the complementary strengths of each topology and to tailor the mechanical response of the sandwich to the specific loading configuration of the application (Fig. I. 20). These topologies are still in the exploratory phase of the research and have yet to reach industrial maturity [72].

The comparative mechanical response of the principal FDM-printable core topologies has been the subject of several targeted investigations. Lu et al [101]. Fabricated PLA honeycomb sandwich structures with Bi-Grid, Tri-Grid, Quadri-Grid and Kagome-Grid cores, bonded them to carbon-fibre/epoxy face sheets, and subjected them to three-point bending; the Quadri-Grid structure delivered the highest load capacity (3391 N) and specific strength (9562 N·m/kg), while the Tri-Grid structure recorded the lowest load capacity (2561 N), and the failure mode shifted from interfacial debonding in the Bi-Grid configuration to core shear in the three grid-based configurations. Pirouzfar and Zeinedini[102] varied the cell orientation and wall thickness of 3D-printed PLA honeycomb cores in E-glass/epoxy sandwich panels; horizontal cores with 1.5 mm walls exhibited the highest energy absorption (208.56 J/kg), and the incorporation of a thin PLA interfacial layer increased the load capacity of vertical cores by 220 %, demonstrating that the core–face-sheet interface is as decisive as the core topology itself. Azzouz et al[103]. compared three PLA lattice geometries as cores for PP–flax sandwich panels and found that the diamond lattice incorporating a vertical strut outperformed the other two designs in out-of-plane compression and shear, whereas the variant without a vertical strut was superior in in-plane compression and flexural strength, confirming that a single geometric

feature can invert the performance ranking depending on the loading mode. Shahkarami and Zeinedini [104] introduced hierarchical sinusoidal corrugated PLA cores and reported that a transverse arrangement with an arch-downward configuration delivered a normalised core shear ultimate strength of 245.78 MPa/kg and an energy absorption of 330.75 J/kg. Wang et al[33]. , using a multi-material additive manufacturing route to produce CFRPC face sheets and thermoplastic foam cores in a single step, found that a rhombus unit-cell core outperformed square, honeycomb and re-entrant honeycomb designs, achieving the highest flexural stiffness and a specific energy absorption of 1273.08 J/kg, and that a functionally graded core with a reduced strut thickness in the middle section further enhanced the energy absorption by 46 % (2445.8 J/kg). Taken together, these comparative studies demonstrate that no single core topology is unconditionally optimal, and that the performance ranking depends simultaneously on the loading mode, the face-sheet material and the core face-sheet interface. This conclusion provides the rationale for the three topologies retained in the present thesis honeycomb, circular and tri-grid and for the systematic comparison of their flexural and energy-absorption responses under identical face-sheet and interface conditions.

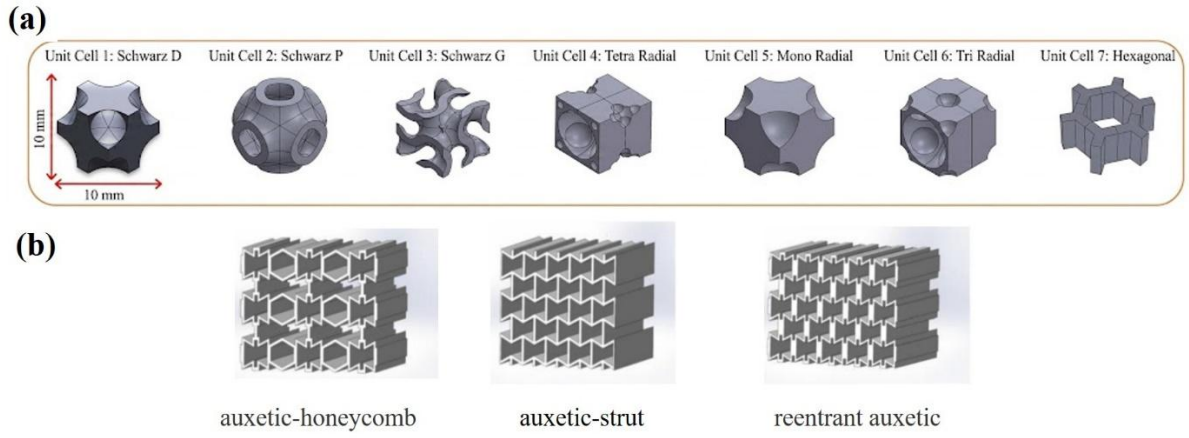


Fig. I. 20 Cellular core topologies for FDM-printed sandwich panels[105,106]**.**

I.8.4 Face-sheet materials and face-sheet/core interface

The face sheets of a sandwich panel are traditionally built from synthetic-fibre-reinforced laminates (glass, carbon, aramid) because of their high specific stiffness and their mature manufacturing routes. The emergence of natural-fibre laminates during the past decade has introduced a bio-based alternative whose mechanical performance, while lower than that of synthetic laminates, is sufficient for a wide range of semi-structural applications and which delivers a substantial reduction in the environmental footprint of the panel. Hybrid face sheets, in which two or more natural fibres with complementary mechanical and thermal signatures are combined within a single laminate, have been shown to deliver a mechanical response that

exceeds the weighted average of the individual constituents, through the activation of hierarchical failure mechanisms that single-fibre laminates cannot reproduce [107].

The face-sheet/core interface is the structural element that transmits the shear load between the core and the face sheets, and its integrity is a determining factor of the overall mechanical response of the sandwich. The interface is typically built through the use of a compliant adhesive (epoxy, polyurethane, methacrylate) whose stiffness sits between that of the face sheet and that of the core. The micro-textured surface generated by the FDM printing of the core enhances the mechanical interlocking of the adhesive and the core, and it contributes to the interfacial robustness that characterises well-designed FDM-printed sandwich panels [108].

I.9 Numerical simulation of biocomposite sandwich panels

The experimental characterisation of sandwich panels is limited by the number of geometrical and material combinations that can be physically produced. Finite element (FE) simulation has therefore become an indispensable tool for exploring a wider design space at a reduced cost, while providing full-field stress and strain distributions that are difficult to obtain experimentally (Fig. I. 21). This section first presents the fundamental principles of FE modelling applicable to composite materials, then details the specific constitutive choices adopted in the present thesis, and finally reviews previous studies that have applied numerical simulation to additively manufactured sandwich panels[109].

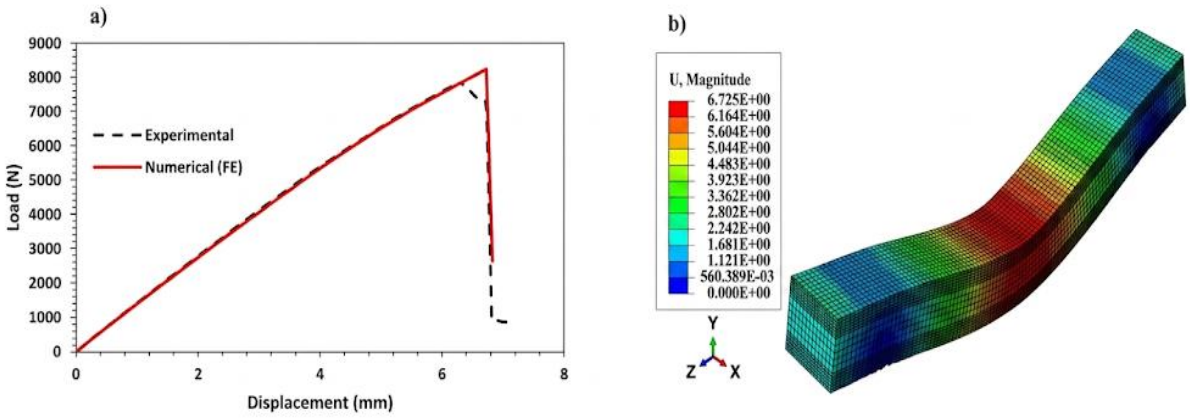


Fig. I. 21 Experimental and numerical simulation load–displacement plots[110]**.**

I.9.1 Governing equations and finite element discretisation

The simulation of a deformable solid under quasi-static loading rests on three conditions that must be satisfied simultaneously at every point of the domain: equilibrium, a constitutive law, and geometric compatibility. The local equilibrium condition requires that the divergence of the Cauchy stress tensor σ balances the body-force vector b at every material point:

$$\nabla \cdot \boldsymbol{\sigma} + \mathbf{b} = \mathbf{0} \qquad (I.1)$$

The geometric compatibility condition relates the infinitesimal strain tensor ε to the displacement field u:

$$\boldsymbol{\varepsilon} = \frac{1}{2}(\nabla \mathbf{u} + \nabla \mathbf{u}^T) \qquad (I.2)$$

The constitutive law closes the system by relating stress to strain through the fourth-order material stiffness tensor D:

$$\boldsymbol{\sigma} = \mathbf{D}\boldsymbol{\varepsilon} \qquad (I.3)$$

For the heterogeneous assemblies typical of composite sandwich structures, an analytical solution of Eqs. (I.1)–(I.3) is rarely tractable, and a finite element discretisation is required. The domain is partitioned into elements within which the displacement field is interpolated from the nodal values through the shape function matrix N:

$$\mathbf{u}(x, y, z) = \mathbf{N}(x, y, z)\mathbf{u}_e \qquad (I.4)$$

The strain field follows from the compatibility condition via the strain–displacement matrix B = L N, where L is the linear differential operator:

$$\varepsilon = \mathbf{B}\mathbf{u}_e \qquad (I.5)$$

Substituting Eqs. (I.3)–(I.5) into the principle of virtual work and requiring the result to hold for all kinematically admissible virtual displacement fields yields the discrete global system:

$$[\mathbf{K}]\mathbf{u} = \mathbf{F} \qquad (I.6)$$

where {F} is the external load vector and [K] is the global stiffness matrix assembled from the element stiffness matrices:

$$\mathbf{K}_e = \int_{\Omega_e} \mathbf{B}^T \mathbf{D} \mathbf{B} d\Omega_e \qquad (I.7)$$

Equation (I.7) is the central quantity that any FE solver assembles and solves; the material stiffness tensor D takes a different explicit form for each constituent of the sandwich, as detailed in the following sections.

I.9.2 Constitutive modelling of composite sandwich constituents

I.9.2.1 Orthotropic elastic model for the face-sheet laminate

Continuous-fibre-reinforced face sheets are intrinsically orthotropic at the ply scale. Under the plane-stress conditions prevailing in a thin lamina referenced to its principal material axes, the in-plane stress–strain relation takes the well-known form:

$$\begin{pmatrix}\sigma_1\\ \sigma_2\\ \tau_{12}\end{pmatrix}=\begin{bmatrix}Q_{11} & Q_{12} & 0\\ Q_{12} & Q_{22} & 0\\ 0 & 0 & Q_{66}\end{bmatrix}\begin{pmatrix}\varepsilon_1\\ \varepsilon_2\\ \gamma_{12}\end{pmatrix} \quad (I.8)$$

where the reduced stiffness coefficients are expressed in terms of the engineering constants of the ply:

$$Q_{11}=\frac{E_1}{1-\nu_{12}\nu_{21}}, Q_{22}=\frac{E_2}{1-\nu_{12}\nu_{21}}, Q_{12}=\frac{\nu_{12}E_2}{1-\nu_{12}\nu_{21}}, Q_{66}=G_{12} \quad (I.9)$$

For a ply oriented at an angle θ to the global reference frame, the reduced stiffness matrix is transformed to the global coordinate system through the standard rotation transformation. When the face sheet consists of multiple plies stacked in a defined sequence, Classical Laminate Theory (CLT) provides the through-thickness integration of the ply constitutive relations. The resulting relation between the mid-plane strains and curvatures and the force and moment resultants is expressed through the well-known ABD matrix:

$$\begin{pmatrix}\mathbf{N}\\ \mathbf{M}\end{pmatrix}=\begin{bmatrix}\mathbf{A} & \mathbf{B}\\ \mathbf{B} & \mathbf{D}\end{bmatrix}\begin{pmatrix}\boldsymbol{\varepsilon}^0\\ \boldsymbol{\kappa}\end{pmatrix} \quad (I.10)$$

where the sub-matrices **A**, **B**, and **D** govern the in-plane extensional response, the bending–extension coupling, and the out-of-plane bending response, respectively. For a symmetric and balanced laminate, the coupling matrix **B** vanishes, which considerably simplifies the formulation.The onset of damage in the orthotropic face-sheet laminate is commonly assessed through the Tsai–Wu quadratic failure criterion, which accounts for the interaction between normal and shear stress components:

$$F_1\,\sigma_1+F_2\,\sigma_2+F_{11}\,\sigma_1^2+F_{22}\,\sigma_2^2+F_{66}\,\tau_{12}^2+2\,F_{12}\,\sigma_1\sigma_2=1 \quad (I.11)$$

where the strength parameters F_i and $F_{\{ij\}}$ are expressed in terms of the uniaxial tensile and compressive strengths (X_T, X_C, Y_T, Y_C) and the in-plane shear strength S {12} of the lamina.

I.9.2.2 Isotropic elastic-plastic model for the core

Cellular cores produced by fused deposition modelling are commonly represented as isotropic elastic-plastic solids. In the elastic regime, the constitutive relation (I.3) reduces under a uniaxial stress state to:

$$\sigma_{11} = E\varepsilon_{11} \quad (I.12)$$

The onset of plastic flow is governed by the von Mises yield criterion, in which the equivalent stress:

$$\sigma_{eq} = \sqrt{\frac{1}{2}[(\sigma_1 - \sigma_2)^2 + (\sigma_2 - \sigma_3)^2 + (\sigma_3 - \sigma_1)^2]} \quad (I.113)$$

is compared with the yield strength of the material. The post-yield hardening response is described by a true stress–true plastic strain curve, derived from the experimental engineering data through the standard conversions:

$$\sigma_{true} = \sigma_{eng}(1 + \varepsilon_{eng}) \quad (I.114)$$

$$\varepsilon_{true} = \ln(1 + \varepsilon_{eng}) \quad (I.115)$$

The onset and progression of damage in the core material can be captured through the ductile damage initiation and evolution framework, where the post-initiation softening behaviour is governed by a linear law based on the fracture energy G_f:

$$G_f = \int_{\bar{\varepsilon}_{pl}^0}^{\bar{\varepsilon}_{pl}^f} L\sigma_y d\bar{\varepsilon}_{pl} \quad (I.116)$$

where L is the characteristic element length, σ_y is the current yield stress, and $\bar{\varepsilon}_{pl}^0$ and $\bar{\varepsilon}_{pl}^f$ are the equivalent plastic strains at damage initiation and final failure, respectively[111,112].

I.9.2.3 Element types and interface treatment

In FE models of sandwich panels, the core is typically discretised with reduced-integration eight-node hexahedral elements (C3D8R in ABAQUS notation), with hourglass stabilisation applied to suppress spurious zero-energy modes. The face sheets are commonly discretised with four-node shell elements (S4R) using a multi-point through-thickness integration scheme. The face-sheet–core interface is treated through a surface-to-surface tied constraint, which enforces displacement continuity across the bonded surface and is appropriate for configurations where no delamination is observed experimentally.

I.9.3 Validation metrics

The fidelity of a finite element model is assessed through three complementary metrics. The peak-load error, computed as the relative deviation between the simulated and experimental maximum load, is the scalar descriptor most commonly reported in the literature; a value within

±10 % is conventionally accepted as the engineering tolerance band for the validation of composite FE models. The pre-failure correlation coefficient R^2, computed over the elastic and early-plastic regime of the force–displacement curve, routinely exceeds 0.95 for well-calibrated models. The load–deflection overlay provides the most complete visual assessment of model fidelity across the full loading history.

I.9.4 Prior work on the numerical simulation of FDM-printed biocomposite sandwich panels

The FE framework described above has been applied to additively manufactured sandwich panels in several recent studies directly relevant to the present thesis.

Lu et al[101]. fabricated PLA sandwich panels with Bi-Grid, Tri-Grid, Quadri-Grid and Kagome-Grid cores bonded to carbon-fibre/epoxy face sheets and developed an ABAQUS model discretised with C3D8R core elements and S4R shell face-sheet elements (Fig. I. 22). The model reproduced the experimental peak loads with errors below 8 % and identified the stress concentration zones at the strut junctions that governed the experimentally observed failure sequence.

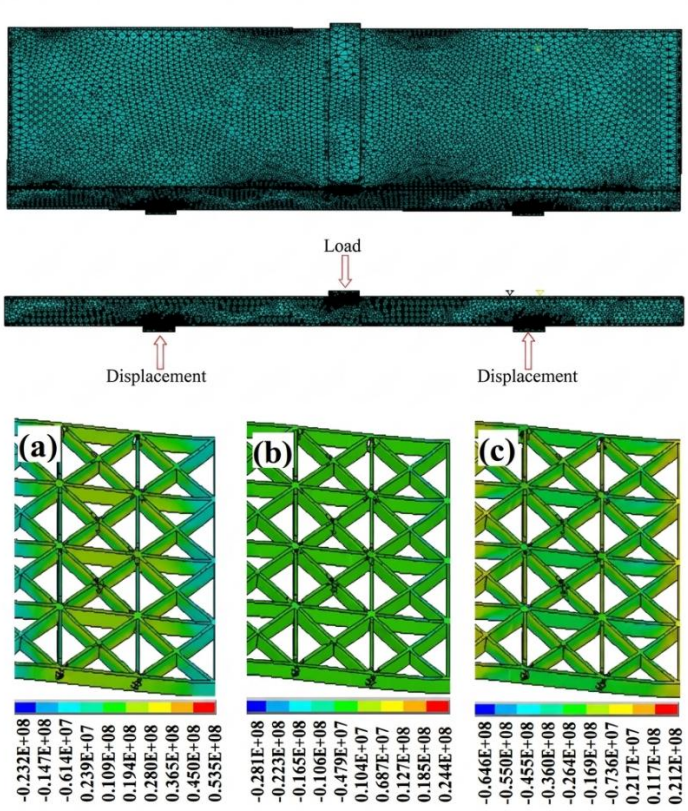


Fig. I. 22 Three-Point Bending Simulation and Stress Analysis of Cellular Structures [101].

Pirouzfar and Zeinedini [102] examined PLA honeycomb cores combined with E-glass/epoxy face sheets under three-point bending and reported close agreement between the

FEA predictions and the experimental force–displacement curves across the full pre-failure range, confirming the adequacy of the isotropic elastic-plastic core model coupled with an orthotropic shell formulation for the face sheets (Fig. I. 23).

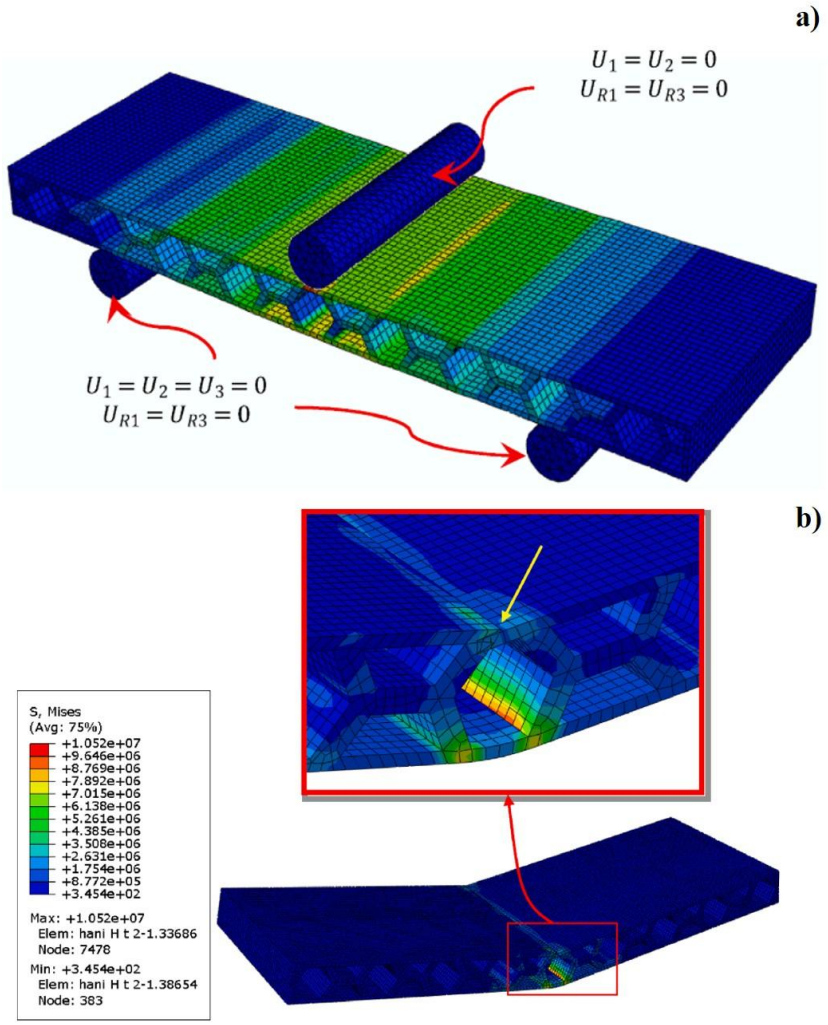


Fig. I. 23 The boundary conditions and sample after failure with the failed region[102]**.**

Kamarian et al[113]. trained a deep neural network on experimental bending data of PLA auxetic-core/flax-epoxy beams and demonstrated that the surrogate reproduced the full load–deflection curve of an unseen specimen with $R^2 \approx 0.99$, illustrating the complementary role that machine-learning surrogates can play alongside classical FE simulations in the design optimisation loop. Cao et al[114]. reported bending and shear strength improvements of approximately 25–34 % in 3D-printed PLA-core sandwich structures through optimisation of the skin/core resin uptake and cell topology. Pino et al[115]. investigated sandwich panels combining vegetable-fibre face sheets with 3D-printed PLA cores and showed that both cell topology and fibre surface treatment significantly influenced the flexural and energy-absorption performance, beyond these core studies, several additional investigations have further consolidated the combined experimental–numerical strategy for FDM-printed sandwich panels.

In this work, Li et al[116]. developed a one-step integrated 3D printing method for sandwich panels with continuous basalt fiber face sheets and TPMS cores (Schwarz Primitive, Gyroid) plus two honeycomb cores (Fig. I. 24). They used a bridging layer and stiff epoxy-prepreg to print the top face sheet over the core without supports. Compared with multi-step bonded samples and unreinforced ones, the integrated panels showed much better flexural properties and avoided brittle failure. The specific energy absorption improved by 162.88% due to strong fusion between the PLA bridging layer and the PLA core. Among all cores, Schwarz Primitive gave the highest flexural strength, modulus, and energy absorption.

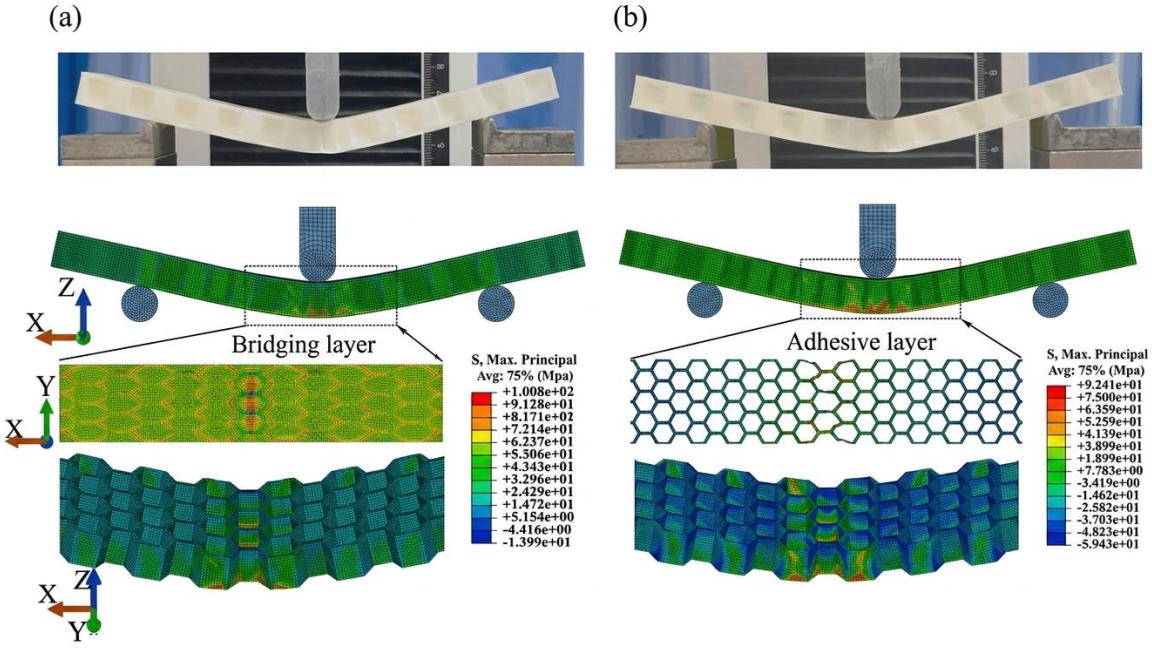


Fig. I. 24 Failure modes of sandwich panels (using a honeycomb structure as an example) at maximum load, as observed in experiments and simulated via finite element (FE) results: (a) O-PLA; (b) B-PLA[116]**.**

This study by Choudhry et al[117]. evaluates the mechanical properties and energy absorption of 3D printed polymeric sandwich structures with various auxetic cores (re-entrant, arrowhead, and anti-tetra chiral) compared to a conventional honeycomb core under quasi-static and low-velocity impact loading. Experimental and numerical (FEM) results indicate that auxetic cores significantly enhance structural performance and resistance to compression. While the arrowhead core achieved the highest energy absorption under quasi-static compression, the anti-tetra chiral structure demonstrated the optimum overall performance across both loading types. Specifically, the anti-tetra chiral design provided the highest specific energy absorption per maximum stroking length during impact tests, making it the most efficient choice for applications prioritizing high energy absorption, minimal deformation, and low overall weight (Fig. I. 25).

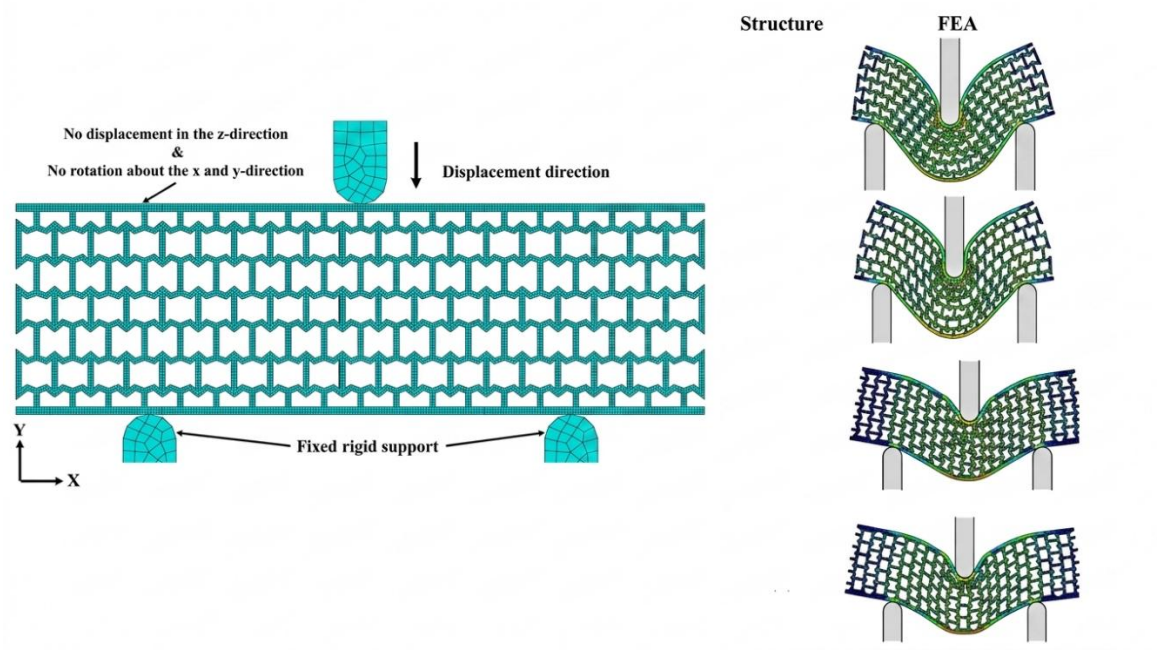


Fig. I. 25 Boundary conditions and loading direction applied in the finite element (FE) model[117]**.**

In their 2026 study, Xu et al[118]. proposed a novel origami-enhanced honeycomb sandwich beam (OHB) featuring a bidirectional re-entrant core designed to significantly improve flexural toughness and energy absorption for high-performance engineering applications. Utilizing 3D-printed Nylon PA12 specimens and ABAQUS numerical simulations (Fig. I. 26), the researchers systematically analyzed the beam's performance under three-point bending, evaluating variables such as loading distance, thickness gradients, and cell size. The findings revealed that the OHB substantially outperforms traditional re-entrant structures, yielding an average 83.99% increase in initial platform force and a 168.61% boost in specific energy absorption.Furthermore, the study identified panel wrinkling as a critical failure mechanism linked to unit cell stiffness, concluding that smaller cell sizes enhance performance through more uniform stress distribution, while thickness gradients can be optimized to reduce peak forces in collision protection without sacrificing overall energy absorption efficiency.

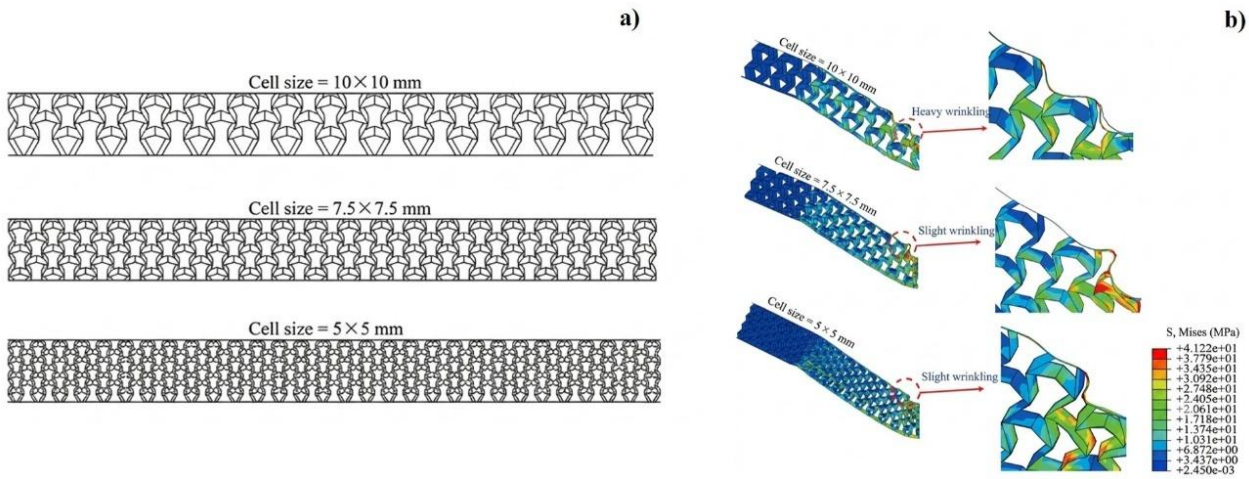


Fig. I. 26 Effect of cell size on the bending response and panel wrinkling deformation in origami-enhanced honeycomb (OHB) sandwich beams[118]**.**

The failure-mechanism perspective was addressed by Sefidi and Taghipoor [119], who combined analytical beam theory, finite element simulation and experimental validation to characterise the progressive failure sequence of lattice cores under quasi-static three-point bending and to quantify the energy absorption capacity as a function of core geometry. The topology-dependent trade-off between stiffness and energy absorption was quantified by Adibi et al[120], whose integrated investigation of FDM-printed PLA+ honeycomb and auxetic cores under compression, three-point bending and Charpy impact revealed that auxetic cores exhibit approximately 51% higher specific energy absorption than honeycomb cores in compression while honeycomb cores provide superior flexural stiffness. Finally, Li et al[121]. demonstrated the feasibility of a fully bio-based lattice sandwich concept by fabricating bi-directional corrugated lattice structures from jute fibre and epoxy resin, combining the structural advantages of lattice sandwich architecture with the sustainability benefits of natural-fibre reinforcement and constituting one of the earliest precedents for the hybrid bio-based sandwich concept in the literature.These precedents collectively confirm that finite element analysis constitutes a reliable and mature predictive tool for the mechanical characterisation of biocomposite sandwich panels.

I.10 Conclusion

A review of the literature has established plant-derived natural fibres as credible, renewable reinforcements whose hierarchical cell-wall architecture, balanced chemical composition, and favourable specific properties translate into competitive physical, mechanical, and thermal performance, particularly when paired with bio-based or thermoset polymeric matrices. The performance of the resulting composites is governed by the species and anatomical origin, by

the extraction route whose optimisation has been shown to substantially elevate the tensile strength of Typha and to tune the cellulose content of Agave across a useful processing window by the surface treatments applied to enhance fibre matrix adhesion, by the reinforcement architecture, and by the manufacturing route, whether conventional layup or fused deposition modelling, for which artificial neural networks have markedly reduced the prediction error relative to classical optimisation frameworks. The literature on additively manufactured cellular cores and biocomposite sandwich panels further confirms that core topology whose performance ranking shifts with the loading mode and the face-sheet material face-sheet core adhesion, and the constitutive modelling strategy adopted in the finite element simulation are equally decisive, and that well-calibrated models now routinely reproduce the experimental load deflection curve with high fidelity in the pre-failure regime.

Nevertheless, studies that integrate regionally sourced lignocellulosic reinforcements with FDM-printed bio-based cores into a single hybrid sandwich architecture remain relatively limited. To address this gap, the next chapter establishes the experimental and numerical framework that underpins the entire thesis, including the complementary extraction routes adopted for Typha latifolia (mild alkaline delignification) and Agave americana (strictly mechanical decortication), their physicochemical and single-fibre mechanical characterisation, the hand layup fabrication of the hybrid face sheets, the FDM printing of the neat PLA and PLA/flax cores in three distinct cellular topologies, and the assembly and mechanical evaluation of the resulting sandwich panels under three-point bending, supported throughout by finite element simulation and non-parametric statistics.

Chapter II

Materials and Methods

II.1 Introduction

This second chapter describes the materials, fabrication routes, characterisation techniques and numerical tools employed throughout the doctoral research programme. The work draws on three coordinated investigations a process-parameter study of FDM-printed PLA (using Taguchi and ANN methodologies), an apertured-tensile study of the same material, and a hybrid bio-based sandwich-panel study that together build a complete picture of the materials and methods adopted in this thesis. The two PLA studies were carried out first to consolidate a quantitative understanding of the printing process before the sandwich panels were designed; the sandwich-panel study followed as the culminating contribution. The chapter is organised along the conventional structure of an engineering Materials and Methods chapter, covering raw materials, fibre extraction and characterisation (FTIR, TGA, DTG, XRD), face-sheet and core fabrication, sandwich assembly, mechanical testing, and the statistical (Kruskal–Wallis) and finite element (ABAQUS) frameworks used throughout. All three investigations share a single methodological commitment: every numerical input is traceable to a documented experimental protocol, no parameter is adjusted post hoc, and the local provenance of the Typha latifolia and Agave americana fibres constitutes the connecting thread of the chapter.

II.2 Raw materials

II.2.1 Lignocellulosic fibres

Two lignocellulosic species native to M'Sila Province (Algeria) were retained as reinforcement. Typha latifolia L. was selected for its abundance along the K'sob Dam wetland and for the low-density fibrous cortex of its stems. Agave americana L. was selected because its mature leaves enclose long, continuous bundles of aligned fibres that can be isolated without any chemical treatment. Detailed provenance, climatic characteristics, and pre-extraction handling are reported in Section II.3.

II.2.2 Epoxy matrix

The matrix used for the face sheets was Genc Ultra Transparent Glossy Casting Epoxy VX100.00 (Genc Polimer Kimya, Turkey), a two-component low-viscosity system processed at a mass ratio of 100 parts resin to 28 parts hardener, as specified by the supplier. Cold pressing at 25–27 °C and 50–55 % relative humidity for 48 h was used for curing, as described in Section II.5.

II.2.3 Thermoplastic filaments

Two 1.75 mm filaments were used as feedstock for the additive manufacturing of the cores. The first was a neat PLA filament (gold pigment). The second was a PLA/flax biocomposite

filament supplied by Nanovia (France), in which short flax fibres are dispersed within a PLA carrier polymer (brown pigment). The nominal values declared by the suppliers, subsequently used as reference inputs for the ABAQUS constitutive cards, are compiled in Table II.1.

Table II. 1 Filament specifications and nominal properties (manufacturer data).

Parameter	Neat PLA	PLA/Flax
Diameter (mm)	1.75	1.75
Spool mass (g)	1000	500
Density (g·cm^{-3})	1.24	1.25
Tensile strength (MPa)	65	41
Young's modulus (MPa)	3100	3100
Recommended nozzle temperature (°C)	220	220
Recommended bed temperature (°C)	60	60
Pigment	Gold	Brown

II.3 Fibre extraction and treatment

Two distinct extraction routes were followed because the two species differ in how tightly their cellulosic bundles are bound to the surrounding tissue. Typha latifolia stems required an alkaline delignification step to liberate the fibre bundles from the lignin/pectin sheath of the cortex, whereas Agave americana leaves delivered long continuous bundles under a purely mechanical route, without any chemical reagent. Both routes were designed to be reproducible with equipment routinely available in a university mechanics laboratory. Both species were processed within 24 h of harvest.

II.3.1 Plant provenance and pre-extraction handling

Typha latifolia L[7]. stems were harvested in spring 2023 from the K'sob Dam wetland (35°26′N, 4°32′E; ≈ 720 m a.s.l., M'Sila Province, Algeria). The site has a semi-arid continental climate (Köppen BSk), with a mean annual precipitation of approximately 250 mm and an ambient temperature range of −5 to 38 °C. Only vegetatively mature stems, with a mean length of 2.5 m and a basal diameter of 8–16 mm, free of visible disease or mechanical damage, were retained.

Agave americana L[6]. leaves were collected from the Ouanougha area (35°41′N, 4°17′E; ≈ 1050 m a.s.l., M'Sila Province), a site with a continental-montane climate and a mean annual precipitation of approximately 300 mm, where the species colonises naturally on degraded calcareous soils. Mature leaves with a length of 1.2–1.8 m and a basal width of 12–18 cm, free of surface lesions, were harvested using ceramic-coated knives to minimise metallic contamination. Geographic and climatic data for both collection sites are summarised in Table II.2.

Table II. 2 Geographical and climatic characteristics of the collection sites.

Parameter	T. latifolia (K'sob Dam)	A. americana (Ouanougha)
Coordinates	35°26′N, 4°32′E	35°41′N, 4°17′E
Elevation (m a.s.l.)	≈ 720	≈ 1050
Climate (Köppen)	BSk (semi-arid)	BSk / Csb (continental-montane)
Mean annual precipitation	≈ 250 mm	≈ 300 mm
Plant part used	Stem	Mature leaf
Harvest season	Spring 2023	Spring 2023

II.3.2 Typha latifolia: alkaline delignification

Typha latifolia stems were sectioned into 250 mm segments and immersed in a 3.25 % (w/v) aqueous sodium hydroxide (NaOH) solution (analytical grade, ≥ 97 %) at a solid-to-liquid ratio of 1:15 g·mL^{-1}. The treatment was conducted at 25 ± 2 °C for 48 h, with visual inspections every 6–8 h to confirm progressive maceration of the parenchyma without over-digestion of the fibres. The mild temperature and dilute NaOH concentration were retained because more aggressive treatments are known to degrade the cellulose I fraction and depress the single-fibre tensile strength of comparable lignocellulosic substrates.

After the 48h soak, the softened stems were removed from the alkaline bath and mechanically separated from residual cortical debris using a stainless-steel scraper. The liberated fibre bundles were then rinsed in three successive distilled-water baths (30 min each) until a neutral effluent pH of 7.0 ± 0.5 was reached, confirming complete removal of residual alkali. Residual non-fibrous fragments were eliminated by dry combing. The clean bundles were shade-dried for 48 h under controlled conditions (22 ± 2 °C, 30 ± 3 % RH) and then stored in sealed polyethylene bags containing silica-gel desiccant.

II.3.3 Agave americana: mechanical decortication

A strictly mechanical extraction route was applied to Agave americana leaves. Terminal spines and marginal teeth were removed from each leaf prior to processing. The de-spined leaves were then passed through stainless-steel rollers (diameter 80 mm, gap 5 mm) that ruptured the parenchymatous tissue without shearing the underlying fibre bundles. A controlled blade-scraping operation was subsequently applied along the leaf axis to release the fibre bundles and eliminate the mucilage, without inducing transverse structural damage.

The crude bundles were refined through a two-stage combing protocol: a coarse steel comb with a tooth spacing of 2 mm was used first to disentangle the ribbon and remove large debris,

followed by a nylon-bristle comb with a tooth spacing of 0.5 mm to align the individual filaments into quasi-parallel ribbons. Residual mucilage and pectins were removed by three successive rinsing cycles in distilled water (10 min each), until the effluent pH stabilised at 6.8 ± 0.3. The cleaned ribbons were shade-dried for 48–72 h at 25 ± 2 °C and 30–40 % RH, and stored under identical conditions to those used for T. latifolia.

A schematic representation of the two extraction routes is presented in Fig. II.1, and a complementary photographic documentation of the executed sequences is given in Fig. II.2. Key parameters of the two routes are compared in Table II.3. All fibre specimens were subsequently conditioned at 23 ± 1 °C and 50 ± 2 % RH for 48 h prior to any characterisation, in accordance with ISO 139:2005.

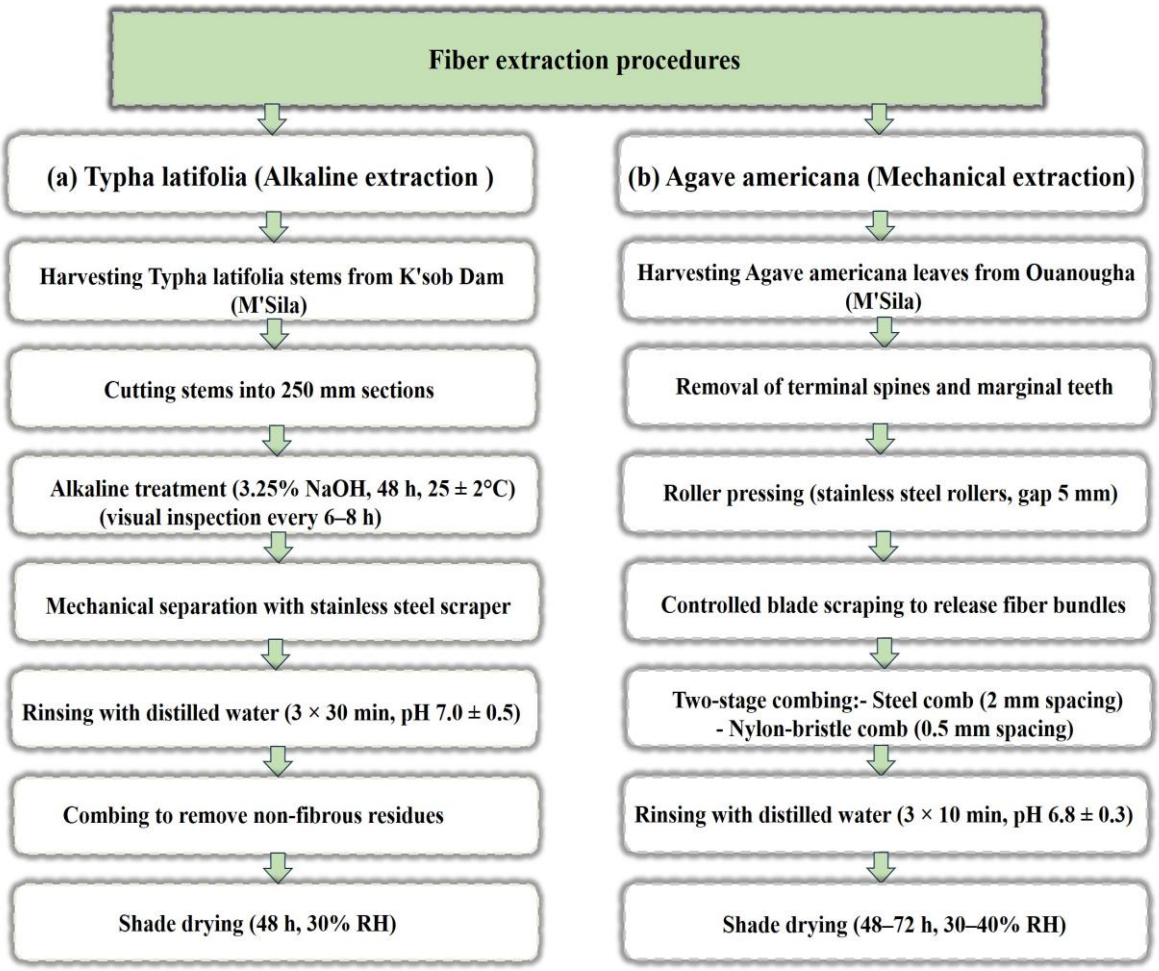


Fig. II. 1 Schematic representation of the fibre extraction procedures.

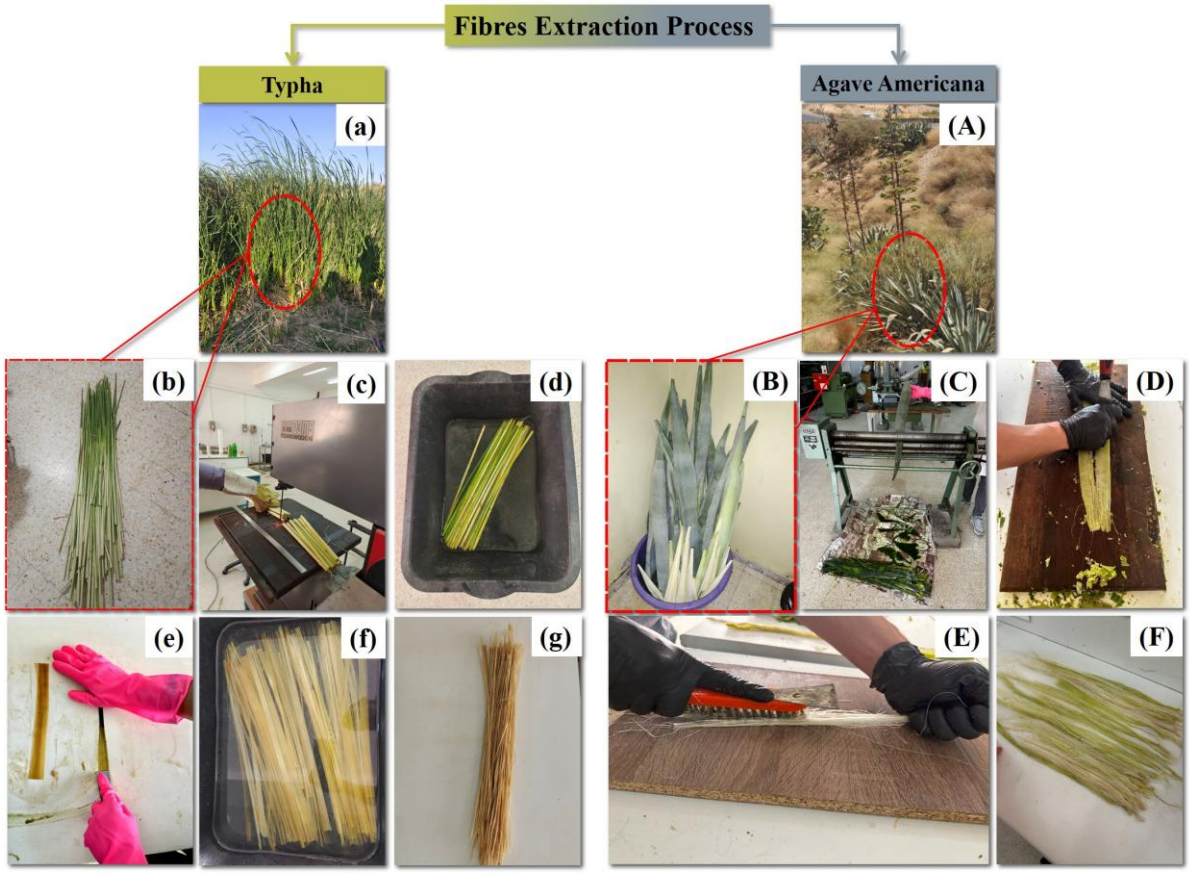


Fig. II. 2 Fibre extraction sequences for Typha latifolia stems and Agave americana leaves.

Table II. 3 Key extraction parameters for both fibre types.

Parameter	**T. latifolia (Alkaline)**	**A. americana (Mechanical)**
Primary process	NaOH immersion	Roller pressing + blade scraping
NaOH concentration	3.25 % (w/v)	N/A
Solid-to-liquid ratio	1:15 g·mL^{-1}	N/A
Treatment temperature / time	25 ± 2 °C / 48 h	Ambient (≈ 23 °C)
Combing stages	1 × steel comb (3 mm)	2 × steel (2 mm) + nylon (0.5 mm)
Rinsing medium	Distilled water (≤ 2 µS·cm^{-1})	Distilled water (≤ 2 µS·cm^{-1})
Rinsing cycles / time	3 × 30 min	3 × 10 min
Rinse endpoint pH	7.0 ± 0.5	6.8 ± 0.3
Drying conditions	22 ± 2 °C, 30 ± 3 % RH, 48 h	25 ± 2 °C, 30–40 % RH, 48–72 h
Post-drying storage	Sealed PE bags + silica gel	Sealed PE bags + silica gel
Conditioning before testing	23 ± 1 °C, 50 ± 2 % RH, 48 h (ISO 139:2005)	23 ± 1 °C, 50 ± 2 % RH, 48 h (ISO 139:2005)

II.4 Physicochemical, thermal and single-fibre mechanical characterisation

Four complementary techniques were applied to the fibres extracted in Section II.3 in order to build a multi-scale picture of their structure–property relationships before any compounding step. Fourier Transform Infrared (FTIR) spectroscopy identified the diagnostic functional groups associated with cellulose, hemicellulose, lignin and extractives. Thermogravimetric analysis (TGA) characterised the thermal stability and the sequence of mass-loss events up to 700 °C. X-ray diffraction (XRD) quantified the cellulose-I crystallinity through the Segal peak-height method, complemented by a Scherrer estimate of the apparent crystallite size along the [200] direction. Single-fibre tensile testing, performed on individual specimens selected under optical microscopy, yielded the ultimate tensile strength and the Young's modulus for both species. All specimens used in this campaign were conditioned at 23 ± 1 °C and 50 ± 2 % RH for 48 h prior to testing (ISO 139:2005), to eliminate moisture variability between measurements.

II.4.1 Fourier transform infrared spectroscopy (FTIR)

The chemical signature of the extracted Typha latifolia and Agave americana fibres was probed by Fourier transform infrared spectroscopy. Spectra were acquired on a Cary 630 FTIR spectrometer (Agilent Technologies) operating at room temperature, in the mid-infrared range from 4000 to 400 cm^{-1} at a spectral resolution of 2 cm^{-1}[124]. Each specimen was finely ground prior to acquisition so that a uniform and reproducible contact was achieved with the measurement window. A consistent baseline correction and a light smoothing procedure were applied to every spectrum, without altering the position of the diagnostic peaks.

The absorption bands that emerged from the acquired spectra were interpreted with reference to the standard band assignments established for lignocellulosic substrates, so that the hydroxyl, aliphatic, carbonyl, aromatic and glycosidic features of cellulose, hemicellulose, lignin and extractives could be identified without ambiguity. The qualitative comparison of the two species, together with the discussion of how the alkaline delignification modified the Typha spectrum relative to the untreated control, is reported in the results chapter that follows. The spectra are reported on a strictly qualitative basis, without intensity normalisation, and are used to identify diagnostic functional groups rather than to derive quantitative compositional ratios.

II.4.2 Thermogravimetric analysis (TGA)

The thermal stability of the two fibre types was assessed in a TA-60WS thermobalance (Shimadzu Corp., Kyoto, Japan). A fibre specimen of approximately 5 to 8 mg was placed in an open alumina crucible and heated from 30 °C to 700 °C at a constant ramp of 10 °C·min^{-1}, under a continuous nitrogen flow of 80 mL·min^{-1} maintained throughout the acquisition to

preserve an inert atmosphere. Prior to analysis, each specimen was oven-dried at 105 °C for 2 h and subsequently cooled in a desiccator to eliminate loosely bound moisture that would otherwise contaminate the early mass-loss region.

The mass-loss data were recorded continuously and the derivative thermogravimetric (DTG) curves were obtained by numerical differentiation of the TGA trace within the instrument software. Three thermal descriptors were then extracted from each acquisition: the onset degradation temperature T_onset, defined at 5 % mass loss; the peak degradation temperature T_max, taken as the position of the main DTG band; and the residual mass fraction remaining at 600 °C. A Savitzky–Golay smoothing was applied to the DTG traces where required, consistently for every specimen, without displacing the inflection points that define T_{max}. All data processing and plotting were performed in OriginLab.

Three thermal decomposition stages are conventionally distinguished in lignocellulosic fibres and are anticipated for the present specimens. Stage 1 (30–200 °C) corresponds to the loss of physisorbed and bound moisture, with a mass loss typically of 5–8 %. Stage 2 (220–360 °C) represents the main devolatilisation step, dominated by hemicellulose and cellulose pyrolysis. Stage 3 (above 360 °C) involves the slow decomposition of lignin and the progressive formation of carbonaceous char[125]. A single run per fibre type was performed (n = 1), which is acknowledged as a limitation; the protocol is sufficient for the qualitative comparison reported in the results chapter, but a future extension to $n \geq 3$ replicates is planned for the publication-grade quantification of the thermal descriptors.

II.4.3 X-ray diffraction and cellulose crystallinity

The crystalline organisation of the two fibre types was examined by powder X-ray diffraction on a Bruker D8 ADVANCE diffractometer (Karlsruhe, Germany) using Cu-Kα radiation of wavelength λ = 1.5406 Å. Powdered fibre samples were scanned over 2θ = 5–90° with a step size of 0.02° and a counting time sufficient to exceed 2000 counts at the maximum of the (200) reflection, in accordance with the recommendations of French [126].

To remove environmental background contributions, the 2θ–intensity profile of an empty sample holder was recorded under identical instrumental conditions and subtracted point-by-point from each fibre pattern using spreadsheet arithmetic Data below 2θ = 8° were discarded, consistent with standard practice. Automatic minimum-finding background routines were deliberately avoided, as they assign zero intensity to local minima and would therefore remove genuine crystalline intensity where the broad cellulose reflections overlap[127] . The background-subtracted patterns were smoothed using a Savitzky–Golay filter (2nd-order polynomial, 11-point window) in OriginPro 2021 prior to peak analysis.

The cellulose crystallinity index (CrI) was calculated from the background-subtracted patterns using the empirical Segal method [169]:

$$CrI(\%) = \frac{I_{200} - I_{am}}{I_{200}} \times 100 \quad \text{(II.1)}$$

where I_200 is the intensity of the (200) lattice reflection of cellulose Iβ at 2θ ≈ 22°, and I_{am} is the intensity at the minimum between the overlapped (1–10)/(110) peak and the (200) peak, located at 2θ ≈ 18.6°. The position of I_{am} at an intensity minimum (and not at the maximum of the peak near 2θ ≈ 16°, which corresponds to the overlapped (1–10) and (110) crystalline reflections of cellulose Iβ rather than to amorphous scattering) is critical for a defensible Segal index[130]. The Segal CrI is reported here as a semi-quantitative comparative metric, in line with current best practice in cellulose crystallinity analysis.

To complement the CrI, the apparent crystallite size along the [200] direction was estimated from the full-width at half-maximum (FWHM) of the (200) reflection using the Scherrer equation [131]:

$$L_{200} = \frac{K \cdot \lambda}{\beta \cdot \cos\theta} \quad \text{(II.2)}$$

with K = 0.9, λ = 1.5406 Å, and the observed FWHM corrected for an estimated instrumental broadening of 0.1° assumed to be Gaussian. FWHM values were extracted by fitting a single Gaussian profile to the isolated (200) reflection over 2θ = 20°–24°, after local straight-line baseline subtraction, using the Quick Peaks gadget in OriginPro 2021. A rigorous separation of crystallite-size and micro-strain contributions by Williamson–Hall analysis was beyond the scope of the present instrumental campaign and is recommended for future work.

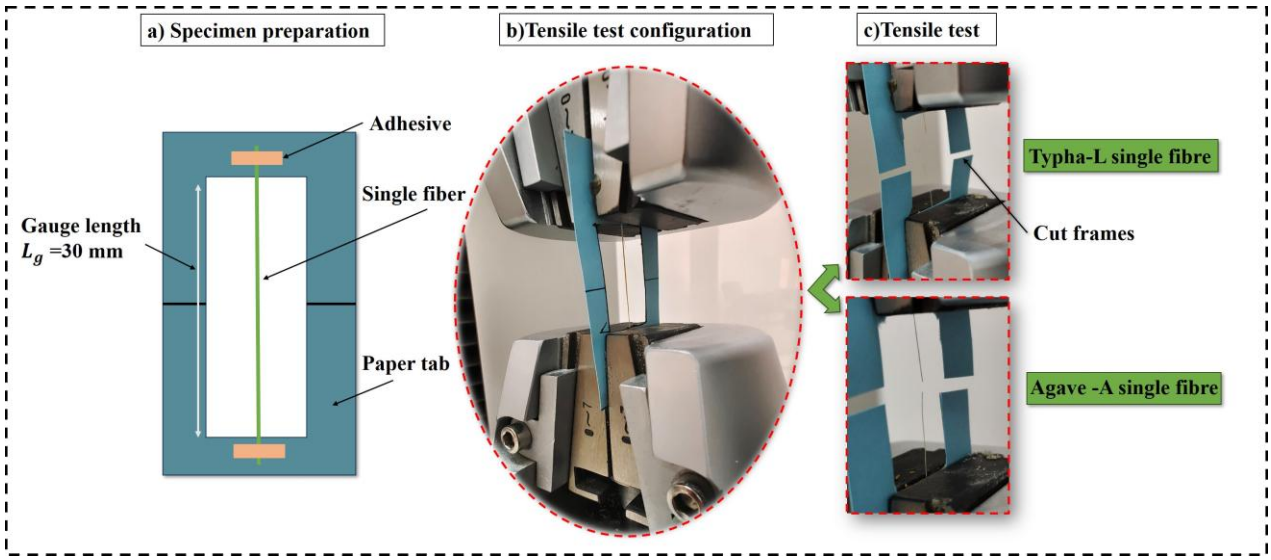
A single diffraction pattern was acquired per fibre (n = 1), which is acknowledged as a limitation; all samples were measured under rigorously identical instrumental conditions so that any residual systematic bias affects all samples equally, preserving the validity of the relative comparison.

II.4.4 Single-fibre tensile testing

The mechanical response of the individual fibres was measured in direct uniaxial tension on isolated specimens selected under optical microscopy. Prior to mounting, each fibre was examined at low magnification so that specimens with visible kinks, surface defects, or signs of processing damage could be discarded. Only structurally representative specimens were retained for the test campaign, so that the measured strength distribution would reflect the intrinsic variability of the fibres rather than the incidental damage introduced during handling.

Fifteen valid specimens of Typha latifolia stem fibres and fifteen valid specimens of Agave americana leaf fibres were tested, in accordance with the recommendations of ASTM D3822

for single-fibre testing. Each fibre was mounted on a cardboard frame with adhesive so that the free gauge length was fixed at 30 mm, and the two lateral sides of the frame were cut immediately before loading in order to transfer the load to the fibre only and to eliminate any residual pre-tension that could otherwise bias the elastic response. The tests were conducted on a universal testing machine (UTM) equipped with a 10 kN load cell, at a constant crosshead speed of 1 mm·min^{-1}. The mounting configuration is shown in Fig. II.3.



II. 3 Single-fibre tensile test configuration on cardboard frame (ASTM D3822, 30 mm gauge length).

Cross-sectional area and stress calculation

The fibre cross-sectional area governs the conversion of the measured force into an engineering stress. The fibre diameter was measured at three positions along the gauge length using an optical microscope, and the average of the three readings was taken as the representative diameter of the specimen. A circular cross-section was assumed, so that the effective area was obtained as:

$$A = \frac{\pi}{4} \cdot d^2 \qquad \text{(II.3)}$$

where d is the average diameter of the three measurement positions. The ultimate tensile strength σ_u was then calculated as the maximum force recorded during the test divided by the cross-sectional area obtained from Eq. (II.3), and the Young's modulus E was computed by linear regression over the initial quasi-linear portion of the stress–strain curve. Tests that exhibited slippage at the grips, premature fracture at the frame edge, or any visible anomaly during loading were discarded from the analysis.

A summary of the four characterisation techniques and their principal parameters is reported in Table II.4.

Table II. 4 Summary of the fibre characterisation techniques.

Technique	Instrument	Principal parameters extracted
FTIR	Cary 630 FTIR (Agilent Technologies); 4000–400 cm^{-1}; 2 cm^{-1} resolution; room temperature	Functional-group signatures of cellulose, hemicellulose, lignin, extractives
TGA	TA-60WS thermobalance (Shimadzu Corp., Kyoto, Japan); 30–700 °C; 10 °C·min^{-1}; N_2 at 80 mL·min^{-1}; 5–8 mg	T_{onset} (5 % mass loss); T_{max} (DTG band); residual mass at 600 °C
XRD	Bruker D8 ADVANCE (Karlsruhe, Germany); Cu-Kα (λ = 1.5406 Å); 2θ = 5–90°; step 0.02°; background subtracted; Savitzky–Golay smoothing	CrI by Segal method (Eq. II.1); apparent crystallite size L_{200} by Scherrer equation (Eq. II.2)
Single-fibre tensile	UTM, 10 kN load cell; 1 mm·min^{-1}; 30 mm gauge length (ASTM D3822); cardboard-frame mounting; circular cross-section assumption	Ultimate tensile strength σ_u; Young's modulus E

II.5 Face-sheet fabrication

The hybrid face sheets of the sandwich panels were manufactured by combining the unidirectional Typha latifolia and Agave americana fibres extracted in Section II.3 with the Genc Ultra Transparent Glossy Casting Epoxy VX100.00 matrix introduced in Section II.2.2. The layup sequence, the resin formulation, the pressing conditions and the subsequent sectioning operations are described in the sub-sections that follow.

II.5.1 Epoxy matrix working properties

The resin system used for the face sheets was Genc Ultra Transparent Glossy Casting Epoxy VX100.00, combined with the corresponding Epoxy Hardener HX100.00 (Genc Polimer Kimya, Turkey) at the mass ratio of 100:28 specified by the supplier. The principal working properties that are relevant to hand-layup lamination, as reported in the manufacturer's technical data sheet, are summarised in Table II.5. The product is a solvent-free bisphenol-A-based casting system formulated for low-foam processing and high surface-wetting efficiency, which is the reason it was retained for infiltration of the densely packed unidirectional fibre bundles.

Table II. 5 Epoxy resin system working properties (manufacturer data, TDS rev. 07, 08/2020).

Parameter	Value
Product type	Bisphenol-A-based epoxy, solvent-free
Colour	Ultra-transparent
Specific gravity	1.13 ± 0.03 kg·L^{-1}
Solid content	99–100 % by weight
Mixing ratio (resin : hardener)	100 : 28 by weight
Recommended film thickness per layer	10 000 – 30 000 µm
Pre-casting rest time after mixing	45–60 min
Minimum application temperature	10 °C
Recommended ambient humidity	10 – 85 % RH
Dust-free time (2 cm, 10–25 °C)	≈ 18 h
Touch-dry time (2 cm, 10–25 °C)	≈ 24 h
Full-service strength at 20 °C	7 days

II.5.2 Layup sequence and hand lamination

Hybrid laminates were fabricated following a four-layer symmetric stacking sequence of the form [Typha / Agave / Typha / Agave]. The extracted fibres were first aligned unidirectionally along the 0° direction on a kraft-paper carrier, fixed in place with double-sided tape, and stitched together with a 200-denier polyester thread in order to minimise delamination and misalignment during the subsequent layup. The laminate planform was fixed at 320 × 220 mm, a size large enough to accommodate the downstream sectioning of multiple test specimens from a single panel.

Resin impregnation was performed by sequential hand layup. For each ply, a measured quantity of the Genc VX100.00 resin and HX100.00 hardener was prepared at the 100:28 mass ratio and allowed to rest for the recommended pre-casting interval before application. Each ply was then wetted out manually with a brush, and a silicone roller was drawn along the fibre direction to consolidate the stack and expel trapped air, the low-foam formulation of the epoxy being particularly helpful at this stage. Successive plies were added following the symmetric stacking sequence above.

II.5.3 Cold pressing, curing, and specimen sectioning

Once the four plies had been laid up and consolidated, the laminate was cold-pressed at an ambient temperature of 25–27 °C and a relative humidity of 50–55 % for 48 h. These conditions were retained because they fall within the application envelope recommended by the

manufacturer's TDS and because they produced a stable, tack-free laminate within a reproducible time window. The final nominal thickness of the cured laminate was 5.0 ± 0.1 mm.After curing, the laminates were sectioned into test specimens measuring 170 × 25 × 5 mm using a diamond-blade cutter, with the cut lines aligned with the 0° fibre direction to preserve the unidirectional character of the reinforcement. Optical microscopy of the cut edges at 50× magnification was used to confirm that the fibre distribution across the thickness was uniform and that the fibre–matrix interfacial bonding was intact, before the specimens were released for downstream mechanical testing. Figure II.4 illustrates the layup and the final face sheet.

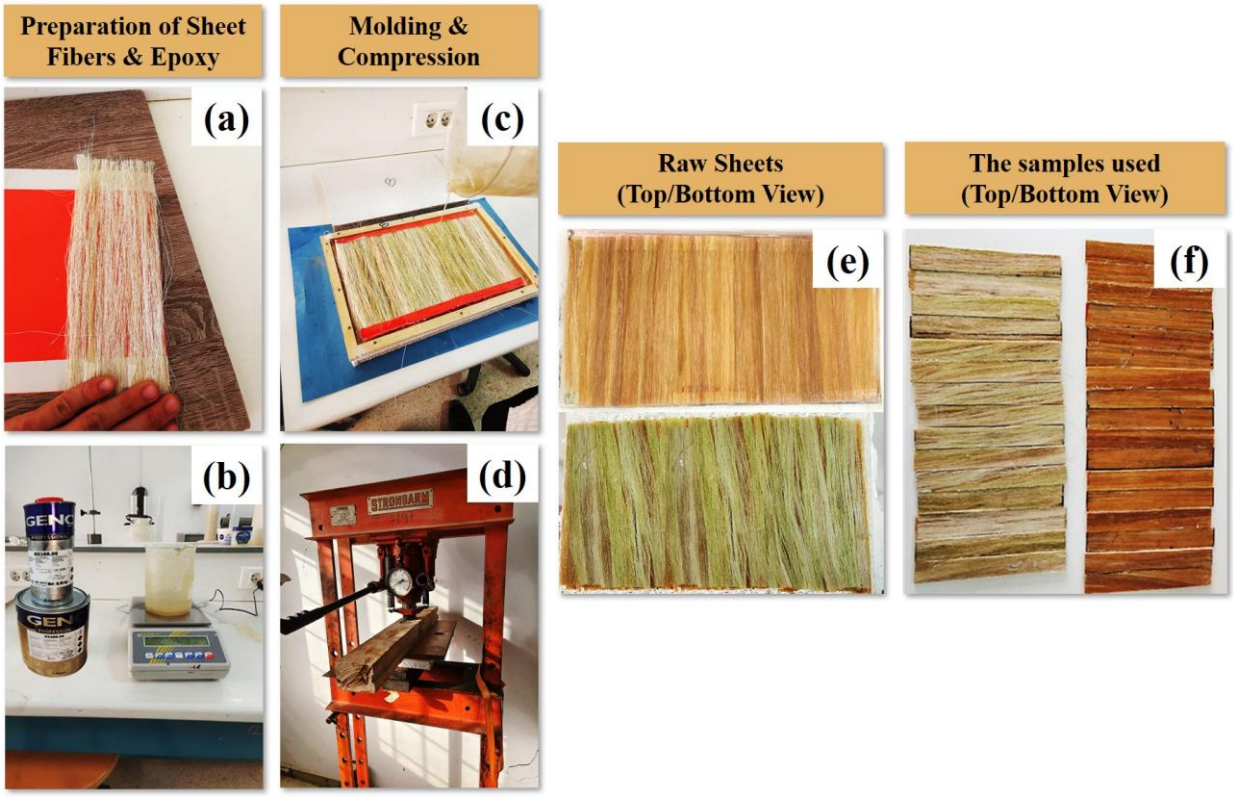


Fig. II. 4 Hybrid Typha/Agave/epoxy face-sheet fabrication.

II.6 Core design and additive manufacturing

The three-dimensional cores of the sandwich panels were produced by fused deposition modelling (FDM) in two material systems and three geometric configurations. Core design was anchored to the requirements of ASTM C393-16, which is the reference standard for the determination of core shear properties of sandwich constructions by beam flexure, so that the downstream flexural test results could be interpreted within an established framework.

II.6.1 Core geometries

All cores were drawn in CATIA V5-R20 under a common envelope of 170 mm in length (L) × 25 mm in width (W) × 20 mm in thickness (T). Three cell topologies were implemented within this envelope: a honeycomb core, a circular-cell core, and a tri-grid core. Each

configuration was replicated three times per material system, so that nine cores were produced per filament type, for a total of eighteen cores. The geometric parameters of the three configurations are summarised in Table II.6. The completed CAD models were exported to high-resolution STL files for further processing in the slicing software.

Table II. 6 Core configuration summary.

Configuration	Geometry parameters (mm)	Overall dimensions (L × W × T)	Replicates per material
Honeycomb	Cell size D = 5 mm; wall thickness tc = 1 mm	170 × 25 × 20	3
Circular	Cell diameter R = 5 mm; wall spacing tc = 1 mm	170 × 25 × 20	3
Tri-grid	Strut length D = 5 mm; strut angle = 30°	170 × 25 × 20	3

II.6.2 Materials, machine and process parameters

Two 1.75 mm filaments were used as feedstock, as already introduced in Section II.2.3: a neat PLA filament and a commercial PLA/flax biocomposite filament (Nanovia, France). The STL models were sliced in Ultimaker Cura 5.9.0 using filament-specific process profiles, and the cores were printed on an Anycubic i3 Mega X fused deposition modelling machine. The principal FDM process parameters adopted for the final cores are reported in Table II.7.

Table II. 7 FDM process parameters used for the sandwich cores.

Parameter	Neat PLA	PLA/Flax
Nozzle temperature (°C)	220	220
Build-plate temperature (°C)	60	60
Layer height (mm)	0.2	0.2
Infill density (%)	100	100
Infill pattern	Tri-hexagon	Tri-hexagon
Print speed (mm·s^{-1})	70	70
Initial layer speed (mm·s^{-1})	10	10
Wall thickness (mm)	1.2	1.2

Post-processing consisted of a 24 h ambient-conditioning interval (23 ± 2 °C, 50 ± 5 % RH) to relieve residual stresses, followed by dimensional verification of every core using a digital calliper of ± 0.01 mm accuracy, in order to confirm compliance with the ASTM C393-16 tolerances. In addition to the cores, tensile coupons were printed from each of the two filaments following the same process parameters, so that the filament-level reference stress–strain curves used in the ABAQUS constitutive cards could be obtained under conditions

strictly identical to those of the core production (Section II.11.2). Figure II.5 illustrates the core preparation sequence.

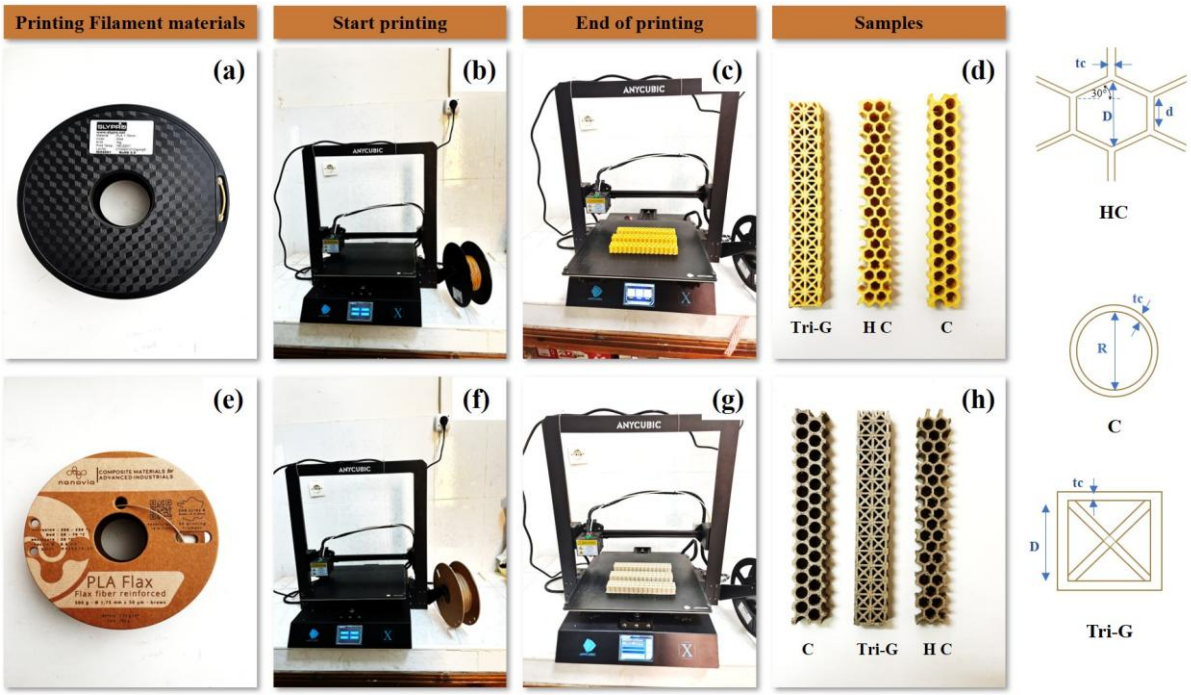


Fig. II. 5 Core preparation: filament feedstock, FDM printing, completed cores, and unit-cell geometry.

II.7 Sandwich panel assembly

The sandwich panels were obtained by bonding the hybrid face sheets of Section II.5 to the FDM-printed cores of Section II.6 using a polyurethane adhesive. The adhesive was applied in a thin, uniform layer on the two bonding surfaces of each core, and the upper and lower face sheets were then brought into contact and held in position under light pressure until the adhesive had reached its handling strength. Two assembly families were produced:

- **PATECs:** sandwich panels with hybrid Agave/Typha-epoxy face sheets bonded to neat PLA cores, in the three core geometries (honeycomb, circular, tri-grid).
- **PFATECs:** sandwich panels with hybrid Agave/Typha-epoxy face sheets bonded to PLA/flax biocomposite cores, in the three core geometries.

With three replicates per configuration per material system (as specified in Section II.6.1), eighteen complete sandwich specimens were produced. The assembled specimens were held at 23 ± 2 °C and 50 ± 5 % RH for a further development of the adhesive bond before mechanical testing. Figure II.6 illustrates the assembly and the final panel geometry.

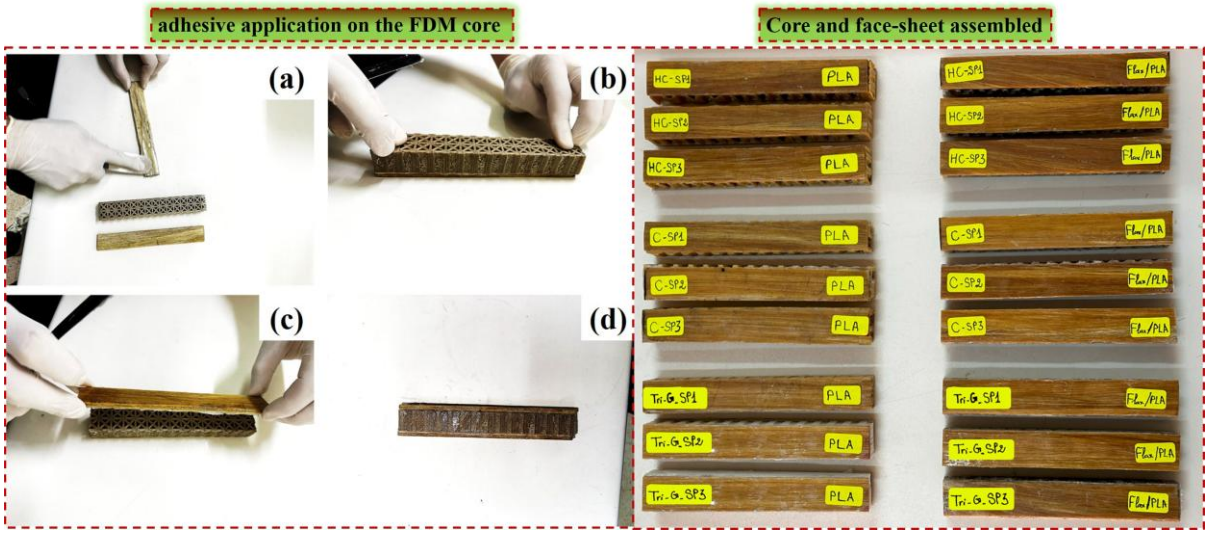


Fig. II. 6 Sandwich panel assembly (PATECs and PFATECs configurations).

II.8 Mechanical testing protocols

The mechanical response of the constituent materials and of the assembled sandwich panels was characterised through three complementary test campaigns: uniaxial tension on the face sheets and on the filament coupons, three-point bending on the sandwich panels, and post-processing of the bending records for the quantification of the energy absorption. Every test was performed on at least three replicates per configuration, in order to support the non-parametric statistical framework described in Section II.9.

II.8.1 Tensile testing

Tensile test specimens were prepared for three material systems: neat PLA (printed by FDM), PLA/flax biocomposite (printed by FDM), and the hybrid Agave/Typha-epoxy laminate (sectioned from the cured face-sheet panels of Section II.5 using a CNC machine) (Fig. II. 7). The specimen geometry was drawn to comply with ASTM D618, with uniform cross-sections and smooth surfaces free of visible defects. For the FDM specimens, the printing parameters were identical to those reported in Table II.7, so that the measured properties could be used as direct inputs for the ABAQUS constitutive cards.

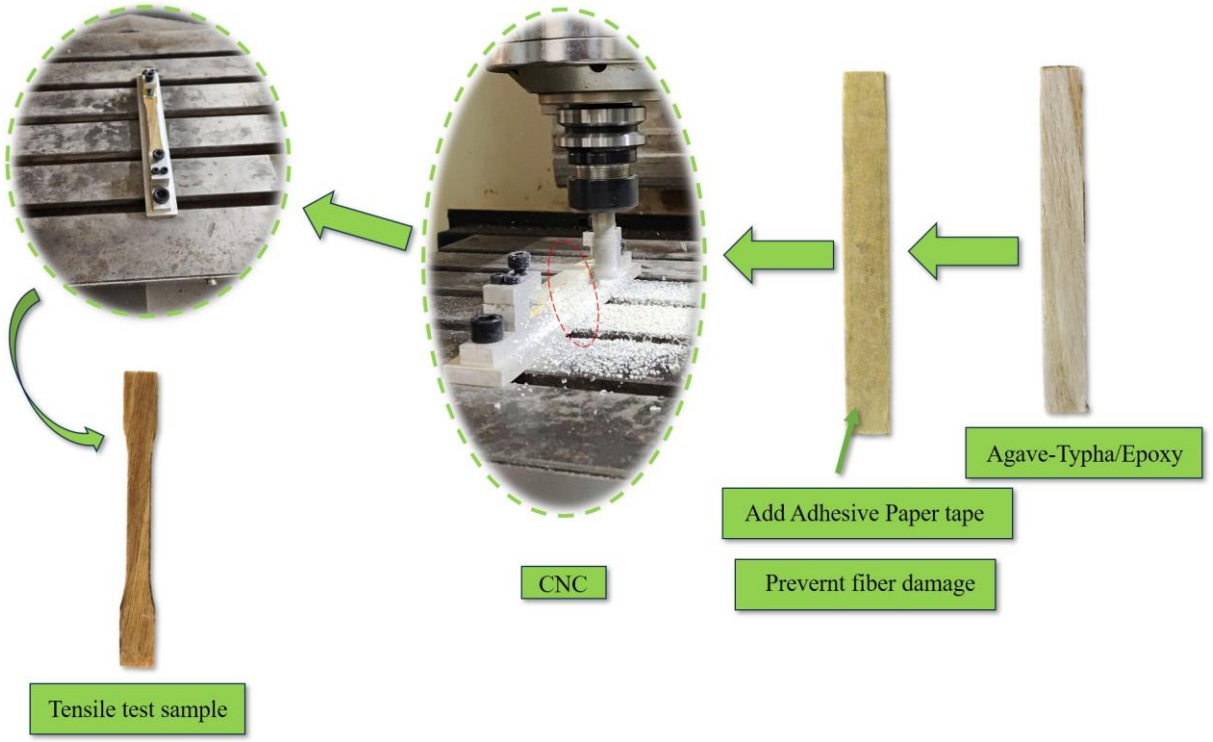


Fig. II. 7 CNC machining of Agave/Typha-epoxy tensile coupons (ASTM D618 geometry).

The tests were conducted on an Instron universal testing machine equipped with a 10 kN load cell and pneumatic grips, chosen to ensure correct specimen alignment and to minimise slippage during loading. The gauge length was measured at the start of each test, and specimens were loaded in tension at a constant crosshead speed of 2 mm·min^{-1} until fracture. The load and the crosshead displacement were continuously recorded throughout the test, and stress–strain curves were constructed from the cross-sectional area and the gauge length of each specimen. The tensile strength was defined as the maximum load divided by the original cross-sectional area, while the Young's modulus was computed by linear regression over the initial linear region of the stress–strain curve. The elongation at break was also recorded.

Three distinct tensile campaigns were conducted under the protocol described above, on three material systems that together cover all the constituents of the sandwich panel. The first campaign was performed on FDM-printed neat PLA coupons, produced under the printing parameters of Table II.7. The second campaign was performed on FDM-printed PLA/flax biocomposite coupons, produced under identical printing conditions to ensure direct comparability. The third campaign was performed on Hybrid Typha/Agave-epoxy coupons, CNC-machined from the cured laminates of Section II.5. The three campaigns deliver the engineering stress–strain curves of the three actual materials integrated into the sandwich panels, each characterised under the manufacturing conditions in which it is used in the final structure. The resulting curves serve two purposes in the present thesis: they supply the raw

data on which the constitutive cards of the three-point bending finite element model (Section II.11.2) are calibrated, and they enable a direct experimental comparison of the three constituent materials when reported in the results chapter. Figure II.8 shows the tensile test configuration.

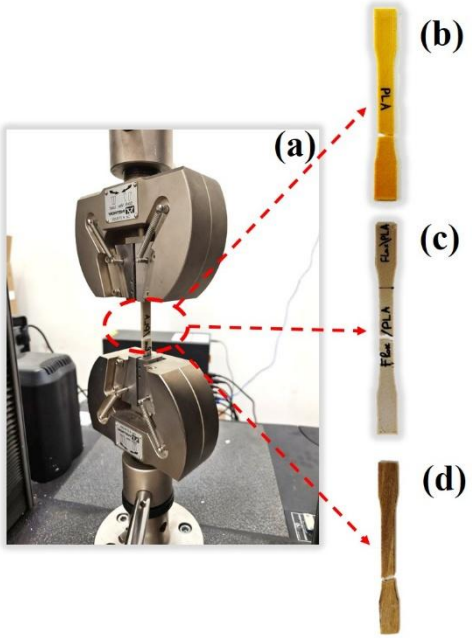


Fig. II. 8 Tensile test setup on Instron UTM (ASTM D618, 10 kN load cell, 2 mm·min⁻¹).

II.8.2 Three-point bending of sandwich specimens

The core shear properties and the apparent flexural stiffness of the sandwich panels were determined in three-point bending in accordance with ASTM C393. Specimens measuring 170 × 25 × 20 mm were polished at the edges to remove any defects left by the sectioning operation, and tested on an Instron 5969 universal testing machine equipped with a 50 kN load cell and a three-point bending fixture. The support span was set at 136 mm, which corresponds to 80 % of the specimen length and was chosen to minimise the edge effects while preserving a uniform stress distribution along the gauge. The crosshead speed was fixed at 2 mm·min^{-1}, identical to the rate used for the tensile tests.

Two mechanical descriptors were derived from the load–displacement records using the ASTM-based equations. The core shear stress was computed as:

$$\tau = \frac{3P}{4b(h+c)} \tag{II.4}$$

and the apparent flexural modulus as:

$$E = \frac{L^3}{4\,b\,(h+c)^3} \cdot \frac{\Delta P}{\Delta \delta} \tag{II.5}$$

where P is the applied load, L is the support span, b is the specimen width, h is the total core thickness, c is the face-sheet thickness, and ΔP/Δδ is the slope of the linear portion of the

load–displacement curve. Failures classified as core shear according to the ASTM C393 criteria were retained for the analysis, with three replicates per configuration tested. Figure II.9 shows the flexural test configuration.

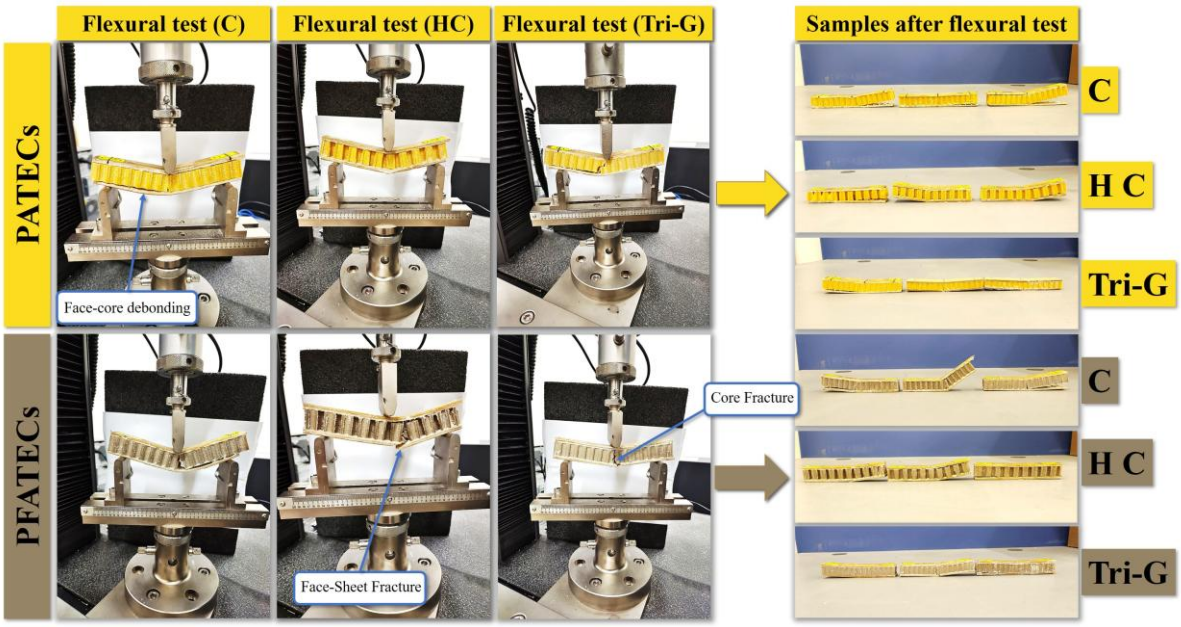


Fig. II. 9 Three-point bending test of sandwich specimens (ASTM C393, Instron 5969, 136 mm support span).

II.8.3 Energy absorption metrics

Sandwich structures dissipate kinetic energy through progressive plastic-deformation mechanisms of the core, including cell-wall folding, buckling, and shear failure. The three-point bending records of Section II.8.2 were therefore post-processed to extract a hierarchy of energy-absorption descriptors, spanning the material scale and the structural scale.

At the material scale, the absorbed strain energy per unit volume was computed by numerical integration of the stress–strain curve up to the maximum strain[132]:

$$U = \int_0^{\varepsilon_{max}} \sigma \, d\varepsilon \approx trapz(\sigma, \varepsilon) \tag{II.6}$$

or, for rapid volumetric comparisons between cores, by the closed-form approximation[133]:

$$U_{vol} = \frac{1}{2} \sigma_{max} \, \varepsilon_{max} \tag{II.7}$$

At the structural scale, three crashworthiness metrics were derived from the force–displacement record. The total energy absorption (EA) represents the cumulative energy dissipation during crushing[134]:

$$EA = \int_0^{\delta} F(\delta) d\delta \tag{II.8}$$

where F is the crushing force and δ is the densification displacement. The specific energy absorption (SEA), which enables a mass-normalised comparison between cores of different densities, was computed as:

$$SEA = \frac{EA}{m} \tag{II.9}$$

and the mean crushing force (MCF), evaluated at 70 % compression, as[135]:

$$MCF = \frac{EA}{\delta}(\delta = 0.7L_0) \tag{II.10}$$

Finally, the crushing force efficiency (CFE), which reflects how evenly the load is distributed during crushing, was defined as the ratio of the mean crushing force to the peak crushing force (PCF):

$$CFE = \frac{MCF}{PCF} \tag{II.11}$$

These hierarchical descriptors are used in the subsequent results chapter to compare the crashworthiness and the structural efficiency of the honeycomb, circular and tri-grid configurations for both the neat PLA and the PLA/flax material systems.

II.9 Statistical analysis (Kruskal–Wallis)

The mechanical-testing campaigns described in Section II.8 produced small-sample datasets (typically n = 3 replicates per configuration), in which neither the normality of the residuals nor the equality of the inter-group variances could be assumed without explicit verification. Under these conditions, the use of parametric tests such as one-way ANOVA would have rested on assumptions that the data could not reasonably support, and the resulting p-values would have been difficult to defend. The non-parametric Kruskal–Wallis test was therefore retained as the inferential framework, in line with the recommendations of Ostertagova et al. for the analysis of small mechanical-engineering datasets.

All statistical computations were carried out in IBM SPSS Statistics version 28 (IBM Corp., Armonk, NY, USA). For each mechanical descriptor of interest, the three core geometries (honeycomb, circular, tri-grid) were treated as independent groups, and the test statistic H was computed from the rank-sum data as[136]:

$$H = \frac{12}{N(N+1)}\sum_{i=1}^{k}\frac{R_i^2}{n_i} - 3(N+1) \tag{II.12}$$

where N is the total number of observations across the three groups, k is the number of groups (k = 3 in the present work), R_i is the sum of ranks for group i, and n_i is the number of observations in group i. The null hypothesis under which Eq. (II.12) is evaluated is that the three core geometries draw their mechanical responses from the same underlying distribution,

so that a sufficiently large value of H provides evidence against the equivalence of the three configurations.

The Kruskal–Wallis test was applied independently to three mechanical descriptors: the core shear strength τ (Eq. II.4), the apparent flexural modulus E (Eq. II.5), and the total energy absorption EA (Eq. II.8). The analysis was further stratified by material system, that is, performed separately on the neat PLA cores and on the PLA/flax biocomposite cores, in order to avoid pooling responses that arise from different constitutive behaviours. Differences between core geometries were declared statistically significant when the associated p-value fell below the conventional threshold of $p < 0.05$.

II.10 Process-parameter study on FDM-printed PLA tensile coupons

Beyond the experimental campaign on the sandwich panels described in Sections II.5–II.9, the broader thesis programme included a parallel investigation of the influence of FDM process parameters on the tensile response of neat PLA. The study examined three process factors extruder temperature, filling density, and specimen weight at three levels each, and was analysed through two complementary predictive frameworks: a Taguchi L9 orthogonal array and an artificial neural network. The present section summarises the experimental design, the two modelling approaches, and the conclusions of that study. The investigation is a standalone component of the thesis, with its own specimen population, its own printing parameters, and its own analytical framework; the FDM parameters adopted for the sandwich cores in Section II.6.2.

II.10.1 Experimental design

Twenty-seven ASTM D638 Type IV tensile specimens were drawn in CATIA, exported to STL, sliced in Ultimaker Cura, and printed on an Anycubic i3 Mega FDM machine equipped and PLA filament with a 0.4 mm nozzle and a heated bed. Three process factors were investigated at three levels each, as listed in Table II.8: the extruder (nozzle) temperature, the filling (infill) density, and the specimen weight. The infill pattern (zigzag), the build-plate temperature (60 °C), the layer height (0.2 mm), the print speed (70 $mm \cdot s^{-1}$) and the wall thickness (1.2 mm) were held constant across the entire test matrix, so that the effect of the three variable factors could be isolated without confounding.

Table II. 8 Factors and levels of the FDM process-parameter study (3³ factorial, 27 specimens).

Factor	Level 1	Level 2	Level 3
Extruder temperature (°C)	200	210	220
Filling density (%)	20	30	40
Specimen weight	W_1	W_2	W_3

Uniaxial tension tests were then performed on the 27 printed coupons according to ASTM D638 on a Test 112 universal testing machine equipped with a 5 kN load cell, at a crosshead speed of 0.1 mm·min⁻¹. The maximum tensile stress, the strain at maximum load and the Young's modulus were recorded for each specimen directly through the instrument software. Figure II.10 shows the printed specimens and the tensile-test setup.

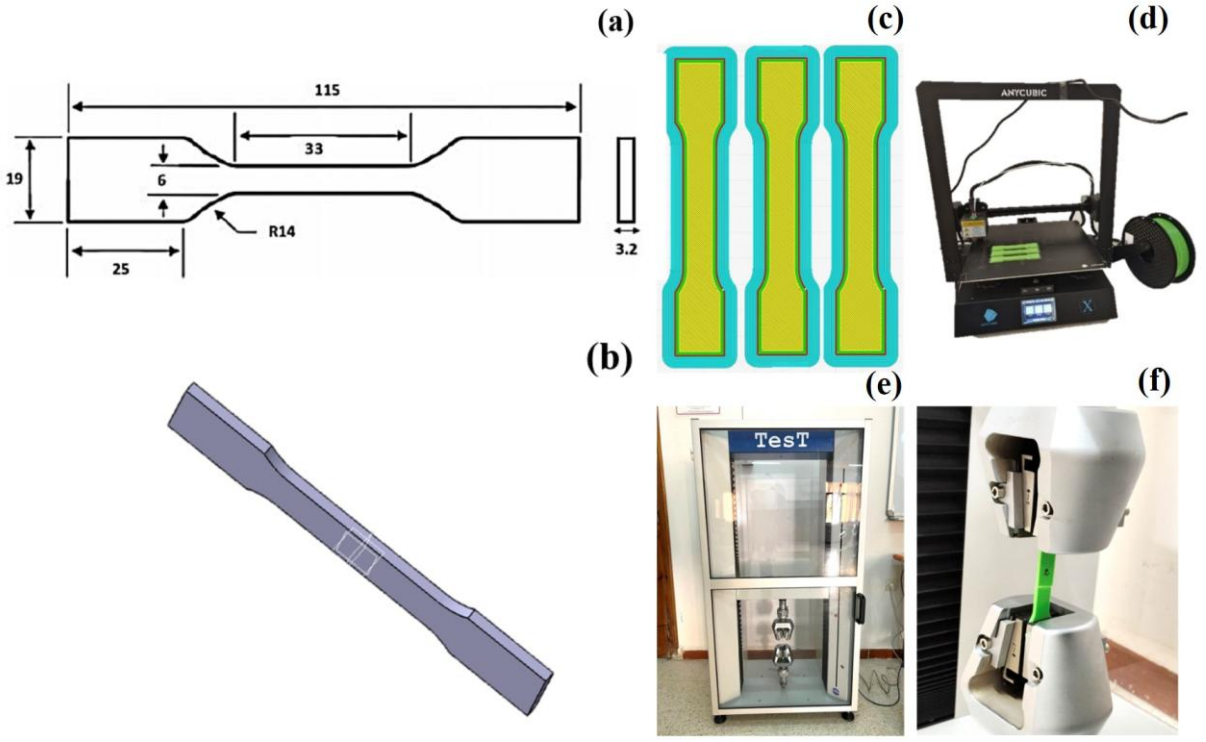


Fig. II. 10 FDM-printed neat PLA tensile specimens (27 coupons) and tensile-test setup.

II.10.2 Taguchi signal-to-noise analysis

The experimental dataset was analysed using Taguchi's L9 orthogonal array, implemented in Minitab. Because the objective of the study was the maximisation of stress, strain and Young's modulus, the signal-to-noise (*S/N*) ratio was computed under the "larger-is-better" convention:

$$\frac{S}{N} = -10\, log_{10}\left(\frac{1}{n}\sum_{i=1}^{n}\left(\frac{y_i}{\sigma}\right)^2\right) \quad \text{(II.13)}$$

where y_i is the measured response of trial i, σ is its standard deviation, and n is the number of repetitions per trial. The factor level associated with the largest S/N ratio was retained as the optimal setting for each response[137].

II.10.3 Artificial neural network modelling

In parallel with the Taguchi analysis, an artificial neural network (ANN)[138] model was trained in MATLAB on the same 27-point dataset to capture the non-linear interactions between the three input factors and the three mechanical responses. The network adopted a feed-forward architecture with one input layer (three neurons, corresponding to extruder temperature, filling density, and specimen weight), one hidden layer, and one output layer (three neurons, corresponding to tensile stress, strain, and Young's modulus). A 3 × 27 input matrix and a 3 × 27 target matrix were imported into the neural-network synthesis tool, and the network weights were fitted by supervised learning until convergence. The network architecture is illustrated in Fig. II.11.

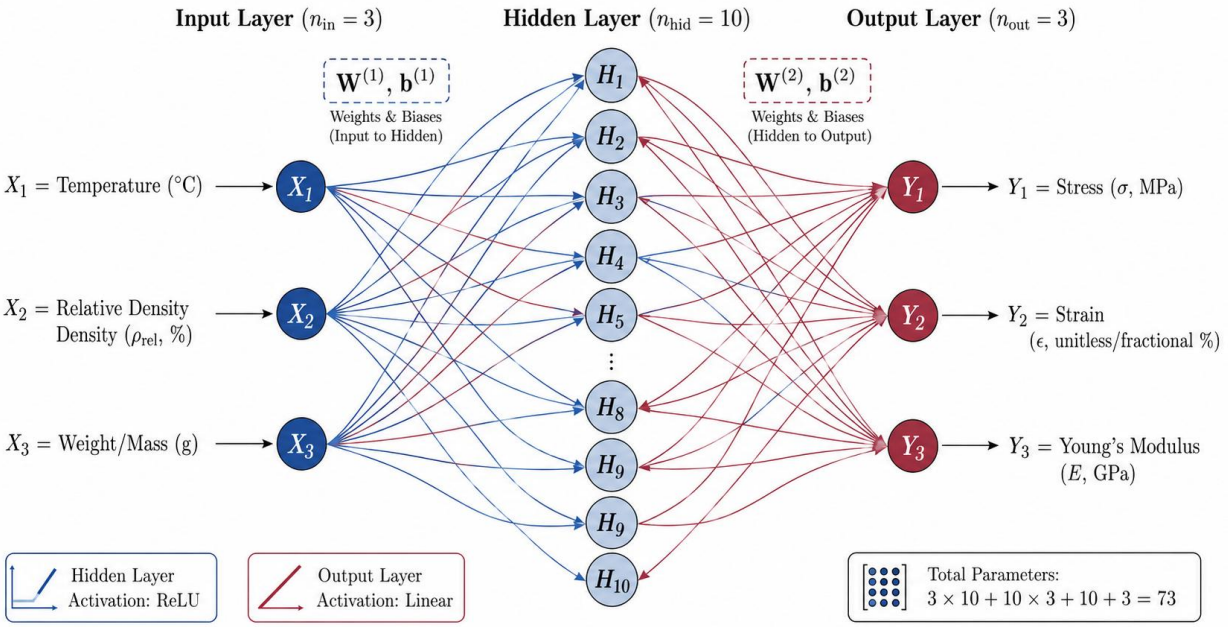


Fig. II. 11 Schematic of the artificial neural network architecture.

Two performance descriptors were used to evaluate the predictive quality of the ANN. The mean squared error (MSE) quantifies the average squared deviation between the predicted and the measured responses:

$$MSE = \frac{1}{n}\sum_{i=1}^{n}(y_i - \hat{y}_i)^2 \quad \text{(II.14)}$$

and the coefficient of determination R^2 quantifies the fraction of the variance in the measured responses that is reproduced by the model:

$$R^2 = 1 - \frac{\sum_{i=1}^{n}(y_i - \hat{y}_i)^2}{\sum_{i=1}^{n}(y_i - \bar{y})^2} \quad \text{(II.15)}$$

where y_i is the measured target, $\hat{y}_i$ is the value predicted by the ANN, and $\bar{y}$ is the mean of the measured values.

The two predictive models were cross-validated against the experimental data. The ANN reached an overall correlation coefficient R = 91.03 %, while the Taguchi analysis returned 80.75 % for the stress, 90.13 % for the strain, and 50.83 % for the Young's modulus. The ANN was therefore selected as the predictive tool of reference for this standalone study, while the Taguchi analysis was retained as an independent confirmation of the main-effect ordering. The Taguchi/ANN study reported in this section is a standalone investigation of the influence of three FDM process parameters on the tensile response of neat PLA coupons; its conclusions are limited to the parameter ranges and the specimen geometry. The FDM parameters adopted for the sandwich cores in Section II.6.2 are those reported in Table 7 and were fixed independently of the present Taguchi/ANN study.

It is worth emphasising that the Kruskal–Wallis framework adopted in Section II.9 is logically distinct from the Taguchi/ANN models of the present section. The latter were applied at the upstream stage of the work, on the 27-point neat-PLA tensile dataset, in order to identify and to model the dominant FDM process parameters. The Kruskal–Wallis test, by contrast, is applied at the downstream stage of the work, on the sandwich-panel test results, in order to compare the three core geometries under the FDM parameters that had already been fixed. The two statistical layers therefore answer different questions and coexist without overlap throughout the thesis.

II.11 Finite element modelling in ABAQUS

Two finite element campaigns were carried out in ABAQUS within the broader programme of this thesis, each within its own published or submitted study and on its own specimen population. The first campaign, presented in Section II.11.1, simulates the uniaxial tensile response of FDM-printed PLA dog-bone specimens with paired through-thickness apertures, in ABAQUS/Explicit. The second campaign, presented in Section II.11.2, simulates the three-point bending response of the hybrid sandwich panels in ABAQUS/CAE Standard. The two campaigns are independent: they involve different specimen geometries, different printing parameters, different loading scenarios, and different constitutive calibrations. They are presented together in this chapter because they are both part of the methodological apparatus of the thesis, not because one feeds the other.

II.11.1 Tensile finite element model of FDM-printed PLA specimens with paired apertures (ABAQUS/Explicit)

The first finite element campaign of the thesis simulates the uniaxial tensile response of FDM-printed PLA specimens that incorporate paired through-thickness circular apertures at controlled angular orientations. The campaign is a standalone investigation of how aperture geometry modulates the apparent tensile response of FDM-printed PLA, and its results are independent of the sandwich-panel work of the present chapter. The specimen population, the printing parameters, and the constitutive calibration described below apply only to this study.

Specimen geometry and test matrix

The test specimens were designed following the general guidelines of ISO 3167:2014, with modifications to accommodate the inclusion of through-thickness circular apertures. Each specimen featured a dog-bone gauge in which two circular holes of equal radius R = 1 mm and inter-centre spacing d = 5 mm were positioned symmetrically about the longitudinal centreline. The angular orientation θ of the line connecting the two aperture centres, measured relative to the axis transverse to the loading direction, was varied across eight configurations: 0°, 15°, 30°, 45°, 60°, 75°, 90° and 105°. A solid (no-aperture) configuration served as the reference. With three replicates per configuration, twenty-seven specimens were produced in total. The specimen geometry and the aperture-angle configurations are illustrated in Fig. II.12.

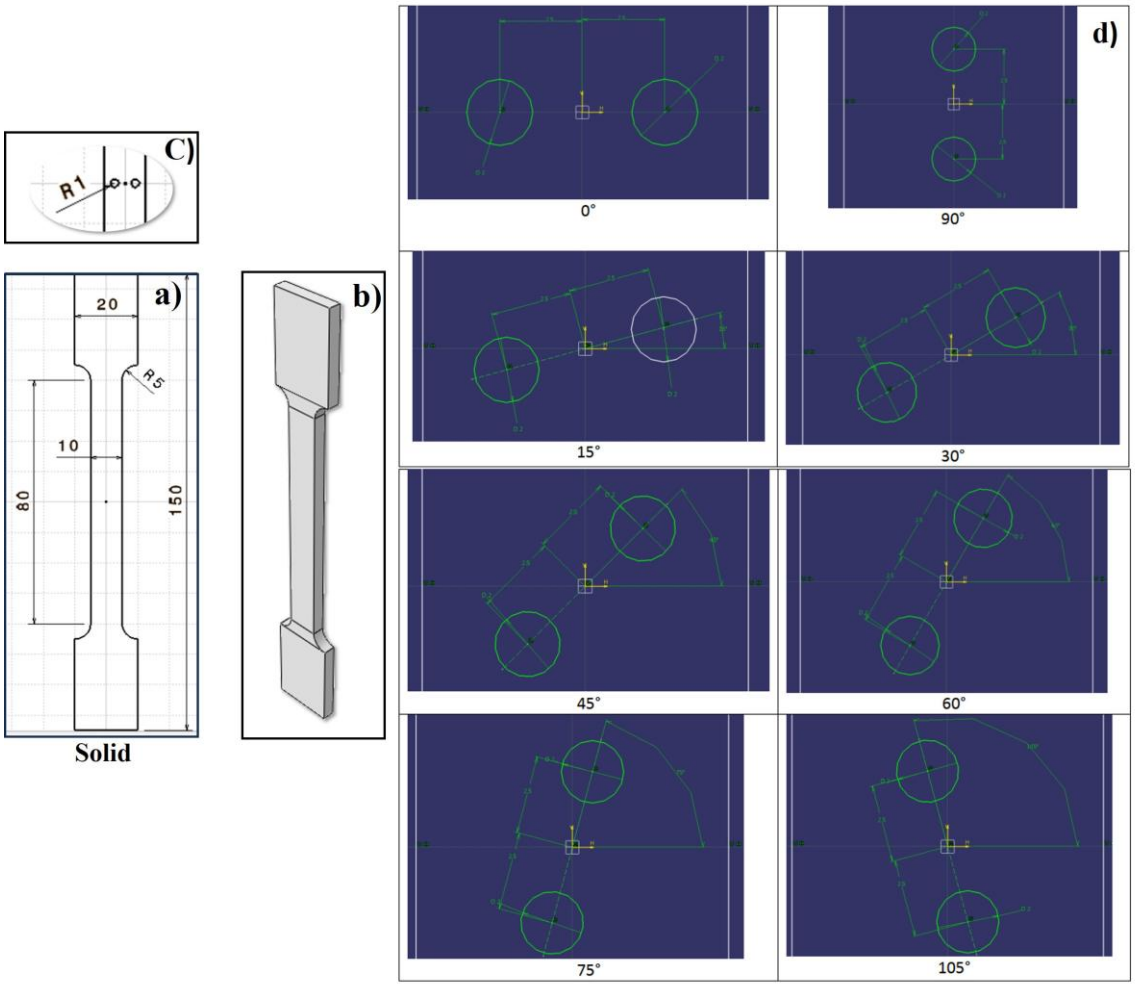


Fig. II. 12 Specimen geometry and aperture-angle configurations.

All specimens were fabricated from PLA filament on the Anycubic i3 Mega X FDM printer used throughout the thesis. The printing parameters were held strictly constant across the 27 specimens to isolate the effect of aperture angle as the sole experimental variable, and they differ from the parameters adopted for the sandwich cores (Section II.6.2). The complete parameter set is reported in Table II.9, and the printed specimens are shown in Fig. II.13.

Table II. 9 Filament specifications and FDM print parameters held constant across all 27 apertured specimens.

Parameter	Symbol	Value	Unit
Filament material	-	PLA, white	-
Filament diameter	d_f	1.75	mm
Filament density	ρ	1.24	g·cm^{-3}
Spool weight	-	1	kg
3D printer	-	Anycubic i3 Mega X	-
Nozzle temperature	T_n	200	°C

Build-plate temperature	T_b	60	°C
Layer height	h_l	0.20	mm
Wall thickness	t_w	1.20	mm
Infill density	ρ_{inf}	100	%
Infill / raster pattern	-	Rectilinear, ±45°	-
Print speed	v	50	$mm \cdot s^{-1}$

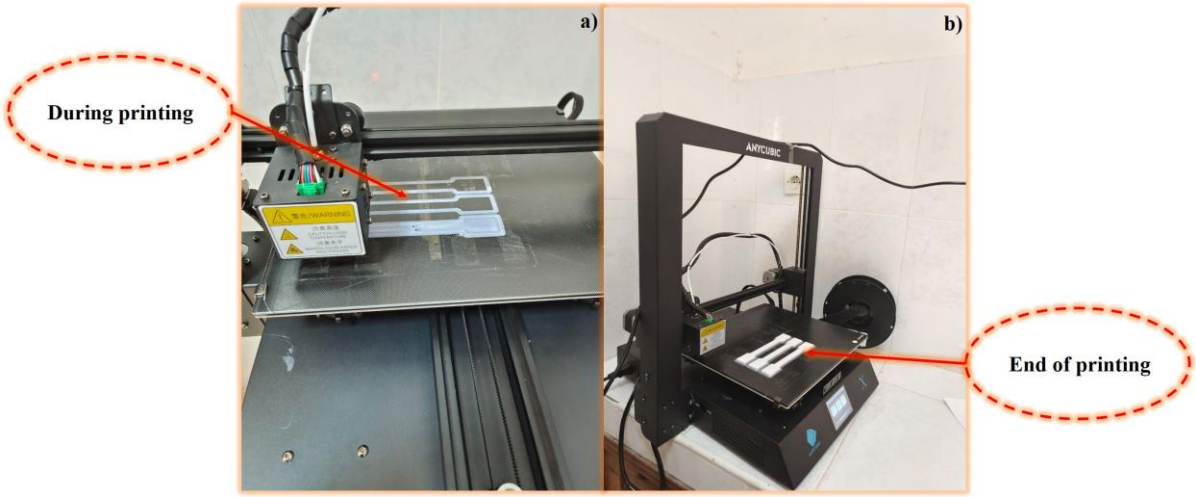


Fig. II. 13 FDM-printed PLA aperture specimens during and after printing.

Net-section analysis and the two geometric regimes

Because the apparent strength of a perforated specimen reflects both the genuine angle-dependent stress concentration around the apertures and the angle-dependent reduction of the minimum load-bearing cross-section, two stress measures are reported throughout the campaign: the maximum gross-section nominal stress $\sigma_{nom,max}$, computed using the unperforated gauge cross-section $A_0 = b \cdot h$ as a fixed reference, and the maximum net-section stress $\sigma_{net,max} = F_{max} / A_{net}(\theta)$, computed from the minimum cross-sectional area $A_{net}(\theta)$ that intersects the perforations for each aperture angle. The two areas are related by[139]:

$$\frac{A_{net}(\theta)}{A_0} = \frac{b - 4\sqrt{R^2 - \left(\frac{d}{2}\right)^2 sin^2\,\theta}}{b} \quad \text{(II.16-a)}$$

$$\frac{A_{net}(\theta)}{A_0} = \frac{b - 2\,R}{b} \quad \text{(II.16-b)}$$

Equation (II.16-a) applies when $d \cdot |\sin\theta| < 2R$ and corresponds to the two-hole-cut regime, in which the minimum-section transverse plane intersects both perforations simultaneously. Equation (II.16-b) applies when $d \cdot |\sin\theta| \geq 2R$ and corresponds to the one-hole-cut regime, in which the minimum-section plane intersects only one of the two holes. The transition between the two regimes occurs at the threshold angle $\theta_c = \arcsin(2R / d)$, which for the present geometry

(R = 1 mm, d = 5 mm) yields $\theta_c \approx 23.58°$. The configurations 0° and 15° therefore lie in the two-hole-cut regime, and the configurations 30°–105° lie in the one-hole-cut regime, where $A_{net}(\theta) / A_0 = 0.800$ is constant. It is emphasised that all eight perforated configurations physically contain two holes; the regime distinction is purely geometric and concerns whether a single transverse plane intersects both holes simultaneously or only one of them.

Constitutive law, mesh, and boundary conditions

The full three-dimensional geometry of the dog-bone specimen was modelled in ABAQUS/Explicit, including the through-thickness apertures with their controlled angular orientation, in order to capture the asymmetric stress distributions arising from the aperture arrangement. The PLA material was modelled as an isotropic elastic–plastic continuum. The elastic part of the constitutive law was defined by the experimentally measured apparent Young's modulus of the corresponding tensile coupon and a Poisson's ratio of $\nu = 0.36$, a value commonly adopted in the literature for FDM-printed PLA. The plastic part was characterised by a tabulated true stress–true plastic strain table, derived from the experimental engineering stress–strain curves through the standard conversions[140]:

$$\sigma_{true} = \sigma_{eng}\left(1 + \varepsilon_{eng}\right) \tag{II.17}$$

$$\varepsilon_{true} = ln\left(1 + \varepsilon_{eng}\right) \tag{II.18}$$

Only the pre-necking portion of each experimental curve was retained for the calibration of the plasticity table, in order to remain within the domain in which the conversions of Eqs. (II.17)–(II.18) are physically meaningful. The onset and the progression of failure were captured through the ABAQUS ductile-damage initiation criterion: in the simplified calibration adopted here, the equivalent plastic strain at damage initiation ε_{pl} was identified as the true plastic strain at the onset of the sharp load drop on the experimental load–extension curve, and the post-initiation damage evolution was defined through a displacement-at-failure parameter[141].

The specimen was discretised using eight-node linear brick elements with reduced integration (C3D8R), with a localised mesh refinement in the regions surrounding the apertures, where the stress gradients are most severe and where the mesh density most strongly conditions the accuracy of the predicted peak stresses[142]. The boundary conditions reproduced the experimental tensile-test fixture: one end of the specimen was fully fixed (encastre, all six degrees of freedom restrained), while a displacement-controlled loading was applied at the opposite end. The analysis was performed as a quasi-static simulation in ABAQUS/Explicit with the NLGEOM (large-deformation) option enabled, in order to account for the geometric

nonlinearity associated with the large deformations developed by the FDM-printed PLA prior to fracture. The loading and meshing scheme is illustrated in Fig. II.14.

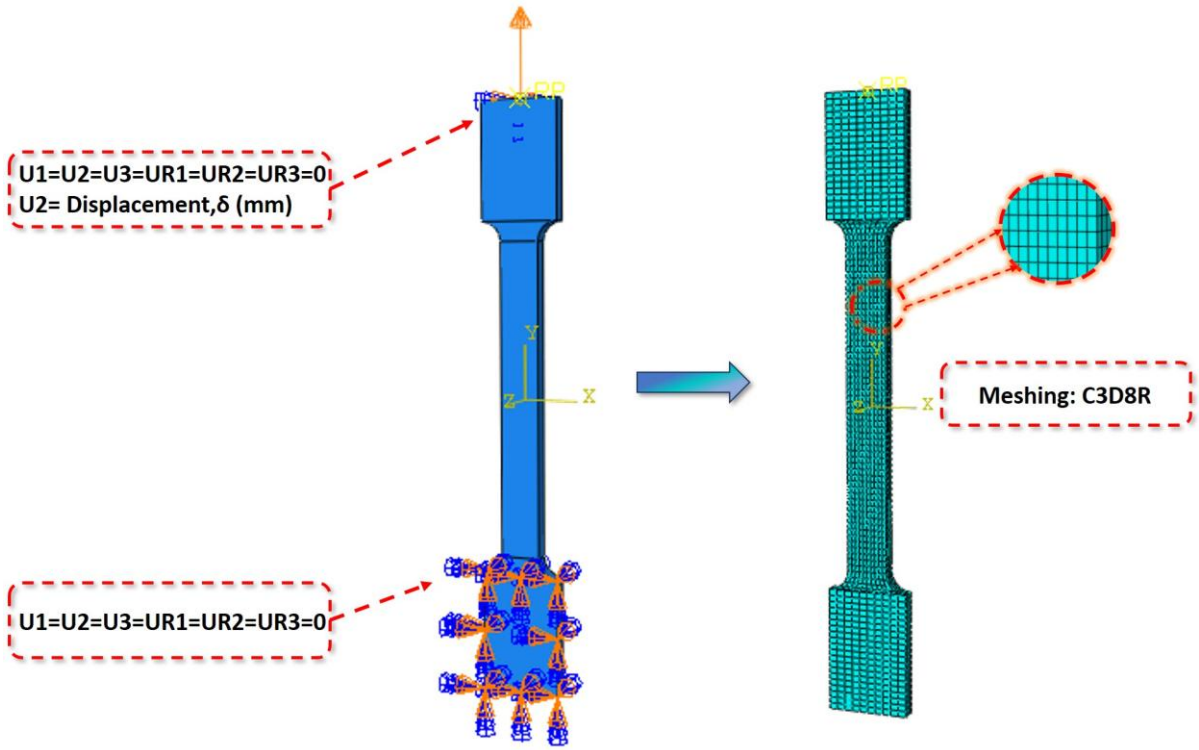


Fig. II. 14 Loading and meshing parameters of the tensile finite element model in ABAQUS/Explicit.

II.11.2 Three-point bending finite element model of the sandwich panels (ABAQUS/CAE Standard)

The second finite element campaign of the thesis simulates the three-point bending response of the hybrid sandwich panels of Section II.7 in ABAQUS/CAE Standard under quasi-static loading conditions. The model replicated the experimental geometry of Section II.8.2 in full: a beam of 170 × 25 × 20 mm composed of a hybrid Agave/Typha-epoxy face-sheet stack bonded to an FDM-printed core. The two material systems retained for the simulation campaign neat PLA and PLA/flax biocomposite coreswere simulated under the same numerical protocol, so that the only changing input between the two simulations was the constitutive card of the core material.

The hybrid Agave/Typha-epoxy face sheet was fabricated as a four-layer unidirectional [Typha / Agave / Typha / Agave] laminate at 0° (Section II.5.2). In the finite element model, however, the face sheet is treated as a homogeneous continuum medium rather than as a stack of distinct plies. This approach is justified by two considerations: (i) the tensile characterisation was conducted on coupons cut from the cured laminate as a whole, so the resulting properties

are global descriptors of the assembled composite, not ply-level constants; and (ii) the three-point bending configuration generates a stress state dominated by the longitudinal component aligned with the fibres, with limited transverse and shear contributions. An isotropic elastic–plastic card calibrated on the longitudinal tensile response therefore captures the dominant stress component with acceptable first-order accuracy Table II.10. The validity of this card is restricted to the present longitudinal-dominated loading scenario; extension to multiaxial loading would require orthotropic recalibration[143] .

Table II. 10 Material Properties.

Component	Material	Mechanical Behavior	Young's Modulus, E (MPa)	Poisson's Ratio, v	Density, p (g/cm³)
Face Sheets	Typha-Agave/Epoxy Hybrid	Isotropic	37,200	0.35	-
Core 1	PLA/Flax Biocomposite	Isotropic	1,357.34	0.33	1.25
Core 2	Neat PLA	Isotropic	1,241.51	0.33	1.24

Calibration of the three constitutive cards

Three independent isotropic elastic–plastic constitutive cards were calibrated for the three-point bending model, one for each constituent of the sandwich panel: the hybrid Agave/Typha-epoxy face sheet, the neat PLA core, and the PLA/flax biocomposite core. The Young's modulus, the yield stress and the hardening response of each card were extracted from the corresponding tensile campaign of Section II.8.1, conducted on coupons produced under exactly the same manufacturing conditions as the structural part they represent in the sandwich. The face-sheet card was calibrated on hybrid Agave/Typha-epoxy coupons CNC-machined from the cured laminates of Section II.5; the neat PLA card was calibrated on FDM-printed neat PLA coupons produced under the printing parameters of Table II.7; and the PLA/flax card was calibrated on FDM-printed PLA/flax biocomposite coupons produced under identical FDM conditions. The Poisson's ratio was set to $\nu = 0.36$ for the two PLA-based cores, in line with the literature for FDM-printed PLA, and to a value extracted from the laminate manufacturer's data for the face sheet, in the absence of a direct biaxial measurement. The numerical values of the

three calibrated cards are reported in the results chapter alongside the experimental tensile curves on which they rest.

Mesh, contacts and boundary conditions

The sandwich beam was discretised using eight-node linear brick elements with reduced integration (C3D8R), the same element family as in the tensile model of Section II.11.1, to keep the two campaigns numerically consistent. A localised mesh refinement was applied at the face-sheet/core interfaces, where the highest stress gradients are anticipated. A mesh-convergence study was carried out by halving the global element seed in successive runs and monitoring the convergence of the peak load and of the mid-span deflection; a global seed size of 0.5 mm was retained as the optimum trade-off between numerical accuracy and computational cost.

The loading nose and the two cylindrical supports were modelled as rigid analytical surfaces, in accordance with the experimental fixture of Section II.8.2. The interaction between the rigid surfaces and the deformable beam was enforced through a frictionless contact pair based on the penalty formulation, which prevents interpenetration without introducing artificial tangential resistance at the contact patches. The two supports were positioned 136 mm apart, replicating exactly the 80 % support span of the experimental fixture.

A static general step was used to apply the loading in displacement control at a rate of 2 $mm \cdot min^{-1}$, identical to the experimental crosshead speed. The two support surfaces were restrained in all six degrees of freedom, while a vertical displacement was prescribed at the loading nose. The total prescribed displacement was set to 3.5 mm for the PLA/flax case and to 4.8 mm for the neat PLA case, in order to reach the load levels observed experimentally for each material system. Field outputs were limited to the nodal displacements and the reaction forces, which together suffice for the construction of the load–deflection curves used in the validation step. The full finite element model is illustrated in Fig. II.15.

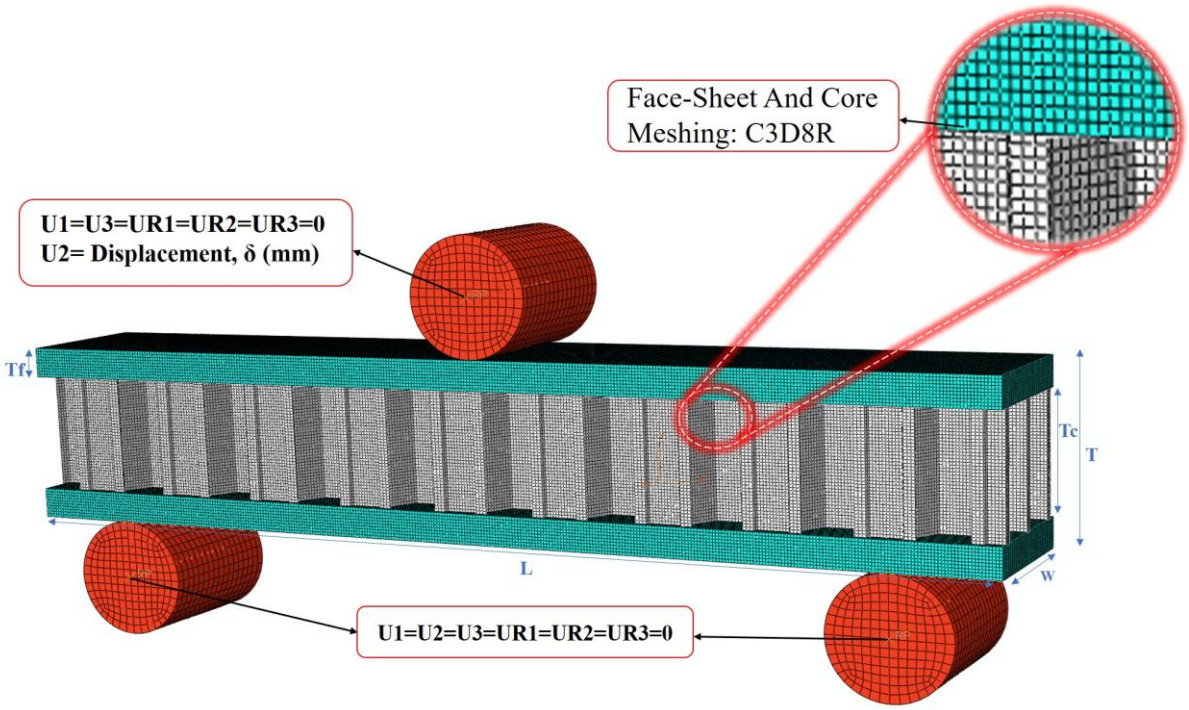


Fig. II. 15 Three-point bending finite element model of the sandwich panel in ABAQUS/CAE Standard.

Validation against the experimental records

The simulated load–deflection curves were validated against the experimental records of Section II.8.2 by direct overlay. The criterion of acceptance was a peak-load deviation within ± 10 %, which is consistent with the tolerance band recommended by ASTM C393 for the comparison of computed and measured flexural responses on sandwich constructions. The pre-failure correlation coefficient R^2 over the elastic and early-plastic portion of the response was used as a complementary descriptor, with an acceptance threshold of $R^2 \geq 0.95$ The results of this validation, together with the von Mises stress contours at peak load and the identification of the critical failure zones, are presented in detail in the results chapter.

II.12 Conclusion

This chapter has set out the materials, the fabrication routes and the experimental and numerical methods adopted in this research work, in direct alignment with the objectives of the doctoral programme.

The first part established a quantitative baseline for the FDM process through a three-factor three-level experimental design on neat PLA tensile coupons, analysed with a Taguchi L9 orthogonal array and a feed-forward artificial neural network.

The second part examined the apparent tensile response of FDM-printed PLA specimens incorporating paired through-thickness apertures, combining uniaxial testing with an

ABAQUS/Explicit simulation and a net-section analysis that distinguished the two-hole-cut and one-hole-cut regimes, to deliver a calibrated isotropic elastic–plastic protocol for the FDM-printed material.

The third and culminating part integrated this accumulated understanding into the design and characterisation of a complete hybrid sandwich panel. Typha latifolia and Agave americana fibres extracted from the M'Sila Province of Algeria were characterised through FTIR, TGA, XRD and single-fibre tensile testing, then combined with a low-viscosity epoxy into hybrid face sheets bonded to neat PLA and PLA/flax additively manufactured cores. The completed panels were tested in three-point bending, analysed under a non-parametric Kruskal–Wallis framework, and reproduced numerically in ABAQUS/CAE Standard.

Through this three-part organisation, the chapter provides the experimental and numerical foundation for the discussion and interpretation of the results in the following chapter.

Chapter III

Characterisation of Typha latifolia and Agave americana fibres

III.1 Introduction

This chapter reports the experimental characterisation of the Typha latifolia and Agave americana fibres extracted in Section II.3, using the four-technique pipeline introduced in Section II.4: FTIR, TGA-DTG, XRD and single-fibre tensile testing. Each technique probes a different aspect of the fibrechemical composition, thermal stability, crystalline organisation and intrinsic mechanical response and the four results are read together to construct a coherent structure–property picture for both species, and to position them against the conventional benchmarks of the natural-fibre family (flax, jute, sisal, kenaf).

The chapter is organised as follows. Section III.2 reports the FTIR spectra; Section III.3 the TGA-DTG thermograms; Section III.4 the XRD diffractograms, the Segal crystallinity index and the apparent crystallite size by Scherrer analysis; Section III.5 the single-fibre tensile testing campaign; Section III.6 the comparative summary against the four reference fibres; and Section III.7 closes the chapter with a synthesis of the structure–property relationships.

III.2 FTIR analysis

III.2.1 Spectral signatures of Typha and Agave

The Agave americana Fig. III.1spectrum exhibits a pronounced C–H stretching doublet in the 2890–2900 cm^{-1} region, characteristic of the methylene and methine groups of the cellulose backbone, and a sharp absorption near 1034 cm^{-1}, which is associated with the C–O and C–O–C stretching vibrations of the pyranose ring and is therefore a marker of the carbohydrate fraction common to cellulose and hemicellulose. Distinct lignin-related absorptions are visible in the 1510–1600 cm^{-1} region, where the aromatic C=C skeletal vibrations of the guaiacyl and syringyl units of lignin are located, together with deformation bands around 1325 cm^{-1} that complete the lignin signature. Taken together, these features confirm that the mechanically extracted Agave leaf fibres retain a complete lignocellulosic chemistry, with the three principal constituents cellulose, hemicellulose and lignin clearly identifiable on a single spectrum.

The Typha latifolia Fig. III.1 spectrum displays the same set of diagnostic features as the Agave spectrum, but with two qualitative differences that are visible without recourse to any quantitative deconvolution. First, the absorption bands of the Typha fibre are markedly broader than those of Agave, which reflects a less ordered local environment around the absorbing groups and is consistent with the partial removal of crystalline-supporting components during the alkaline treatment described in Section II.3.2. Second, the absolute intensity of the Typha bands is lower than that of the corresponding Agave bands under identical measurement conditions, which mirrors the alkaline removal of a fraction of the amorphous and extractive constituents from the Typha cortex. The two effects, broadening and intensity reduction, are

consistent with one another and point to the same underlying phenomenon: the alkaline delignification has thinned the non-cellulosic fraction of the Typha fibres without erasing it.

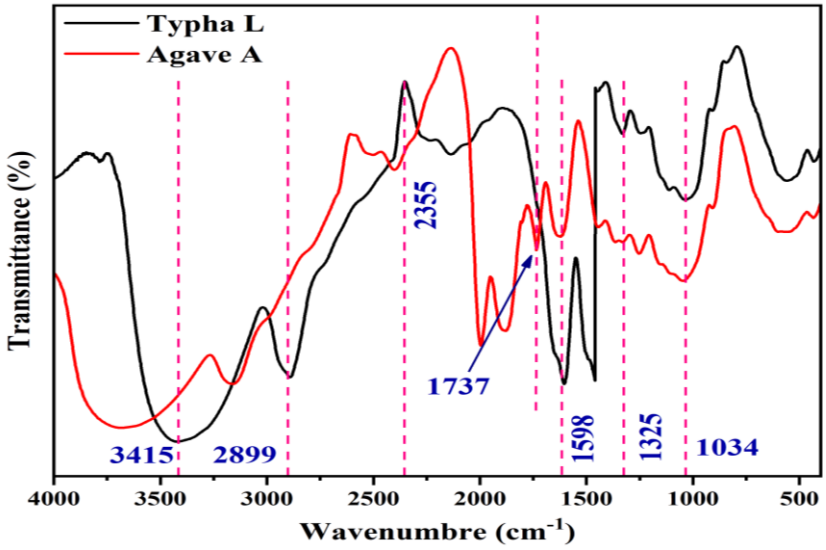


Fig. III. 1 FTIR spectra of Typha latifolia and Agave americana fibres.

III.2.2 Comparative interpretation

The qualitative comparison of the two spectra confirms, at the chemical level, the suitability of both fibres as lignocellulosic reinforcements and demonstrates that the mild alkaline treatment acted as a selective purification rather than a destructive degradation: the cellulose backbone is preserved, while the attenuated hemicellulose and lignin signatures indicate partial dissolution of amorphous constituents, which justifies the choice of the 3.25 % NaOH protocol. The FTIR analysis was intentionally kept qualitative, because ATR-FTIR intensities are sensitive to contact pressure, fibre packing and surface roughness; quantitative compositional ratios are instead derived from the TGA-DTG and XRD analyses that follow. In the characterisation pipeline, the FTIR section therefore establishes the chemical baseline and validates the alkaline extraction route before the thermal and crystalline analyses are presented.

III.3 Thermogravimetric and derivative thermogravimetric analysis (TGA-DTG)

III.3.1 Mass-loss curves and decomposition stages

The TGA traces of Fig. III.2 reveal the canonical three-stage decomposition pattern of lignocellulosic biomass for both fibres. A first, modest mass loss between approximately 30 °C and 200 °C corresponds to the desorption of physisorbed and bound moisture, with a mass loss typically of 5–8 %. A second, much larger mass-loss event develops between approximately 220 °C and 360 °C and accounts for the bulk of the thermal decomposition of both fibres; this stage encompasses the depolymerisation of hemicellulose and the more rapid devolatilisation

of cellulose, which dominates the 300–360 °C range. A third, slower mass loss extends from approximately 360 °C up to 600 °C and reflects the gradual decomposition of the more thermally resistant lignin fraction together with the progressive carbonisation of the residual char[196].

The DTG traces of Fig. III.2 sharpen the interpretation of the TGA curves by isolating the rate of mass loss as a function of temperature. The two species exhibit qualitatively similar DTG profiles, with a single dominant peak corresponding to the main devolatilisation event. The position and the shape of this peak, however, differ markedly between Typha and Agave, and these differences carry the structural information that the TGA curves alone cannot resolve. Typha latifolia exhibits a single, sharp DTG peak centred at approximately 340 °C with a maximum decomposition rate of approximately −8 %·min^{-1}, characteristic of a predominantly cellulosic residue in which the hemicellulose has been largely removed by the alkaline extraction. Agave americana shows a broader degradation profile with a maximum of approximately −7 %·min^{-1} near 325 °C, preceded by a distinct shoulder in the 260–290 °C region. This shoulder is a well-established signature of hemicellulose decomposition and indicates that a significant hemicellulose fraction is retained in Agave under the present extraction protocol; the lower peak temperature and the broader profile of Agave are consistent with a less chemically uniform fibre.

III.3.2 Char residue and thermal stability indicators

The three quantitative thermal descriptors the onset degradation temperature (T_{onset}, at 5 % mass loss), the peak DTG temperature (T_{max}), and the residual char fraction at 600 °C are reported in Table III.1.

Table III. 1 Thermal stability indicators of Typha latifolia and Agave americana fibres extracted from the TGA-DTG analysis.

Fibre	T_{onset} (°C, 5 % loss)	T_{max} (°C, DTG peak)	Residue at 600 °C (%)
Typha latifolia (chemically extracted)	246	340	46.0
Agave americana (mechanically extracted)	349	≈325	36.5

Typha exhibits a markedly earlier onset of devolatilisation than Agave (T~onset~ = 246 °C vs. 349 °C), reflecting the higher accessibility of its residual hemicellulose after the alkaline treatment. Conversely, Typha delivers a substantially higher char residue at 600 °C (46.0 % vs. 36.5 %), which is the more meaningful indicator of long-term thermal resistance. This apparent divergence reflects two distinct phenomena: the onset temperature is governed by the most

labile constituent (hemicellulose), whereas the char yield depends on the ordered crystalline cellulose that sustains an efficient char-forming pathway. Importantly, the thermal stability of both fibres lies well above the ambient-temperature curing cycle of the epoxy face sheets, confirming their full compatibility with the hand-layup and cold-pressing route adopted in this thesis.

The thermal signatures are fully consistent with the chemical and structural picture emerging from FTIR and XRD. The earlier devolatilisation of Typha mirrors its attenuated hemicellulose and lignin bands, while its higher char residue reflects the enrichment in ordered cellulose. TGA thus confirms that the mild alkaline route has produced a thermally resistant, cellulose-rich fibre.

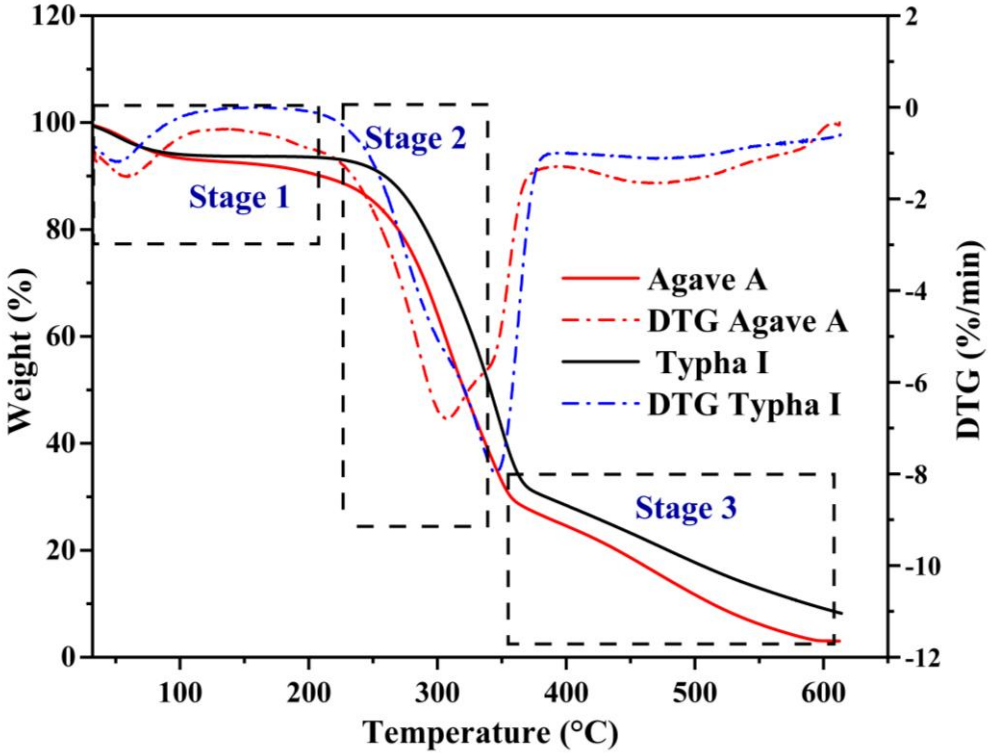


Fig. III. 2 Thermal decomposition analysis of Typha latifolia and Agave americana fibres.

III.4 X-ray diffraction and cellulose crystallinity

III.4.1 Diffractograms and cellulose-Iβ identification

Both patterns exhibit the characteristic reflections of native cellulose Iβ: the overlapped (1–10) and (110) peak at 2θ ≈ 16°, the dominant (200) reflection at 2θ ≈ 22°, and the weaker (004) reflection at 2θ ≈ 34.5° (Thygesen et al., 2005; French, 2014). The intensity minimum used as the amorphous reference Iam for the Segal index is therefore taken at 2θ ≈ 18.6°, in accordance with current best practice in cellulose crystallinity analysis [145]. The presence of

the (200) reflection on both diffractograms confirms that neither extraction route has converted the native cellulose Iβ into the cellulose II polymorph. [130] (Fig. III. 3).

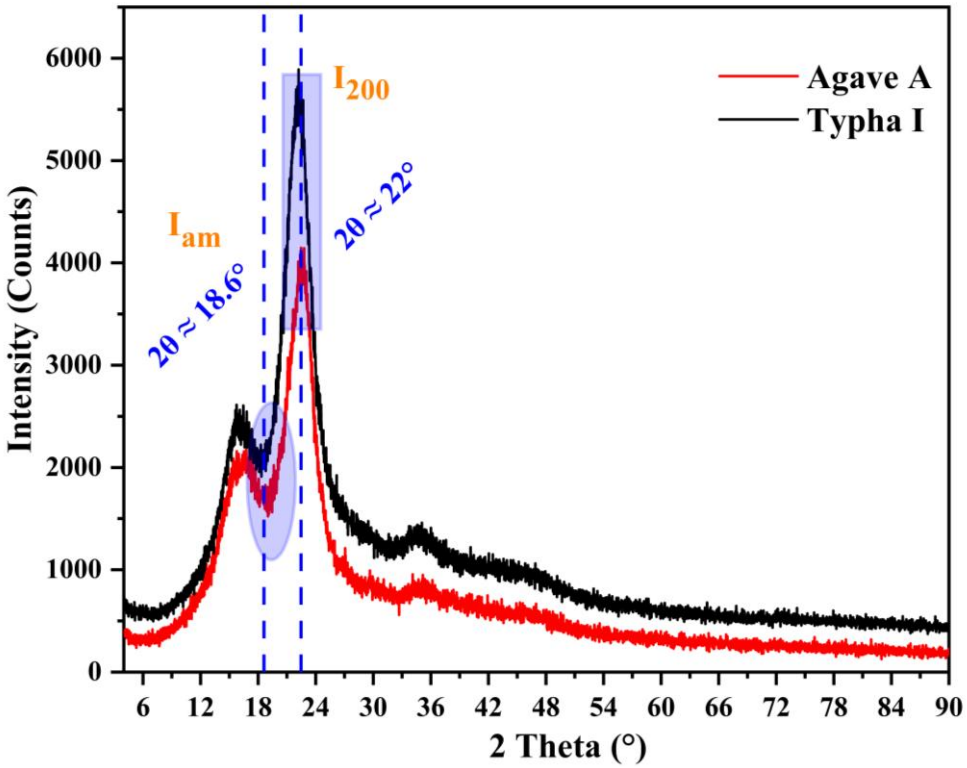


Fig. III. 3 X-ray diffraction patterns of Typha latifolia and Agave americana fibres.

III.4.2 Segal crystallinity index

The cellulose crystallinity index (CrI) of each fibre was computed from the background-subtracted diffractogram using the Segal peak-height method introduced in Eq. (II.1) of Section II.4.3, recalled here as Eq. (III.1):

$$CrI(\%) = \frac{I_{200} - I_{am}}{I_{200}} \times 100 \qquad \text{(III.1)}$$

where I_{200} is the intensity of the (200) lattice reflection at 2θ ≈ 22°, and I_{am} is the intensity at the minimum between the overlapped (1–10) / (110) peak and the (200) peak, located at 2θ ≈ 18.6°. The intensity values measured from the background-subtracted diffractograms of Fig. III.3, together with the resulting CrI values, are reported in Table III.2.

Table III. 2 Segal crystallinity index of Typha latifolia and Agave americana fibres.

Fibre	I_{200} (counts)	I_{am} (counts)	*CrI* (%)
Typha latifolia (chemically extracted)	5243	1910	63.6
Agave americana (mechanically extracted)	3590	1740	51.5

The Segal crystallinity index of Typha latifolia (63.6 %) is substantially higher than that of Agave americana (51.5 %). Both I_{200} values exceed 2000 counts, which ensures that the Poisson

noise ($\sigma \approx \sqrt{N}$) remains below approximately 1.5 % of the peak intensity, and provides a robust quantitative basis for the comparison. The result is consistent with the structural rationale developed throughout this chapter: the alkaline delignification of Typha selectively dissolves a fraction of the amorphous constituents hemicellulose, residual lignin, and extractives without damaging the crystalline cellulose backbone, with the consequence that the relative weight of the crystalline fraction in the residual fibre is increased. The mechanical decortication of Agave, by contrast, preserves all three constituents in their native proportions, so that the crystallinity index of the Agave fibres reflects the natural composition of the leaf without any selective enrichment of the crystalline phase.

The Segal CrI values reported here are nevertheless to be interpreted as semi-quantitative comparative metrics rather than absolute crystallographic measurements, in line with current best practice in cellulose crystallinity analysis. To complement them, an estimate of the apparent crystallite size along the [200] direction is reported in the next subsection.

III.4.3 Apparent crystallite size along the [200] direction

Apparent crystallite sizes along the [200] direction were estimated from the full-width at half-maximum (FWHM) of the (200) reflection using the Scherrer equation introduced in Eq. (II.2) of Section II.4.3, recalled here as Eq. (III.2):

$$L_{200} = \frac{K \cdot \lambda}{\beta \cdot \cos\theta} \quad \text{(III.2)}$$

with K = 0.9, λ = 1.5406 Å, and the observed FWHM corrected for an estimated instrumental broadening of 0.1° assumed to be Gaussian. The FWHM values were extracted by fitting a single Gaussian profile to the isolated (200) reflection over 2θ = 20°–24°, after local straight-line baseline subtraction, in OriginPro 2026. The resulting parameters and apparent crystallite sizes are reported in Table III.3.

Table III. 3 Apparent crystallite size along the [200] direction obtained from the Scherrer equation (K = 0.9, λ = 1.5406 Å, instrumental broadening 0.1° assumed Gaussian).

Fibre	2θ of (200) (°)	FWHM of (200) (°)	L_{200} (nm)
Typha latifolia (chemically extracted)	22.13	2.63	3.08
Agave americana (mechanically extracted)	22.40	2.37	3.42

Both crystallite-size values fall within the range commonly reported for native plant cellulose Iβ (≈ 3–5 nm). The two fibres therefore exhibit comparable apparent crystallite sizes, with a tentatively slightly larger value in Agave. The ≈ 11 % difference between the two

estimates is within the combined uncertainty arising from the Gaussian fit, the assumed instrumental broadening, and the neglected contribution of micro-strain, so no definitive ranking of crystallite sizes is claimed here. A rigorous separation of crystallite-size and micro-strain contributions by Williamson–Hall analysis was beyond the scope of the present instrumental campaign and is recommended for future work .

Crucially, the Scherrer analysis shows that the lower Segal CrI of Agave cannot be attributed to substantially smaller crystallites a scenario that would otherwise inflate the apparent amorphous contribution at $2\theta \approx 18.6°$. Since the crystallite sizes of the two fibres are comparable, the ≈ 12 percentage-point difference in Segal CrI is most consistently interpreted as a genuinely lower fraction of ordered crystalline cellulose in Agave americana relative to Typha latifolia, rather than as a crystallite-size artefact. This interpretation is supported by the independent FTIR band-intensity ratios (Section III.2.1) and by the lower TGA char yield of Agave (Section III.3.2), providing convergent evidence from three orthogonal techniques.

The CrI ranking established here (Typha > Agave) explains three independent observations made earlier in this chapter. First, it is consistent with the broader and weaker FTIR bands of Typha relative to Agave (Section III.2.1): the FTIR signal in the fingerprint region is dominated by the disordered fraction, which is precisely what the alkaline treatment has reduced. Second, it is consistent with the higher TGA char residue of Typha relative to Agave (Section III.3.2): a higher crystalline fraction supports a more efficient char-forming pathway. Third, it provides a structural basis for the differences in tensile behaviour reported in Section III.5: a higher cellulose crystallinity is generally associated with a higher intrinsic stiffness but a lower elongation at break, a trade-off that the single-fibre tests will quantify directly.

The results of this section therefore consolidate the picture that emerged from the FTIR and the TGA-DTG analyses. The two extraction routes, which were chosen to match the native microstructure of each species (Section II.3), have not only delivered chemically intact lignocellulosic fibres but have also produced two materials with measurably different crystalline organisations, opening the way for a meaningful mechanical comparison in the next section.

III.5 Single-fibre tensile testing

III.5.1 Fibre cross-section measurement

Prior to the tensile testing campaign, the cross-sectional dimensions of the two fibre types were measured by optical microscopy at the three positions specified in the protocol of Section II.4.4. Representative micrographs of the two species are shown in Fig. III.4, with the local diameter values overlaid directly on the corresponding fibre bodies. The three positional

measurements yield a mean diameter of 142 µm for Agave americana and 172 µm for Typha latifolia. The within-fibre dispersion is modest in both cases, which confirms that the assumption of a quasi-uniform diameter along the gauge length, adopted for the conversion of force into engineering stress in Section II.4.4, is justified for both species. The morphological gap between the two fibres is approximately 30 µm in mean diameter, and the Typha fibres are consistently coarser than the Agave fibres along the entire gauge length.

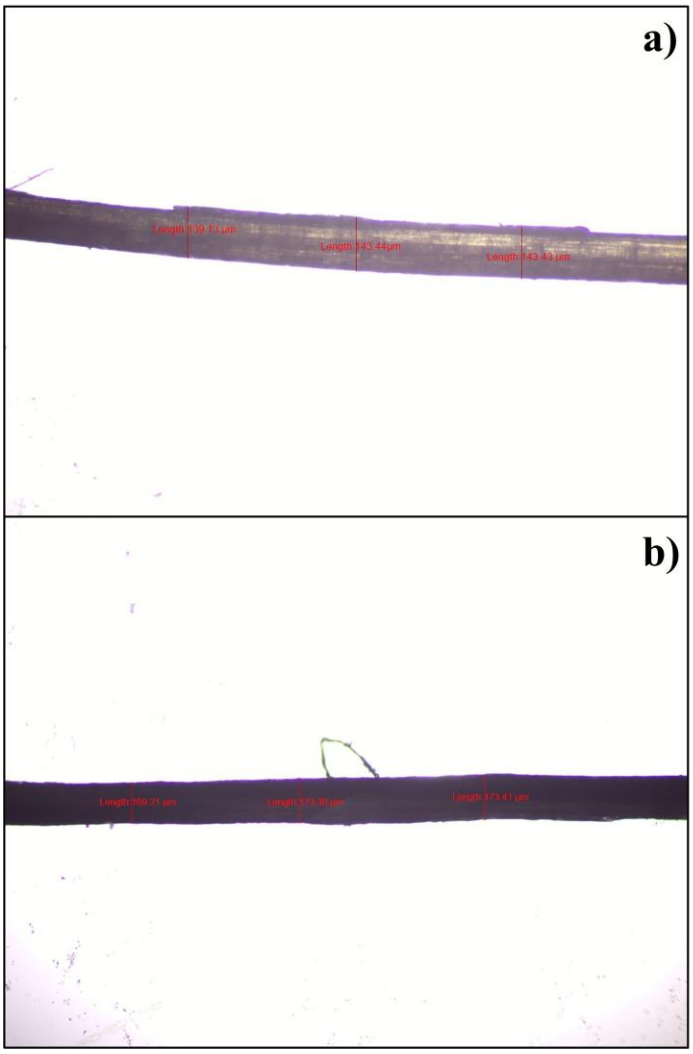


Fig. III. 4 Optical micrographs of single fibres with positional diameter measurements.

III.5.2 Test campaign and stress–strain behaviour

For each species, three representative stress–strain curves were extracted from the validated dataset and grouped according to their position relative to the population mean: a lower-bound curve denoted G01, a median curve denoted G02, and an upper-bound curve denoted G03. This three-curve representation, illustrated in Fig. III.5, captures the natural scatter of single-fibre tensile data without obscuring the central tendency of each species, and it provides a more informative picture of the mechanical behaviour than a single average curve would.

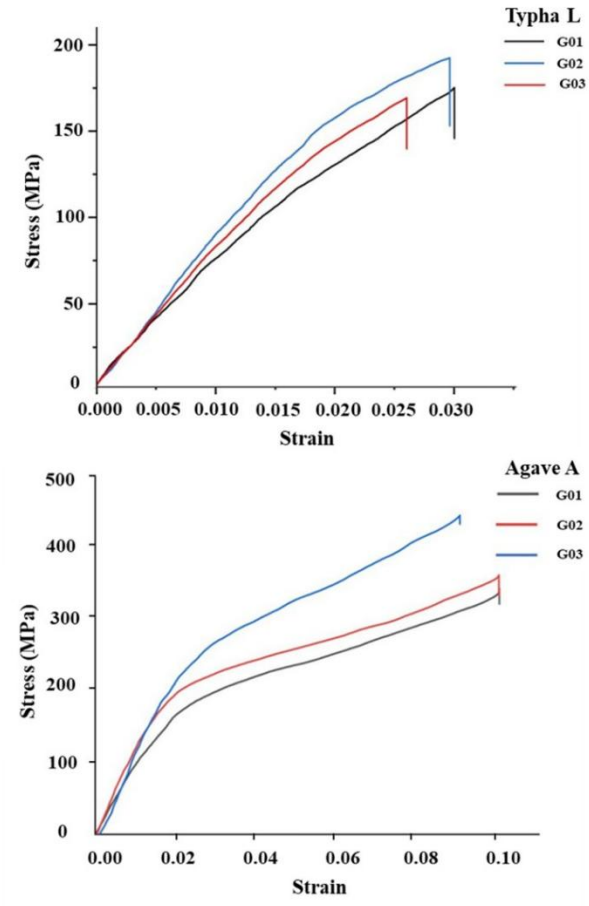


Fig. III. 5 Representative stress–strain curves of single Agave and Typha fibres.

The stress–strain responses of the two species reveal qualitatively distinct deformation modes. The Agave americana curves rise smoothly along a near-linear path from the origin, sustain the linear behaviour up to a substantial strain level, and reach fracture at ultimate stresses in the range of approximately 350 to 400 MPa with strains close to 0.10 (10 %). The **G01**, **G02** and **G03** curves of Agave differ from one another mainly in the magnitude of the ultimate stress reached at fracture, while their slopes in the elastic region remain comparable. This pattern is consistent with a fibre population whose stiffness is reproducible from one specimen to the next, and whose scatter is concentrated in the strength values rather than in the deformation kinematics.

The Typha latifolia curves tell a different story. The three representative responses lie significantly below those of Agave on both axes: the ultimate stresses are confined to the range of approximately 150 to 180 MPa, and the elongation at break does not exceed 0.025 (2.5 %). The G01–G02–G03 envelope of Typha is therefore both shorter and lower than that of Agave, which reflects a fundamentally different mechanical behaviour rather than a simple downscaling of the Agave response. The Typha fibres reach fracture at lower stresses and at

lower strains, which is the signature of a more brittle deformation mode consistent with the higher crystallinity index quantified in Section III.4.

III.5.3 Statistical scatter and coefficient of variation

The natural variability of single-fibre tensile data was quantified through the coefficient of variation (CV) of the ultimate tensile strength, computed for each species from the full set of fifteen valid specimens. The Typha latifolia fibres display a coefficient of variation of approximately 16.7 %, while the Agave americana fibres display a lower CV of approximately 10.0 %. Both values fall within the canonical range of 10 to 35 % reported in the literature for lignocellulosic fibres, which is itself the consequence of the biological variability inherent to plant tissues variations in lumen size, in microfibril angle, and in the local distribution of vascular bundles all contribute to the dispersion of single-fibre measurements. Within this canonical range, however, the Agave fibres are noticeably more reproducible than the Typha fibres.

The lower CV of Agave relative to Typha admits a structural interpretation that connects directly to the morphological differences between the two species. Agave americana leaves enclose long, continuous bundles of aligned fibres of comparable diameter, isolated from a relatively homogeneous parenchyma by the mechanical decortication of Section II.3.3. The resulting specimens are therefore drawn from a structurally uniform source, and their mechanical scatter reflects only the second-order biological variability of the leaf. Typha latifolia stems, by contrast, contain a less homogeneous mix of vascular bundles, aerenchyma channels and parenchymatous tissues, and the alkaline delignification of Section II.3.2, while it removes part of the non-cellulosic phase, does not equalise the underlying anatomical heterogeneity. The Typha specimens are therefore drawn from a more heterogeneous source, and their higher CV is a faithful expression of that heterogeneity.

Despite this elevated scatter, the trends observed between the two species remain clear and consistent: the Agave fibres are systematically stronger and more compliant than the Typha fibres across the full range of validated specimens, and the CV values, while different in magnitude, do not invalidate the comparison. The supporting structural justification for this ordering higher cellulose crystallinity in Typha leading to higher local stiffness but lower elongation was established in Sections III.3 and III.4 and is now confirmed at the macroscopic mechanical level.

III.5.4 Tensile strength and Young's modulus

The mean ultimate tensile strength (σ_u) and the mean Young's modulus (E) of the two fibre types, computed from the fifteen valid specimens of each species, are reported in Table III.4.

Table III. 4 Single-fibre tensile properties of Typha latifolia and Agave americana: ultimate tensile strength, Young's modulus, and coefficient of variation (n = 15 per species). CE = chemically extracted; ME = mechanically extracted.

Property	Typha latifolia (stem, CE)	Agave americana (leaf, ME)
Ultimate tensile strength σ_u (MPa)	130 – 260	300 – 450
Young's modulus E (GPa)	9.8 ± 5.0	38.5 ± 2.1
Coefficient of variation, CV (%)	≈ 16.7	≈ 10.0
Number of valid specimens, n	15	15

Three observations follow from Table III.4. First, the ultimate tensile strength of Agave americana is more than twice that of Typha latifolia across the corresponding ranges (300–450 MPa versus 130–260 MPa). The Agave fibres are therefore the stronger of the two species in absolute terms, and they emerge as the more competitive candidate for load-bearing biocomposite applications.

Second, the gap between the two species is even more pronounced when expressed in terms of stiffness. The Young's modulus of Agave americana (38.5 ± 2.1 GPa) is nearly four times that of Typha latifolia (9.8 ± 5.0 GPa), and the standard deviation of the Agave modulus is much smaller in both absolute and relative terms. This means that the Agave fibres are not only stiffer on average but also more reproducible in their elastic response, which is a decisive advantage when the fibres are intended to act as the load-transferring phase of a unidirectional composite.

Third, the wide standard deviation of the Typha modulus (±5.0 GPa on a mean of 9.8 GPa, or roughly ±50 %) reflects the same anatomical heterogeneity already invoked to explain the higher CV of the Typha tensile strength. The Typha specimens therefore represent a less reliable reinforcement candidate when used alone, but their lower stiffness and their broader scatter do not disqualify them from a hybrid configuration in which they can play a complementary role to the stiffer Agave fibres. This complementarity is precisely the rationale that motivated the [T/A/T/A] hybrid stacking sequence adopted for the face sheets in Section II.5.2: the rigid Agave layers provide the bulk of the stiffness, while the more compliant Typha layers contribute energy-dissipation pathways through sequential pull-out and crack-bridging mechanisms.

III.5.5 Synthesis of the single-fibre tensile results

The single-fibre tensile testing campaign establishes three results that will guide the interpretation of the composite-level tests reported in the next chapters of this thesis. First,

Agave americana is confirmed as the stronger and stiffer of the two species, with an ultimate tensile strength range of 300–450 MPa and a Young's modulus of 38.5 ± 2.1 GPa. Second, Typha latifolia, while mechanically inferior in absolute terms, exhibits a tensile response that remains within the bounds reported for several conventional natural fibres and that is structurally compatible with a hybrid reinforcement strategy. Third, the variability of both species falls within the canonical range for lignocellulosic substrates, which means that no anomalous behaviour can be invoked to dismiss the comparison; the differences observed between Typha and Agave are real and they reflect the underlying structural differences quantified in Sections III.3 and III.4.

Taken together with the FTIR signatures of Section III.2, the thermal stability indicators of Section III.3, and the cellulose crystallinity values of Section III.4, the tensile results of this section close the four-technique characterisation pipeline opened in Section II.4 and provide the experimental basis on which the comparative summary of Section III.6 will rest.

III.6 Comparative summary and benchmarking

III.6.1 Synthesis table

The four characterisation campaigns reported in Sections III.2 to III.5 yield, for each of the two species studied in this thesis, a coherent set of physical, chemical, mechanical, crystallographic and thermal descriptors. In order to position the locally extracted Typha latifolia and Agave americana fibres against the conventional benchmarks of the natural-fibre family, the descriptors obtained in this work are compiled in Table III.5 alongside literature values for four reference natural fibres flax, jute, sisal and kenaf drawn from peer-reviewed sources of the past decade.

Table III. 5 Comparison of physical, chemical, mechanical, crystallographic and thermal properties of Typha latifolia and Agave americana (this study) with literature data for four reference natural fibres. CE = chemical extraction; ME = mechanical extraction; (in) = inferred from FTIR / TGA analyses.

Fibre	Type	Density (g·cm⁻³)	Diameter (µm)	Cellulose (wt %)	Hemi (wt %)	Lignin (wt %)	σ_u (MPa)	E (GPa)	CrI (%)	L_{200} (nm)	T_{onset} (°C)	T_{max} (°C)	Residue 600 °C (%)	Ref.
Typha latifolia	Stem (CE)	-	172	≈68–75 (in)	≈12–18 (in)	≈8–12 (in)	130–260	9.8 ± 5.0	63.6	3.08	246	340	46.0	This study
Agave americana	Leaf (ME)	-	142	≈65–70 (in)	≈12–18 (in)	≈8–12 (in)	300–450	38.5 ± 2.1	51.5	3.42	349	≈325	36.5	This study
Flax	Stem	1.4–1.5	40–80	70–80	7–19	2–3	800–1500	50–80	-	-	≈300	≈350	15–20	[146]
Jute	Stem	1.3–1.5	50–200	61–73	14–23	12–16	393–773	13–30	-	-	280–320	≈350	20–25	[51]
Sisal	Leaf	1.3–1.5	100–300	60–72	10–20	8–12	400–700	9–22	-	-	280–320	≈340	18–22	[54]
Kenaf	Stem	1.04	150–300	70	3	19	1000	53	-	-	-	-	-	[147]

The values reported in the rows of Table III.5 corresponding to Typha latifolia and Agave americana are those measured in the present study and discussed in Sections III.2 to III.5. The cellulose, hemicellulose and lignin fractions of the two species are reported as inferred ranges, derived qualitatively from the FTIR and TGA-DTG analyses of Sections III.2 and III.3 rather than from a quantitative chemical assay; this convention is denoted by the "(in)" marker in the table and is acknowledged here as a limitation of the present characterisation pipeline. The four reference fibres flax, jute, sisal and kenaf are reported with the value ranges established in their respective source publications, without modification.

III.6.2 Comparative interpretation

Three readings of Table III.5 deserve to be highlighted, because they inform the discussion of the composite-level results that will follow in the next chapters of this thesis.

The first reading concerns the morphological positioning. The mean diameter of Typha latifolia (172 µm) and that of Agave americana (142 µm) place both species in the upper-middle range of the natural-fibre diameter spectrum: they are substantially coarser than flax (40–80 µm) but comparable to or finer than jute, sisal and kenaf, all of which exceed 100 µm. Coarser fibres carry an implicit penalty on the specific surface area available for matrix bonding, which is one of the reasons why flax remains the benchmark for high-performance natural-fibre composites. The diameter values reported for Typha and Agave are not, however, prohibitive: they fall within the range routinely accepted for hand-layup and FDM-compatible biocomposites, and they are compensated by the regional availability and the absence of irrigation requirements, which constitute the practical advantage of the M'Sila-sourced fibres.

The second reading concerns the mechanical positioning. The ultimate tensile strength of Agave americana (300–450 MPa) places it within the lower band of the jute range (393–773 MPa) and above the lower bound of the sisal range (400–700 MPa), while remaining substantially below the flax range (800–1500 MPa) and the kenaf single value (1000 MPa). The Young's modulus of Agave americana (38.5 ± 2.1 GPa) is highly competitive: it exceeds the upper bound of the jute and sisal ranges (30 GPa and 22 GPa, respectively) and approaches the lower bound of the flax range (50 GPa). Agave therefore emerges from this comparison as a credible alternative to jute and sisal for stiffness-driven applications, while flax retains its leadership for strength-driven applications. Typha latifolia, with σ_u in the range 130–260 MPa and $E \approx 9.8$ GPa, falls below all four reference fibres, and it should be regarded as a complementary rather than a primary reinforcement a positioning that is consistent with its role in the [T/A/T/A] hybrid layup adopted in Section II.5.2.

The third reading concerns the thermal and crystallographic positioning. The residual char fraction at 600 °C is the descriptor in which the locally extracted fibres compete most favourably with the benchmarks. Typha latifolia delivers 46.0 % residue at 600 °C, more than twice the value reported for flax (15–20 %), jute (20–25 %) and sisal (18–22 %). Agave americana delivers 36.5 % residue, which is also substantially above all three benchmarks. The Segal crystallinity index of Typha (63.6 %) is competitive with that of the high-end natural fibres, while the apparent crystallite size along the [200] direction (3.08 nm for Typha, 3.42 nm for Agave) lies within the canonical range reported for native plant cellulose Iβ. The high char-forming capacity, traced in Section III.3.3 to the higher cellulose crystallinity of Typha and to the structurally intact lignocellulosic chemistry of Agave, opens a specific application window for the M'Sila-sourced fibres in fire-retardant or thermally demanding biocomposite systems, where the residual char acts as a protective layer against heat propagation. This is a domain in which Typha and Agave are not merely catching up with the benchmarks but actually outperforming them.

III.6.3 Structure property synthesis

The four characterisation campaigns reported in this chapter converge on a consistent structural picture for both species. Typha latifolia, processed through the mild alkaline delignification of Section II.3.2, delivers fibres with attenuated FTIR signatures (Section III.2), an earlier onset of devolatilisation but a higher char residue (Section III.3), a markedly higher cellulose crystallinity (CrI = 63.6 %, Section III.4), comparable apparent crystallite sizes to Agave ($L_{200} \approx 3.08$ nm), and a brittle tensile response of moderate strength (Section III.5). The structural thread running through these results is the selective enrichment of the crystalline cellulose fraction effected by the alkaline treatment: the removal of part of the amorphous constituents leaves a stiffer but less compliant fibre, more thermally resistant in the long term but less mechanically reproducible.

Agave americana, processed through the strictly mechanical decortication of Section II.3.3, delivers fibres with intact FTIR signatures, a later onset of devolatilisation, a moderate cellulose crystallinity (CrI = 51.5 %), comparable or marginally larger apparent crystallite sizes ($L_{200} \approx$ 3.42 nm), and a more compliant and substantially stronger tensile response. The structural thread running through these results is the preservation of the native lignocellulosic composition: the absence of any chemical treatment leaves all three constituents in their natural proportions, which produces a fibre whose mechanical and thermal behaviours reflect the intrinsic anatomy of the Agave leaf.

The complementarity between the two species, established at the level of the individual characterisation techniques, is therefore confirmed at the integrated level: Typha contributes thermal resistance and low cost, Agave contributes mechanical strength and stiffness, and the combination of the two through a hybrid layup exploits both contributions simultaneously.

III.7 Conclusion

This chapter has reported the experimental characterisation of the Typha latifolia and Agave americana fibres extracted in Section II.3 through the four-technique pipeline of Section II.4. The FTIR spectra confirm the lignocellulosic nature of both species, with attenuated bands for Typha reflecting the selective amorphous removal effected by the alkaline delignification. The TGA-DTG analysis reveals a canonical three-stage decomposition, with Typha exhibiting an earlier onset (T_{onset} = 246 °C) but a higher residual char fraction (46.0 %), while Agave exhibits a later onset (349 °C) and a lower residual char (36.5 %); both fibres remain compatible with the polymer-processing temperatures used in this thesis (≤ 220 °C). The XRD analysis, conducted under a rigorous background-subtraction protocol, confirms the cellulose Iβ polymorph in both species and yields Segal crystallinity indices of 63.6 % for Typha and 51.5 % for Agave, complemented by Scherrer apparent crystallite sizes of 3.08 nm and 3.42 nm respectively along the [200] direction. The comparable crystallite sizes show that the ≈ 12 percentage-point difference in Segal CrI reflects a genuinely lower fraction of ordered crystalline cellulose in Agave rather than a crystallite-size artefact. The single-fibre tensile tests show that Agave is markedly stronger and stiffer (σ_u = 300–450 MPa, E = 38.5 ± 2.1 GPa, CV ≈ 10 %) than Typha (σ_u = 130–260 MPa, E = 9.8 ± 5.0 GPa, CV ≈ 16.7 %).

Benchmarked against flax, jute, sisal and kenaf, Agave americana competes directly with jute and sisal in stiffness-driven applications, while Typha latifolia takes a complementary role as a moderate-strength, high-thermal-resistance fibre; both species outperform the four reference fibres in terms of residual char fraction at 600 °C. The complementarity between the two species Typha providing thermal resistance and Agave providing mechanical strength and stiffness is the experimental foundation on which the hybrid [T/A/T/A] face-sheet design adopted in Section II.5.2 rests, and validates, at the level of the individual fibre, the design rationale of the composite-manufacturing chain of the thesis.

Chapter IV

Mechanical and numerical study of FDM-printed PLA

IV.1 Introduction

This chapter reports the experimental and numerical investigation of the mechanical response of FDM-printed polylactic acid (PLA), the polymer used as the core material of the sandwich panels of this thesis. The work is structured around two complementary studies; both performed on the same Anycubic FDM platform and on tensile coupons drawn to ASTM D638 geometry. The first study, presented in Sections IV.2 to IV.4, identifies the FDM process parameters that govern the tensile response of neat PLA: it begins with the raw experimental tensile data of the 27 coupons of the Taguchi L9 matrix, then introduces the Taguchi signal-to-noise analysis as a structured way of extracting the dominant factors from those data, and finally complements the Taguchi analysis with an artificial neural network (ANN) model capable of capturing non-linear interactions between the process parameters and the mechanical responses. The second study, presented in Sections IV.5 and IV.6, investigates the effect of through-thickness circular apertures inclined at controlled angles on the tensile behaviour of FDM-printed PLA, and validates the experimental observations through a finite element model built in ABAQUS/Explicit.

The two studies are presented together in this chapter not because one feeds into the other in a literal numerical sense, but because they constitute, together, the experimental and numerical methodology developed in this thesis for the mechanical characterisation of FDM-printed PLA. Each study has its own specimen population, its own printing parameters, and its own analytical framework, and the parameters adopted for the printing of the sandwich cores of the next chapter are documented independently in Section II.6.2 of the Materials and Methods. The chapter therefore plays a double role in the architecture of the thesis: it establishes, in its first half, a rigorous process-parameter understanding of FDM-printed PLA through a structured design-of-experiments approach, and it documents, in its second half, the mechanical and numerical analysis of a representative loading configuration on the same material. Section IV.7 closes the chapter with a methodological synthesis that consolidates the contribution of both studies to the broader thesis programme.

IV.2 Tensile response of FDM-printed PLA

IV.2.1 Test campaign

The full experimental protocol of the Taguchi L9 test matrix has been described in Chapter II. In the present chapter, only the elements strictly necessary to the reading of the results are recalled. All 27 ASTM D638 Type IV tensile coupons were printed and loaded to fracture under the conditions detailed in Section II.10. The engineering stress–strain curves obtained from the test campaign are presented together in Fig. IV.1.

IV.2.2 Stress–strain behaviour of the 27 specimens

The 27engineering stress–strain curves obtained from the test campaign are presented together in Fig. IV.1. All 27 curves exhibit the qualitative response characteristic of unfilled FDM-printed PLA: an initial quasi-linear elastic region, a short yielding plateau, and a brittle fracture without any extended plastic plateau.Within this common pattern, however, the magnitude of the stress, the elongation at break and the elastic slope vary significantly between the nine factor combinations of the L9 matrix, which confirms that the three process factors retained in the test campaign do influence the mechanical response of the printed coupons (Fig. IV. 2).

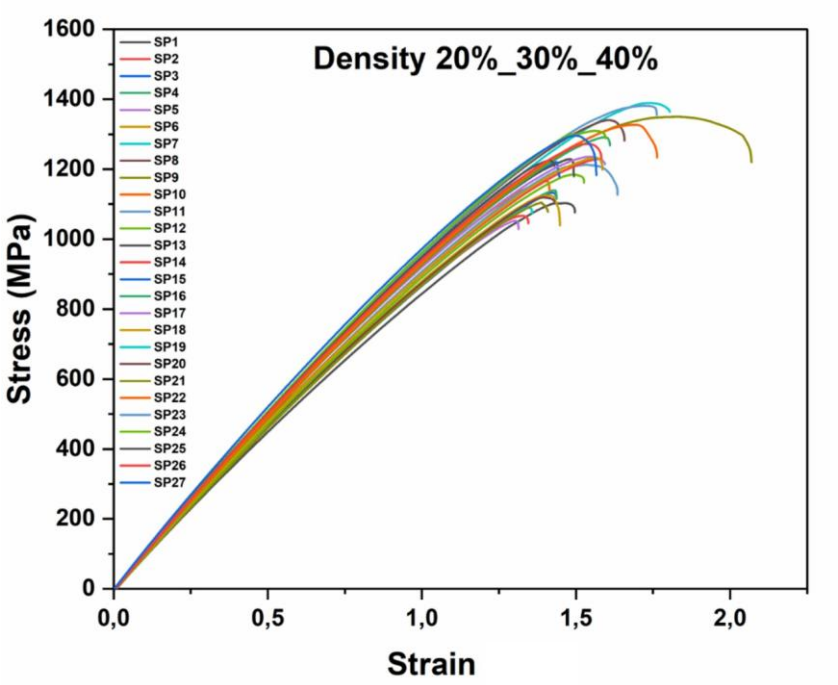


Fig. IV. 1 Engineering stress vs strain curves of the 27 FDM-printed PLA coupons.

Two qualitative trends emerge directly from the inspection of Fig. IV.1, without recourse to any structured statistical analysis. The first trend concerns the influence of the filling density. At a fixed extruder temperature of 200 °C, the strain, the tensile stress and the Young's modulus are recorded at approximately 0.010, 30.46 MPa and 2774 MPa for a density of 20 %, and they rise to approximately 0.013, 39.70 MPa and 2828 MPa when the density is increased to 40 %. The same monotonic trend is observed at the other temperature levels, and it confirms that increasing the raster density produces a more continuous load path, reduces the volume fraction of inter-bead voids, and improves the three mechanical descriptors simultaneously.

The second trend concerns the influence of the extruder temperature. At a fixed density of 20 %, the strain, the tensile stress and the Young's modulus are recorded at approximately 0.011, 32.29 MPa and 2630 MPa for a temperature of 200 °C, and they evolve to approximately 0.010,

30.82 MPa and 2785 MPa when the temperature is increased to 220 °C. The pattern is therefore not monotonic across the three responses: the strain and the tensile stress decrease slightly with increasing temperature, while the Young's modulus increases. This dual behaviour suggests that higher extrusion temperatures improve the inter-layer bonding (which raises the elastic stiffness) but also induce a slight thermal degradation of the polymer chains (which reduces the strain and the strength at fracture).

The qualitative fingerprint of the specimen weight is, by contrast, much weaker than that of the other two factors. The 27 curves grouped by weight level do not exhibit a clearly visible ordering, which already suggests that the weight, at the levels investigated here, plays a marginal role in the tensile response of the coupons. This first impression will be confirmed by the structured signal-to-noise analysis of Section IV.3.

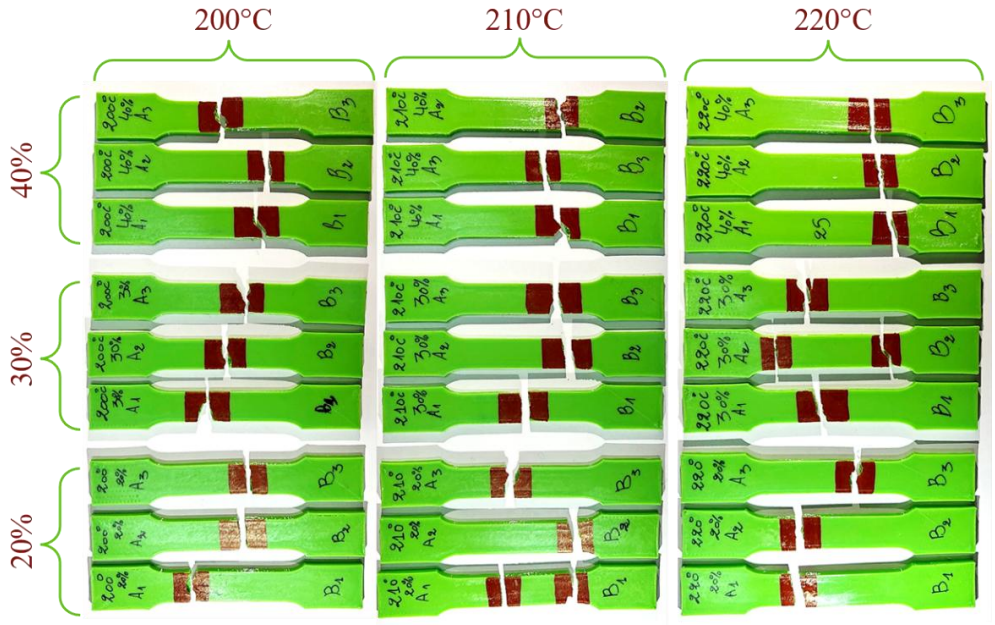


Fig. IV. 2 FDM-printed PLA tensile specimens grouped by extruder temperature and filling density.

IV.2.3 Rationale for predictive modelling

The qualitative reading of Fig. IV.1 has identified the filling density as the dominant influence and the extruder temperature as a secondary, non-monotonic influence, while leaving the specimen weight in the background. These observations, however, remain qualitative: they do not quantify the relative weight of each factor, they do not identify the optimal combination of levels, and they do not exploit the orthogonality of the L9 design that motivated the choice of the test matrix in the first place. Two complementary modelling tools are therefore brought to bear on the same dataset in the next two sections.

Section IV.3 applies the Taguchi signal-to-noise analysis to the 27-point dataset, in order to rank the three factors according to their contribution to the variance of each mechanical response, to identify the optimal level of each factor, and to extract a single optimal parameter combination for the maximisation of the tensile performance. Section IV.4 then develops an artificial neural network model of the same dataset, in order to capture the non-linear interactions that the linear main-effect framework of the Taguchi analysis cannot resolve, and to provide an independent predictive tool whose accuracy can be cross-checked against the Taguchi outputs. The two models are deliberately treated as complementary rather than redundant: the Taguchi analysis offers an interpretable factor ranking that supports the interpretation of the experimental dataset, while the ANN model provides a higher-fidelity predictive surface that can be queried for parameter combinations not explicitly tested in the L9 matrix.

The juxtaposition of the two predictive frameworks on the same experimental dataset is the central methodological contribution of the first half of this chapter, and its outcome a self-consistent ranking of the FDM process parameters validated by two independent statistical and numerical routes is the standalone result of this study.

IV.3 Taguchi L9 signal-to-noise analysis

IV.3.1 Main-effect analysis

The Taguchi signal-to-noise (S/N) analysis framework was applied to the 27-point tensile dataset of Section IV.2, following the methodology and the equation described in Section II.10.2. The analysis was implemented in Minitab and was performed independently on the three mechanical responses ultimate tensile stress, strain at break, and Young's modulus so that the relative contribution of each process factor could be identified separately on each response. The "larger-is-better" S/N formulation was adopted throughout, in accordance with the objective of maximising the three responses simultaneously. The resulting main-effect plots are presented together in Fig. IV.3.

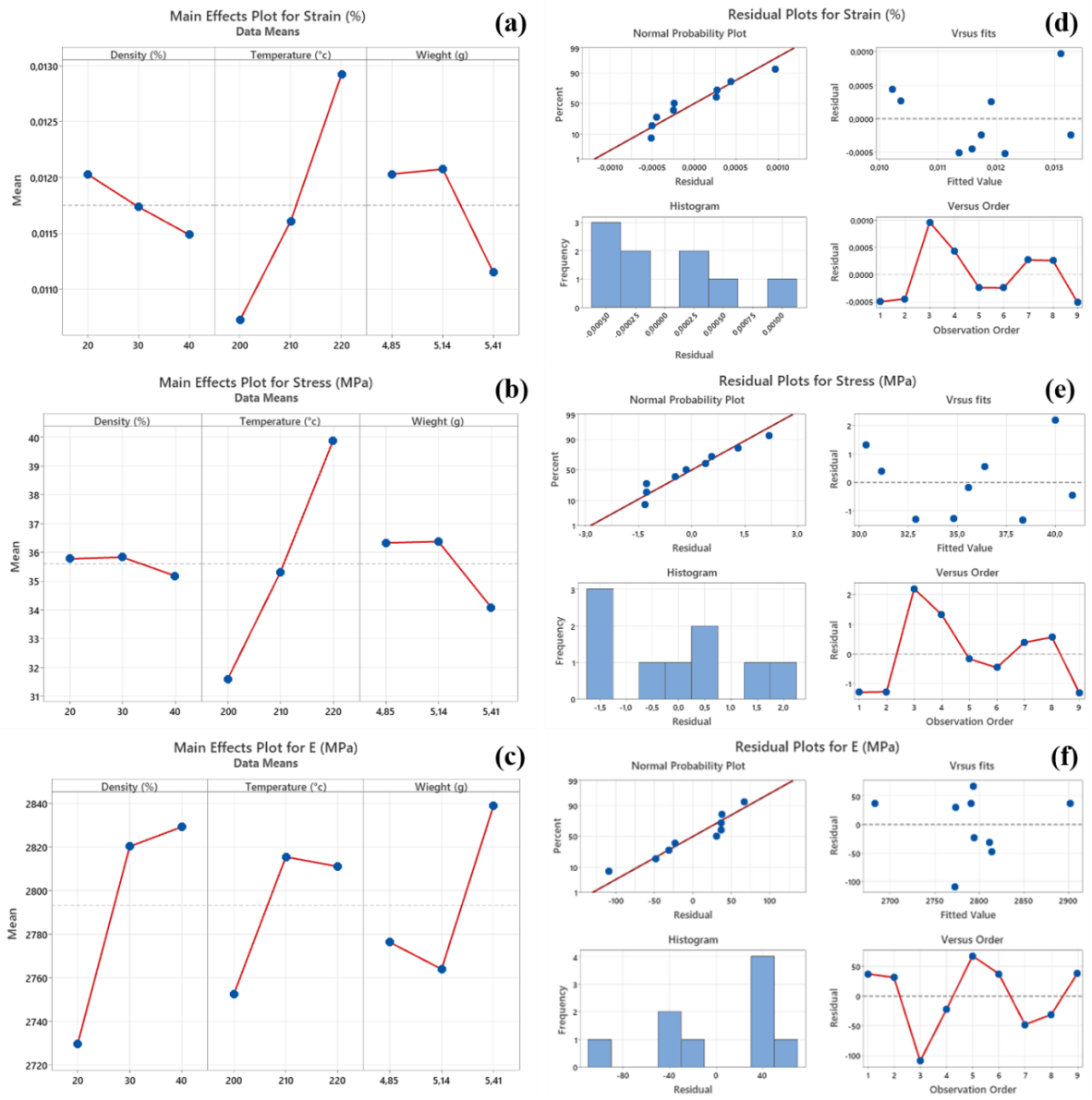


Fig. IV. 3 Taguchi main-effect plots of the three mechanical responses.

The main-effect plots confirm, in a quantitative and structured way, the qualitative trends already visible in the raw stress–strain curves of Fig. IV.1. The filling density emerges as the factor whose S/N ratio varies the most across its three levels on all three mechanical responses. The S/N ratio for the tensile stress rises monotonically from the 20 % level to the 40 % level, and the same monotonic trend is recovered on the strain and on the Young's modulus.

This result confirms that the filling density is the dominant process factor of the FDM printing window, a finding in line with prior Taguchi-based studies on FDM-printed PLA which also identified infill density as the primary factor governing tensile strength[201].

The extruder temperature exhibits a smaller S/N variation across its three levels, and its main-effect plot does not follow the monotonic pattern of the filling density. On the tensile stress and on the strain, the S/N ratio reaches its maximum at the intermediate temperature of

210 °C, which is consistent with the dual effect of the temperature already observed qualitatively in Section IV.2.2: at 200 °C the inter-layer bonding is incomplete, while at 220 °C a slight thermal degradation of the polymer chains reduces the strength and the strain at fracture. On the Young's modulus, by contrast, the S/N ratio continues to rise between 210 °C and 220 °C, which reflects the stiffening effect of the improved inter-layer bonding that is not yet offset by the thermal degradation at the elastic scale.

The specimen weight, finally, exhibits the smallest S/N variation of the three factors across all three responses. Its main-effect plot is essentially flat, which confirms the qualitative observation made in Section IV.2.2 and establishes that, at the levels investigated in the L9 matrix, the mass of the specimen does not play a statistically meaningful role in the tensile response of the printed coupons.

IV.3.2 Optimal parameter set and correlation with the experimental data

The optimal level of each factor was identified as the level associated with the largest S/N ratio on the main-effect plots of Fig. IV.3. When the three responses are considered simultaneously, the optimal combination corresponds to the highest filling density (40 %), the intermediate extruder temperature (210 °C), and a weight level whose contribution is statistically insignificant. This optimal combination is consistent with the physical interpretation developed in the preceding paragraphs: a dense raster provides a continuous load path, a moderate extrusion temperature balances inter-layer bonding against thermal degradation, and the mass of the specimen does not influence the intrinsic material response.

The Taguchi predictive model was then cross-validated against the experimental data through the computation of the correlation coefficient between the predicted and the measured responses on each of the three mechanical descriptors. The correlation coefficients obtained are reported in Table IV.1.

Table IV. 1 Correlation coefficients between the Taguchi-predicted and the experimentally measured responses of the 27 FDM-printed PLA coupons.

Mechanical response	Correlation (%)
Ultimate tensile stress	80.75
Strain at break	90.13
Young's modulus	50.83

The three correlation values tell a consistent story. The high correlation on the strain at break (90.13 %) confirms that the linear main-effect model adopted in the Taguchi framework captures the dominant trends of the deformation kinematics, which are themselves governed by a small number of first-order mechanisms (raster density, inter-layer bonding). The moderate

correlation on the tensile stress (80.75 %) indicates that part of the experimental scatter on the strength is not accounted for by the first-order main effects, and therefore suggests the presence of second-order interactions between the factors that the Taguchi analysis is not designed to resolve. The substantially lower correlation on the Young's modulus (50.83 %) points to a more fundamental limitation: The elastic modulus of an FDM-printed coupon depends on the local quality of the inter-bead contacts in a strongly non-linear way, and the linear framework of the Taguchi S/N analysis cannot capture that dependence. This limitation of linear models in FDM parameter optimisation was previously noted by Dina et al.[150] , who found that an ANN model significantly outperformed a linear mathematical model in predicting tensile strength.

This last observation motivates the artificial neural network analysis presented in the next section. The ANN model, by construction, is capable of representing non-linear interactions between the three input factors and the three mechanical responses, and should therefore deliver a better predictive accuracy than the Taguchi framework, particularly on the Young's modulus.

IV.4 Artificial neural network modelling

IV.4.1 Network architecture and training

The artificial neural network model was built in MATLAB according to the architecture described in Section II.10.3. The network follows a classical feed-forward topology with one input layer, one hidden layer and one output layer. The input vector contains the three process factors used in the L9 matrix (extruder temperature, filling density, specimen weight), and the output vector contains the three mechanical responses of interest (tensile stress, strain at break, Young's modulus). A 3 × 27 input matrix and a 3 × 27 target matrix were imported into the MATLAB neural network synthesis tool, and the network weights were fitted by supervised learning on the full experimental dataset.

The training convergence was monitored through the mean squared error (MSE) of the three outputs across successive epochs. The training, validation and testing phases converged after a small number of iterations, and the optimum was achieved at the eleventh iteration through gradient analysis, with a validation MSE of 0.00070939 a value low enough to confirm that the network had captured the dominant trends of the dataset without overfitting the residual experimental scatter. Figure IV.4 presents the training convergence history and the regression plots between the predicted and the experimental responses.

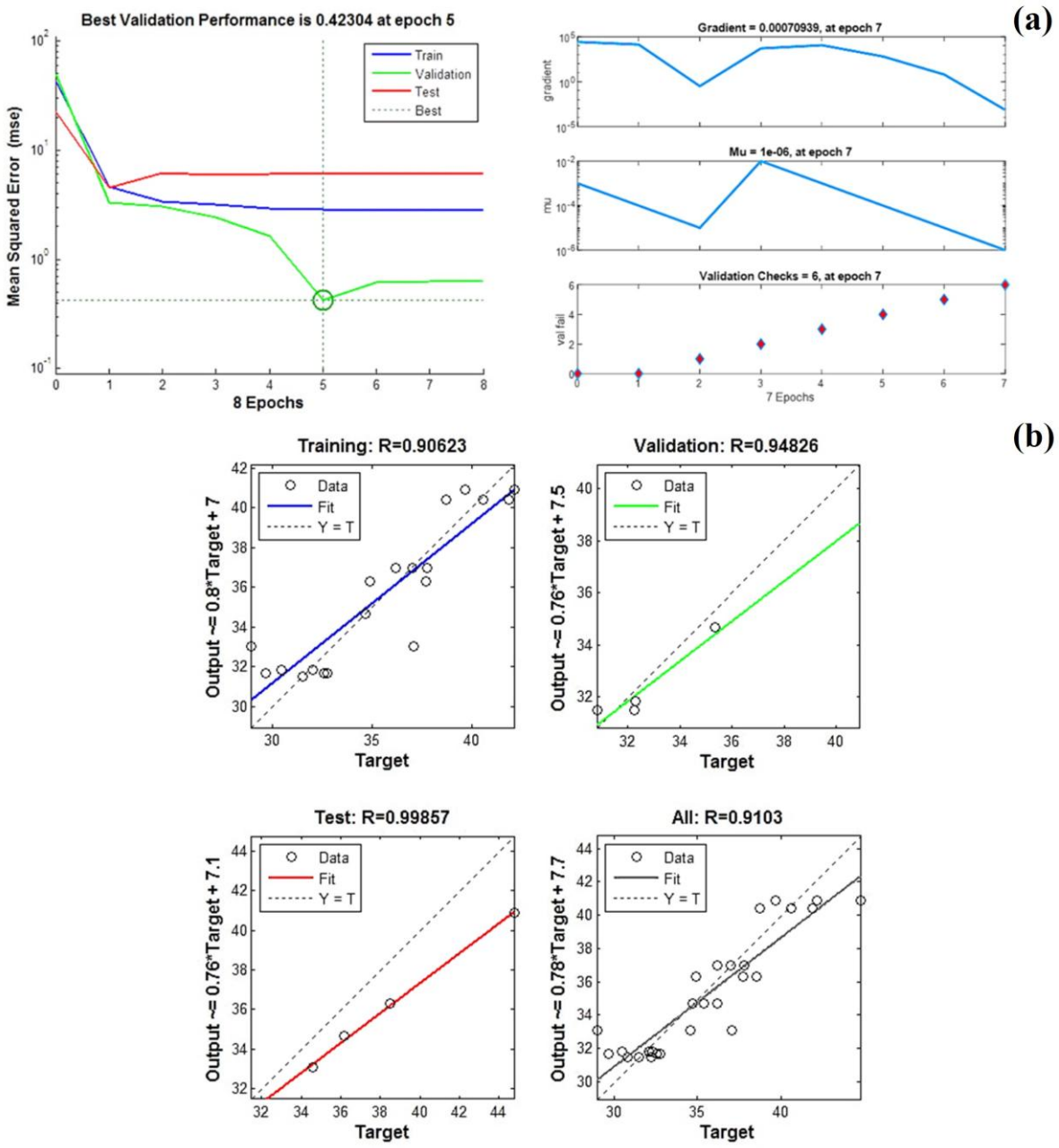


Fig. IV. 4 ANN training convergence and regression plots.

IV.4.2 Predicted versus experimental responses

The correlation coefficient obtained between the ANN-predicted responses and the experimental measurements, evaluated across the full 27-point dataset, is 91.03 %. This single correlation value, representing the overall predictive capacity of the network across all three mechanical descriptors, is consistent with the predictive accuracy reported for similar ANN architectures applied to FDM process optimization [151]. The ANN regression plots of Fig. IV.4(b) confirm that the predicted points cluster closely around the $y = x$ reference line, with no systematic bias at either end of the response range, which is the qualitative signature of a well-trained predictive model.

IV.4.3 Comparison with the Taguchi predictive model

The comparative performance of the Taguchi and the ANN predictive models on the 27-point dataset is summarised in Table IV.2.

Fig. IV. 5 Comparative predictive performance of the Taguchi signal-to-noise analysis and the artificial neural network model on the 27 FDM-printed PLA coupons.

Mechanical response	Taguchi correlation (%)	ANN correlation (%)
Ultimate tensile stress	80.75	-
Strain at break	90.13	-
Young's modulus	50.83	-
Combined output	-	91.03

Three observations follow from Table IV.2. First, the ANN correlation of 91.03 %, computed on the combined output, is of the same order as the Taguchi correlation on the strain at break (90.13 %) and substantially higher than the Taguchi correlation on the Young's modulus (50.83 %). This confirms that the ANN model delivers a more uniform predictive accuracy across the three responses than the Taguchi framework, and that its non-linear representation of the input–output relationships is particularly useful for the Young's modulus, where the Taguchi linear main-effect model had reached its resolution limit.

Second, the ANN and the Taguchi models are not redundant but complementary. The Taguchi analysis offers an interpretable factor ranking the filling density is the dominant factor, the extruder temperature plays a secondary non-monotonic role, the specimen weight is negligible that directly informs the physical reading of the dataset. The ANN model, by contrast, offers a higher-fidelity predictive surface that can be queried for parameter combinations not explicitly tested in the L9 matrix, which is useful for extrapolation but less useful for the identification of the dominant physical mechanisms. The two models therefore answer different questions on the same dataset and their joint use is more informative than either model alone.

Third, the convergence of the two models on the qualitative conclusions the filling density is the most influential factor, the optimal combination lies at the highest density and the intermediate temperature, and the specimen weight can be safely ignored establishes a robust and self-consistent picture of the FDM process-parameter window for neat PLA. This outcome constitutes the standalone contribution of the first half of this chapter and concludes the process-parameter study reported in Sections IV.2 to IV.4.

IV.5 Effect of aperture (hole) angle on FDM-PLA tensile behaviour

IV.5.1 Experimental stress–strain response

The engineering stress–strain curves obtained from the twenty-seven specimens are presented together in Fig. IV.6, grouped by aperture configuration. Three qualitative observations can be made on direct inspection of Fig. IV.6, before any numerical analysis is introduced.

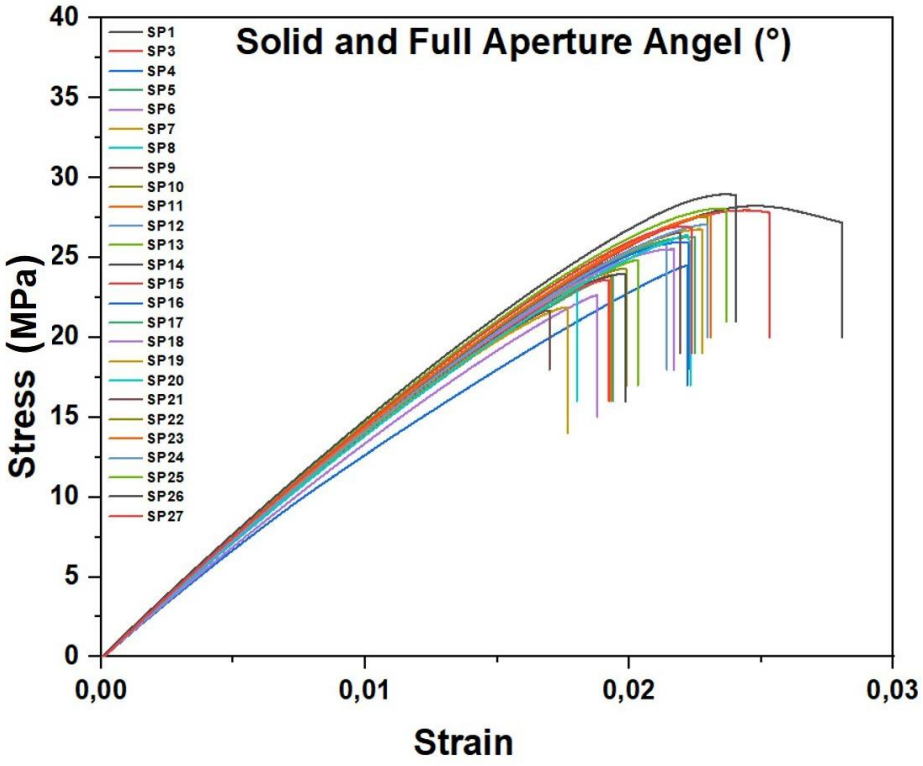


Fig. IV. 6 Stress vs strain curves of the apertured FDM-PLA specimens.

The first observation is that all twenty-seven curves share the qualitative fingerprint already identified in Section IV.2.2. The aperture orientation does not, therefore, alter the fundamental deformation mode of the material, a behaviour consistent with open-hole tensile tests on FDM-printed polymers. It modulates the position of the fracture point along the stress–strain curve without changing its shape. The aperture orientation does not, therefore, alter the fundamental deformation mode of the material it modulates the position of the fracture point along the stress–strain curve without changing its shape (Fig. IV. 7).

The second observation is that the elastic slopes of the nine configurations are remarkably similar. The curves overlay one another closely in the elastic region, up to approximately half of the ultimate load, and begin to diverge only when the material enters the yielding plateau. This qualitative observation anticipates the quantitative result that will be reported in Section IV.5.3: the apparent Young's modulus is essentially insensitive to the aperture angle, which

means that the geometric discontinuity affects primarily the post-yield behaviour and the failure point rather than the intrinsic elastic stiffness.

The third observation is that the ultimate stress reached at fracture varies clearly between the nine configurations. Some groups fracture at stress levels comparable to the solid reference, while others fracture at substantially lower stresses. The identification of the angle at which the ultimate stress reaches its minimum, and the interpretation of that minimum in terms of stress-concentration severity, is the subject of the next subsection.

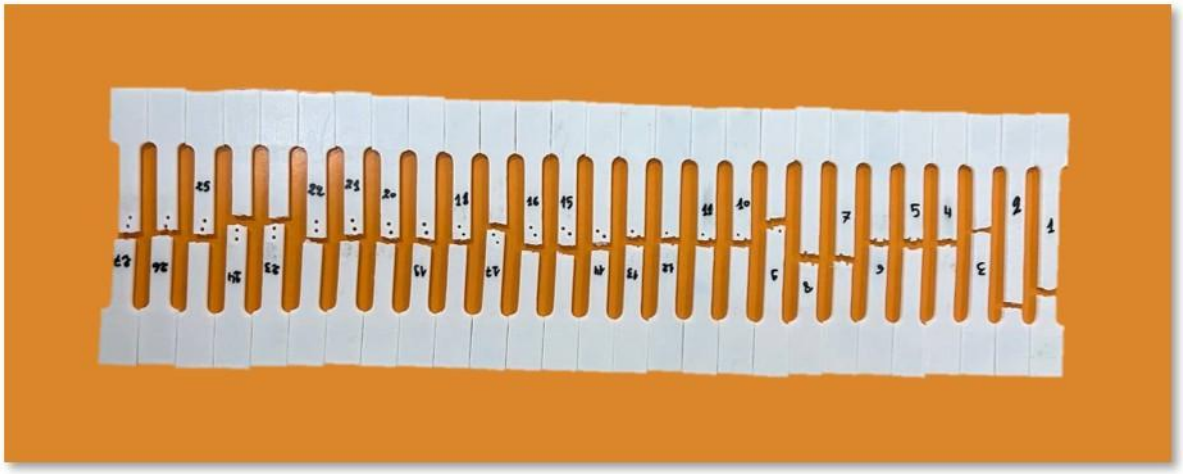


Fig. IV. 7 All 27 specimens after tensile test

IV.5.2 Maximum gross-section nominal stress ($\sigma_{nom,max}$) versus aperture angle

The mean maximum gross-section nominal stress ($\sigma_{nom,max}$) of each of the nine configurations, computed over the three replicates per group on the gross-section convention $\sigma_{nom,max}$, is reported in Table IV.3 and plotted against the aperture angle in Fig. IV. 8.

Table IV. 2 Experimental maximum gross-section nominal stress ($\sigma_{nom,max}$)for all nine configurations, n = 3 replicates per configuration. The percentage reduction is computed against the solid reference (27.23 MPa).

Aperture angle	$\sigma_{nom,1}$ (MPa)	$\sigma_{nom,1}$ (MPa)	$\sigma_{nom,1}$ (MPa)	Mean (MPa)	SD (MPa)	% Reduction (vs solid)
Solid	28.24	25.51	27.96	27.23	1.50	-
0°	24.48	23.87	22.65	23.67	0.94	13.1
15°	21.87	23.19	21.68	22.25	0.82	18.3
30°	24.12	23.92	25.94	24.66	1.11	9.4
45°	24.85	23.97	23.57	24.13	0.65	11.4
60°	25.97	26.27	25.52	25.92	0.37	4.8
75°	26.71	26.40	26.55	26.56	0.15	2.5
90°	27.55	27.65	27.08	27.42	0.30	−0.7

105°	28.07	28.95	26.92	27.98	1.01	−2.8

Three quantitative results emerge from Table IV.3 and Fig. IV. 8.

The minimum UTS is reached at θ = 15°, where the mean strength falls to 22.25 ± 0.82 MPa, approximately 18.3 % below the solid reference. This value corresponds to the most unfavourable orientation of the aperture pair relative to the loading direction. At θ = 15°, the configuration lies in the two-hole-cut regime defined in Section II.11.1 (since $15° < \theta_c \approx 23.58°$), so that the line connecting the two aperture centres lies almost perpendicular to the loading axis and the two holes are placed in close proximity along the transverse direction
The net section of the specimen is effectively reduced by the two apertures acting in parallel, and the stress risers at the aperture edges interact constructively to initiate fracture at a substantially lower far-field stress than in the solid reference [152,153].

The maximum UTS is reached at θ = 105°, where the mean strength climbs to 27.98 ± 1.01 MPa. This value is effectively identical to the solid-specimen reference (27.23 ± 1.50 MPa) within the experimental scatter, which is the notable result of the study: at certain angular configurations, the presence of the two apertures does not significantly degrade the ultimate tensile strength of the FDM-printed PLA specimen. The physical mechanism behind this recovery is that, at θ = 105°, the two apertures are positioned almost along the loading axis, so that their local stress-concentration zones do not interact with one another, and the effective load-bearing area of the specimen is close to that of the solid reference even though the configuration still lies geometrically in the one-hole-cut regime, with $A_{net} / A_0 = 0.800$.

$\sigma_{nom,max}$ varies non-monotonically with the aperture angle across the 0°–105° range. The envelope defined by the minimum at 15° (in the two-hole-cut regime) and the maximum at 105° (in the one-hole-cut regime) spans approximately 5.7 MPa, or roughly 25 % of the solid reference strength. This spread, which is markedly larger than the static geometric reduction A_net / A₀ = 0.800 of the one-hole-cut regime would predict, establishes the aperture orientation and not the net-section reduction alone as the first-order parameter governing the apparent strength of FDM-printed PLA components that must accommodate through-thickness holes.

IV.5.3 Apparent (structural) Young's modulus (E_{app}) versus aperture angle

The Young's modulus of the nine configurations, by contrast, exhibits a markedly different behaviour. The complete dataset is reported in Table IV.4.

Table IV. 3 Experimental apparent (structural) Young's modulus (E_{app})for all nine configurations, extracted from the linear regression of σ_{nom} on engineering strain over the 5–40 % $\sigma_{nom,\,max}$ range, n = 3 replicates per configuration.

Aperture angle	E_{app1} (MPa)	E_{app2} (MPa)	E_{app3} (MPa)	Mean (MPa)	SD (MPa)
Solid	1437.0	1442.2	1442.0	1440.40	2.96
0°	1308.8	1411.1	1372.4	1364.08	51.61
15°	1446.7	1483.5	1457.7	1462.64	18.87
30°	1453.1	1436.2	1435.9	1441.75	9.86
45°	1445.3	1448.0	1450.1	1447.77	2.43
60°	1448.5	1454.7	1451.5	1451.56	3.10
75°	1460.2	1408.6	1447.5	1438.76	26.86
90°	1453.2	1466.0	1445.0	1454.72	10.59
105°	1496.4	1501.4	1485.8	1494.49	7.97
Overall mean	-	-	-	1444.02	37.53

The overall average across all nine groups is E = 1444.02 ± 37.53 MPa, and the group-by-group variations around this global mean remain essentially within the standard deviation of the average itself. The Young's modulus is therefore essentially independent of the aperture angle, confirming the qualitative observation made in Section IV.5.3 that the elastic slopes of the nine stress–strain groups are closely superimposed.

This result admits a direct physical interpretation. The elastic modulus is a far-field descriptor of the material response: it is governed by the average elastic deformation of the gauge section under a small load increment, and it is therefore relatively insensitive to local stress-concentration effects that affect only a small fraction of the gauge volume. This near-constancy of the elastic modulus with varying aperture geometry is in line with recent work on perforated FDM-PLA specimens[154]. The aperture edges, while they do produce local stress amplification, do not modify the average elastic response of the specimen, which explains why the Young's modulus does not follow the aperture-angle dependence observed on the ultimate tensile strength.

The practical conclusion of the elastic analysis is that the aperture geometry affects primarily the post-yield and fracture regime of the FDM-printed PLA specimens, while leaving the elastic domain essentially untouched. This observation is of direct relevance to the design of FDM components containing holes: the choice of the aperture orientation does not alter the

stiffness of the part, and therefore does not affect its deflection under service loads, but it does determine the margin against fracture and should be optimised accordingly.

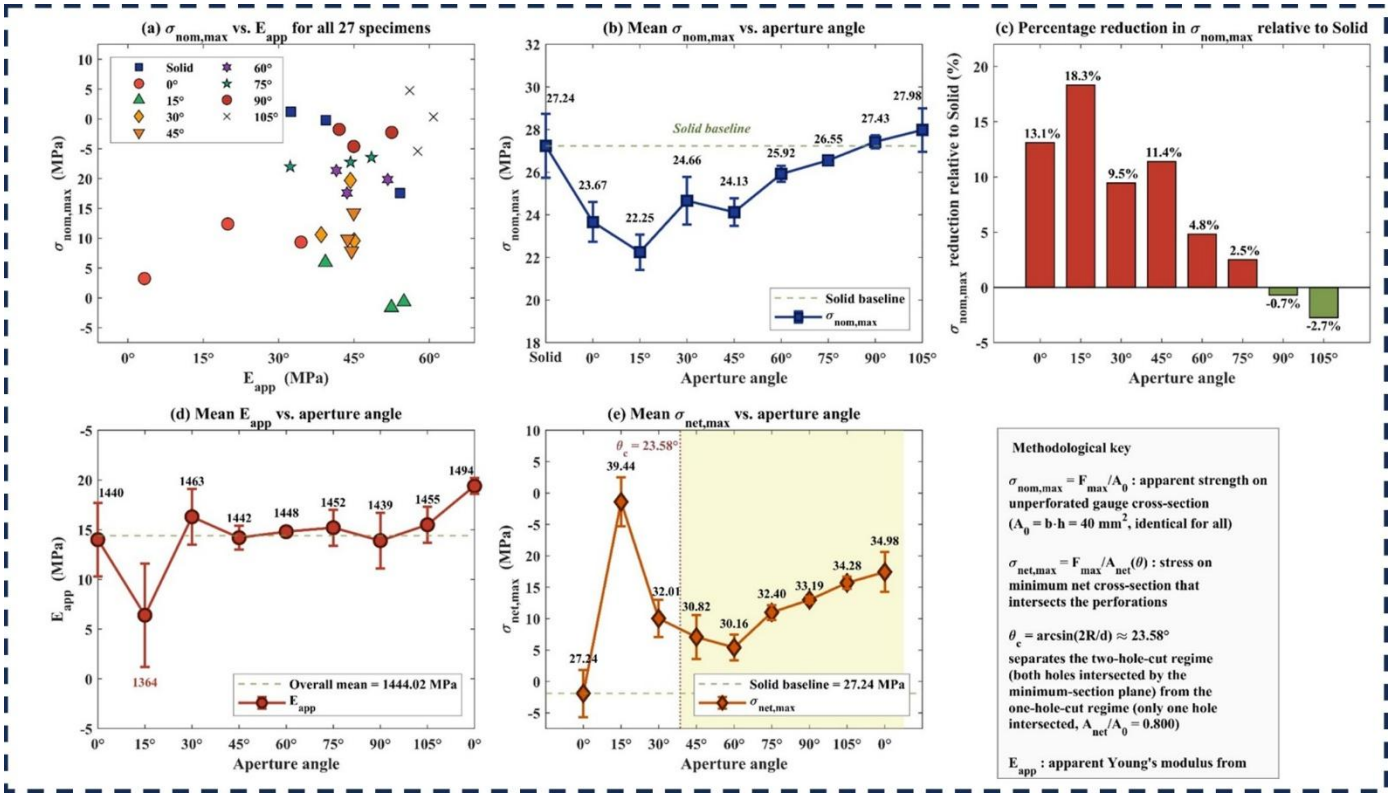


Fig. IV. 8 Comprehensive mechanical properties analysis: (a) σnom,max vs. Eapp scatter plot for all 27 specimens, (b) Mean σnom,max variation with aperture angle, (c) Percentage reduction in σnom,max relative to solid configuration, and (d) Mean Eapp variation with aperture angle.

IV.5.4 Synthesis of the experimental results

The aperture-angle study has established two complementary results that will guide the interpretation of the finite element model of Section IV.6. First, the ultimate tensile strength (gross-section convention $\sigma_{nom,max}$) of the FDM-printed PLA specimens varies non-monotonically with the aperture angle, reaching a minimum of 22.25 ± 0.82 MPa at θ = 15° (in the two-hole-cut regime) and a maximum of 27.98 ± 1.01 MPa at θ = 105° (in the one-hole-cut regime), against a solid-specimen reference of 27.23 ± 1.50 MPa. The envelope of this variation spans roughly 25 % of the reference strength. Second, the apparent Young's modulus is essentially independent of the aperture angle, with an overall average of 1444.02 ± 37.53 MPa across all nine configurations, which confirms that the aperture effect is confined to the post-yield and fracture regime.

These two observations raise a specific modelling question: can a three-dimensional finite element model of the FDM-printed PLA, calibrated on the elastic–plastic constitutive response of the material, reproduce the non-monotonic evolution of $\sigma_{nom,max}$ with the aperture angle, and can it identify the stress-concentration mechanism responsible for the minimum at 15° and the

recovery at 105°? The finite element analysis of Section IV.6.3 is designed to answer these two questions.

IV.6 ABAQUS/Explicit finite element modelling of the apertured specimens

IV.6.1 Constitutive calibration from the experimental tensile data

The full methodology of the ABAQUS/Explicit finite element model has been described in Section II.11.1. The constitutive calibration was performed on a representative specimen of each configuration the one whose UTS was closest to the group mean reported in Table IV.3 so that the model inputs reflect the central tendency of each group rather than an extreme outlier.

IV.6.2 Validation against the experimental stress–strain curves

The nine calibrated finite element simulations were run to fracture under displacement-controlled loading, and the predicted engineering stress–strain curves were compared directly to the experimental records of the corresponding representative specimens. Across all nine configurations, three observations characterise the comparison.

The most consistent agreement between the FEA and the experimental curves is observed in the elastic region, which is the expected outcome given that the elastic modulus of the model was directly calibrated from the experimental data. The elastic slopes of the simulated and measured curves overlay one another almost exactly on every configuration, and the transition from elastic to plastic behaviour occurs at the same stress level on both curves.

The agreement in the plastic region is also satisfactory across all nine configurations. The tabulated true stress – true plastic strain formulation adopted in Section II.11.1 captures the strain-hardening behaviour of FDM-printed PLA with sufficient accuracy to reproduce the peak stress within a few per cent, and the model correctly predicts the progressive increase in ductility that accompanies the rotation of the aperture angle from 0° towards 105°. The failure strains predicted by the simulations fall in the range 0.025–0.030, in close agreement with the experimentally measured values, and the extended plastic plateau observed at the 105° configuration is well reproduced by the model.

The primary discrepancies between the FEA and the experimental curves occur in the post-peak softening regime. The finite element model consistently predicts a more abrupt failure than is observed experimentally, a limitation that is well known in the literature for continuum elastic–plastic models with element-deletion damage. These models do not resolve raster anisotropy, inter-layer interfaces, or the diffuse fracture mechanisms typical of FDM-printed PLA. This discrepancy does not affect the prediction of the peak load or of the elastic response, and therefore does not undermine the use of the model for the identification of the stress-concentration mechanism, which is the primary objective of this finite element campaign.

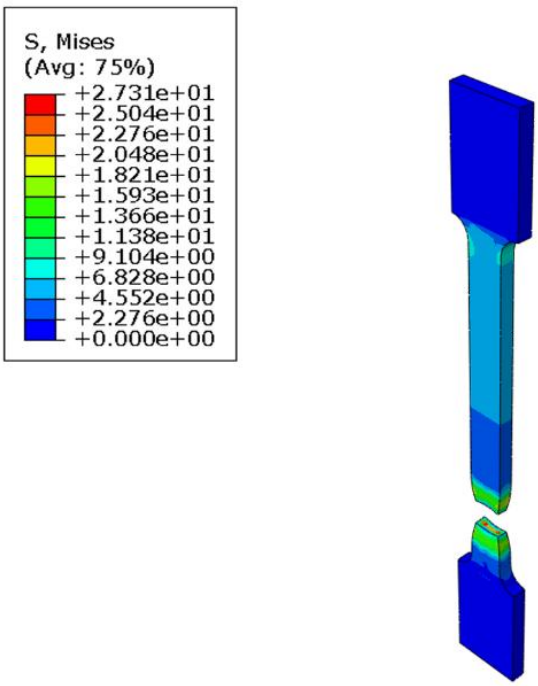


Fig. IV. 9 Finite element prediction of Von Mises stress field and fracture at $\sigma_{nom,max}$ for solid specimen.

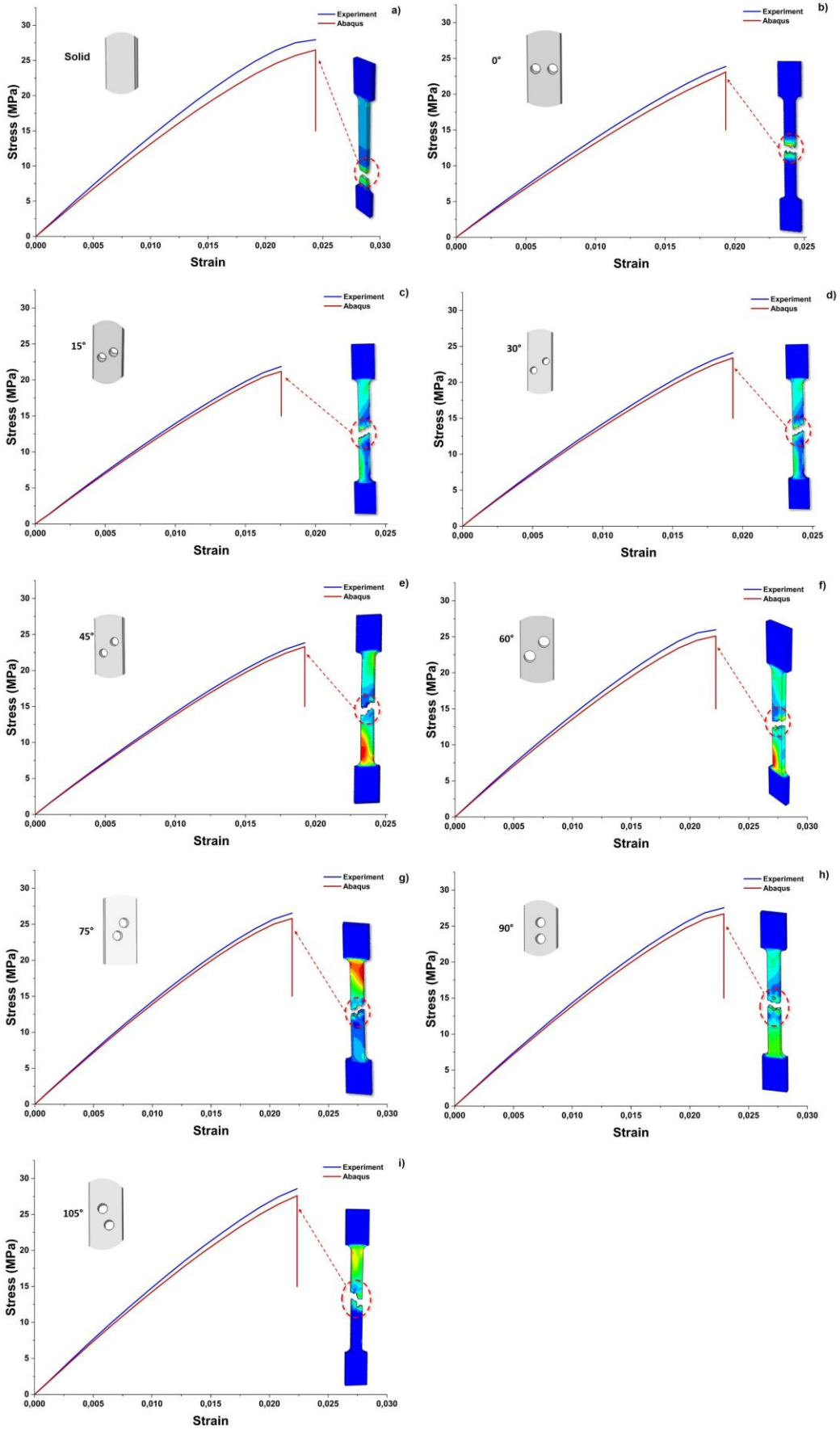


Fig. IV. 10 Finite element validation: experimental vs. simulated curves.

IV.6.3 Von Mises stress field analysis

The von Mises stress fields computed at the peak load of each simulation provide the mechanistic explanation of the angle-dependent $\sigma_{nom,max}$ trends documented in Table IV.3. Four configurations are described below to span the angular range of the study (0°, 15°, 60° and 105°), and the qualitative reading of the predicted stress fields explains the non-monotonic behaviour observed in the experimental campaign.The 0° configuration exhibits a stress concentration that is strongly localised in the narrow ligament between the two apertures. The two stress risers associated with each hole interact constructively across this ligament, producing a high-stress band that lies perpendicular to the loading direction. This band corresponds to the most direct fracture path through the net section of the specimen, and it explains the 13.1 % reduction in UTS relative to the solid reference reported in Table IV.3.

The 15° configuration intensifies the mechanism identified at 0°. The small rotation of the aperture pair brings the two stress-concentration zones closer together along the transverse direction, while also reducing the effective net section available to sustain the load. The constructive interaction between the two stress risers reaches its maximum at this angle, which lies just below the threshold $\theta_c \approx 23.58°$ of the two-hole-cut regime, and the predicted high-stress band is both narrower and more intense than at 0°. This is the mechanistic explanation for the global UTS minimum of 22.25 MPa observed experimentally.

The 60° configuration illustrates the progressive transition from a concentrated stress field to a more distributed one. The rotation of the aperture pair shifts the high-stress region away from the narrow ligament between the holes and towards an inclined band connecting the two aperture peripheries. The stress risers no longer interact constructively at a single cross-section, and the load path can redistribute around the holes, which reduces the severity of the local stress amplification and explains the recovery of $\sigma_{nom,max}$ to within 5 % of the solid reference.

The 105° configuration completes the mechanistic picture. At this angle, the two apertures lie almost along the loading axis, and the stress risers associated with each hole develop independently of one another. The local high-stress regions are spatially separated and do not form a continuous fracture path through the net section. The effective load-bearing area of the specimen is therefore close to that of the solid reference, and the predicted UTS is marginally higher than the solid-specimen reference a counter-intuitive result that becomes understandable in the light of the von Mises contours, because the local plastic deformation around each aperture acts as a small energy-dissipation zone that delays the onset of catastrophic failure. A similar recovery of apparent strength for staggered hole configurations was reported by Khosravani & Reinicke [155] for open-hole polymer plates.

Taken together, the four configurations described above provide the mechanistic explanation of the non-monotonic $\sigma_{nom,max}$ evolution reported in Table IV.3: the severity of the stress concentration, and not the net-section reduction alone, is the first-order parameter governing the apparent strength of the FDM-printed PLA specimens with angled apertures.This interpretation is consistent with Digital Image Correlation (DIC) analyses of strain fields in geometrically discontinuous FDM parts[210]. The finite element model therefore answers the two questions posed at the end of Section IV.5.4 in the affirmative: it reproduces the non-monotonic evolution of $\sigma_{nom,max}$ with the aperture angle within the experimental scatter, and it identifies the stress-concentration mechanism responsible for both the minimum at $\theta = 15°$ and the recovery at $\theta = 105°$.

IV.7 Conclusion

This chapter investigated the mechanical response of FDM-printed PLA through two complementary studies. The first, a 27-point Taguchi L9 campaign analysed by signal-to-noise ratios and an artificial neural network, established the filling density as the dominant process parameter and the extruder temperature as a secondary, non-monotonic factor, with the ANN model reaching a combined correlation of 91.03 %. The second study examined paired through-thickness circular apertures across nine angular orientations (0° to 105°). The ultimate tensile strength varied non-monotonically with the aperture angle, from a minimum of 22.25 ± 0.82 MPa at 15° (two-hole-cut regime) to a maximum of 27.98 ± 1.01 MPa at 105° (one-hole-cut regime), against a solid reference of 27.23 ± 1.50 MPa, while the apparent Young's modulus remained essentially constant at approximately 1444 MPa. An ABAQUS/Explicit model corroborated the experiments and identified the severity of the local stress concentration, not the net-section reduction alone, as the first-order mechanism governing the angle-dependent strength, in agreement with recent open-hole FDM-PLA studies. Together, the two studies consolidate a rigorous process–property understanding and a calibrated elastic–plastic protocol on which the sandwich-bending simulations of the next chapter rest.

Chapter V

Sandwich panels: mechanical performance, energy absorption and finite element simulation

V.1 Introduction

This chapter reports the mechanical and numerical characterisation of the sandwich panels assembled in Section II.7 from the hybrid Typha/Agave/epoxy face sheets and the FDM-printed cores of neat PLA and PLA/flax bio composite. The chapter integrates five complementary analyses on the same specimen population: a tensile campaign on the three constituent materials of the sandwich (Section V.2), a three-point bending campaign on the assembled panels with the three core geometries (Section V.3), a quantitative analysis of the energy-absorption behaviour (Section V.4), a non-parametric statistical evaluation of the inter-geometry differences through the Kruskal–Wallis test and its Dunn post-hoc pairwise comparisons (Section V.5), and a finite element validation of the flexural response in ABAQUS/CAE Standard (Section V.6). Section V.7 closes the chapter with a synthesis of the operational conclusions.

The chapter is the culminating point of the experimental programme of this thesis: it combines the lignocellulosic fibres characterised in Chapter III, the FDM-printed PLA whose process window was fixed in Chapter IV, and the manufacturing chain described in Chapter II, into a single structural artefact whose performance can be assessed against the engineering requirements of lightweight sandwich applications.

V.2 Tensile behaviour of the sandwich constituents

V.2.1 Test matrix

The tensile response of the three constituent materials of the sandwich was measured on a common ASTM D618 dog-bone geometry, so that the three systems could be compared on a strictly equal footing. The three material systems investigated are the neat PLA filament printed by FDM, the PLA/flax biocomposite filament printed under identical FDM parameters, and the hybrid Typha/Agave/epoxy laminate sectioned by CNC machining from the cured face-sheet panels of Section II.5. At least three replicates were tested for each material system, in accordance with the protocol described in Section II.8.1.

V.2.2 Stress–strain response

The engineering stress–strain curves of the three material systems are presented together in Fig. V.1. The three curves exhibit qualitatively distinct deformation signatures that reflect their different internal architectures, and the ultimate tensile strengths and elongation-at-break values recorded in the campaign are summarised in Table V.1.

Table V. 1 Tensile properties of the three sandwich constituents (ASTM D618).

Material	UTS (MPa)	Elongation at break (%)
Hybrid Typha/Agave/epoxy laminate	87.6	6.2
Neat PLA (FDM)	47.3	brittle (≈ 1.5–2.0)
PLA/flax (FDM)	40.5	+52 % plastic deformation vs neat PLA

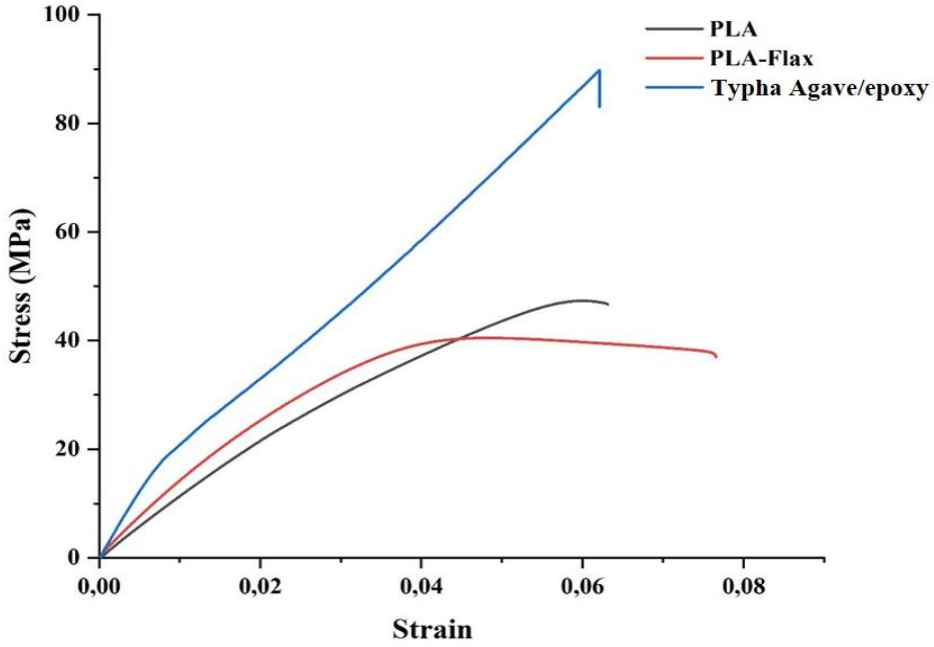


Fig. V. 1 Tensile stress–strain responses of neat PLA, PLA/flax biocomposite and Typha/Agave/epoxy hybrid laminate under ASTM D618 testing conditions.

V.3 Three-point bending of the sandwich panels

V.3.1 Flexural response by core geometry

The flexural behaviour of the six sandwich configurations three core geometries (honeycomb, circular, tri-grid) × two core materials (neat PLA, PLA/flax) was characterised in three-point bending according to the protocol of Section II.8.2. The maximum bending stresses recorded for each configuration at peak load are compiled in Table V.2, and the corresponding load–deflection curves are presented in Fig. V.2.

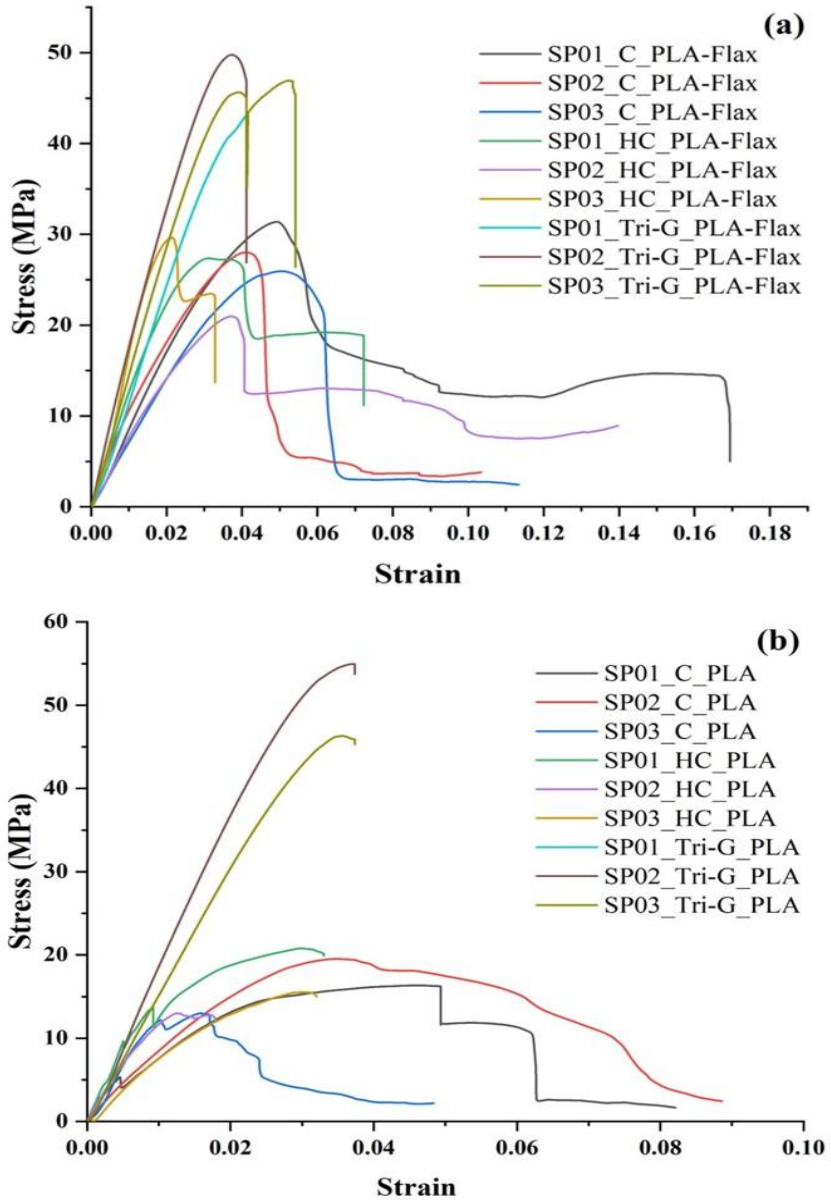


Fig. V. 2 Load–deflection response of the six sandwich configurations in three-point bending: (a) neat PLA cores with three core geometries (honeycomb, circular, tri-grid); (b) PLA/flax biocomposite cores with the same three core geometries.

Table V. 2 Maximum bending stress of the six sandwich configurations in three-point bending (ASTM C393).

Core material	Honeycomb (MPa)	Circular (MPa)	Tri-grid (MPa)
Neat PLA	20.79	19.52	**54.97**
PLA/flax	29.62	31.38	**49.77**

Two non-trivial observations emerge from the direct comparison of the six configurations in Table V.2, and together they structure the discussion that will follow in the three next subsections.

The first observation is the overwhelming superiority of the tri-grid core geometry for both core materials. For neat PLA, the tri-grid core reaches a peak bending stress of 54.97 MPa, which represents a 164 % increase over the honeycomb configuration (20.79 MPa) and a 182 % increase over the circular configuration (19.52 MPa). For PLA/flax, the tri-grid core reaches 49.77 MPa, which represents a 68 % increase over the honeycomb (29.62 MPa) and a 58 % increase over the circular configuration (31.38 MPa). The tri-grid topology is therefore confirmed as the most efficient core architecture across both material systems, and its mechanical advantage admits a clear structural interpretation: the interconnected struts of the tri-grid disperse the applied stresses through redundant load paths, which delays the onset of crack propagation and prevents the localisation of damage at any single cell wall. The honeycomb architecture, by contrast, relies on the controlled buckling of its hexagonal cells to balance stiffness against energy absorption, and its peak stress is therefore lower than that of the tri-grid but its response remains structured and predictable. The circular architecture exhibits stress concentrations at the void edges and therefore underperforms the two other geometries in the neat PLA case, although it recovers part of its competitiveness in the PLA/flax case (31.38 MPa against 29.62 MPa for honeycomb), where the flax reinforcement mitigates the severity of the local stress concentrations.A comparable influence of core topology on load distribution and failure initiation has been reported in studies on 3D-printed sandwich structures with various cellular architectures[140].

The second observation is the non-trivial effect of the core material on the ranking of the three geometries. For neat PLA, the ranking is tri-grid >> honeycomb ≈ circular, with honeycomb marginally exceeding circular by 6 %. For PLA/flax, the ranking rearranges to tri-grid >> circular > honeycomb, with circular now exceeding honeycomb by 5.6 %. The presence of the flax reinforcement therefore inverts the relative performance of the honeycomb and circular configurations: the circular geometry, which suffers from stress concentrations in the neat PLA case, benefits disproportionately from the micro-crack deflection mechanism introduced by the flax fibres, and its performance overtakes that of the honeycomb. This inversion which will be revisited in the energy-absorption analysis of Section V.4 reveals that the choice of the optimal core geometry cannot be made independently of the core material, and that the material–geometry coupling is itself a first-order design parameter of the sandwich panel.

In quantitative terms, the comparison between the neat PLA and the PLA/flax systems reveals that the PLA/flax cores sacrifice 9.5 % of the peak bending stress in the tri-grid

configuration (54.97 → 49.77 MPa), but they recover that loss and more through the substantial enhancement of the bending response of the honeycomb (+42 %, from 20.79 to 29.62 MPa) and of the circular (+61 %, from 19.52 to 31.38 MPa) configurations. The PLA/flax biocomposite therefore delivers a more balanced flexural performance across the three geometries than neat PLA does, at the cost of a modest reduction in the peak stress of the best-performing tri-grid configuration. Comparable observations regarding the influence of core topology on load distribution have been reported in studies on 3D-printed sandwich structures[101,102] .The detailed analysis of the core shear stress, the flexural modulus, and the failure modes of the six configurations is the subject of the two next subsections.

V.3.2 Core shear stress and flexural modulus

Beyond the peak bending stresses reported in Section V.3.1, two additional mechanical descriptors were extracted from the load–deflection records of the three-point bending campaign: the core shear stress τ, computed from Eq. (II.4), and the apparent flexural modulus E, computed from Eq. (II.5). These two descriptors characterise the load-bearing response of the sandwich panels more directly than the peak bending stress alone, because they isolate the shear contribution of the core and the stiffness contribution of the composite system from the geometrical effects of the testing configuration.

Material-level comparison. At the material level, averaged across the three core geometries, the PLA/flax cores consistently outperform the neat PLA cores on both descriptors. The PLA/flax cores exhibit an average core shear stress of 3.63 MPa against 2.46 MPa for neat PLA, which corresponds to a 48 % improvement, and an average flexural modulus of 1.04 GPa against 0.78 GPa, which corresponds to a 34 % improvement. Both enhancements are attributed to the flax-induced micro-crack deflection mechanism already invoked in the tensile analysis of Section V.2, which improves the damage tolerance of the core without compromising its structural integrity.

Geometry-level comparison. At the geometry level, the tri-grid core delivers the highest values of both descriptors across both material systems. The peak values, recorded on the PLA/flax tri-grid specimens, are τ = 5.27 MPa and E = 1.53 GPa, which exceed the honeycomb configuration by 68 % and 38 %, respectively, and the circular configuration by 60 % and 139 %. The origin of this superiority is the interconnected strut architecture of the tri-grid, which redistributes the applied stresses across multiple redundant load paths and delays the localisation of failure at any single cell wall. The mass cost of this architecture is modest a 15 to 20 % mass increase relative to the honeycomb designs and the mass-normalised descriptors

remain competitive, with the PLA/flax tri-grid delivering 2.1× higher τ/mass and 1.8× higher E/mass than the neat PLA alternatives.

Intermediate geometries. The honeycomb cores occupy an intermediate position in the ranking. They deliver a moderate but consistent stiffness, with an average flexural modulus of 1.00 GPa in the PLA/flax case, although their shear stress variability reaches ±29 % in the neat PLA specimens, which indicates a less reliable response in the unreinforced material. The circular cores, by contrast, consistently underperform the other two geometries: stress concentrations at the void interfaces dominate their mechanical response, and in the neat PLA configuration the flexural modulus falls below 0.56 GPa, the lowest value recorded in the six-configuration matrix.

Scatter and reliability. The statistical reliability of the six configurations follows the same ordering as their mean performance. The PLA/flax tri-grid cores exhibit the lowest property scatter of the campaign, with relative standard deviations of ±3 % on the shear stress and ±16 % on the flexural modulus, which confirms the highly reproducible response of this configuration. At the opposite end, the neat PLA circular cores exhibit the highest scatter, with ±43 % on the flexural modulus, which reflects the combined effect of the stress concentrations at the void interfaces and the absence of the stabilising flax reinforcement. These reliability trends correlate directly with the failure modes documented in Section V.3.3: the high-τ configurations (tri-grid, honeycomb) fail predominantly in core shear, whereas the low-τ circular configurations tend to fail through face-sheet debonding, which is both more variable and more damaging to the overall structural response. This correlation between failure mode and property scatter is a recognised feature of cellular core architectures[103].

Design synthesis. The PLA/flax tri-grid combination emerges as the single most efficient configuration of the six tested. Its specific properties τ/mass = 0.049 $MPa \cdot g^{-1}$ and E/mass = 0.014 $GPa \cdot g^{-1}$ exceed those of conventional honeycomb structures by more than 50 % on an energy-absorption-per-unit-mass basis, which positions this configuration as a credible candidate for lightweight crashworthy components in automotive and aerospace applications.

V.3.3 Interface integrity and failure modes

The interface between the hybrid Typha/Agave/epoxy face sheets and the FDM-printed cores was not separately instrumented during the three-point bending campaign, but its integrity can be inferred from the failure modes observed during testing. Across the six configurations, the dominant failure mechanism was core shear rather than interfacial debonding, which is the qualitative signature of a sufficiently strong adhesive bond between the face sheets and the core.

In no configuration did the panels separate at the face-sheet/core interface before the core itself reached its shear strength.

Two concurrent mechanisms account for this interfacial robustness. The first is the intrinsic micro-textured surface generated by the layer-by-layer FDM printing process, which produces a corrugated topography at the core surface whose peak-to-valley amplitude is commensurate with the thickness of a single extruded bead. This micro-texture enhances the mechanical interlocking between the polyurethane adhesive and the core surface, and it provides a distributed anchoring of the face sheet that is more resistant to peel loading than a smooth bonding surface would be. The second mechanism is the choice of a polyurethane adhesive compatible with both the thermoplastic PLA of the core and the thermoset epoxy of the face sheet. The polyurethane forms a compliant interphase between the two rigid adherends, which accommodates the stiffness mismatch between the core and the face sheet without generating the interfacial stress peaks that would otherwise drive premature debonding.

The correlation between failure mode and shear-stress ranking identified in Section V.3.2 is consistent with this interpretation. The high-τ configurations the tri-grid and the honeycomb failed predominantly in core shear because the interfacial bond remained stronger than the core cells themselves, and the progressive collapse of the core walls absorbed the applied energy before the adhesive interface was mobilised. The low-τ circular configurations, by contrast, reached their peak load at a lower applied force, and the stress concentrations at the void interfaces generated local peel loading at the adhesive edge that triggered face-sheet debonding before the core had fully developed its shear resistance. The failure mode of the sandwich panel is therefore governed not only by the intrinsic strength of the core but also by the ratio between the core shear strength and the peel strength of the adhesive interface.

V.4 Energy absorption analysis

V.4.1 Analytical and numerical integration

The energy absorption capacity of the six sandwich configurations was quantified on the load–deflection records of Section V.3 through two complementary integration routes, following the definitions introduced in Section II.8.3. The numerical route used trapezoidal integration (Eq. II.6, here denoted Utrapz) to compute the area under the load–deflection curve, while the analytical route used the closed-form approximation of Eq. (II.7) (here denoted Uvol) as a fast comparative descriptor. The close agreement between the two routes across the six configurations confirmed the robustness of the extracted energy-absorption values, and it justified the use of the closed-form approximation for the comparative analysis that follows.

V.4.2 Energy absorption by core material and geometry

The mean energy absorption per unit volume of the six configurations is reported in Table V.3 and Fig. V. 3. For the neat PLA cores, the ranking from lowest to highest is circular (0.74 ± 0.41) < honeycomb (0.83 ± 0.33) < tri-grid (1.47 ± 0.23) MJ·m^{-3}. The tri-grid configuration outperforms the honeycomb by 77 % and the circular by 99 %, which is consistent with the flexural ranking of Section V.3.1 and reflects the role of the interconnected struts in sustaining progressive deformation before the onset of catastrophic failure.

Table V. 3 Mean energy absorption per unit volume of the six sandwich configurations (MJ·m^{-3}).

Core material	Honeycomb	Circular	Tri-grid
Neat PLA	0.83 ± 0.33	0.74 ± 0.41	**1.47 ± 0.23**
PLA/flax	1.19 ± 0.47	**1.71 ± 0.89**	1.52 ± 0.23

The ranking of the PLA/flax configurations, however, departs markedly from that of the neat PLA cores and delivers the most striking result of the energy-absorption analysis. For the PLA/flax cores, the ranking from lowest to highest is honeycomb (1.19 ± 0.47) < tri-grid (1.52 ± 0.23) < circular (1.71 ± 0.89) MJ·m^{-3}. The circular geometry, which was the weakest performer in the neat PLA case, becomes the best performer in the PLA/flax case, and it outperforms the tri-grid by 12 % and the honeycomb by 44 %. This is a counter-intuitive result: the geometry whose stress concentrations were the limiting factor in the unreinforced material becomes the dominant configuration once the flax reinforcement is introduced. The PLA/flax circular core also represents a 131 % increase in energy absorption over its neat PLA counterpart (1.71 vs 0.74 MJ·m^{-3}), which is the largest material-induced enhancement observed in the campaign.

The inversion admits a mechanistic interpretation consistent with the flax-induced mechanisms invoked elsewhere in this chapter. In the neat PLA case, the voids of the circular cells act as stress concentrators whose effect is not mitigated by any secondary toughening mechanism, and the energy absorption is limited by the early crack initiation at the void edges. In the PLA/flax case, the flax fibres act as crack arrestors: they deflect the crack tips propagating from the void edges into the surrounding raster, they bridge the newly formed crack faces, and they localise the microcracks into a diffuse damage field that absorbs energy over a larger volume of the core. The circular geometry, whose voids are the nucleation sites of the crack population, therefore benefits disproportionately from the flax toughening,the role of natural fibre reinforcement in enhancing the damage tolerance and energy dissipation of PLA-based cores has similarly been established by Shahkarami & Zeinedini [104] and Kamarian et al[113].

The honeycomb configuration, by contrast, delivers only a moderate enhancement in the PLA/flax case (1.19 MJ·m⁻³, against 0.83 MJ·m⁻³ for neat PLA). Its PLA/flax version exhibits a heightened buckling susceptibility under asymmetric loading, which partially offsets the toughening contribution of the flax fibres. The tri-grid, finally, maintains a consistent performance across both materials (1.47 MJ·m⁻³ in neat PLA, 1.52 MJ·m⁻³ in PLA/flax), which is itself a useful design feature: the tri-grid delivers a predictable energy-absorption response that is largely insensitive to the core material, and its absolute value places it above the honeycomb configuration in both material systems.

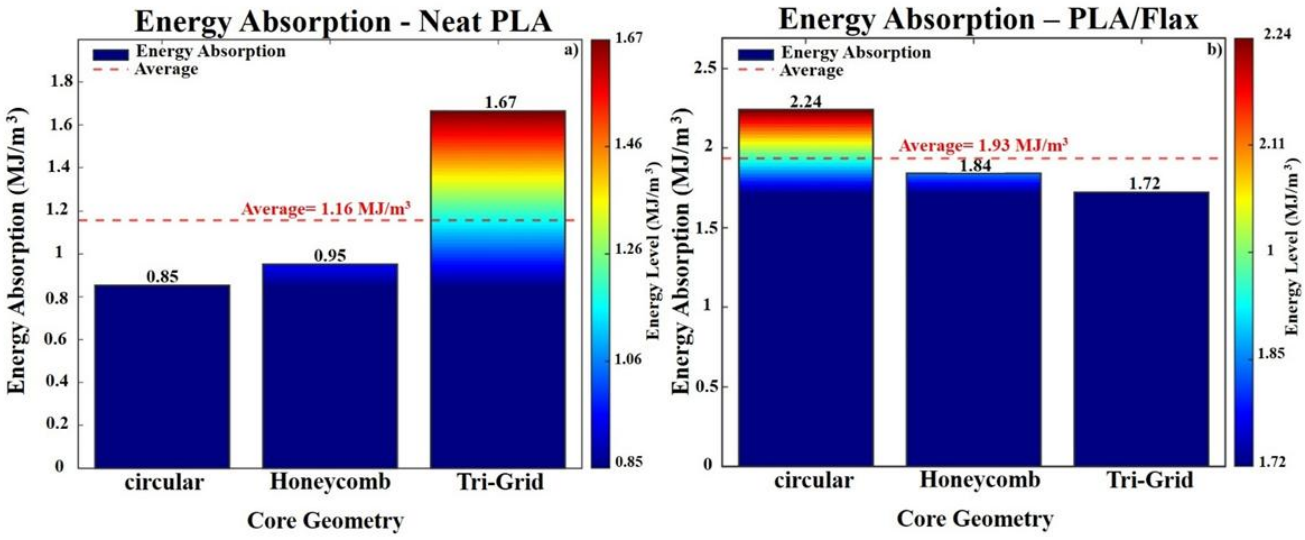


Fig. V. 3 Energy absorption per unit volume of the six sandwich configurations, grouped by core material and core geometry.

V.4.3 Specific energy absorption (SEA)

The specific energy absorption (Fig.V.4), defined as the total energy absorption normalised by the mass of the panel (Eq. II.9), provides a mass-efficient comparison between configurations whose densities differ substantially. Within the six-configuration matrix, the PLA/flax cores systematically outperform the neat PLA cores in EA terms, although their SEA values are partly moderated by their higher mass.

The single best-performing specimen of the entire campaign was identified within the PLA/flax circular group, denoted SP01. This specimen delivered an energy absorption of 2.7526 MJ·m⁻³, which corresponds to an absorbed energy of approximately 234 J and a specific energy absorption of approximately 3.44×10^3 J·kg⁻¹. The outperformance of SP01 is a direct expression of the flax-toughened circular geometry mechanism described in Section V.4.2: the combination of a high density of void nucleation sites (circular geometry) and a strong crack-

arrest mechanism (flax reinforcement) produces, in this specimen, the most efficient energy-absorption pathway of the campaign.

Within the honeycomb family, the PLA/flax variants reach values up to 1.5627 MJ·m^{-3}, against ≤ 1.1698 MJ·m^{-3} for the neat PLA counterparts, but their higher cell-wall mass depresses the SEA below that of the best circular cores. Within the tri-grid family, the PLA/flax cores reach values up to 1.7219 MJ·m^{-3}, which is the highest value of any neat PLA configuration (≈ 1.60 MJ·m^{-3}), but the tri-grid's heavier strut architecture places its SEA in the mid-range of the campaign.

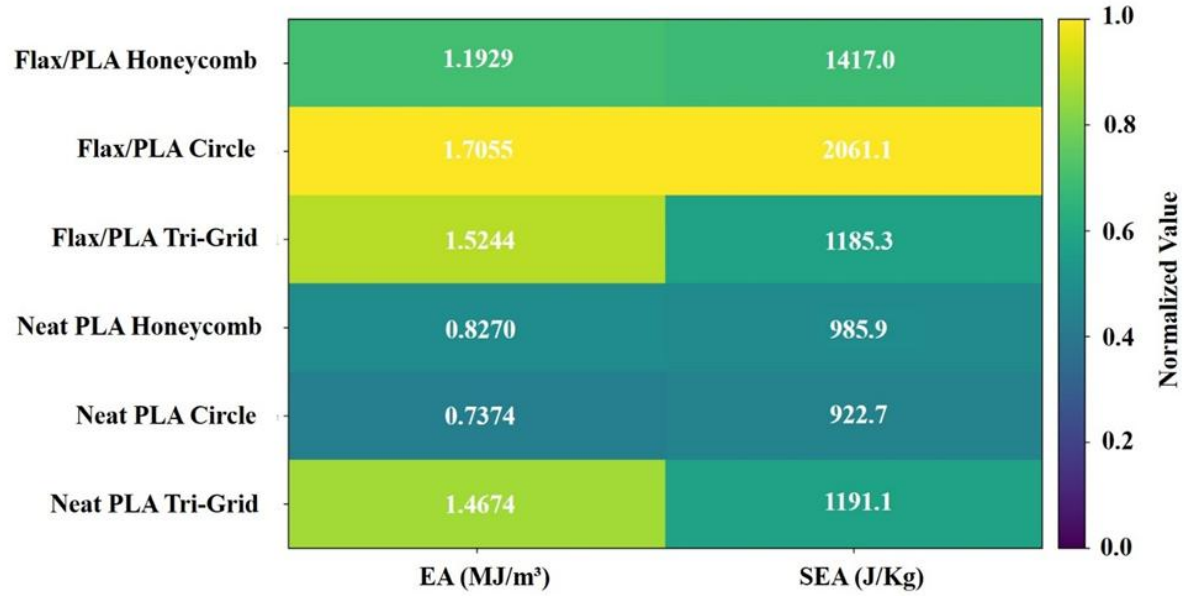


Fig. V. 4. Specific energy absorption (SEA) of the six sandwich configurations.

V.4.4 Mechanistic synthesis

The energy-absorption analysis therefore delivers three synthesis points that will guide the design recommendations of Section V.7. First, the tri-grid configuration offers the most consistent and material-independent energy-absorption response, with values clustered around 1.5 MJ·m^{-3} for both neat PLA and PLA/flax cores. Second, the circular configuration offers the highest absolute energy absorption, but only when combined with the PLA/flax biocomposite (1.71 ± 0.89 MJ·m^{-3}), and its performance is strongly material-dependent. Third, the honeycomb configuration occupies a middle ground in the energy-absorption ranking and represents the most conservative design choice when reliability is the primary objective. The subsequent statistical analysis of Section V.5 will quantify the significance of these inter-geometry differences through the Kruskal–Wallis framework.

V.5 Statistical analysis of the mechanical performance

The mechanical-testing campaigns described in Sections V.3 and V.4 produced small-sample datasets (typically n = 3 replicates per configuration), on which parametric tests such as one-way ANOVA could not be safely applied without first verifying the normality of the residuals and the homogeneity of the inter-group variances. The non-parametric Kruskal–Wallis test, introduced methodologically in Section II.9, was therefore retained as the primary inferential tool for the comparison of the three core geometries on the three mechanical descriptors of interest: the core shear strength τ, the apparent flexural modulus E, and the energy absorption EA. Where the Kruskal–Wallis test identified a significant overall difference between the three geometries, post-hoc pairwise comparisons were performed through Dunn's test with Bonferroni correction in order to identify which specific geometry pairs were responsible for the detected differences.

V.5.1 Kruskal–Wallis analysis

The Kruskal–Wallis test was applied independently to each of the three mechanical descriptors, using the three core geometries (honeycomb, circular, tri-grid) as the grouping variable. The analysis was further stratified by core material, so that the neat PLA and the PLA/flax datasets were tested separately, in accordance with the methodology laid out in Section II.9. The test statistics H, the associated p-values, and the group means and standard deviations are compiled in Table V.4, and the corresponding box-plot visualisations are presented in Fig. V.5.

Table V. 4 Kruskal–Wallis analysis of the mechanical properties of the sandwich panels.

Property	Material	Honeycomb (Mean ± SD)	Circle (Mean ± SD)	Tri-grid (Mean ± SD)	H-value	P-value
τ (MPa)	Flax/PLA	2.75 ± 0.48	3.01 ± 0.29	5.12 ± 0.15	11.453	0.003
	Neat PLA	1.60 ± 0.53	1.72 ± 0.34	4.93 ± 0.90		
E (GPa)	Flax/PLA	1.00 ± 0.24	0.78 ± 0.12	1.31 ± 0.22	9.785	0.008
	Neat PLA	0.83 ± 0.12	0.56 ± 0.16	0.94 ± 0.04		
EA (MJ/m³)	Flax/PLA	1.19 ± 0.49	1.71 ± 0.91	1.52 ± 0.23	5.514	0.043
	Neat PLA	0.83 ± 0.33	0.74 ± 0.42	1.47 ± 0.23		

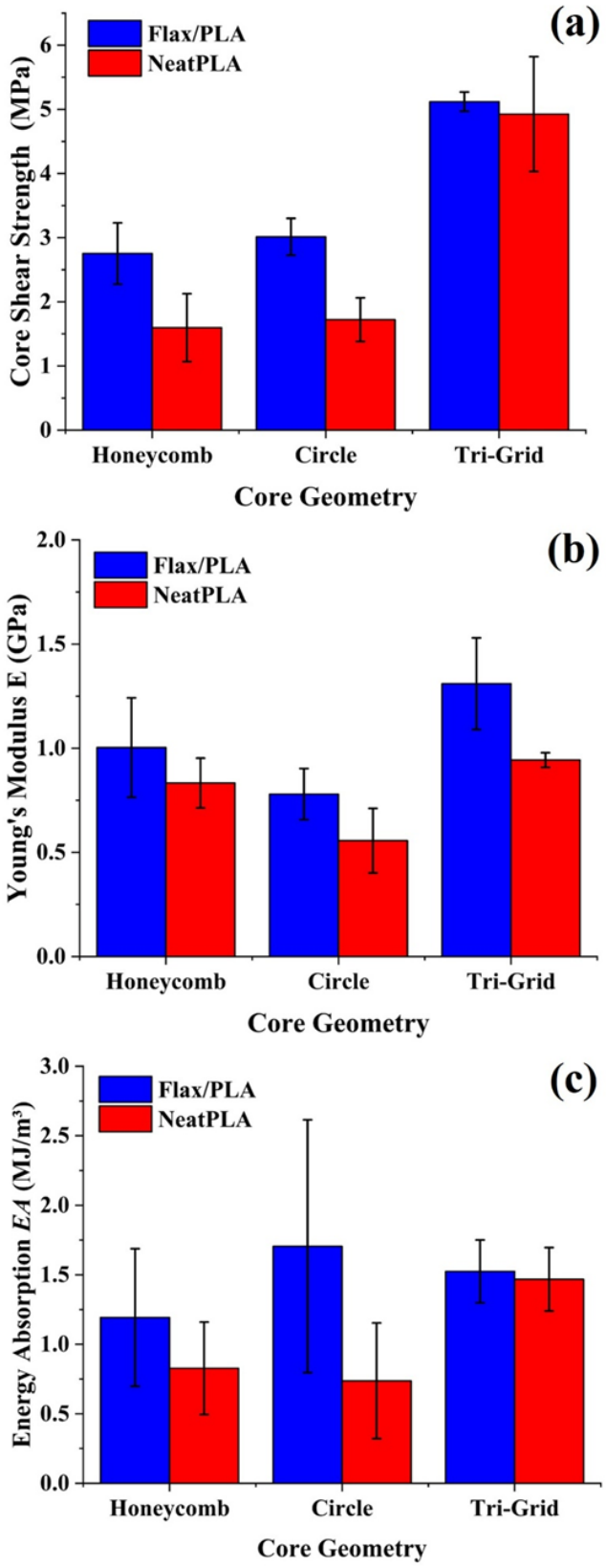


Fig. V. 5. Box-plot visualisation of the mechanical performance of the sandwich panels with the three core geometries: (a) core shear strength τ; (b) flexural modulus E; (c) energy absorption EA. Each panel reports the PLA/flax and the neat PLA data side by side.

The three Kruskal–Wallis tests produce three distinct levels of statistical significance, which reflect three different magnitudes of inter-geometry separation on the three mechanical descriptors.

The core shear strength τ exhibits the highest H statistic of the three descriptors ($H = 11.453$) and the lowest p-value ($p = 0.003$), which confirms a strong influence of the core topology on the shear resistance of the sandwich panel. The tri-grid architecture consistently delivers the largest mean shear strength for both materials 5.12 ± 0.15 MPa for PLA/flax and 4.93 ± 0.90 MPa for neat PLA and these values sit well above the shear strengths of the honeycomb (2.75 and 1.60 MPa, respectively) and of the circular configurations (3.01 and 1.72 MPa, respectively). The shear strength is therefore the descriptor on which the choice of the core geometry matters the most, and the tri-grid is the superior option regardless of the core material.

The apparent flexural modulus E also varies significantly across the three geometries ($H = 9.785$, $p = 0.008$), with the tri-grid again retaining the highest stiffness in the PLA/flax configuration (1.31 ± 0.22 GPa). The circular geometry exhibits the lowest flexural modulus across both materials (0.78 GPa for PLA/flax, 0.56 GPa for neat PLA), which is consistent with the stress-concentration mechanism already invoked in Section V.3.2 and which confirms that the circular cells, while effective at dissipating energy in the PLA/flax case, do not translate that energy-absorption capacity into an elastic-stiffness advantage.

The energy absorption EA exhibits the lowest H statistic of the three descriptors ($H = 5.514$) and a p-value ($p = 0.043$) that sits just below the conventional significance threshold of 0.05. The inter-geometry differences on the EA are therefore real but modest, and the circular configuration in the PLA/flax material system records the highest mean value (1.71 ± 0.91 $MJ \cdot m^{-3}$), which corroborates the paradoxical recovery of the circular geometry in the reinforced material identified in Section V.4.2. The higher standard deviation of the PLA/flax circular EA (± 0.91) reflects the sensitivity of this configuration to the stochastic distribution of the flax fibres, which while globally effective varies in its local deflection action from specimen to specimen.

Taken together, the three Kruskal–Wallis tests confirm that the mechanical performance of the sandwich panels is governed by the synergistic interaction between the core geometry and the core material. The tri-grid architecture dominates the shear-strength and the flexural-modulus rankings, while the circular architecture dominates the energy-absorption ranking specifically in the PLA/flax case. No single geometry is universally optimal across all three

descriptors, which means that the design of a sandwich panel must explicitly trade off the three descriptors against the requirements of the target application.

V.5.2 Post-hoc pairwise comparisons (Dunn–Bonferroni)

Because the Kruskal–Wallis test identified significant overall differences on all three descriptors, post-hoc pairwise comparisons were performed through Dunn's test with Bonferroni correction for multiple comparisons. The significance level was set at $\alpha = 0.05$, and the three pairwise contrasts of interest honeycomb–circular, honeycomb–tri-grid, and circular–tri-grid were evaluated for each of the three mechanical descriptors. The resulting mean rank differences and the associated p-values are reported in Table V.5.

Table V. 5 Dunn–Bonferroni post-hoc pairwise comparisons of core shear strength (τ), apparent flexural modulus (E), and energy absorption (EA) across the three core geometries.

Variable	Comparison	Mean ± SD	p-value
τ (MPa)	Honeycomb − Circle	−0.83 ± 3.08	0.787
	Honeycomb − Tri-Grid	**−9.42 ± 3.08**	**0.002**
	Circle − Tri-Grid	**−8.58 ± 3.08**	**0.005**
E (GPa)	Honeycomb − Circle	5.67 ± 1.84	0.198
	Honeycomb − Tri-Grid	**−9.58 ± 3.11**	**0.006**
	Circle − Tri-Grid	−3.92 ± 1.27	0.611
***EA* (MJ·m⁻³)**	Honeycomb − Circle	1.08 ± 3.08	0.745
	Honeycomb − Tri-Grid	**−7.17 ± 3.08**	**0.023**
	Circle − Tri-Grid	−6.08 ± 3.08	0.051

The post-hoc comparisons of Table V.5 reveal a consistent pattern across the three mechanical descriptors. The tri-grid is statistically distinguishable from the honeycomb on all three descriptors (τ: $p = 0.002$; E: $p = 0.006$; EA: $p = 0.023$) and from the circular geometry on τ ($p = 0.005$), while the circular–tri-grid contrast on EA lies marginally above the conventional threshold ($p = 0.051$). By contrast, the honeycomb and circular geometries are statistically indistinguishable from one another on all three descriptors (τ: $p = 0.787$; E: $p = 0.198$; EA: $p = 0.745$). The overall Kruskal–Wallis significance on all three descriptors is therefore driven primarily by the superiority of the tri-grid, with the honeycomb and circular configurations forming a single statistically equivalent group.

V.5.3 Reliability and scatter analysis

Beyond the mean rankings, the Kruskal–Wallis and the Dunn post-hoc analyses of Tables V.4 and V.5 also provide useful information on the reliability of each configuration through the

standard deviations reported on each group mean. Three reliability patterns emerge from the combined dataset.

The PLA/flax tri-grid configuration delivers the lowest coefficient of variation on the shear strength of the entire campaign (σ/μ = 0.15/5.12 ≈ 2.9 %). This exceptional reproducibility reflects the combined effect of the interconnected strut architecture, which stabilises the failure path against local defects, and the flax reinforcement, which mitigates the sensitivity of the response to the stochastic distribution of inter-bead voids in the FDM print.

The neat PLA circular configuration delivers the highest coefficient of variation on the flexural modulus (σ/μ = 0.16/0.56 ≈ 29 %). This poor reliability is the direct consequence of the stress-concentration mechanism at the void interfaces, which amplifies the effect of any local printing defect on the global response. The scatter of the neat PLA circular configuration on the energy absorption is even more pronounced (σ/μ = 0.42/0.74 ≈ 57 %), which confirms that this configuration is the least reliable of the six tested.

The PLA/flax circular configuration, while delivering the highest mean energy absorption of the campaign (1.71 $MJ \cdot m^{-3}$), also exhibits a substantial scatter on this descriptor (σ/μ = 0.91/1.71 ≈ 53 %). This large scatter reflects the stochastic nature of the flax-induced crack-arrest mechanism: each specimen samples a different local distribution of flax fibres around the circular voids, and the efficiency of the micro-crack deflection varies accordingly from specimen to specimen. The PLA/flax circular configuration therefore offers the highest performance ceiling but with the lowest reliability, a trade-off that should be taken into account in any design decision that prioritises energy absorption over reproducibility.

The three reliability patterns correlate directly with the failure modes documented in Section V.3.3: the high-τ configurations (tri-grid, honeycomb) fail predominantly through core shear, a failure mode that is intrinsically more reproducible than the face-sheet debonding observed in the low-τ circular configurations. The statistical framework of this section therefore confirms, on quantitative grounds, the qualitative ordering already established by the failure-mode analysis.

V.6 Finite element modelling of the honeycomb sandwich

V.6.1 Modelling scope and calibration

The finite element campaign of this chapter was restricted to the honeycomb core configuration with both core materials (neat PLA and PLA/flax biocomposite), rather than extended to the three core geometries. This scope reflects a deliberate methodological choice: the honeycomb configuration is the most widely standardised sandwich core in the composites

literature, and a validated numerical framework for the honeycomb geometry provides a transferable template that can subsequently be extended to the circular and tri-grid topologies in future work.

The face sheet, although manufactured as a four-ply unidirectional [Typha/ Agave/ Typha/ Agave] laminate, was treated in the present model as a homogeneous continuum medium and assigned an isotropic elastic–plastic card calibrated on the longitudinal tensile response of the assembled laminate. The justification of this continuum-medium approach is given in detail in Section II.11.2 and rests on two arguments: (i) the experimental tensile characterisation of the face sheet was conducted on coupons sectioned from the cured laminate as a whole, so that the resulting properties are global descriptors of the assembled laminate rather than ply-level constants; and (ii) the three-point bending configuration generates a stress state in which the longitudinal component aligned with the fibre direction is dominant, while the transverse and in-plane shear components are limited by the small thickness of the face sheet relative to the panel span.

The full methodology of the ABAQUS/CAE Standard finite element model including the isotropic elastic–plastic constitutive cards of the face sheet and the core, the continuum-medium treatment of the four-ply [Typha/Agave/Typha/Agave] laminate, the C3D8R element family, the global mesh seed of 0.5 mm, the frictionless contact pairs, and the static general loading step has been described in Section II.11.2. The elastic and plastic parameters of all three phases were calibrated on the tensile coupons reported in Section V.2, with one independent constitutive card per material: the isotropic card of the hybrid Typha/Agave/epoxy face sheet was built from the 87.6 MPa ultimate strength and the associated elastic properties of Section V.2.2, while the isotropic cards of the neat PLA and the PLA/flax cores were built from the tensile responses of the corresponding filament coupons.

V.6.2 Load–deflection validation

The simulated load–deflection curves of the two honeycomb configurations were compared directly to the experimental records of Section V.3. The key validation metrics are reported in Table V.6 and the overlay of the experimental and the simulated curves is shown in Fig. V.6.

Table V. 6 Finite element validation metrics for the honeycomb sandwich configurations.

Core material	Simulated-peak load (N)	Experimental-peak load (N)	Absolute-error (%)	Pre-failure R^2
PLA/flax	2356.6	2602.6	**−9.5**(under-prediction)	**0.98**
Neat PLA	1899.2	1726.5	**+10.0**(over-prediction)	**0.97**

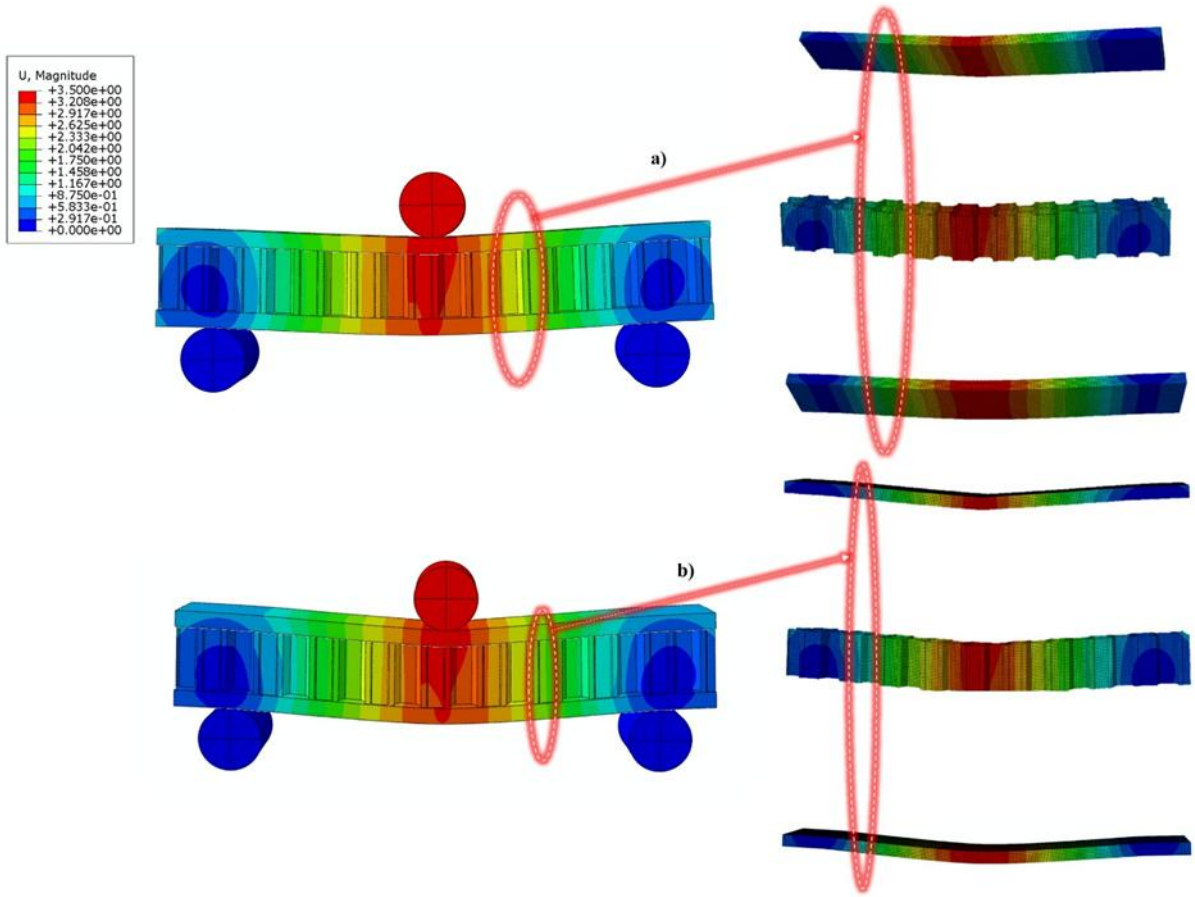


Fig. V. 6. Load–deflection validation: overlay of the experimental (solid lines) and the ABAQUS/CAE-predicted (dashed lines) responses for (a) the PLA/flax honeycomb sandwich and (b) the neat PLA honeycomb sandwich.

The two validation errors fall within the engineering tolerance band of approximately ±10 % that is conventionally accepted for the validation of finite element models of composite sandwich structures, and they therefore confirm the applicability of the adopted numerical framework to the two material systems investigated here. The PLA/flax configuration is under-predicted by the model (−9.5 %), while the neat PLA configuration is slightly over-predicted (+10.0 %), which indicates that the isotropic elastic–perfectly-plastic constitutive card captures the reinforced and the unreinforced cores with similar accuracy but with opposite sign of the

residual error. Importantly, the simulations reproduce the pre-failure behaviour of both configurations with exceptional fidelity: the correlation coefficients between the simulated and the experimental load–deflection curves, evaluated over the elastic-to-early-hardening displacement range of 0 to 3.5 mm, reach $R^2 = 0.98$ for the PLA/flax configuration and $R^2 = 0.97$ for the neat PLA configuration. The elastic-to-plastic transition phase of the sandwich response is therefore the domain in which the finite element model is most reliable, and it is precisely the domain that matters the most for structural design, where the working point of the panel is kept well below the onset of catastrophic failure. Such a degree of agreement ($R^2 > 0.97$, error $\leq \pm 10$ %) is consistent with the performance of recently validated FE models for additively manufactured sandwich panels [212].

The computational cost of the adopted framework is also a point worth highlighting. The static-general-step formulation combined with the isotropic elastic–plastic constitutive cards of the core materials delivered a 78 % reduction in CPU time relative to the progressive-damage models reported elsewhere in the literature, without any appreciable loss of accuracy on the peak-load prediction or on the pre-failure correlation. The framework therefore offers an attractive compromise between fidelity and computational efficiency for the preliminary design of sandwich panels with FDM-printed cores.

V.6.3 Deformation field and failure zones

The von Mises stress contours computed at peak load are presented in Fig. V.7 for both honeycomb configurations. The contours identify the face-sheet tension regions at the mid-span of the beam as the critical failure zones, with the maximum stress intensity localised in the lower face sheet, directly below the loading nose. This prediction is consistent with the matrix-cracking and core-shear failure modes documented experimentally in Section V.3.3, where the transverse shear loading of the honeycomb cells was shown to drive the failure of the panel before the interfacial bond between the face sheets and the core was compromised.

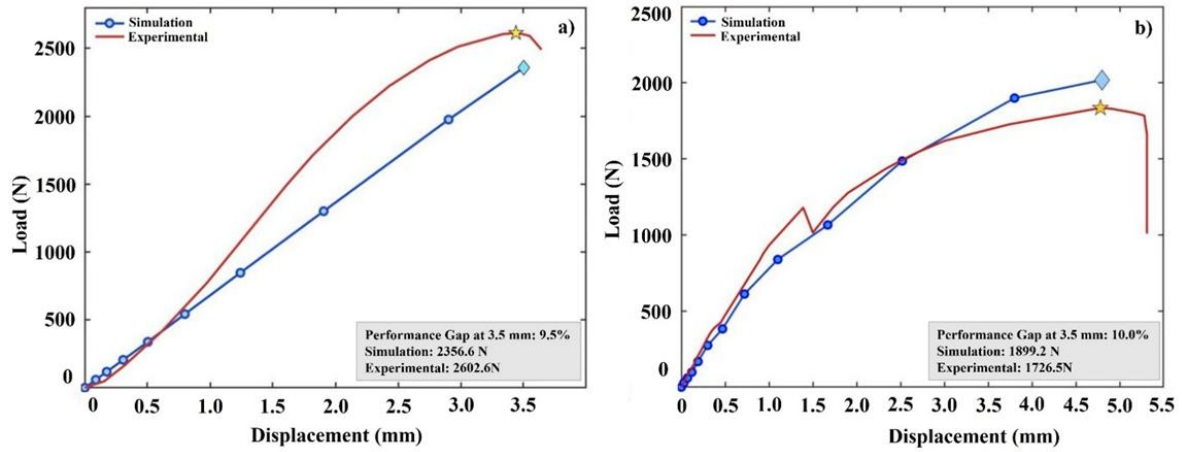


Fig. V. 7 ABAQUS/CAE-predicted deformation patterns and von Mises stress contours at peak load of the honeycomb sandwich configurations: (a) PLA/flax core; (b) neat PLA core.

The two configurations exhibit qualitatively similar stress contours, which is consistent with the shared honeycomb geometry. The magnitude of the maximum stress is higher in the PLA/flax configuration, which reflects its higher peak load, while the spatial distribution of the stress field is effectively identical in the two cases. This similarity of the deformation field, combined with the difference in peak-load magnitude, supports the interpretation developed in Section V.4.2: the flax reinforcement modifies the load-bearing capacity of the core without altering the dominant failure mechanism, which remains the transverse-shear failure of the honeycomb cells at the mid-span of the beam.

V.6.4 Limitations and implications

Three limitations of the finite element framework adopted here deserve to be stated explicitly so that the reader can assess the scope of the numerical conclusions.

The first limitation concerns the scope of the validated geometries. The campaign reported in this section was restricted to the honeycomb configuration, and the validation metrics of Table V.6 therefore apply only to that topology. The extension of the framework to the circular and tri-grid configurations would require a dedicated validation campaign, which was outside the scope of the present thesis.

The second limitation concerns the post-peak softening regime. As in the finite element campaign of Chapter IV, the continuum damage model adopted here predicts a more abrupt failure than is observed experimentally in the load–deflection curves, a limitation that is well known in the literature for continuum approaches applied to materials that exhibit diffuse rather than localised failure mechanisms .This discrepancy does not affect the prediction of the peak

load or of the pre-failure correlation, but it does limit the usefulness of the framework for the simulation of full-collapse or crashworthiness scenarios.

The third limitation concerns the loading scenario. The campaign was restricted to quasi-static three-point bending. Dynamic, fatigue and multiaxial loading conditions, all of which are relevant to the practical application of the sandwich panels in automotive and aerospace components, were not investigated, and they constitute the principal avenues for future work on this numerical framework.

Within these three limitations, the finite element model of this section delivers a validated tool for the preliminary design of honeycomb sandwich panels with hybrid natural-fibre face sheets and FDM-printed cores. The combination of a ±10 % peak-load accuracy, an $R^2 > 0.97$ pre-failure correlation, and a 78 % reduction in computational cost relative to progressive-damage alternatives positions the framework as a credible design aid for the sustainable-composites community.

V.7 Conclusion

This chapter characterised the hybrid sandwich panels through tensile, flexural, energy-absorption, statistical and finite element analyses. The hybrid face sheet outperformed both core materials in tension (87.6 MPa, 6.2 % elongation). In bending, the tri-grid core delivered the highest strength for both PLA and PLA/flax (54.97 and 49.77 MPa), while PLA/flax cores improved the average core shear strength and flexural modulus by 48 % and 34 %, respectively, over neat PLA. The energy-absorption analysis revealed a notable inversion: the circular core, weakest with neat PLA, became the highest absorber with PLA/flax (1.71 ± 0.91 $MJ \cdot m^{-3}$, +131 %), whereas the tri-grid maintained a stable, material-independent response of approximately 1.5 $MJ \cdot m^{-3}$. Kruskal–Wallis tests confirmed the significant effect of core geometry on all three mechanical descriptors, and the ABAQUS/CAE model reproduced the experimental load–deflection response within ±10 % on the peak load ($R^2 > 0.97$) at a 78 % reduction in CPU time. Three operational design guidelines emerge: (i) the PLA/flax tri-grid combination is optimal for stiffness- and reliability-driven applications; (ii) the PLA/flax circular configuration offers the highest energy-absorption ceiling and is suited to crashworthy components, albeit with higher scatter; (iii) the honeycomb remains the most conservative and readily standardisable option when predictability is paramount.

General Conclusion

General Conclusion

The research conducted in this thesis addressed hybrid bio-based sandwich panels combining regionally sourced Typha latifolia and Agave americana fibres from the M'Sila Province as face-sheet reinforcement with FDM-printed neat PLA and PLA/flax cores. Following a three-stage strategy complementary fibre extraction, preparatory FDM studies, and three-point bending evaluation of the assembled panels, supported by finite element simulation and non-parametric statistics, the principal outcomes are summarised as follows:

- **Fibre characterisation.** Thermogravimetric analysis quantified the thermal stability of the fibres, with residual char yields of 46.0 % for Typha and 36.5 % for Agave. X-ray diffraction yielded crystallinity indices of 63.6 % for Typha and 51.5 % for Agave, confirming a markedly higher cellulose crystallinity in Typha. Single-fibre tensile testing established Agave as the stronger and stiffer reinforcement, with a tensile strength in the 300–450 MPa range and an elastic modulus of 38.5 ± 2.1 GPa, whereas Typha exhibited a strength of 130–260 MPa and a modulus of 9.8 ± 5.0 GPa, emerging as a complementary moderate-strength fibre with elevated thermal resistance.
- **FDM process optimisation and polymer mechanics.** The combined Taguchi and artificial neural network campaign, conducted on a 27-point L_9 orthogonal array, identified the filling density as the dominant parameter governing the tensile response of printed PLA. The ANN model captured the nonlinear process property relationships with a prediction accuracy substantially superior to that of classical linear frameworks. The apertured-tensile investigation, corroborated by an ABAQUS/Explicit finite element model, demonstrated that local stress concentration around the geometric discontinuities, rather than the mere reduction of the net cross-section, constitutes the first-order mechanism dictating the angle-dependent strength of the printed polymer.
- **Hybrid sandwich performance.** Three-point bending tests conducted on six core-material/geometry combinations and analysed within a non-parametric Kruskal–Wallis statistical framework ($p < 0.05$) established the tri-grid core as the configuration delivering the highest flexural strength for both core materials, with peak values of 54.97 MPa and 49.77 MPa for the neat PLA and PLA/flax variants, respectively. A notable inversion of the energy-absorption ranking was observed: the circular core, which did not lead in absorption when filled with neat PLA, became the most energy-absorbent configuration once the flax-reinforced core was employed, delivering a mean energy absorption of 1.71 ± 0.91 $MJ \cdot m^{-3}$, representing a 131 % increase over its neat PLA counterpart.
- **Numerical simulation.** The continuum-medium finite element model developed in ABAQUS/CAE Standard reproduced the experimental pre-failure load–deflection

response of the honeycomb sandwich configuration with a peak-load prediction within ± 10 % of the measured value and a correlation coefficient $R^2 \geq 0.97$ over the pre-failure regime, while achieving a 78 % reduction in CPU time relative to more complex progressive-damage alternatives.

Limitations and future perspectives

While the present thesis establishes a robust experimental and numerical framework, certain limitations delineate the trajectory for future investigations. The X-ray diffraction and thermogravimetric acquisitions were conducted on single acquisitions ($n = 1$); extending these measurements to a statistically representative number of replicates ($n \geq 3$) would consolidate the parametric distributional assumptions underlying the comparative analyses. Expanding the fibre database to other Algerian lignocellulosic species notably date palm and esparto grassand to specimens harvested across successive seasons would further quantify the influence of biological and climatic variability on the engineering properties of these regional reinforcements.

The mechanical validation reported herein was restricted to quasi-static tension and bending. Extending the experimental envelope to dynamic, fatigue, and impact loading scenarios is an essential prerequisite for qualifying these hybrid panels for crashworthy applications in the automotive and aerospace sectors. On the numerical front, the continuum elastic–plastic formulation adopted in the present work predicts a sharper post-peak softening than that experimentally observed. Transitioning toward a discrete fibre-bundle representation for the face sheets and a progressive damage formulation for the core would extend the predictive capability of the finite element framework into the full-collapse and post-failure regimes.

In closing, this work demonstrates that lignocellulosic fibres from the semi-arid lands of M'Sila can be transformed, through mild delignification or mechanical decortication, hand-layup lamination, and fused deposition modelling, into hybrid sandwich structures that are mechanically competitive with conventional composite systems. The thesis contributes directly to sustainable engineering by replacing petroleum-derived synthetics with renewable, regionally sourced equivalents, and establishes a reproducible experimental and numerical template for valorising underutilised indigenous bio-resources in lightweight structural applications.

References

References

[1] R. Geyer, J.R. Jambeck, K.L. Law, Production, use, and fate of all plastics ever made., Sci. Adv. 3 (2017) e1700782. https://doi.org/10.1126/sciadv.1700782.

[2] R. Narayan, Biobased & Biodegradable Plastics: Rationale, Drivers, and Technology Exemplars, in: Degrad. Polym. Mater. Princ. Pract. (2nd Ed., American Chemical Society, 2012: pp. 2–13. https://doi.org/doi:10.1021/bk-2012-1114.ch002.

[3] A. Le Duigou, D. Correa, M. Ueda, R. Matsuzaki, M. Castro, A review of 3D and 4D printing of natural fibre biocomposites, Mater. Des. 194 (2020) 108911. https://doi.org/https://doi.org/10.1016/j.matdes.2020.108911.

[4] L. Mohammed, M.N.M. Ansari, G. Pua, M. Jawaid, M.S. Islam, A Review on Natural Fiber Reinforced Polymer Composite and Its Applications, Int. J. Polym. Sci. 2015 (2015) 243947. https://doi.org/https://doi.org/10.1155/2015/243947.

[5] P. Peças, H. Carvalho, H. Salman, M. Leite, Natural Fibre Composites and Their Applications: A Review, J. Compos. Sci. 2 (2018) 66. https://doi.org/10.3390/jcs2040066.

[6] P. Madhu, M.R. Sanjay, M. Jawaid, S. Siengchin, A. Khan, C.I. Pruncu, A new study on effect of various chemical treatments on Agave Americana fiber for composite reinforcement: Physico-chemical, thermal, mechanical and morphological properties, Polym. Test. 85 (2020) 106437.

[7] M. Syduzzaman, M.A. Al Faruque, K. Bilisik, M. Naebe, Plant-Based Natural Fibre Reinforced Composites: A Review on Fabrication, Properties and Applications, Coatings 10 (2020) 973. https://doi.org/10.3390/coatings10100973.

[8] M.F. Ashby, M.F. Ashby, Materials Selection in Mechanical Design, Elsevier Science, 2011. https://books.google.dz/books?id=asp4jgEACAAJ.

[9] H.E.L. Etri, M.Z. Polat, E.B. Özyılmaz, Classification, applications, and impact behavior of composite materials: A review, Mech. Adv. Mater. Struct. 31 (2024) 12592–12635. https://doi.org/10.1080/15376494.2024.2326665.

[10] M. Khan, M. Cao, M. Ali, Cracking behaviour and constitutive modelling of hybrid fibre reinforced concrete, J. Build. Eng. 30 (2020) 101272. https://doi.org/https://doi.org/10.1016/j.jobe.2020.101272.

[11] H. Altenbach, J. Altenbach, W. Kissing, Classification of Composite Materials BT - Mechanics of Composite Structural Elements, in: H. Altenbach, J. Altenbach, W. Kissing (Eds.), Springer Singapore, Singapore, 2018: pp. 3–18. https://doi.org/10.1007/978-981-10-8935-0_1.

[12] M. Bhong, T.K.H. Khan, K. Devade, B. Vijay Krishna, S. Sura, H.K. Eftikhaar, H. Pal Thethi, N. Gupta, Review of composite materials and applications, Mater. Today Proc. (2023). https://doi.org/https://doi.org/10.1016/j.matpr.2023.10.026.

[13] L. Singh, B. Singh, K.K. Saxena, Manufacturing techniques for metal matrix composites (MMC): an overview, Adv. Mater. Process. Technol. 6 (2020) 441–457. https://doi.org/10.1080/2374068X.2020.1729603.

[14] R. Casati, M. Vedani, Metal Matrix Composites Reinforced by Nano-Particles—A Review, Metals (Basel). 4 (2014) 65–83. https://doi.org/10.3390/met4010065.

[15] A. Mussatto, I.U.I. Ahad, R.T. Mousavian, Y. Delaure, D. Brabazon, Advanced

production routes for metal matrix composites, Eng. Reports 3 (2021) e12330. https://doi.org/https://doi.org/10.1002/eng2.12330.

[16] O. Gavalda-Diaz, E. Saiz, J. Chevalier, F. Bouville, Toughening of ceramics and ceramic composites through microstructure engineering: A review, Int. Mater. Rev. 70 (2025) 3–30.

[17] S.P. Dwivedi, A.K. Srivastava, N.K. Maurya, R. Sahu, A. Tyagi, R. Maurya, Microstructure and mechanical behaviour of Al/SiC/Al2O3 hybrid metal matrix composite, Mater. Today Proc. 25 (2020) 789–792. https://doi.org/https://doi.org/10.1016/j.matpr.2019.09.023.

[18] S. Shrivastava, D.K. Rajak, T. Joshi, D.K. Singh, D.P. Mondal, Ceramic Matrix Composites: Classifications, Manufacturing, Properties, and Applications, Ceramics 7 (2024) 652–679. https://doi.org/10.3390/ceramics7020043.

[19] K. Ramachandran, J.C. Bear, D.D. Jayaseelan, Oxide-Based Ceramic Matrix Composites for High-Temperature Environments: A Review, Adv. Eng. Mater. 27 (2025) 2402000. https://doi.org/https://doi.org/10.1002/adem.202402000.

[20] G. Karadimas, K. Salonitis, Ceramic Matrix Composites for Aero Engine Applications—A Review, Appl. Sci. 13 (2023) 3017. https://doi.org/10.3390/app13053017.

[21] S. Antony Jose, J. Crosby, P.L. Menezes, Additive Manufacturing of Ceramics and Ceramic-Based Composites: Processing, Properties, and Engineering Applications, Ceramics 9 (2026) 43. https://doi.org/10.3390/ceramics9050043.

[22] T. Li, Y. Zhang, C. Ma, X. Gong, X. Li, H. Sun, K. Liu, C. Yan, Y. Shi, Robotic arm-assisted additive manufacturing of continuous SiCf/SiC ceramic matrix composites with high performance via precursor infiltration and pyrolysis, J. Eur. Ceram. Soc. 46 (2026) 117914. https://doi.org/https://doi.org/10.1016/j.jeurceramsoc.2025.117914.

[23] T. Aziz, F. Haq, A. Farid, L. Cheng, L.F. Chuah, A. Bokhari, M. Mubashir, D.Y.Y. Tang, P.L. Show, The epoxy resin system: function and role of curing agents, Carbon Lett. 34 (2024) 477–494. https://doi.org/10.1007/s42823-023-00547-7.

[24] D. Popescu, A. Zapciu, C. Amza, F. Baciu, R. Marinescu, FDM process parameters influence over the mechanical properties of polymer specimens: A review, Polym. Test. 69 (2018) 157–166. https://doi.org/https://doi.org/10.1016/j.polymertesting.2018.05.020.

[25] G. Sumithra, R.N. Reddy, G. Dheeraj Kumar, S. Ojha, G. Jayachandra, G. Raghavendra, Review on composite classification, manufacturing, and applications, Mater. Today Proc. (2023). https://doi.org/https://doi.org/10.1016/j.matpr.2023.04.637.

[26] M.A. Al Faruque, M. Salauddin, M.M. Raihan, I.Z. Chowdhury, F. Ahmed, S.S. Shimo, Bast Fiber Reinforced Green Polymer Composites: A Review on Their Classification, Properties, and Applications, J. Nat. Fibers 19 (2022) 8006–8021. https://doi.org/10.1080/15440478.2021.1958431.

[27] G. Struzziero, M. Barbezat, A.A. Skordos, Consolidation of continuous fibre reinforced composites in additive processes: A review, Addit. Manuf. 48 (2021) 102458. https://doi.org/https://doi.org/10.1016/j.addma.2021.102458.

[28] D. Bino Prince Raja, B. Stanly Jones Retnam, Effect of short fibre orientation on the mechanical characterization of a composite material-hybrid fibre reinforced polymer matrix, Bull. Mater. Sci. 42 (2019) 111. https://doi.org/10.1007/s12034-019-1813-5.

[29] S. Biswas, S. Shahinur, M. Hasan, Q. Ahsan, Physical, Mechanical and Thermal Properties of Jute and Bamboo Fiber Reinforced Unidirectional Epoxy Composites, Procedia Eng. 105 (2015) 933–939. https://doi.org/https://doi.org/10.1016/j.proeng.2015.05.118.

[30] M. Slamani, J.-F. Chatelain, S. Jammel, Comprehensive Analysis of Lubricant and Nanofiller Contributions to Surface Roughness Control in Drilling of GFRP Composites, J. Compos. Sci. 10 (2026) 81. https://doi.org/10.3390/jcs10020081.

[31] A. Bentur, S. Mindess, Fibre reinforced cementitious composites, CRC press, 2006.

[32] Y. Wang, W. Zhao, L. Tan, Y. Li, L. Qin, S. Li, Review of Polymer-Based Composites for Electromagnetic Shielding Application, Molecules 28 (2023) 5628. https://doi.org/10.3390/molecules28155628.

[33] Z. Wang, Y. Wang, J. He, K. Dong, G. Zhang, W. Li, Y. Xiong, Additive manufacturing of continuous fiber-reinforced polymer composite sandwich structures with multiscale cellular cores, Chinese J. Mech. Eng. Addit. Manuf. Front. 2 (2023) 100088.

[34] J. Wei, L. Ke, P. Wang, W. Li, C.K.Y. Leung, Microstructure, mechanical properties and interaction mechanism of seawater sea-sand engineered cementitious composite (SS-ECC) with Glass Fiber Reinforced Polymer (GFRP) bar, Compos. Struct. 343 (2024) 118302. https://doi.org/https://doi.org/10.1016/j.compstruct.2024.118302.

[35] J. Qureshi, A Review of Fibre Reinforced Polymer Structures, Fibers 10 (2022) 27. https://doi.org/10.3390/fib10030027.

[36] M. Ertekin, 7 - Aramid fibers, in: M.Ö. Seydibeyoğlu, A.K. Mohanty, M.B.T.-F.T. for F.-R.C. Misra (Eds.), Woodhead Publ. Ser. Compos. Sci. Eng., Woodhead Publishing, 2017: pp. 153–167. https://doi.org/https://doi.org/10.1016/B978-0-08-101871-2.00007-2.

[37] H. El Etri, M.E. Korkmaz, M.K. Gupta, M. Gunay, J. Xu, A state-of-the-art review on mechanical characteristics of different fiber metal laminates for aerospace and structural applications, Int. J. Adv. Manuf. Technol. 123 (2022) 2965–2991. https://doi.org/10.1007/s00170-022-10277-1.

[38] M. Hughes, Defects in natural fibres: their origin, characteristics and implications for natural fibre-reinforced composites, J. Mater. Sci. 47 (2012) 599–609. https://doi.org/10.1007/s10853-011-6025-3.

[39] Y.G. Thyavihalli Girijappa, S. Mavinkere Rangappa, J. Parameswaranpillai, S. Siengchin, Natural Fibers as Sustainable and Renewable Resource for Development of Eco-Friendly Composites: A Comprehensive Review, Front. Mater. Volume 6- (2019). https://www.frontiersin.org/journals/materials/articles/10.3389/fmats.2019.00226.

[40] S. Nautiyal, S. Dimri, I. Riyal, H. Sharma, C. Dwivedi, Natural fibres and their composites: a review of chemical composition, properties, retting methods, and industrial applications, Cellulose 32 (2025) 3497–3527. https://doi.org/10.1007/s10570-025-06487-x.

[41] R.M. Rowell, 25 - The use of biomass to produce bio-based composites and building materials, in: K.B.T.-A. in B. Waldron (Ed.), Woodhead Publishing, 2014: pp. 803–818. https://doi.org/https://doi.org/10.1533/9780857097385.2.803.

[42] F. Martí-Ferrer, F. Vilaplana, A. Ribes-Greus, A. Benedito-Borrás, C. Sanz-Box, Flour rice husk as filler in block copolymer polypropylene: Effect of different coupling agents,

J. Appl. Polym. Sci. 99 (2006) 1823–1831. https://doi.org/https://doi.org/10.1002/app.22717.

[43] S. Hattalli, A. Benaboura, F. Ham-Pichavant, A. Nourmamode, A. Castellan, Adding value to Alfa grass (Stipa tenacissima L.) soda lignin as phenolic resins 1. Lignin characterization, Polym. Degrad. Stab. 76 (2002) 259–264. https://doi.org/https://doi.org/10.1016/S0141-3910(02)00022-8.

[44] A. Khan, V. Raghunathan, D.L. Singaravelu, M.R. Sanjay, S. Siengchin, M. Jawaid, K.A. Alamry, A.M. Asiri, Extraction and Characterization of Cellulose Fibers from the Stem of Momordica Charantia, J. Nat. Fibers 19 (2022) 2232–2242. https://doi.org/10.1080/15440478.2020.1807442.

[45] A.K. Mohanty, M. Misra, L.T. Drzal, Surface modifications of natural fibers and performance of the resulting biocomposites: An overview , Compos. Interfaces 8 (2001) 313–343. https://doi.org/10.1163/156855401753255422.

[46] M. Jawaid, H.P.S. Abdul Khalil, Cellulosic/synthetic fibre reinforced polymer hybrid composites: A review, Carbohydr. Polym. 86 (2011) 1–18. https://doi.org/https://doi.org/10.1016/j.carbpol.2011.04.043.

[47] S.O. Amiandamhen, M. Meincken, L. Tyhoda, Natural Fibre Modification and Its Influence on Fibre-matrix Interfacial Properties in Biocomposite Materials, Fibers Polym. 21 (2020) 677–689. https://doi.org/10.1007/s12221-020-9362-5.

[48] M. Mohammadi, M.R. Ishak, M.T.H. Sultan, Exploring Chemical and Physical Advancements in Surface Modification Techniques of Natural Fiber Reinforced Composite: A Comprehensive Review, J. Nat. Fibers 21 (2024) 2408633. https://doi.org/10.1080/15440478.2024.2408633.

[49] C. Baley, M. Gomina, J. Breard, A. Bourmaud, P. Davies, Variability of mechanical properties of flax fibres for composite reinforcement. A review, Ind. Crops Prod. 145 (2020) 111984. https://doi.org/https://doi.org/10.1016/j.indcrop.2019.111984.

[50] A.P. More, Flax fiber–based polymer composites: a review, Adv. Compos. Hybrid Mater. 5 (2022) 1–20. https://doi.org/10.1007/s42114-021-00246-9.

[51] R.M. Iqbal, R. Ahammad, M. Arifuzzaman, M.S. Islam, M.M. Islam, Manufacturing and Properties of Jute Fiber-Reinforced Polymer Composites—A Comprehensive Review, Materials (Basel). 18 (2025) 1016.

[52] S. Amroune, A. Elhadi, M. Slamani, M. Arslane, A. Belaadi, M.M.S. Abdullah, H.A. Al-Lohedan, T. Bidi, H. Mukalazi, A. Al-Khawlani, Quality Evaluation and Predictive Analysis of Drilled Holes in Jute/Palm/Polyester Hybrid Bio-Composites Using CMM and ANN Techniques, J. Nat. Fibers 22 (2025) 2495929. https://doi.org/10.1080/15440478.2025.2495929.

[53] H. Singh, J. Inder Preet Singh, S. Singh, V. Dhawan, S. Kumar Tiwari, A Brief Review of Jute Fibre and Its Composites, Mater. Today Proc. 5 (2018) 28427–28437. https://doi.org/https://doi.org/10.1016/j.matpr.2018.10.129.

[54] W. Qu, B. Niu, C. Lv, J. Liu, A review of sisal fiber-reinforced geopolymers: preparation, microstructure, and mechanical properties, Molecules 29 (2024) 2401.

[55] G. Sathishkumar, A.U. Devi, M.P.K. Reddy, V.N. Kanthe, D. Palaniswamy, P.R.K. Chakravarthy, M. Dubey, H. Majumder, A.K. Srivastava, Experimental study on mechanical performance and microstructural characterization of optimized sisal fiber

reinforced polyester composites, Sci. Rep. 15 (2025) 36348. https://doi.org/10.1038/s41598-025-20177-5.

[56] M. Ramesh, Kenaf (Hibiscus cannabinus L.) fibre based bio-materials: A review on processing and properties, Prog. Mater. Sci. 78–79 (2016) 1–92. https://doi.org/https://doi.org/10.1016/j.pmatsci.2015.11.001.

[57] M.M. Harussani, S.M. Sapuan, Development of Kenaf Biochar in Engineering and Agricultural Applications, Chem. Africa 5 (2022) 1–17. https://doi.org/10.1007/s42250-021-00293-1.

[58] S. Awad, Y. Zhou, E. Katsou, Y. Li, M. Fan, A Critical Review on Date Palm Tree (Phoenix dactylifera L.) Fibres and Their Uses in Bio-composites, Waste and Biomass Valorization 12 (2021) 2853–2887. https://doi.org/10.1007/s12649-020-01105-2.

[59] Abdelmalek Elhadi, Salah Amroune, Mohamed Slamani, Ugur Köklü, Mustapha Arslane, Madani Grine, Borhen Louhichi, Evaluation of thrust force, delamination and hole quality during drilling an alfa-jute/epoxy natural fiber hybrid composite, J. Compos. Mater. 60 (2026) 303–320. https://doi.org/10.1177/00219983251362295.

[60] S. Amroune, A. Bezazi, A. Belaadi, C. Zhu, F. Scarpa, S. Rahatekar, A. Imad, Tensile mechanical properties and surface chemical sensitivity of technical fibres from date palm fruit branches (Phoenix dactylifera L.), Compos. Part A Appl. Sci. Manuf. 71 (2015) 95–106. https://doi.org/https://doi.org/10.1016/j.compositesa.2014.12.011.

[61] M. Slamani, S. Amroune, R. Benyettou, H. Fouad, M. Jawaid, R. Khiari, Water Absorption Behavior of Date Palm Fruit Branches Fiber (DPF) Composites: Experimental and Statistical Analyses, J. Nat. Fibers 21 (2024) 2375530. https://doi.org/10.1080/15440478.2024.2375530.

[62] R. Benyettou, S. Amroune, M. Slamani, M. Jawaid, A. Dufresne, H. Fouad, T. Bidi, Investigating the Impact of Drill Point Angles on the Drilling Behavior of Date Palm Biocomposites: Experimental, ANN, and Taguchi Modeling, J. Nat. Fibers 22 (2025) 2520843.

[63] S. Amroune, A. Bezazi, A. Dufresne, F. Scarpa, A. Imad, Investigation on Microstructure, Tensile Properties and Fatigue Characterization of Porous Date Palm Fiber, J. Nat. Fibers 19 (2022) 15751–15764. https://doi.org/10.1080/15440478.2022.2134255.

[64] R.M.N. Arib, S.M. Sapuan, M.M.H.M. Ahmad, M.T. Paridah, H.M.D.K. Zaman, Mechanical properties of pineapple leaf fibre reinforced polypropylene composites, Mater. Des. 27 (2006) 391–396. https://doi.org/https://doi.org/10.1016/j.matdes.2004.11.009.

[65] Y. Du, N. Yan, M.T. Kortschot, 4 - The use of ramie fibers as reinforcements in composites, in: O. Faruk, M.B.T.-B.R. in C.M. Sain (Eds.), Woodhead Publishing, 2015: pp. 104–137. https://doi.org/https://doi.org/10.1533/9781782421276.1.104.

[66] G. Rajeshkumar, V. Hariharan, T.P. Sathishkumar, Characterization of Phoenix sp. natural fiber as potential reinforcement of polymer composites, J. Ind. Text. 46 (2016) 667–683.

[67] T.P. Sathishkumar, P. Navaneethakrishnan, S. Shankar, R. Rajasekar, Characterization of new cellulose sansevieria ehrenbergii fibers for polymer composites, Compos. Interfaces 20 (2013) 575–593. https://doi.org/10.1080/15685543.2013.816652.

[68] N. Saba, M.T. Paridah, M. Jawaid, Mechanical properties of kenaf fibre reinforced polymer composite: A review, Constr. Build. Mater. 76 (2015) 87–96. https://doi.org/https://doi.org/10.1016/j.conbuildmat.2014.11.043.

[69] J.R.M. d'Almeida, R.C.M.P. Aquino, S.N. Monteiro, Tensile mechanical properties, morphological aspects and chemical characterization of piassava (Attalea funifera) fibers, Compos. Part A Appl. Sci. Manuf. 37 (2006) 1473–1479. https://doi.org/https://doi.org/10.1016/j.compositesa.2005.03.035.

[70] M. Maache, A. Bezazi, S. Amroune, F. Scarpa, A. Dufresne, Characterization of a novel natural cellulosic fiber from Juncus effusus L., Carbohydr. Polym. 171 (2017) 163–172. https://doi.org/https://doi.org/10.1016/j.carbpol.2017.04.096.

[71] A. Ramachandran, S. Mavinkere Rangappa, V. Kushvaha, A. Khan, S. Seingchin, H.N. Dhakal, Modification of Fibers and Matrices in Natural Fiber Reinforced Polymer Composites: A Comprehensive Review, Macromol. Rapid Commun. 43 (2022) 2100862. https://doi.org/https://doi.org/10.1002/marc.202100862.

[72] T.D. Ngo, A. Kashani, G. Imbalzano, K.T.Q. Nguyen, D. Hui, Additive manufacturing (3D printing): A review of materials, methods, applications and challenges, Compos. Part B Eng. 143 (2018) 172–196. https://doi.org/https://doi.org/10.1016/j.compositesb.2018.02.012.

[73] I. Gibson, D. Rosen, B. Stucker, M. Khorasani, D. Rosen, B. Stucker, M. Khorasani, Additive manufacturing technologies, Springer, 2021.

[74] J. Borrello, P. Nasser, J.C. Iatridis, K.D. Costa, 3D printing a mechanically-tunable acrylate resin on a commercial DLP-SLA printer, Addit. Manuf. 23 (2018) 374–380. https://doi.org/https://doi.org/10.1016/j.addma.2018.08.019.

[75] M.M. Rahman, S. Islam, Mubasshira, M.S. Islam, R. Ahammad, M.A. Islam, M.A. Hasib, M.S. Rahman, R. Moshwan, M.M. Ehsan, M.S. Rabbi, M. Moniruzzaman, M.A. Nazir, W.-D. Liu, Polymer Composites in Additive Manufacturing: Current Technologies, Applications, and Emerging Trends, Polymers (Basel). 18 (2026) 192. https://doi.org/10.3390/polym18020192.

[76] J. Saroia, Y. Wang, Q. Wei, M. Lei, X. Li, Y. Guo, K. Zhang, A review on 3D printed matrix polymer composites: its potential and future challenges, Int. J. Adv. Manuf. Technol. 106 (2020) 1695–1721. https://doi.org/10.1007/s00170-019-04534-z.

[77] R. Jones, P. Haufe, E. Sells, P. Iravani, V. Olliver, C. Palmer, A. Bowyer, RepRap – the replicating rapid prototyper, Robotica 29 (2011) 177–191. https://doi.org/DOI: 10.1017/S026357471000069X.

[78] B. N. Turner, R. Strong, S. A. Gold, A review of melt extrusion additive manufacturing processes: I. Process design and modeling, Rapid Prototyp. J. 20 (2014) 192–204. https://doi.org/10.1108/RPJ-01-2013-0012.

[79] A.W. Hashmi, H.S. Mali, A. Meena, K.K. Saxena, A.P.V. Puerta, U.S. Rao, D. Buddhi, K.A. Mohammed, Design and modeling of abrasive flow finishing of freeform surfaces of FDM printed femoral component of knee implant pattern, Int. J. Interact. Des. Manuf. 17 (2023) 2507–2526. https://doi.org/10.1007/s12008-022-01048-z.

[80] M. Ueda, S. Kishimoto, M. Yamawaki, R. Matsuzaki, A. Todoroki, Y. Hirano, A. Le Duigou, 3D compaction printing of a continuous carbon fiber reinforced thermoplastic, Compos. Part A Appl. Sci. Manuf. 137 (2020) 105985. https://doi.org/https://doi.org/10.1016/j.compositesa.2020.105985.

[81] G.D. Goh, Y.L. Yap, S. Agarwala, W.Y. Yeong, Recent Progress in Additive Manufacturing of Fiber Reinforced Polymer Composite, Adv. Mater. Technol. 4 (2019) 1800271. https://doi.org/https://doi.org/10.1002/admt.201800271.

[82] P. Ghabezi, O. Sam-Daliri, T. Flanagan, M. Walls, N.M. Harrison, Mechanical and microstructural analysis of glass Fibre-Reinforced high density polyethylene thermoplastic waste composites manufactured by material extrusion 3D printing technology, Compos. Part A Appl. Sci. Manuf. 194 (2025) 108930. https://doi.org/https://doi.org/10.1016/j.compositesa.2025.108930.

[83] M.A. Morales, C.L. Atencio Martinez, A. Maranon, C. Hernandez, V. Michaud, A. Porras, Development and Characterization of Rice Husk and Recycled Polypropylene Composite Filaments for 3D Printing, Polymers (Basel). 13 (2021) 1067. https://doi.org/10.3390/polym13071067.

[84] R. Anitha, S. Arunachalam, P. Radhakrishnan, Critical parameters influencing the quality of prototypes in fused deposition modelling, J. Mater. Process. Technol. 118 (2001) 385–388. https://doi.org/https://doi.org/10.1016/S0924-0136(01)00980-3.

[85] S. Tablit, R. Krache, S. Amroune, M. Jawaid, A. Hachaichi, A.S. Ismail, A. Meraj, Effect of chemical treatments of arundo donax L. fibre on mechanical and thermal properties of the PLA/PP blend composite filament for FDM 3D printing, J. Mech. Behav. Biomed. Mater. 152 (2024) 106438. https://doi.org/https://doi.org/10.1016/j.jmbbm.2024.106438.

[86] S. Wickramasinghe, T. Do, P. Tran, FDM-Based 3D Printing of Polymer and Associated Composite: A Review on Mechanical Properties, Defects and Treatments, Polymers (Basel). 12 (2020) 1529. https://doi.org/10.3390/polym12071529.

[87] M. Algarni, S. Ghazali, Comparative Study of the Sensitivity of PLA, ABS, PEEK, and PETG's Mechanical Properties to FDM Printing Process Parameters, Crystals 11 (2021) 995. https://doi.org/10.3390/cryst11080995.

[88] A. Alafaghani, A. Qattawi, M.A. Ablat, Design Consideration for Additive Manufacturing: Fused Deposition Modelling, Open J. Appl. Sci. 07 (2017) 291–318. https://doi.org/10.4236/ojapps.2017.76024.

[89] A. Mathew, S.R. Kishore, A.T. Tomy, M. Sugavaneswaran, S.G. Scholz, A. Elkaseer, V.H. Wilson, A. John Rajan, Vapour polishing of fused deposition modelling (FDM) parts: a critical review of different techniques, and subsequent surface finish and mechanical properties of the post-processed 3D-printed parts, Prog. Addit. Manuf. 8 (2023) 1161–1178. https://doi.org/10.1007/s40964-022-00391-7.

[90] D. Zenkert, The Handbook of Sandwich Construction, Engineering Materials Advisory Services, 1997.

[91] A. Kausar, I. Ahmad, S.A. Rakha, M.H. Eisa, A. Diallo, State-Of-The-Art of Sandwich Composite Structures: Manufacturing—to—High Performance Applications, J. Compos. Sci. 7 (2023) 102. https://doi.org/10.3390/jcs7030102.

[92] D. Gay, Composite materials: design and applications, CRC press, 2022.

[93] V. Birman, G.A. Kardomateas, Review of current trends in research and applications of sandwich structures, Compos. Part B Eng. 142 (2018) 221–240. https://doi.org/10.1016/j.compositesb.2018.01.027.

[94] A. Monti, A. El Mahi, Z. Jendli, L. Guillaumat, Mechanical behaviour and damage

mechanisms analysis of a flax-fibre reinforced composite by acoustic emission, Compos. Part A Appl. Sci. Manuf. 90 (2016) 100–110. https://doi.org/https://doi.org/10.1016/j.compositesa.2016.07.002.

[95] F. Tarlochan, Sandwich Structures for Energy Absorption Applications: A Review., Mater. (Basel, Switzerland) 14 (2021). https://doi.org/10.3390/ma14164731.

[96] Y. Fu, P. Sadeghian, Flexural and shear characteristics of bio-based sandwich beams made of hollow and foam-filled paper honeycomb cores and flax fiber composite skins, Thin-Walled Struct. 153 (2020) 106834. https://doi.org/10.1016/j.tws.2020.106834.

[97] X. Song, S. Hong, J. Wang, X. Zhu, S. Guo, Y. Fu, Y. Yang, M. Yang, W. He, Y. Tang, B. Gao, Mechanical Properties of a Honeycomb Structure Dispersed with 3D-Printed Fe3O4 Nanomaterials, ACS Omega 9 (2024) 14287–14296. https://doi.org/10.1021/acsomega.3c10138.

[98] D. Nie, L. Kong, Y. Zhang, X. Qiu, Y. Fu, J. Gu, Mechanical Performance and Failure Analysis of a 3D-Printed "Continuous Layer–Lattice Layer–Continuous Layer" Sandwich Structure, Polymers (Basel). 15 (2023) 4283. https://doi.org/10.3390/polym15214283.

[99] S. Hou, T. Li, Z. Jia, L. Wang, Mechanical properties of sandwich composites with 3d-printed auxetic and non-auxetic lattice cores under low velocity impact, Mater. Des. 160 (2018) 1305–1321. https://doi.org/https://doi.org/10.1016/j.matdes.2018.11.002.

[100] T. Li, Y. Chen, X. Hu, Y. Li, L. Wang, Exploiting negative Poisson's ratio to design 3D-printed composites with enhanced mechanical properties, Mater. Des. 142 (2018) 247–258. https://doi.org/https://doi.org/10.1016/j.matdes.2018.01.034.

[101] C. Lu, M. Qi, S. Islam, P. Chen, S. Gao, Y. Xu, X. Yang, Mechanical performance of 3D-printing plastic honeycomb sandwich structure, Int. J. Precis. Eng. Manuf. Technol. 5 (2018) 47–54.

[102] S. Pirouzfar, A. Zeinedini, Effect of geometrical parameters on the flexural properties of sandwich structures with 3D-printed honeycomb core and E-glass/epoxy Face-sheets, in: Structures, Elsevier, 2021: pp. 2724–2738.

[103] L. Azzouz, Y. Chen, M. Zarrelli, J.M. Pearce, L. Mitchell, G. Ren, M. Grasso, Mechanical properties of 3-D printed truss-like lattice biopolymer non-stochastic structures for sandwich panels with natural fibre composite skins, Compos. Struct. 213 (2019) 220–230. https://doi.org/https://doi.org/10.1016/j.compstruct.2019.01.103.

[104] M. Shahkarami, A. Zeinedini, Flexural Properties of 3D-printed hierarchical-sinusoidal corrugated core sandwich panels with natural fiber reinforced skins, Polym. Polym. Compos. 30 (2022) 09673911221101299.

[105] Y. Feng, H. Qiu, Y. Gao, H. Zheng, J. Tan, Creative design for sandwich structures: A review, Int. J. Adv. Robot. Syst. 17 (2020). https://api.semanticscholar.org/CorpusID:221766452.

[106] N. Iranmanesh, H. Yazdani Sarvestani, B. Ashrafi, M. Hojjati, Beyond honeycombs: Core topology's role in 3D-printed sandwich panels, Mater. Today Commun. 37 (2023) 107548. https://doi.org/https://doi.org/10.1016/j.mtcomm.2023.107548.

[107] R. Bhoopathi, M. Ramesh, C. Deepa, Fabrication and Property Evaluation of Banana-Hemp-Glass Fiber Reinforced Composites, Procedia Eng. 97 (2014) 2032–2041. https://doi.org/https://doi.org/10.1016/j.proeng.2014.12.446.

[108] D. Cao, S. Malakooti, V.N. Kulkarni, Y. Ren, Y. Liu, X. Nie, D. Qian, D.T. Griffith, H. Lu, The effect of resin uptake on the flexural properties of compression molded sandwich composites, Wind Energy 25 (2022) 71–93. https://doi.org/https://doi.org/10.1002/we.2661.

[109] M. Kurhe Nikhil, B. Shedbale Indrajeet, D. Charapale Utkarsh, R. Manoharan, Modal Analysis of Hybrid Laminated Composite Sandwich Plate, Mater. Today Proc. 5 (2018) 12453–12466. https://doi.org/https://doi.org/10.1016/j.matpr.2018.02.225.

[110] A.M. Adole, I. Anum, M.Y. Jamaludin, A.R. Suhaimi, Mechanical characterization of green sandwich composites from kenaf fiber skins and sawdust core, Discov. Civ. Eng. 2 (2025) 76. https://doi.org/10.1007/s44290-025-00241-9.

[111] M.G. Atahan, M. Erikli, E. Ozipek, F. Ozgun, Comparative study on bending behavior and damage analysis of 3D-printed sandwich core designs with bio-inspired reinforcements, Eng. Fail. Anal. 163 (2024) 108439.

[112] S. Zu, J. Huang, Y. Du, Q. Wang, H. Wang, H. Wu, Y. Zhao, Bending behavior and failure mechanisms of CFRP hyperbolic foldcore sandwich beams: Experimental and numerical investigations, Structures 81 (2025) 110341. https://doi.org/https://doi.org/10.1016/j.istruc.2025.110341.

[113] S. Kamarian, A. Teimouri, M. Alinia, S. Saber-Samandari, J. Song, Machine learning for bending behavior of sandwich beams with 3D-printed core and natural fiber-reinforced composite face sheets, Polym. Compos. 45 (2024) 3043–3054.

[114] D. Cao, D. Bouzolin, H. Lu, D.T. Griffith, Bending and shear improvements in 3D-printed core sandwich composites through modification of resin uptake in the skin/core interphase region, Compos. Part B Eng. 264 (2023) 110912.

[115] G.G. del Pino, A. Bezazi, A.C. Kieling, J.C. de M. Neto, S.D. Garcia, J.L.V. Rivera, M. Valin Fernández, A.R. Torres, F.R. Valenzuela Diaz, The evaluation of sandwich composite materials with vegetable fibers in a castor oil polyurethane matrix with their faces and honeycomb core made in a 3D printer, Polymers (Basel). 16 (2024) 2980.

[116] X. Li, P. Qu, H. Kong, Y. Lei, A. Guo, S. Wang, Y. Wan, J. Takahashi, Enhanced mechanical properties of sandwich panels via integrated 3D printing of continuous fiber face sheet and TPMS core, Thin-Walled Struct. 204 (2024) 112312. https://doi.org/https://doi.org/10.1016/j.tws.2024.112312.

[117] N.K. Choudhry, S.R. Bankar, B. Panda, H. Singh, Experimental and numerical analysis of the bending behavior of 3D printed modified auxetic sandwich structures, Mater. Today Proc. 56 (2022) 1356–1363. https://doi.org/https://doi.org/10.1016/j.matpr.2021.11.425.

[118] W. Xu, S. Han, N. Ma, Q. Han, C. Li, Superior flexural toughness and load-bearing performance of origami-enhanced honeycomb sandwich beams, Acta Mech. Sin. 42 (2026) 424955. https://doi.org/10.1007/s10409-025-24955-x.

[119] M. Sefidi, H. Taghipoor, Analysis of deformation and failure mechanism of sandwich beams with lattice core under three-point bending load., Sci. Rep. 14 (2024) 13302. https://doi.org/10.1038/s41598-024-64198-y.

[120] H. Adibi, A.A. Lalaei, A. Nakhaei, Unified experimental and finite element analysis of the mechanical performance of 3D-printed honeycomb and auxetic sandwich cores, Compos. Part C Open Access 18 (2025) 100656. https://doi.org/https://doi.org/10.1016/j.jcomc.2025.100656.

[121] S. Li, Y. Feng, M. Wang, Y. Hu, Mechanical Behavior of Natural Fiber-Based Bi-Directional Corrugated Lattice Sandwich Structure, Materials (Basel). 11 (2018) 2578. https://doi.org/10.3390/ma11122578.

[122] M. Kamali Moghaddam, Typha leaves fiber and its composites: A review, J. Nat. Fibers 19 (2022) 4993–5007.

[123] M. Rahman, N. Cicek, K. Chakma, The optimum parameters for fibre yield (%) and characterization of Typha latifolia L. fibres for textile applications, Fibers Polym. 22 (2021) 1543–1555.

[124] S. Arif, A.A. Maan, R.M. Aadil, M.K.I. Khan, Assessing canola residue: A comprehensive analysis of composition, cellulose extraction and characterization, Cellulose 32 (2025) 8185–8200.

[125] H. Yang, R. Yan, H. Chen, D.H. Lee, C. Zheng, Characteristics of hemicellulose, cellulose and lignin pyrolysis, Fuel 86 (2007) 1781–1788. https://doi.org/https://doi.org/10.1016/j.fuel.2006.12.013.

[126] A.D. French, How Crystalline is My Cellulose Specimen? Probing the Limits of X-ray Diffraction, BioResources 17 (2022) 5557–5561. https://ojs.bioresources.com/index.php/BRJ/article/view/22009.

[127] A.D. French, Increment in evolution of cellulose crystallinity analysis, Cellulose 27 (2020) 5445–5448. https://doi.org/10.1007/s10570-020-03172-z.

[128] L. Segal, J.J. Creely, A.E. MartinJr, C.M. Conrad, An Empirical Method for Estimating the Degree of Crystallinity of Native Cellulose Using the X-Ray Diffractometer, Text. Res. J. 29 (1959) 786–794. https://doi.org/10.1177/004051755902901003.

[129] A. Thygesen, J. Oddershede, H. Lilholt, A.B. Thomsen, K. Ståhl, On the determination of crystallinity and cellulose content in plant fibres, Cellulose 12 (2005) 563–576. https://doi.org/10.1007/s10570-005-9001-8.

[130] A.D. French, Idealized powder diffraction patterns for cellulose polymorphs, Cellulose 21 (2014) 885–896. https://doi.org/10.1007/s10570-013-0030-4.

[131] P. Scherrer, Bestimmung der Größe und der inneren Struktur von Kolloidteilchen mittels Röntgenstrahlen, in: n.d. https://api.semanticscholar.org/CorpusID:136663851.

[132] S. Gowid, E. Mahdi, F. Alabtah, Modeling and optimization of the crushing behavior and energy absorption of plain weave composite hexagonal quadruple ring systems using artificial neural network, Compos. Struct. 229 (2019) 111473. https://doi.org/https://doi.org/10.1016/j.compstruct.2019.111473.

[133] Y. Ding, K. Yu, Chapter 3 - All-strength-grade polyethylene engineered cementitious composite (PE-ECC): Mechanical performance, energy parameters and its performance-based design method, in: Y.X. Zhang, K.B.T.-A. in E.C.C. Yu (Eds.), Woodhead Publ. Ser. Civ. Struct. Eng., Woodhead Publishing, 2022: pp. 39–76. https://doi.org/https://doi.org/10.1016/B978-0-323-85149-7.00007-0.

[134] A. Baroutaji, A. Arjunan, G. Singh, J. Robinson, Crushing and energy absorption properties of additively manufactured concave thin-walled tubes, Results Eng. 14 (2022) 100424. https://doi.org/https://doi.org/10.1016/j.rineng.2022.100424.

[135] N.S. Ha, T.-U. Lee, H. Lu, J. Li, G. Lu, Y.M. Xie, Energy absorption characteristics of fractal multi-cell square tubular structures under axial crushing, Thin-Walled Struct. 205

(2024) 112365. https://doi.org/https://doi.org/10.1016/j.tws.2024.112365.

[136] E. Ostertagova, O. Ostertag, J. Kováč, Methodology and application of the Kruskal-Wallis test, Appl. Mech. Mater. 611 (2014) 115–120.

[137] M. Mia, P.R. Dey, M.S. Hossain, M.T. Arafat, M. Asaduzzaman, M. Shoriat Ullah, S.M. Tareq Zobaer, Taguchi S/N based optimization of machining parameters for surface roughness, tool wear and material removal rate in hard turning under MQL cutting condition, Measurement 122 (2018) 380–391. https://doi.org/https://doi.org/10.1016/j.measurement.2018.02.016.

[138] G.R. Yang, X.-J. Wang, Artificial Neural Networks for Neuroscientists: A Primer, Neuron 107 (2020) 1048–1070. https://doi.org/10.1016/j.neuron.2020.09.005.

[139] J.R.C. Dizon, A.H. Espera, Q. Chen, R.C. Advincula, Mechanical characterization of 3D-printed polymers, Addit. Manuf. 20 (2018) 44–67. https://doi.org/https://doi.org/10.1016/j.addma.2017.12.002.

[140] I. Manoj, A. Kumar Shah, A. Jain, Strength and failure assessments of 3D printed PLA single lap joints: Experimental and numerical analysis, Eng. Fail. Anal. 161 (2024) 108257. https://doi.org/https://doi.org/10.1016/j.engfailanal.2024.108257.

[141] M.R. Adibeig, M.-A. Saeimi-Sadigh, F. Vakili-Tahami, M.R. Karimani, G. Marami, Quasi-static simulation and fatigue life estimation of fused filament fabrication of polylactic acid specimens using finite element method, J. Manuf. Process. 106 (2023) 202–213. https://doi.org/https://doi.org/10.1016/j.jmapro.2023.09.071.

[142] M.A. Kazemi, S. Jafari, M. akbari, Experimental and numerical damage assessment of PLA based on young's modulus reduction using the bonora damage model, Forces Mech. 22 (2026) 100345. https://doi.org/https://doi.org/10.1016/j.finmec.2025.100345.

[143] K. Panbarasu, V.R. Ranganath, R. V Prakash, An investigation on static failure behaviour of CFRP quasi isotropic laminates under in-plane and out-of-plane loads, Mater. Today Proc. 39 (2021) 1465–1471. https://doi.org/https://doi.org/10.1016/j.matpr.2020.05.367.

[144] M. Poletto, H.L. Ornaghi, A.J. Zattera, Native Cellulose: Structure, Characterization and Thermal Properties, Materials (Basel). 7 (2014) 6105–6119. https://doi.org/10.3390/ma7096105.

[145] S. Park, J.O. Baker, M.E. Himmel, P.A. Parilla, D.K. Johnson, Cellulose crystallinity index: measurement techniques and their impact on interpreting cellulase performance., Biotechnol. Biofuels 3 (2010) 10. https://doi.org/10.1186/1754-6834-3-10.

[146] J. Zhu, H. Zhu, J. Njuguna, H. Abhyankar, Recent development of flax fibres and their reinforced composites based on different polymeric matrices, Materials (Basel). 6 (2013) 5171–5198.

[147] M.H. Hamidon, M.T.H. Sultan, A.H. Ariffin, A.U.M. Shah, Effects of fibre treatment on mechanical properties of kenaf fibre reinforced composites: a review, J. Mater. Res. Technol. 8 (2019) 3327–3337.

[148] A.W. Nugroho, A.H. Mahardika, Improving the tensile properties of 3D printed PLA by optimizing the processing parameter, J. Energy, Mech. Mater. Manuf. Eng. 4 (2019).

[149] A.R. Kafshgar, S. Rostami, M.R.M. Aliha, F. Berto, Optimization of Properties for 3D Printed PLA Material Using Taguchi, ANOVA and Multi-Objective Methodologies, Procedia Struct. Integr. 34 (2021) 71–77.

https://doi.org/https://doi.org/10.1016/j.prostr.2021.12.011.

[150] D. Ali, A.F. Huayier, A. Enzi, Parametric Prediction of FDM Process to Improve Tensile Properties Using Taguchi Method and Artificial Neural Network, Adv. Sci. Technol. Res. J. 17 (2023) 130–138. https://doi.org/10.12913/22998624/169572.

[151] R. Teharia, R.M. Singari, H. Kumar, Optimization of process variables for additive manufactured PLA based tensile specimen using taguchi design and artificial neural network (ANN) technique, Mater. Today Proc. 56 (2022) 3426–3432. https://doi.org/10.1016/j.matpr.2021.10.376.

[152] A.E. Mohan, H.A. Habeeb, A.H. Abood, Experimental and modeling stress concentration factor (SCF) of a tension poly lactic acid (PLA) plate with two circular holes, Period. Eng. Nat. Sci. 7 (2019) 1733–1742.

[153] A. Zabihollah, S. Bardowell, B. Does, R. Vuddandam, Experimental Determination of tensile stress concentration factors of 3D-printed PLA polymers: fillet radius, hole diameter, and infill density, Adv. Mater. Res. 1180 (2024) 13–22.

[154] R.M. Mazarbhuiya, D. Veeman, Tensile performance of 3D-printed PLA material with conventionally drilled and additively fabricated holes, Prog. Addit. Manuf. (2026). https://doi.org/10.1007/s40964-025-01483-w.

[155] M.R. Khosravani, T. Reinicke, Mechanical strength of 3D-printed open hole polymer plates, Procedia Struct. Integr. 41 (2022) 664–669. https://doi.org/https://doi.org/10.1016/j.prostr.2022.05.075.

[156] A. Sabik, M. Rucka, A. Andrzejewska, E. Wojtczak, Tensile failure study of 3D printed PLA using DIC technique and FEM analysis, Mech. Mater. 175 (2022) 104506. https://doi.org/https://doi.org/10.1016/j.mechmat.2022.104506.

[157] M. Seifollahi, M.Z. Kabir, Fatigue Life Assessment of Notched PLA Manufactured Using FDM 3D-Printing Technique, Polymers (Basel). 18 (2026) 1. https://doi.org/10.3390/polym18010001.

[158] Z. Wang, Z. Li, W. Xiong, Numerical study on three-point bending behavior of honeycomb sandwich with ceramic tile, Compos. Part B Eng. 167 (2019) 63–70.